NASA SP-256

ASTRONOMICAL USE OF TELEVISION-TYPE IMAGE SENSORS

A symposium held at
PRINCETON UNIVERSITY
PRINCETON, N.J.
May 20–21, 1970

NATIONAL AERONAUTICS AND SPACE ADMINISTRATION

NASA SP-256

ASTRONOMICAL USE OF TELEVISION-TYPE IMAGE SENSORS

The proceedings of a symposium sponsored by the
National Aeronautics and Space Administration
and the American Astronomical Society and held
at Princeton University, May 20–21, 1970

Edited by
V. Richard Boscarino
Princeton University

Scientific and Technical Information Office 1971
NATIONAL AERONAUTICS AND SPACE ADMINISTRATION
Washington, D.C.

ORGANIZING COMMITTEE

John L. Lowrance
Martin Schwarzchild
Lyman Spitzer, Jr.

For sale by the National Technical Information Service, Springfield, Virginia 22151 — Price $3.00

PREFACE

Early attempts to apply television sensors to astronomical measurement programs yielded marginal results. However, the potential gain in sensitivity and efficiency with these photoelectric sensors was a strong incentive for continued effort and support. Emphasis was increased by the advent of space probes and orbiting observatories where few acceptable alternatives to television exist.

This symposium was organized to bring together the small but active group of workers in the field at this time when progress is rapidly being made and interest is mounting.

The papers presented were selected to cover most of the techniques and applications under serious consideration today. The first day of the program was devoted to television type sensors and systems used as photometers. The second day was addressed to the processing of raw video data, in particular, computer processing to achieve rectification and enhancement.

In addition to the papers recorded in these Proceedings, two additional speakers added greatly to the value of the symposium. Professor Martin Schwarzchild's address, "Astronomers vs New Technology," on Wednesday evening was an inspiration to those of us working to apply new technology from an astronomer for whom there has never been a feeling of "versus." Professor John Tukey, upon whose work modern data processing is greatly dependent, gave a summation of the second day's program.

As the reader will note, television type sensors combined with digital computer data processing promise to become powerful tools for a wide range of scientific applications.

John W. Lowrance
Chairman, Organizing Committee

Page intentionally left blank

FOREWORD

It has been widely recognized by the scientific community that television-type sensors could provide significant advantages for astronomical measurements both in space and on the ground. The National Aeronautics and Space Administration has supported research and development on both image tubes for astronomy and digital computer processing of astronomical data over the past several years. During this time substantial advances have been made, in which Princeton University has been a leader. Thus, we welcomed the opportunity to cosponsor, with the American Astronomical Society, this symposium on Astronomical Uses of Television Type Image Sensors as an important event in the continued progress in these techniques for improved astronomical measurements.

Jesse L. Mitchell, Director
Physics and Astronomy Programs
Office of Space Science and Applications
National Aeronautics and Space Administration

Page intentionally left blank

CONTENTS

EXPERIENCE WITH TV SENSOR SYSTEMS

COMPUTER PROCESSING OF IMAGE DATA

EXPERIENCE FROM MARINER TV EXPERIMENTS[*]

G. Edward Danielson, Jr.[**]

Jet Propulsion Laboratory
California Institute of Technology
Pasadena, California

ABSTRACT

Television (TV) cameras equipped with vidicons which were operated in a "slow-scan" mode were the principal experiments on the Mariner 1964 and 1969 missions to Mars. This paper describes the key characteristics of the data relevant to obtaining photometric and geometric scientific information about the surface of Mars. Extensive pre-launch calibrations of these cameras were carried out to determine such properties as light-transfer functions, erasure or residual characteristics of the vidicons, thermal and temporal effects, and spectral response of each complete system. These calibration data characterized each picture element of the flight vidicons. The known properties which limit both photometric and geometric measurements in the data are discussed.

INTRODUCTION

The TV cameras were those experiments on Mariners 1964 and 1969 which successfully acquired and transmitted pictures of the Martian surface to Earth.[***] The pictures from Mariner 4 (1964) gave scientists their first high-resolution glimpse of Mars and revealed a surface densely populated with impact craters similar to the surface of the Moon. In 1969, NASA sent two spacecraft on fly-by trajectories to Mars. Mariner 6 sent back 76 full-resolution pictures (two and a half complete playbacks of the analog tape recorder) and Mariner 7 was re-programmed in-flight to send back 126 full-resolution pictures (4 tape loads). In addition, over 1777 low-resolution photometric pictures were obtained via the real-time telemetry.

---

[*] This paper presents the results of one phase of research carried out at the Jet Propulsion Laboratory, California Institute of Technology, under Contract No. NAS 7-100, sponsored by the National Aeronautics and Space Administration.

[**] Television Experiment Representative, Mariner Mars 1969 Project.

[***] The Principal Investigator for both of these experiments was Dr. Robert B. Leighton of the California Institute of Technology.

These data recorded five full rotations of the planet at a resolution better than that obtained by the best Earth-based photography. These data were taken at phase angles which ranged from 25° to 80° and through color filters which will provide information concerning the photometric function and its spectral dependence. The geometrically rectified pictures make it possible to measure the radius of Mars and establish an accurate cartographic control net using surface markings in both the near and far encounter pictures. These data are rich in scientific information but depend on careful computer restoration and decalibration(1).

INSTRUMENT DESCRIPTIONS

Both Mariner 1964 and Mariner 1969 TV experiments utilized General Electrodynamics Corporation vidicons which were operated in a "slow-scan" mode. The Mariner 1964 system used an electrostatic deflection and focus system, while the Mariner 1969 system employed an electromagnetic system. Detailed descriptions of these systems are given in references (2), (3) and (4). Both systems were designed to maximize the scientific data return within the data storage and bandwidth limitations of the mission. The Mariner 4 camera consisted of an f/8 Cassegrain reflecting telescope with a focal length of 305 mm and a 1.05° field of view. The format on the vidicon faceplate was a 5.5-mm x 5.5-mm square area. The Mariner 6 and 7 TV experiments employed two vidicon cameras. The wide-angle camera had an f/5.6 multi-element refractor lens with a 50-mm focal length whose shutter assembly incorporated broad-band optical filters sequenced in the order: red, green, blue, green. The narrow-angle camera utilized an f/2.5, 500-mm-focal-length, modified Schmidt-Cassegrain telescope. The active formats of the vidicons had an area 9.6 x 12.5 mm. The functional descriptions of these systems are compared in Table 1.

VIDICON PROPERTIES

A vidicon tube was selected as the camera sensing device because of the ruggedness, light weight, small size and ability to handle a 50-to-1 range of illumination with fixed operating voltages. The vidicon photoconductive target material is an amphorous selenium compound developed by the manufacturer, General Electrodynamics Corporation, which provided adequate storage properties for the "slow-scan" mode of operations.

One of the outstanding properties of these vidicons is the reproducibility on a point-by-point basis. The target noise which is analogous to photographic grain is considerably less than that of photographic emulsion in addition to being the same from picture to picture. In Figure 1 this reproducibility is demonstrated quite vividly where the data numbers (dn values) were averaged over a 2 x 2 picture element square and plotted against the element number for lines 60 and 61 for all uniformly illuminated frames of similar gain state (5). These data show a striking consistency in point-to-point variation.

Table 1.—Comparison of the Function Descriptions of Mariner 1964 and Mariner 1969

Characteristic	Mariner 1969 camera A	Mariner 1969 camera B	Mariner 1964
Focal length, mm . . .	52	508	305
Field of view, deg . . .	11 x 14	1.1 x 1.4	1 x 1
Active scan lines	704	704	200
Active pixels/line . . .	945	945	200
Best surface scale, m/TV line	1110	115	770
Shutter speed, msec . .	90	6	200
Quantization/pixel, bits	8	8	6
Frame time, sec	42.24	42.24	24
System weight, lb. . . .	48	48	12
System power, W	32	32	8

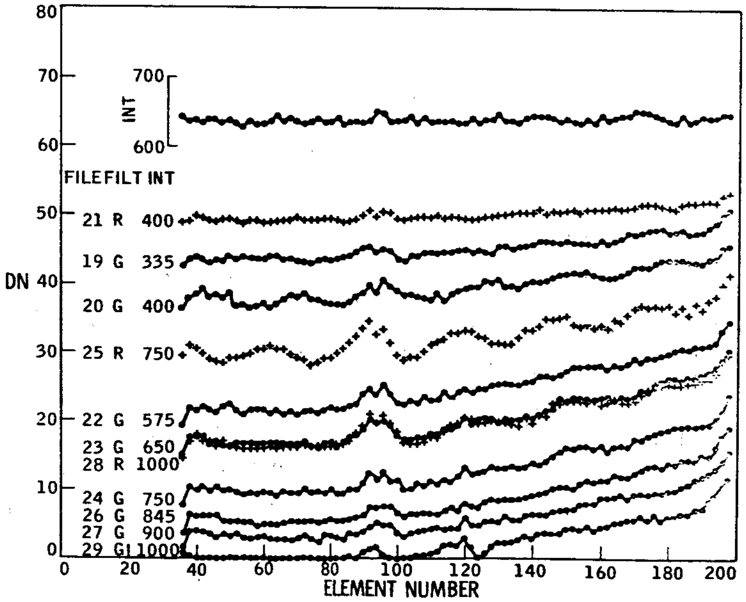

Figure 1.–Plot of 2 x 2 averages of data numbers for lines 60 and 61 of Mariner 1964 uniformly illuminated calibration pictures. The averaging minimized the efforts of periodic noise. At the top is plotted the corresponding average of picture 23 after calibration.

Figure 2 illustrates this reproducibility on a frame-by-frame comparison of the same exposures from test to test for Mariner 1969. The contours were produced by clipping the most significant bits of the binary data.

The vidicons were calibrated and tested extensively prior to installation into the camera heads and calibrated again as part of the various integrated subsystem calibrations. The tubes were subjected to well-established screening tests prior to selection for use in the flight systems. The vidicon's sensitivity, spectral response, light-transfer function, shading, residual or erasure, dark current and modulation transfer properties are measured.

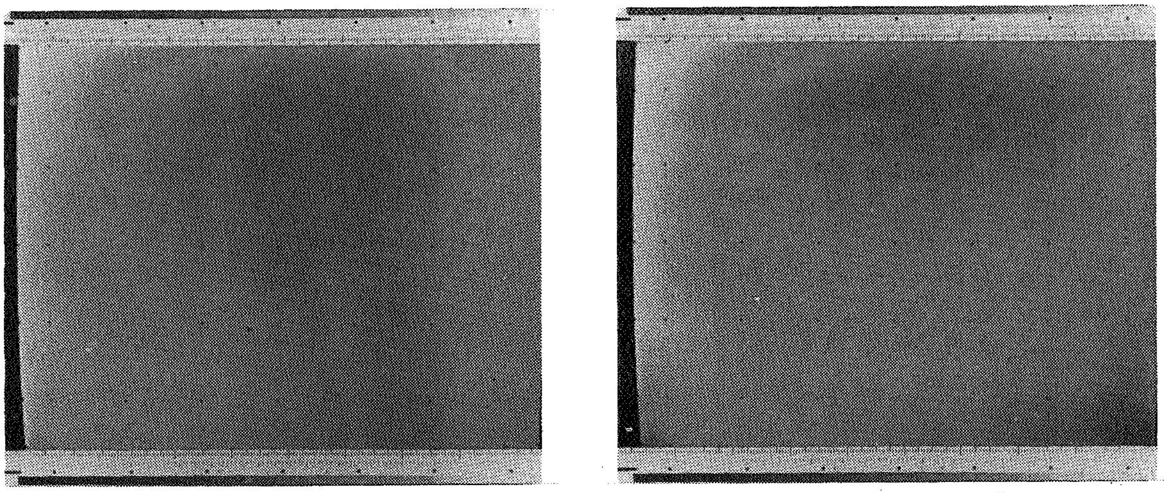

CALIBRATION 7163 FRAME CALIBRATION 7183 FRAME

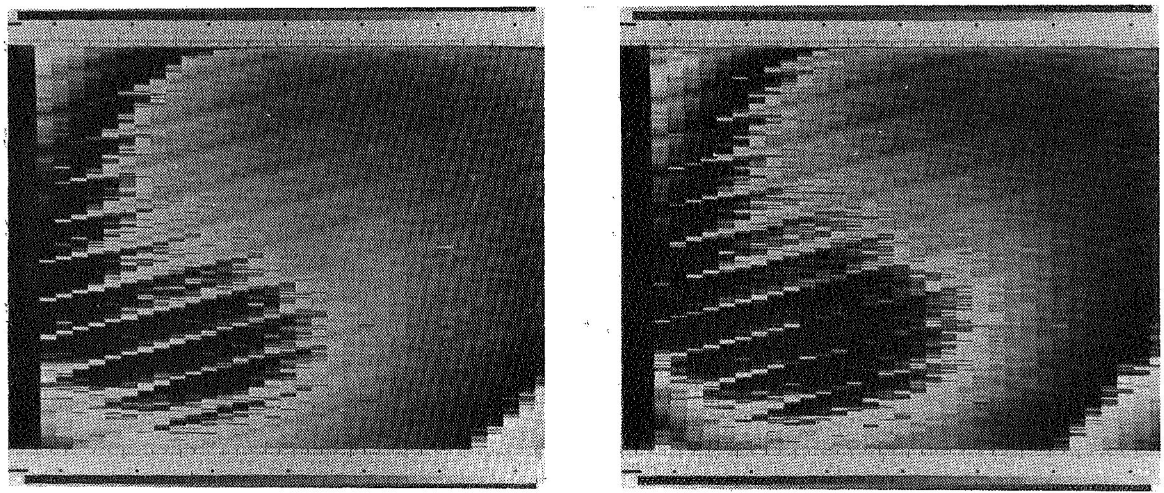

CALIBRATION 7163 FRAME CALIBRATION 7183 FRAME

Figure 2. -Identical flat field calibration frames from two separate tests illustrating the reproducibility from test to test. The data are displayed with the two most significant bits suppressed to illustrate the gradual shading. The contoured data were also sampled once every 28 elements for this display.

Typical values for each of these properties are listed in Figure 3. These vidicons are tested for susceptibility to aging and temperature effects in the subsystem calibration tests.

PHOTOMETRIC MEASUREMENTS WITH VIDICONS

The calibration and environmental test programs were designed to duplicate the full range of conditions inherent in launch, transit and encounter and, in addition, define the performance characteristics of the TV system in the Mars encounter environment. These calibrations were able to characterize the sensitivity of the vidicon surface to a fineness limited by the sampling of the data in spatial resolution. In the Mariner 4, 6 and 7 TV experiments, it had been found that the binary encoding limit of the data in intensity could have been extended. The information in the least significant bit of the six-bit binary encoding(0-63) of the Mariner 4 data was not limited by the thermal noise of the preamplifier circuit or the vidicon random noise. The Mariner 1969 TV system employed an eight-bit binary encoding (0-255) in which the least significant bit was also not limited by the vidicon random

PEAK SENSITIVITY (SLOW SCAN)	5-8 na/μ watt
DARK CURRENT	.1 na
DYNAMIC RANGE	50-1
RANGE OF SPECTRAL SENSITIVITY	NEAR UV, VISIBLE TO ~670 nm (POOR RED RESPONSE)
MTF FOR HIGH CONTRAST SINE WAVE	10% RESPONSE AT 40 O.L.P./min
SHADING	10 TO 35% ACROSS FRAME
RESIDUAL (ONE ERASE CYCLE)	3-16%

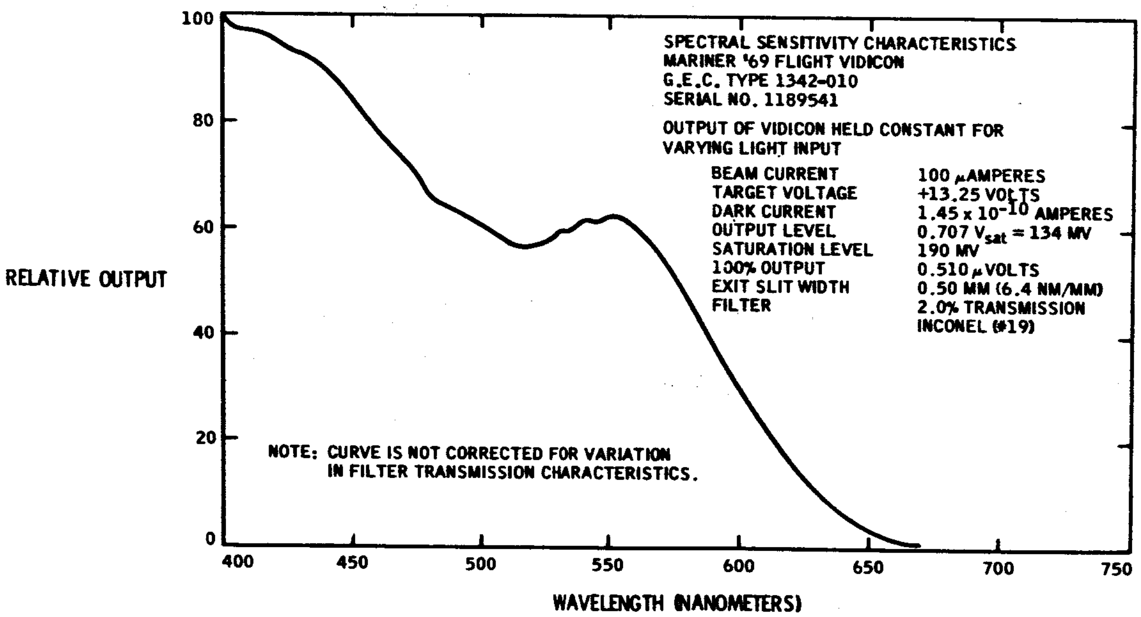

BEAM CURRENT	100 μAMPERES
TARGET VOLTAGE	+13.25 VOLTS
DARK CURRENT	1.45×10^{-10} AMPERES
OUTPUT LEVEL	$0.707\ V_{sat} = 134$ MV
SATURATION LEVEL	190 MV
100% OUTPUT	0.510 μVOLTS
EXIT SLIT WIDTH	0.50 MM (6.4 NM/MM)
FILTER	2.0% TRANSMISSION INCONEL (#19)

Figure 3. -Typical values obtained from the General Electrodynamic Corp. vidicons which were used in the Mariner 1969 TV system when it was in a slow-scan mode.

noise or the thermal noise of the preamplifier. The Mariner 1969 television cameras were unfortunately very susceptible to coherent or periodic noises. The techniques used to remove this noise are covered in reference (1); see also Figure 4. Here the experience of Mariners 1964 and 1969 has influenced the design of the Mariner 1971 TV cameras. This system will be using nine-bit binary encoding of the data (512 shades of gray) at the expense of a 5% loss in both resolution and coverage. Preliminary tests on the Mariner Mars 1971 prototype system revealed the random noise to be statistically a small fraction of the next to the least significant bit (6).

The photometric decalibration process involves relating each data number in the pictures with the known pre-flight properties from the various tests mentioned above. A detailed description of this decalibration is found in references (3), (7) and (8). The key unknown in this process is the aging effects of the vidicon. Certain accelerated aging tests are performed to decrease the probability of flight tubes exhibiting extreme changes in any of its characteristics in the vidicon screening process. Testing facilities and schedule constraints have limited the determination of these aging effects. It has also been found that one cannot relate this complex property from one system to the other due to the inconsistency among the vidicons. As an example, the spare Mariner 1969 TV subsystem was found to have a 16% change in sensitivity between tests. This system had been in a dormant, "on-the-shelf" condition for 9 months in the interval between these tests. In contrast, the Mariner 6 flight systems sensitivity showed no change over a 6-month period (with repeated careful checks) during the pre-launch calibration and system tests.

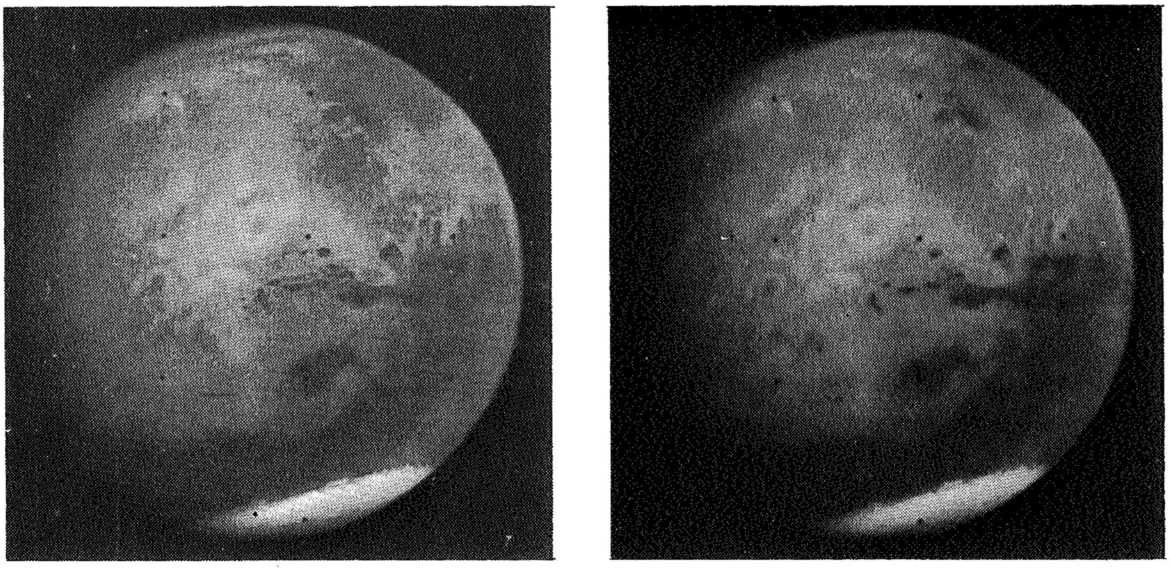

7F70 RAW (CONTRAST ENHANCED) 7F70 NOISE REMOVED

Figure 4.-Noise removal. The presence of periodic noise is somewhat evident as stripes in the upper left-hand corner running diagonally from left to right.

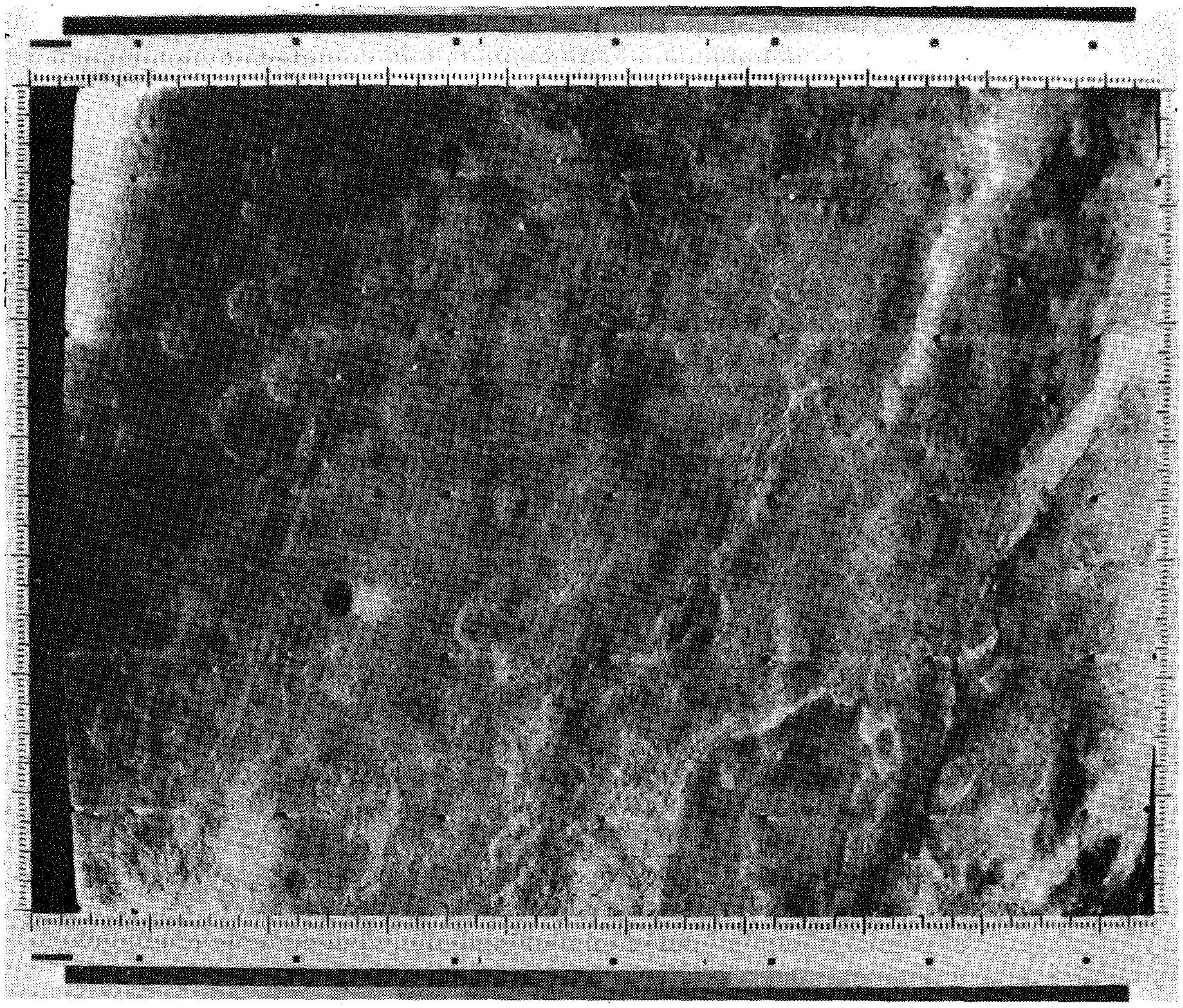

6N7

Figure 5.— Photograph illustrating the saturation of the upper left-hand corner of the seventh picture of Mariner 6 near encounter caused by the shading effects of the deflection coils.

Another interesting phenomenon which has been found to be a function of temperature, aging and incident light level is the shading or variation in sensitivity across the vidicon photoconductive surface. The majority of this shading present in the Mariner 1969 TV systems was due to the deflection and focusing coils. This was very pronounced in the upper left-hand corner of all the frames, as seen in Figure 5.

One of the most troublesome properties has been erasure or residual image. This can be characterized by exposing the vidicon and subjecting the system to a normal read and erasure cycle, then capping the optics for the next picture and determining what percentage of the original scene is present in the subsequent read cycle. Figure 6 illustrates the persistence properties of this residual as a function of the number of erase cycles. A dramatic example of this effect in the Mariner 7 "A" camera near-encounter pictures is shown in Figure 7. One can readily see the limb in all four frames. A test target (Figure 8) was designed by Dr. Leighton, of the California Institute of Technology, which was incorporated into the subsystem calibration to characterize this residual. This test target correlated the percentage of residual to the original scene gray level (or data number). It was found that this residual could be defined for the majority of types of residuals, but that certain cases such as the bright limb of a planet contrasted against black space were peculiar and required hand manipulation of the residual map for complete removal. The Mariner 1971 Orbiter TV design has incorporated eleven erasure cycles in addition to switching the target voltage during these erasure cycles to reduce this residual problem. Preliminary data show their residuals to be substantially lower than the 5 to 16 % range for the Mariner 1969 vidicons (6).

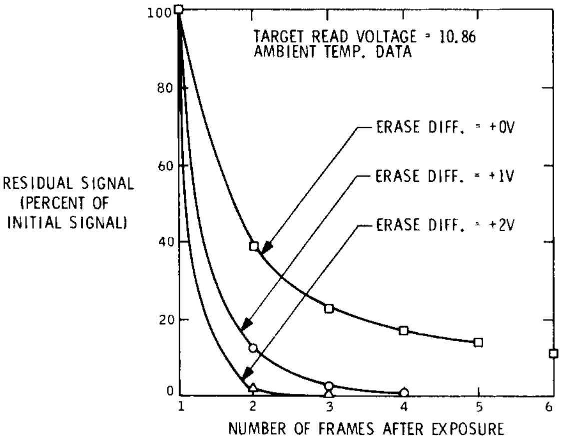

Figure 6.-Test data from a vidicon which is a worst-case example of percentage of of residual as a function of frames after exposure. The improved erasure characteristics were obtained by changing the target voltage during the erasure cycle.

GEOMETRIC MEASUREMENTS WITH VIDICONS

The accuracy of the measurement of the planet's diameter, orientation of its spin axis, and the location of various surface features and impact craters all depend on the geometric properties of both the vidicon's electron optics and the camera's optics. To determine the contributions due to the camera optics and those due to the vidicon, a reseau pattern was placed on the photoconductive faceplate of the vidicon. This geometric pattern was measured to obtain a scale factor accurate to one part in 10^4 for each vidicon prior to installation into the camera head. A calibration test target with a measured orthogonal grid pattern was used to characterize the geometric corrections needed to accurately reconstruct the flight pictures. The test target calibrated the optics' geometric contributions from object space to image space. The reseau pattern determined the distortions in the vidicon electron optics. Recent measurements by Dr. Leighton (who used a two-dimensional polynomial interpolation technique) for locating the limb in the Mariner 1969 far-encounter pictures indicate that one can consistently locate the limb profile to 0.2 of a picture element. The flight pictures have revealed a reseau pattern which is consistent from picture to picture, again to 0.2 of a pixel (picture element). A random component of 2 to 3 pixels' error has been detected in these data. The origin of this random phenomenon has not been determined to date. These measurements will allow the complete complement of far-encounter photos to be cataloged for variations in limb profile and location of the morning terminator to an accuracy of 0.2 ±0.1 of a picture element(9). Dr. Leighton has coined this particular type of data reduction as "Mars phrenology."

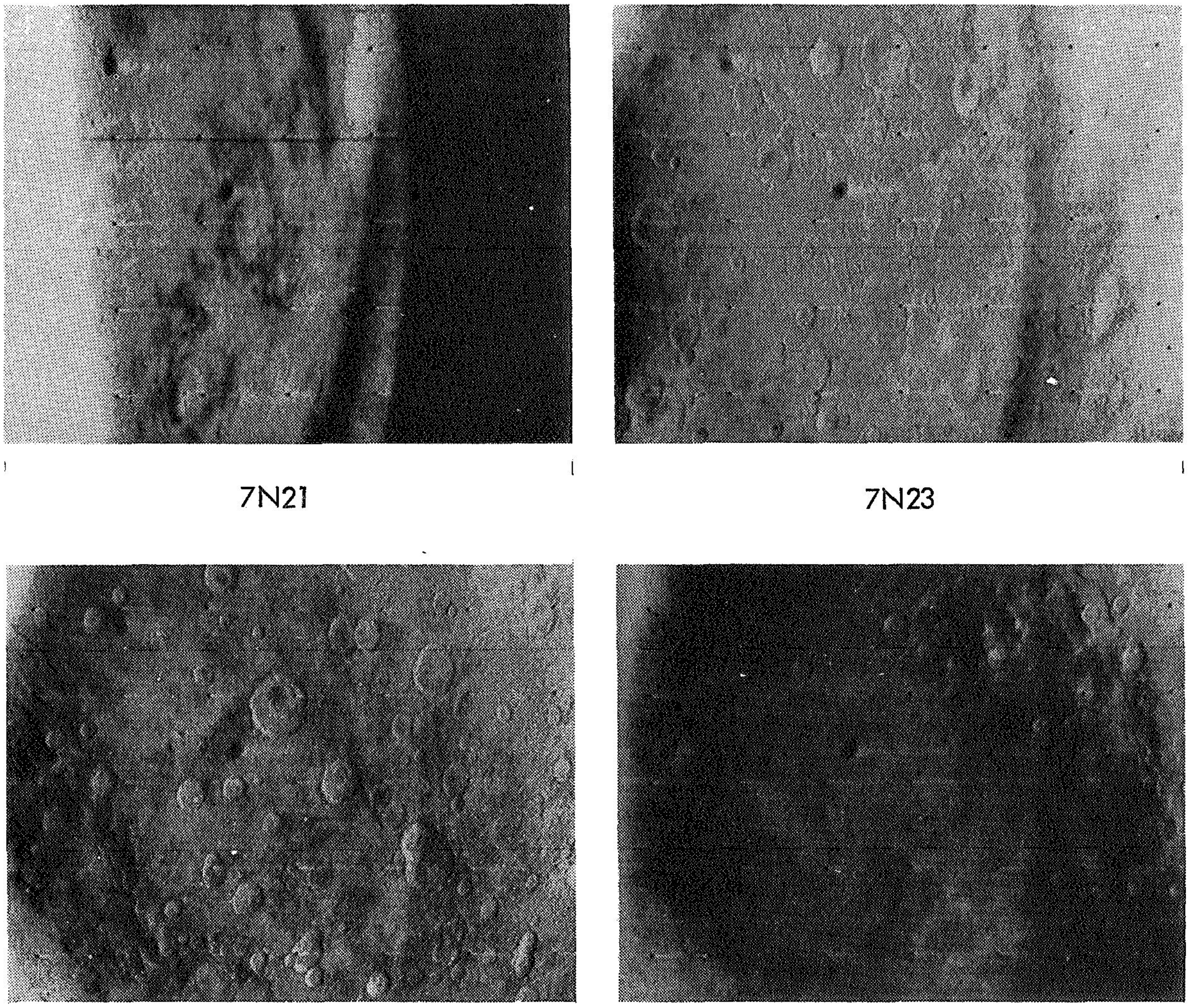

7N21

7N23

7N25

7N27

Figure 7.-Persistence properties of the vidicon. The limb in picture 7N21 is clearly evident in subsequent frames 7N23, 7N25, and 7N27.

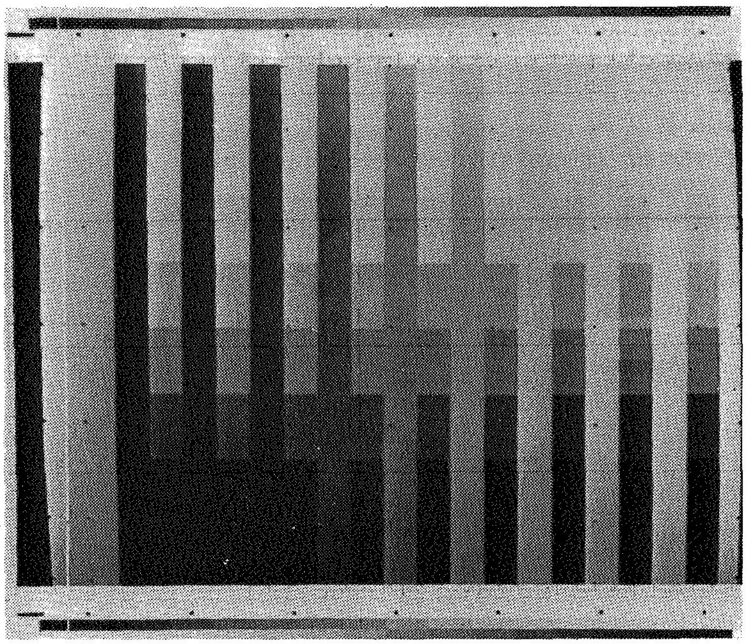

5385 LEIGHTON TEST TARGET

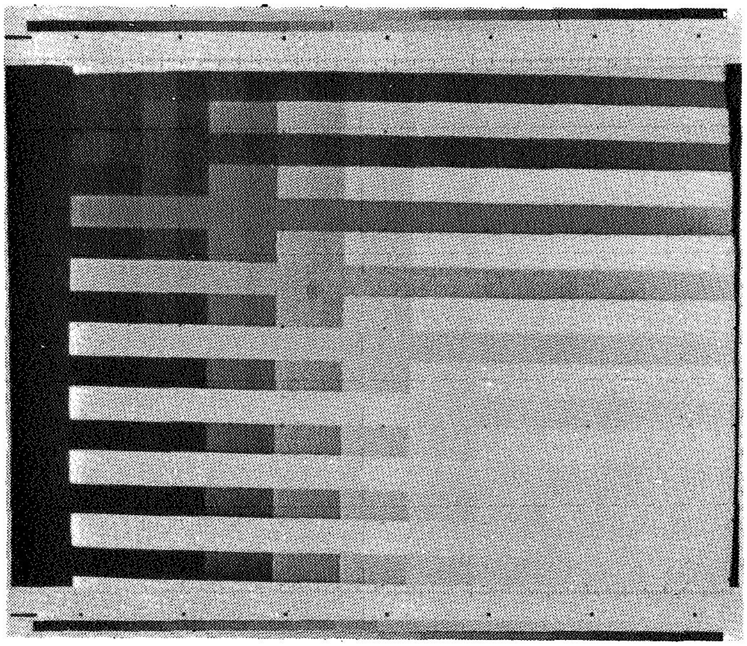

5387 ROTATED LEIGHTON TARGET

Figure 8.-Interlaced gray scale which comprised the Leighton test target. Picture 5385 is proceeded by 5387 in which the erasure characteristics as a function of previous and present gray levels are characterized.

CONCLUSION

The Mariner TV experiments demonstrated the unique photometric properties of the vidicon which potentially allow relative photometry within a picture frame to be accurately measured. (NOTE: absolute measurement of better than 5% will require the development of very precise in-flight calibration sources and techniques.) This relative photometry is ultimately limited by the preamplifier noise and the quantization noise if it is properly designed. The Mariner Mars Orbiter 1971 TV experiment has incorporated a deliberate design to utilize these measurement properties of the vidicon by encoding the nine binary bits and to decrease the susceptibility of the electronics to coherent noise on the spacecraft. Utilization of the pre-flight geometric calibrations on the Mariner Mars 1969 flight data has demonstrated the capability of geometrically locating limb profiles, crater edges, and other surface features to a small fraction of a picture element. These results demonstrate the quantity of scientific information in these data. An obvious, but previously unmentioned, fact is the dependence of these experiments on high-speed digital image processing to handle the very large quantities of data and perform the many tasks of calibrations, rectification, decalibration, noise removal, and other cosmetically pleasing manipulations to the TV pictures.

ACKNOWLEDGMENTS

The author is grateful to the entire Mariner Mars 1969 TV Experiment Team and especially to Dr. Robert B. Leighton for his support and encouragement. The efforts and support of G. M. Smith, D. D. Norris, R. A. Becker, A. G. Herriman and S. A. Collins are also gratefully acknowledged.

REFERENCES

1. Rindfleisch, T. C., Digital Image Processing for the Rectification of Television Camera Distortions, Symposium on Astronomical Use of Television Type Image Sensors, Princeton, New Jersey, May 20-21, 1970.

2. Leighton, R. B., Horowitz, N. H., Murray, B. C., Sharp, R. P., Herriman, A. G., Young, A. T., Smith, B. A., Davies, M. E., and Leovy, C. B., Mariner 6 and 7 Television Pictures: Preliminary Analysis, Science, Vol. 166, October 3, 1969, pp. 49-67.

3. Danielson, G. E., Jr., and Salomon, P. M., Environmental Testing and Calibration of the Mariner Mars 1969 Television System, AIAA 4th Space Simulation Conference, Los Angeles, September 8, 1969, Paper No. 69-994.

4. Montgomery, D. R., and Adams, L. A., Optics and the Mariner Imaging Instrument, Applied Optics, February 1970.

5. Mariner IV Pictures of Mars, Technical Report 32-884, Part I, Jet Propulsion Laboratory, Pasadena, Calif., December 1967.

6. Norris, D. D., private communication; Becker, R. A., private communication.

7. Mariner Mars 1969 Television Experiment Science Calibration Report, Mariner Mars 1969 Project Report 605-149, Jet Propulsion Laboratory, Pasadena, Calif., February 1970.

8. Dunne, J., Technical report in preparation for the Jet Propulsion Laboratory, Pasadena, Calif.

9. Leighton, R. B., private communication.

SOME FACTORS AFFECTING THE ACCURACY OF A SPACE-BORNE ASTRONOMICAL TELEVISION PHOTOMETER*

Yasushi Nozawa and Robert J. Davis

Smithsonian Astrophysical Observatory
Cambridge, Massachusetts

INTRODUCTION

The Celescope experiment consists of a set of four ultraviolet broad-band television photometers in the Orbiting Astronomical Observatory 2 (OAO 2). Intended for mapping the sky in the ultraviolet, the experiment had as its design goal the measurement of stellar brightness to an accuracy of ± 10% over a range from 0 to 10 mag. Position was to be measured to an accuracy of 1 arcmin over a field of view 2° square.

The objective of this paper is to describe a basic source of system inaccuracy in the Celescope experiment and to provide useful information for future work of a similar nature, in addition to stimulating research effort in this field.

Ideally, we should have liked to specify that the television system have an output accurately proportional to the logarithm of the input intensity over the entire dynamic range, with a response accurately uniform throughout the field of view. In practice, it was necessary to relax these specifications, requiring only that the output be repeatable to an accuracy corresponding to ±10% when referred to the input intensity and that the amplitude of the output signal be uniform to within a factor of 2 for moderate input intensity. We intended to satisfy the remainder of our system requirements by an accurate mathematical modeling of the operation of the system, supported by thorough calibration and computer programing.

As illustrated later, our initial processing of Celescope orbital data indicated that we were attaining a total system accuracy of approximately 40%. We believe that the primary sources of error are inaccuracies in the tabulated results of our calibration procedures, inadequacies in our computer modeling of Celescope system operation, and inadequacies in our mathematical model of changes of sensitivity occurring under orbital operating conditions. Many of our difficulties in analyzing orbital data would have been eliminated if we had insisted on the same degree of quality control and documentation for software as was required for hardware.

---

*This research has been supported by Contract NAS 5-1535 from the National Aeronautics and Space Administration.

TOTAL-SYSTEM CONCEPT AND SYSTEM-MODIFICATION CYCLES

Under the total-system concept, a television photometer consists of both hardware (experiment package) and software (data-processing system). Both these subsystems contribute equally to the final (total) system performance. As shown in Figure 1, a data-processing system in a television photometer is basically a reconstruction of hardware characteristics in mathematical form. As indicated later, the hardware characteristics depend also on the characteristics of the software. That is, they are inseparable partners in the television-photometer total system and cannot be developed independently. The system must be designed as a total system, including both software and hardware. In practical terms, the development of software should be emphasized as much as that of hardware. Also, proper communication between both development activities is essential for obtaining the best results. As seen in Figure 1, the quality of the data-processing system is as good as the knowledge of the hardware characteristics.

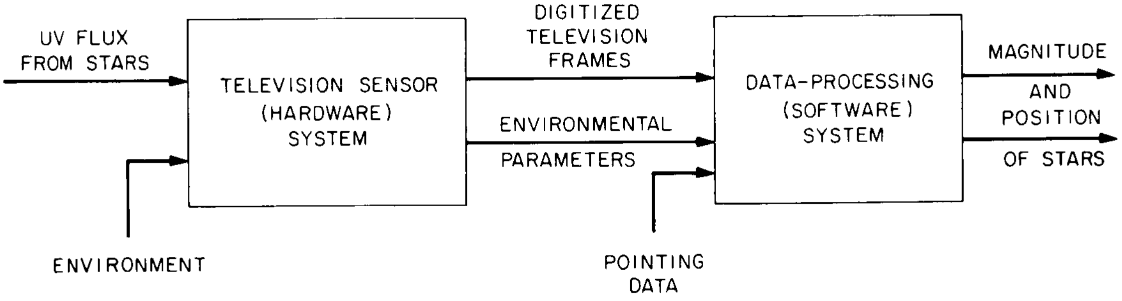

Figure 1.— Fundamental components in Celescope system.

When a television photometer is designed, especially one for space application, parallel development of hardware and software is inevitable. This means that basic designs of hardware and software are fixed in the very early stages of system development, when details of the hardware are not well known. This further implies that improvement of the data-processing system must continue during the entire life of the hardware or beyond, whenever any inadequacy of the mathematical model is revealed. Let us examine the actual situation in the system development.

Figure 2 shows the modification loop for a tentatively completed system. In the past, the major effort during prelaunch system testing has been concentrated on correcting hardware deficiency. Hardware tests that produce special data for software testing were seldom performed. Usually, these were limited to interface check or debugging (coding error correction). Therefore, the completed total system at the time of launch contained an unrecognized deficiency—that is, large discrepancies between the actual hardware characteristics and those in its mathematical model in the data-processing system. This deficiency resulted from a lack of understanding of the total-system concept.

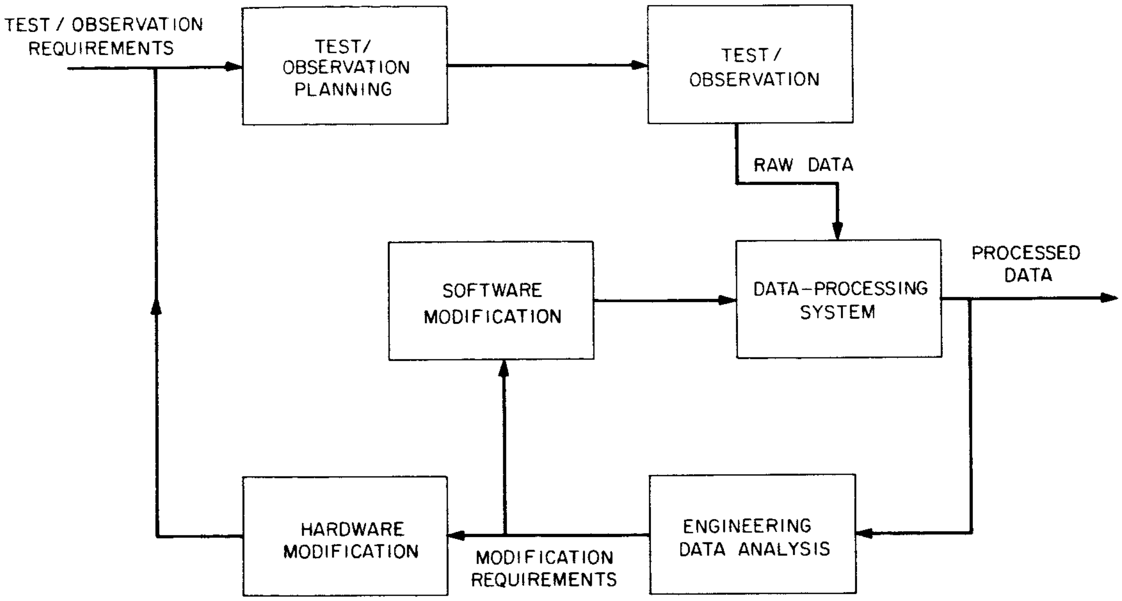

Figure 2.— System-modification cycles in Celescope development.

If there is no chance to correct this deficiency at ground, then what chance is there in orbit? Let us examine our experience again. When the satellite was launched, we experienced unexpected environmental effects on the experiment. Naturally, efforts were concentrated on solving these hardware problems. We had no time to pay attention to possible discrepancies between hardware characteristics and the mathematical model. Once these initial problems were solved, we proceeded with our observing program, which included a minimum number of operations aimed at maintaining and improving our knowledge of system calibration. After many months had passed and many data had been processed, it became obvious that there were discrepancies between the actual hardware characteristics and our mathematical model. Since then, much effort has been spent in resolving them. Naturally, they are much more difficult to resolve now than they would have been earlier.

DESCRIPTION OF CELESCOPE EXPERIMENT

Since details of the Celescope experiment have been reported elsewhere (1 to 3), we shall describe them only briefly here. The experiment consists of ultraviolet-sensitive broad-band stellar television photometers, four of which flew in the OAO 2. The television sensors are ultraviolet-sensitive SEC-type (Secondary-Electron Conduction) vidicons, called Uvicons, which were specially developed by Westinghouse (4). As a television system, Celescope is a still-picture transmission system of variable exposure duration (controllable integration time). That is, exposure and readout are sequentially but independently performed by ground commands. To maintain image-position accuracy, digitized scanning (256 × 256) is used. The speed of scanning, 10.5 sec per frame, is mainly determined by the spacecraft transmission channel. This speed corresponds to 160 μsec per television element. To overcome the reduced output amplitude due to this long beam dwell time, EMR, the prime contractor of the Celescope experiment, developed a special scanning technique called superscan (5). This is a sample scan technique in which the readout beam scans a television element rapidly during a signal-generating period. For the rest of the time — that is, beam idle time between consecutive signal-generating periods — the readout beam is deflected away from the television element by offset deflection voltages. Thus, the readout beam produces signals only during signal-generating periods. Then the output video signal becomes amplitude-modulated pulse trains. The amplitude of each pulse is digitized (up to 127 levels) by an onboard processor and transmitted in pulse-code modulation (PCM) format to the ground via a spacecraft transmitter. For photometric application, we use a special signal-processing method to increase the dynamic range and the accuracy of the instruments. When the ultraviolet flux from a star enters a telescope of the Celescope experiment, a point image is formed on the photocathode of the Uvicon tube. The photocathode produces a photocurrent that can be expressed as

$$i = \int_{\lambda_1}^{\lambda_2} S(\lambda)\ \phi(\lambda)\ d\lambda$$

where i is the photocurrent produced by the input flux ϕ from a star, $S(\lambda)$ is the spectral sensitivity of the optics (telescope, optical filter, and photocathode), $\phi(\lambda)$ is the ultraviolet spectral flux density from a star, and λ_1, λ_2 are the cutoff wavelengths of the optics.

Once we determine the photocurrent, the ultraviolet intensity I is calculated as

$$I = \frac{i}{\int_{\lambda_1}^{\lambda_2} S(\lambda)\ d\lambda} = \frac{E}{U \cdot tex}$$

where U is the optical sensitivity of the optics, tex is the exposure time or the integration duration, and $E = i \cdot tex$ is the total number of photoelectrons produced by $\phi(\lambda)$. In Celescope, where the integration mode is used, E (not i) is the quantity to be derived from the television signal and I becomes as shown on the right-hand side of the above equation. The most difficult part of the problem is the determination of E from the television output. When E is small, the number of pulses in the video output is small (5 to 10) and the maximum peak amplitude of the pulse train depends on E. If we use the maximum peak amplitude of the video pulse train as the television output signal, then the dynamic range of input becomes 100 or less. The lower limit of this dynamic range is set by preamplifier noise, in-tube noise, and external interference. The upper limit is restricted by signal-amplitude saturation. If E is increased beyond the amplitude-saturation range, then the number of pulses in the video output increases. That is, an increase of input photons causes a spread of image size. Then we can adopt the sum of all peak amplitudes in a pulse train (called Sigma), which was produced by a star, as an output television signal. By using this method, we can extend the dynamic range to 10^4 or 10^5.

SYSTEM ACCURACY IN THE PRELIMINARY PROCESSED DATA

During 16 months of its useful orbital life, the Celescope experiment produced approximately 8700 frames of stellar television pictures for ultraviolet photometric measurement. We based our first careful study of system accuracy on a small number of frames (48, to be exact), selected from available data, which had been produced by the preliminary data-processing system. Since this data-processing system was developed principally during the prelaunch period, it is not expected to produce the best results, but it will give us some idea of system accuracy and may suggest where the system should be modified to improve it. The selected data cover January 4 to 10, 1969, which corresponds to one of the earliest operational periods after the break-in of the experiment for orbital operation. These 48 pictures contain more than 450 different stars, of which about 200 were observed more than once. Since we do not have enough reliable ultraviolet measurements to compare the absolute intensity of measurement, our system-accuracy study is based on a consistency check, or repeatability of observed data. As a measure of system accuracy, the mean magnitude discrepancy is used. When a star is observed twice by the same ultraviolet passband (which is determined by the image-tube and filter combination), the magnitude discrepancy (dm) is defined as

$$dm = \frac{|m_1 - m_2|}{2}$$

Then we can take an overall average for multiple events. Table 1 summarizes the results, along with other related statistical quantities of magnitude discrepancy. As can be seen from this table, the magnitude discrepancy is much greater than the demonstrated ultimate accuracy of the instrument (see the next section for details). Then what causes this large magnitude discrepancy becomes the main question. Preliminary results indicate that we can achieve an average magnitude discrepancy of 0.2 mag or better for the bulk of our observational material. This paper may be considered the first installment of the complete answer to the system-accuracy problem.

ULTIMATE ACCURACY OF THE CELESCOPE EXPERIMENT

The Celescope experiment, like any other instrument, has its ultimate accuracy, or the maximum achievable accuracy of measurement. That ultimate accuracy can be determined by testing the repeatability of measurements. During the Vacuum Optical Bench (VOB) test, the following ideal condition for the repeatability was created: a constant temperature of $72° \pm 5°$F, a vacuum of better than 10^{-5} torr, and a fixed orientation and computer control of operational sequence with a timing accuracy of better than 1 msec. During about a month of the test period, many measurements were repeated for the on-board calibrator lamps, which have a monochromatic constant-level light output. The results are shown in Table 2. The probable error in the Sigma is less than 3%, which corresponds to a magnitude error of 0.04 for Camera 1 and 0.08 for Camera 3.

The fluctuation of Sigma may be caused by 1) output-flux fluctuation of the calibrator lamp and/or 2) Uvicon sensitivity fluctuation. To identify the source

Table 1. — Discrepancy of Measured Magnitude Between Repeated Observations

Category		Number of double observations	Magnitude discrepancy		
Image tube	Optical filter		Mean	Median	Probable error
Camera 1	Filter 1	36	0.298	0.262	0.152
Camera 1	Filter 2	70	.404	.345	.246
Camera 3	Filter 1	58	.403	.315	.259
Camera 3	Filter 2	66	.520	.427	.343
Camera 4	Filter 3	39	.324	.155	.249
Camera 4	Filter 4	20	.623	.637	.266
Camera 1	F1/F2 data combined	106	.368	.282	.221
Camera 3	F1/F2 data combined	124	.465	.350	.310
Camera 4	F3/F4 data combined	59	.425	.295	.272
All data		289	0.425	0.327	0.275

Table 2. — Fluctuation of Calibrator Output Measured by Celescope During Ground Test

Image tube	Number of observations	Sigma		
		Average (av)	Probable error (p.e.)	p.e./av, %
Camera 1	82	1357.0	29.9	2.2
Camera 3	72	3211.8	85.6	2.6

of fluctuation, the intensities of artificial stars were measured. These intensities were known to be constant to the same order of calibrator output and Uvicon sensitivity. First the magnitudes of the artificial stars were determined directly from the earlier Uvicon calibration. Then the measured magnitudes of artificial stars were modified by using calibrator-output measurements from the same television picture. The first method is directly related to the hypothesis that all fluctuations are caused by the calibrator lamp; the second, that all fluctuations are caused by Uvicon sensitivity. Table 3, showing a sample result of such measurements, indicates that the major source of the fluctuation is Uvicon sensitivity. The fluctuation of Uvicon sensitivity is correctable by the second method. Therefore, the ultimate prelaunch accuracy of the Celescope experiment was ~ 3% or better.

Table 3. — Identification of Source of Output Fluctuation by Minimizing Magnitude Difference for Double Observations

Magnetic calculating method (assumption for source of output fluctuation)	Calculated magnitude for an artificial star		
	Measurement 1	Measurement 2	Difference
Calibrator output	9.207	9.095	0.112
Uvicon sensitivity	9.138	9.133	.005

Measurement of real stars in the orbital environment will be less accurate than the above ultimate accuracy. The amount of inaccuracy depends on prelaunch system calibration, on usage of the calibration data, and on changes occurring after launch. Roughly speaking, any deviation of system accuracy from its ultimate accuracy is caused by inadequate calibration of the system and/or an inadequate mathematical model, which uses the calibration data. Postlaunch changes must be included by recalibration in orbit and appropriate mathematical modeling. Since the ultimate goal of Celescope accuracy is 0.1 mag (the goal for the near future is 0.2 mag), present hardware seems adequate. Therefore, we can say that the less-than-ultimate accuracy of the Celescope experiment is caused by the improper mathematical model in the data-processing system. In turn, the mathematical model may be based on an insufficient number of calibration data. It is possible that some unidentified parameters that influence system accuracy were omitted from the calibration process. We do not believe that to be the case, but part of our effort is still spent in attempting to identify any such additional parameters.

EFFECTS OF THE NUMBER OF CALIBRATION POINTS

As shown in the previous section, the major source of error is probably in the mathematical model used in the data-processing system. Then, what is the most likely cause of error in the mathematical model? In the present state of the art, the characteristics of the television photometer are determined empirically. That is, a number of calibration points are chosen, and characteristics for the noncalibrated points are estimated by interpolation. More calibration points produce a better mathematical model, and more sophisticated interpolation methods produce less error. But, for practical considerations — namely, schedule and finances — the fewer are the calibration points, the better. Consequently, some compromise is required. Some finite number of calibration points is chosen. This implies that we have some kind of mathematical model in mind (even though we claim to have no bias concerning the type of model). We may call this an intuitive model. Since the quality of the resulting mathematical model depends on the number of calibration points, the mathematical model is not very different from the intuitive model.

For an example, we will present the calibration of target gain. When we calibrate target gain (the ratio between the number of photoelectrons and Sigma) as function of target position, 26-hole reticles are used (in some cases there are 14 holes). That means that at most six (usually five) positions along a line across the target plane are calibrated. An example is shown in Figure 3.

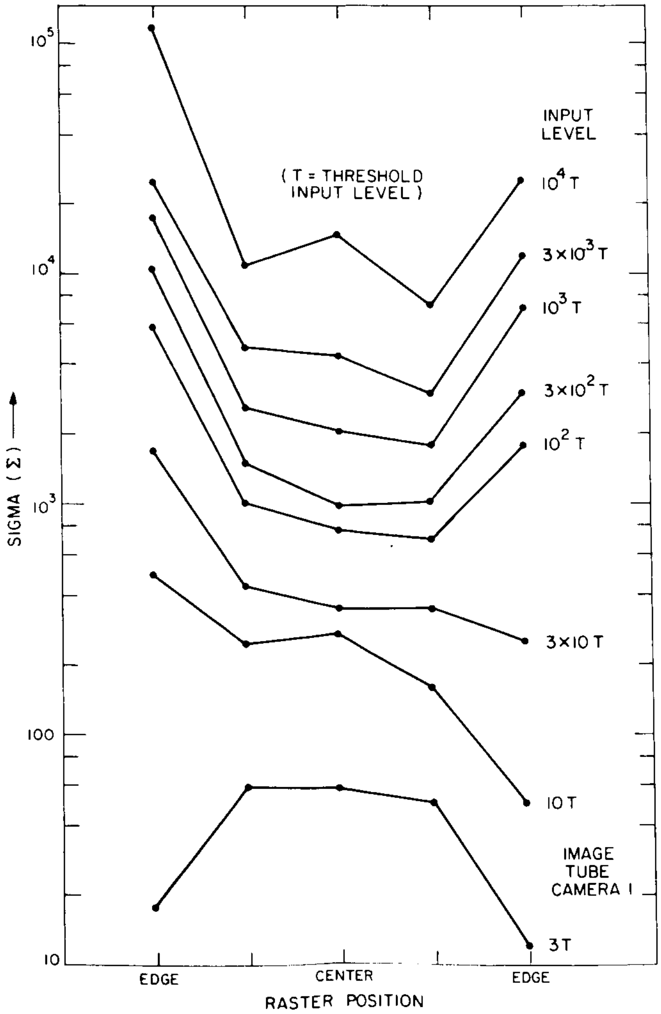

Figure 3.— Target sensisitivity variation across raster.

Increasing the number of positions was a great difficulty at the time of calibration, and we thought this number was sufficient since the maximum deviation of sensitivity was a factor of 2. (The acceptance specification for the tube was ±50%.) What we forgot was that the nonuniformity measure during the tube acceptance test was not Sigma but peak amplitude, which may vary up to a factor of 100. At present, this problem is solved by improving the interpolation method. Again, if we had realized early enough that the mathematical model is also part of the system, we could have improved system accuracy much more easily (for instance, by recalibration or by special tests).

EXAMPLES OF IMPROPERLY ASSUMED CONDITIONS

Other causes of the inaccurate mathematical model are invalid assumptions for calibration. As part of our "intuitive model," we assumed certain operating conditions for types of input, environment, etc. If these assumptions are not valid, then the calibrated data are not accurate. Recalibration was required if it was possible. When we performed the calibration, we assumed implicitly the input to be a point source (a quasi-point source), and fixed position, no background light, and a steady-state input. In actual orbital operation, some of these assumptions are invalid. For instance, geocorona (1216 Å) emission produced a very high background in the shorter wavelength region (Figure 4). Therefore, the magnitude of a star appearing in this region could not be determined accurately, nor could the intensity of the Lyman-alpha. This category of error cannot be predicted during prelaunch. Therefore, recalibration in orbit and supplementary ground tests are required.

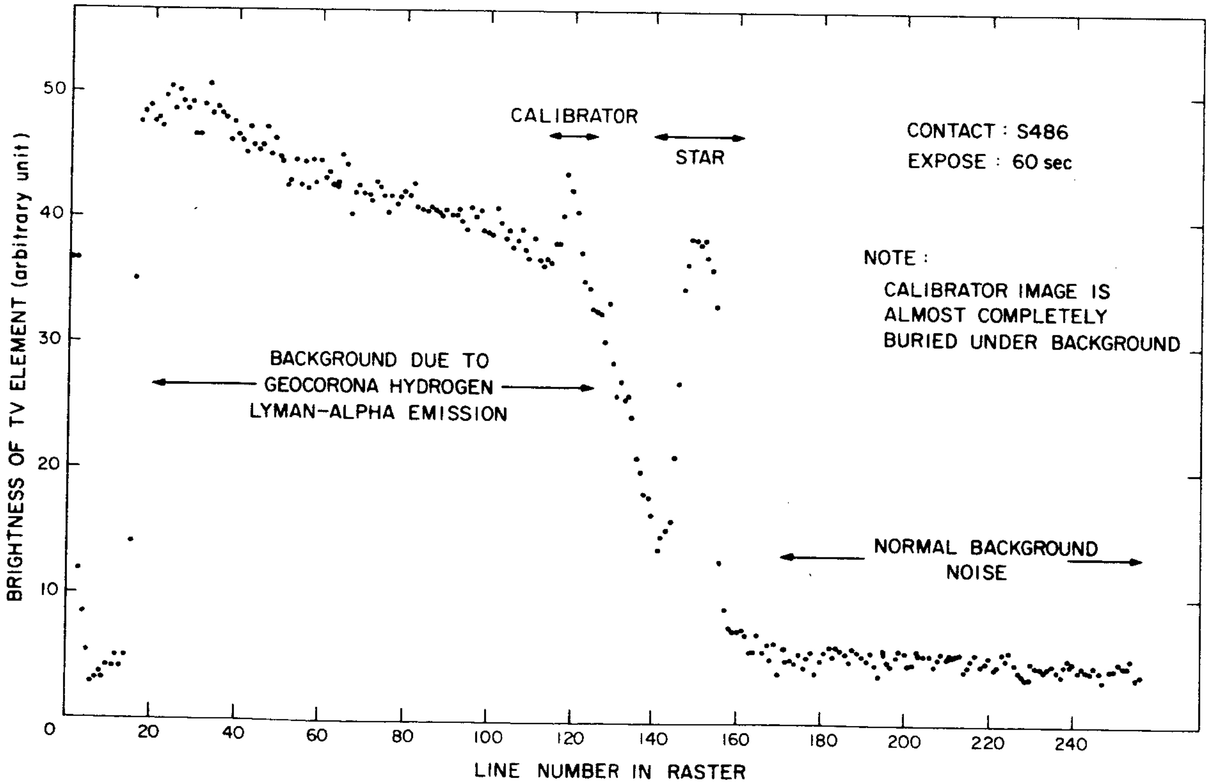

Figure 4.— Brightness distribution along vertical center line of camera 4 pictures.

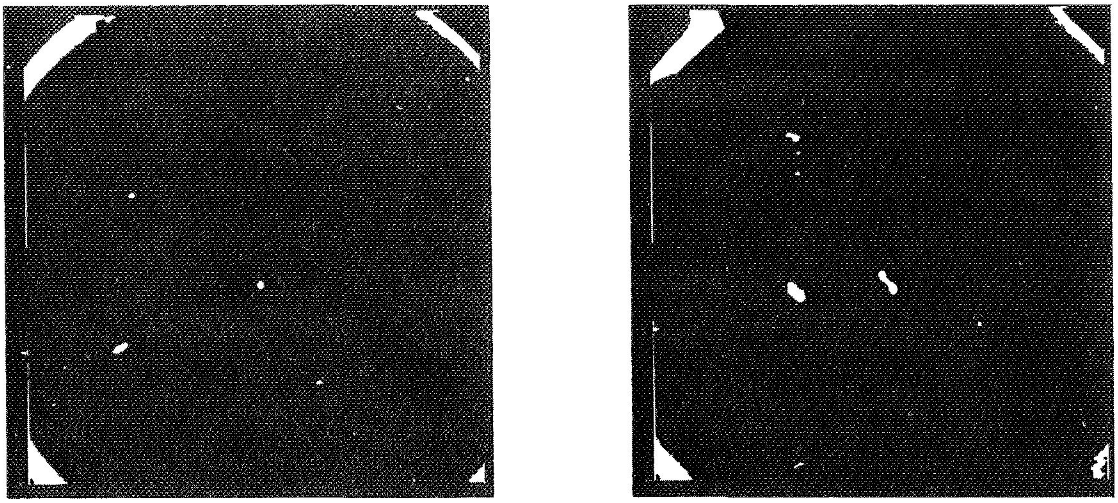

NORMAL ENVIRONMENT
(Contact R127)

WITH MAGNETIC DISTURBANCE
(Contact R128)

Figure 5. -Effect of magnetic disturbance. Both pictures contain an identical set of three stars and a calibrator image at the center of the pictures.

Similarly, for calibration purposes, the assumed environment, especially the magnetic field, was considered to be in a steady state. During the first 3 days of orbital operation, the dynamic magnetic field produced by the Magnetic Unloading System (MUS) caused drastic effects in the output image. Figure 5 shows an example. The resulting image is deformed and its Sigma has a much higher value than it should. This problem was avoided by stopping operation of MUS during expose and readout periods. The earth's magnetic field is a very important factor for all electrostatic SEC tubes. Since the satellite travels around the earth and changes orientation, the magnetic field around the tube slowly changes. This causes apparent shifts of position in the output raster. Table 4 indicates a good example. Since the position of the optical image of the calibration lamp is fixed on the Uvicon faceplate, any change in the calibration image is due to external electronic shift caused by the magnetic field or by a change of sweep voltage. Since the target has a large positional gradient for its sensitivity, the difference between the apparent image position in the raster and the true image position on the target may cause a large error. Therefore, the mathematical model should include a correction factor for this apparent position change. The true target position should be measured in the same way as during calibration (that is, some bias for magnetic field should be included).

The original calibration also assumed that time degradation of the system is negligible. But as shown in Figure 6, the system deteriorated very rapidly, mainly from overtesting and overstorage at the ground. The physical causes of deterioration are readout-beam reduction (due to loss of cathode emission), target-gain reduction, photocathode-sensitivity change, and deterioration of optical components. Since even the present calibration is not sufficient, reduced testing is not likely. Therefore, a future system should incorporate a long-life design and a deterioration monitor. In Celescope, the deterioration model has been developed by using orbital data and has been incorporated into the preliminary data-processing system (6). The results of this model are very encouraging, as shown in Table 5. Currently, further improvement of the model is being attempted.

Table 4. — Shift of Calibrator Image Position in the Raster

[Raster consists of 256 x 256 points. Position is measured by horizontal and vertical element numbers (H, V); H, V = 1 to 256.]

Image tube	Horizontal		Vertical	
	Average position	Maximum shift from average position	Average position	Maximum shift from average position
Camera 1	134	24	156	15
Camera 3	135	21	145	21

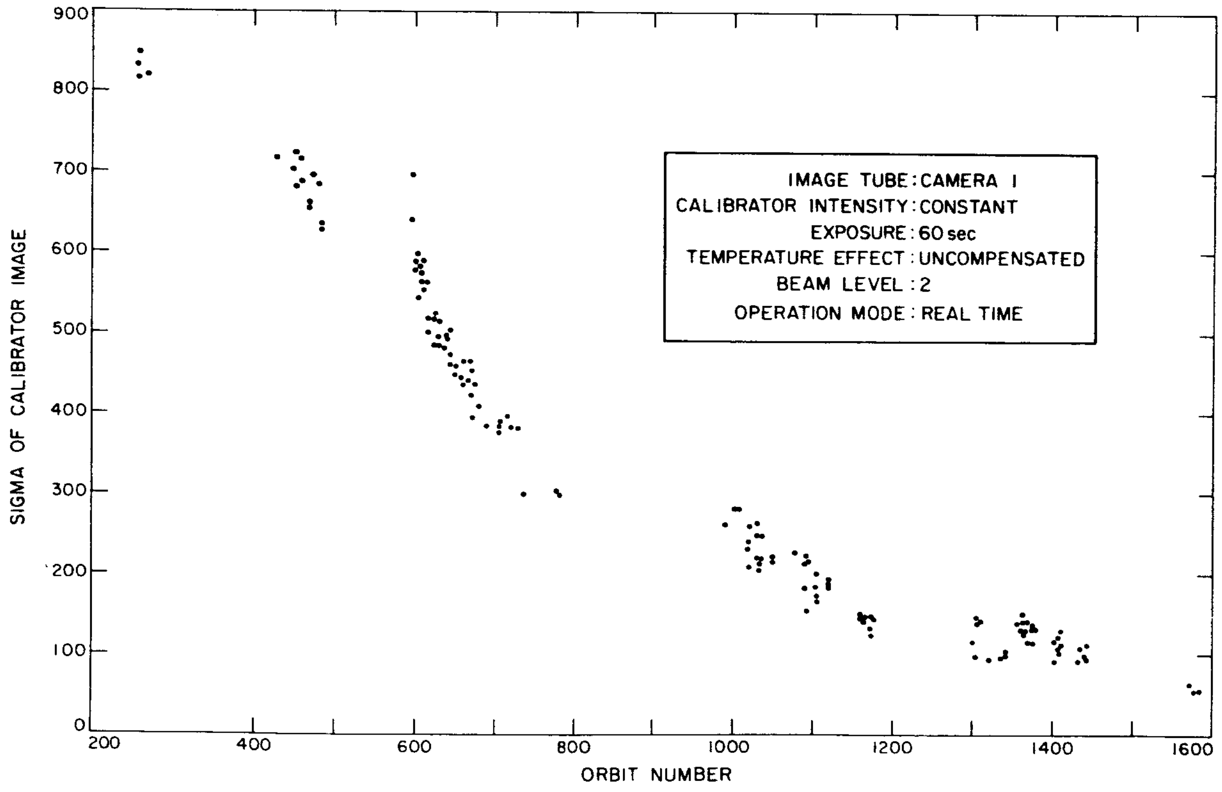

Figure 6. — Deterioration of Uvicon sensitivity.

Table 5. — System-Accuracy Improvement by Deterioration Correction

Image tube	Optical filter	Observed star	Measured magnitude at contact				Deterioration correction
			S415	Q428	M1301	M1574	
Camera 1	Filter 1	A	10.12	----	13.89	-----	Without
			9.39	----	9.27	-----	With
Camera 1	Filter 2	B	-----	8.27	11.97	13.08	Without
			-----	7.49	7.38	7.68	With
Camera 1	Filter 2	C	-----	7.59	-----	12.25	Without
			-----	6.94	-----	6.90	With
Camera 3	Filter 1	D	-----	10.22	13.38	-----	Without
			-----	9.95	10.22	-----	With
Camera 3	Filter 2	E	9.96	----	-----	13.63	Without
			9.77	----	-----	9.48	With

CONCLUSIONS

1. The largest error is the result of an inaccurate mathematical model of the hardware characteristics.

2. The causes of the inaccurate mathematical model are the insufficient number of calibration points and inaccurate assumptions concerning operating conditions.

3. The impact of these problems can be lessened by increasing the number of calibration points or by investigating and perfecting a theoretical model of hardware characteristics so that calibration means simple determination of numerical coefficients.

4. As part of the system test, the software-accuracy tests should be held while the system is still on the ground. That is, the system test should check the total system, not simply the hardware.

5. Since all possibility of inaccurate assumptions for operating conditions cannot be eliminated, whenever such a case occurs proper recalibration should be performed by remeasuring standard stars.

6. Monitoring of system time degradation should be incorporated as part of the system.

ACKNOWLEDGMENT

The authors wish to thank all personnel in Project Celescope, especially Dr. W. A. Deutschman and his group for operating the experiment, Mrs. K. Haramundanis and her group for processing the data, and Mr. P. Sylvester for analysis of the data.

REFERENCES

1. Davis, R. J., The Celescope Experiment, Smithsonian Astrophys. Obs. Special Report No. 282, July 1968.
2. Davis, R. J., The Use of the Uvicon-Celescope Television System for Ultraviolet Astronomical Photometry, Advances in Electronics and Electron Physics, Vol. 22, ed. by J. D. McGee, D. McMullan, and E. Kahan, Academic Press, New York, 1968, pp. 875-884.
3. Nozawa, Y., and Tucker, B. J., Digital Video Data Transmission System for Photometric Television, Supplement to the IEEE Transactions, Aerospace and Electronic System, Vol. AES-2, July 1966, pp. 388-391.
4. Doughty, D. D., Ultraviolet Sensitive Camera Tubes Incorporating the SEC Principles, Advances in Electronics and Electron Physics, Vol. 22, ed. by J. D. McGee, D. McMullan, and E. Kahan, Academic Press, New York, 1966, pp. 261-271.
5. Nozawa, Y., A Digital Television System for Satellite-Borne Ultraviolet Photometer, Advances in Electronics and Electron Physics, Vol. 22, ed. by J. D. McGee, D. McMullan, and E. Kahan, Academic Press, New York, 1966, pp. 865-874.
6. Nozawa, Y., Overcoming System Deterioration in a Satellite-Borne Television Photometer, Proceedings of First Electro-Optical System Design Conference, September 16-18, 1969.

Page intentionally left blank

PROGRESS REPORT ON DEVELOPMENT OF THE SEC VIDICON FOR ASTRONOMY

P. M. Zucchino
and
J. L. Lowrance

Princeton University Observatory
Princeton, New Jersey

For the past several years Princeton has been pursuing the development and application of television tubes for astronomy. The primary objective is to develop a sensor for space astronomy applications, especially those of diffraction limited imagery and high-resolution spectroscopy.

Ground based applications have been included in the development program, both to exploit the intrinsic capabilities of integrating television tubes for certain ground based observational work and to gain application experience with television for actual astronomy observational tasks.

The primary sensor characteristics that are relevant to the basic choice of a sensor are:

(a) A capability for exposure periods of the order of 10 hours
(b) A modulation transfer function (MTF) of at least 0.5 at 10 cycles/mm over an image format of at least 250,000 image elements, that is, a 25 mm square
(c) Stable photometric and geometric transfer functions
(d) Good quantum efficiency with a quantum noise limited signal to noise ratio over most of the dynamic range

Background information on the subject is given in references 1 to 8.

TECHNICAL DISCUSSION

Sensor Selection

The long exposure requirement limits the choice of television type sensors to those with very high resistivity storage targets, so that the image accumulating during the longest exposure does not degrade significantly prior to the end of exposure and subsequent readout of the stored image. This eliminates all photo-conductive type sensors unless a system for accumulating detected photon events outside the tube in an external memory is feasible for the particular application.

There are just two general types of TV tubes with the required integrating and storage capability. They are the SEC vidicon and the image isocon or image orthicon. (The image isocon has basic integrating and storage capabilities the same as those of the image orthicon.)

We have evaluated the SEC-vidicon and the image isocon for the general astronomy application and have selected the SEC-vidicon because of its higher effective quantum efficiency and better first scan modulation transfer function.

The obscuration or interception of photoelectrons by the target mesh effectively lowers the quantum efficiency of the image isocon by approximately 40 percent relative to the SEC-vidicon which does not have a mesh between the photocathode and its storage target.

Resolution

The attainable modulation transfer function of storage tubes in general is determined by the thickness of the electrostatic storage element. In image sensors where an electrostatic image is formed, the reading electron beam senses the potential distribution rather than charge distribution on the storage target. The potential distribution is a degraded image of the charge distribution.(5)

If t_1 is the target thickness and t_2 is the target to mesh spacing, the theoretical sine wave response of an image isocon target, as determined solely from its geometry, is given by the equation

$$\psi(K) = \frac{e^{-\pi K t_1} \left(1 - e^{-2 \pi K t_2}\right)}{2 \pi K t_2}$$

where K is the number of half cycles of spatial frequency per unit length.

The target thickness is 0.2 mil in the image isocon. A graph of the sine wave response versus the target to mesh spacing is shown in Figure 1. Spacings closer than 1 mil appear to be impractical to manufacture. At the 1 mil spacing the theoretical response is only 22% at 10 cycles per mm. This compares with 60% response for the latest SEC-vidicon. The Isocon that was evaluated had a target-to-mesh spacing of 1.4 mil. The measured response was 12% and the theoretical response from Figure 1 is 16%.

Similar analysis of a vidicon or SEC target yields the equation

$$\psi(K) = \frac{1 - e^{-2 \pi K t_2}}{2 \pi K t_2}$$

The thickness of the SEC target is not directly measurable; however, the effective thickness can be calculated from the measured apparent capacitance. The effective capacitance is a function of the total number of electrons stored on the target and the corresponding voltage modulation. In the latest tube, V = 2.5 volts corresponds to 44,000 electrons per 33 x 33 micron picture element

$$C = \frac{\Delta Q}{\Delta V}$$

$$C = \frac{4.4 \times 10^{4} \times 1.6 \times 10^{-19}}{2.5} = 0.28 \times 10^{-14} \text{ farad}$$

and

$$t_2 = \frac{8.85 \times 10^{-12} \times (33 \times 10^{-6})^2}{0.28 \times 10^{-14}}$$

$$= 3.56 \quad \text{microns}$$

From Figure 1 one finds that the MTF at 10 cycles/mm is 81%. This is consistent with the measured value of 60%. The difference is attributable to the resolving power of the scanning electron beam and the uncertainty in the thickness of the target.

From both the analytical and experimental data one concludes that the thin vidicon or SEC type target provides a significant gain in first scan resolution over the mesh-target arrangement used in image orthicons and Image Isocons.

It should be noted that continuous scan of the same image in an Image Isocon or Orthicon results in improved resolution due to a charge equilibrium that builds up in the steady state. However, the "first scan" condition analyzed above is the mode of operation that is relevant in most applications for stellar astronomy.

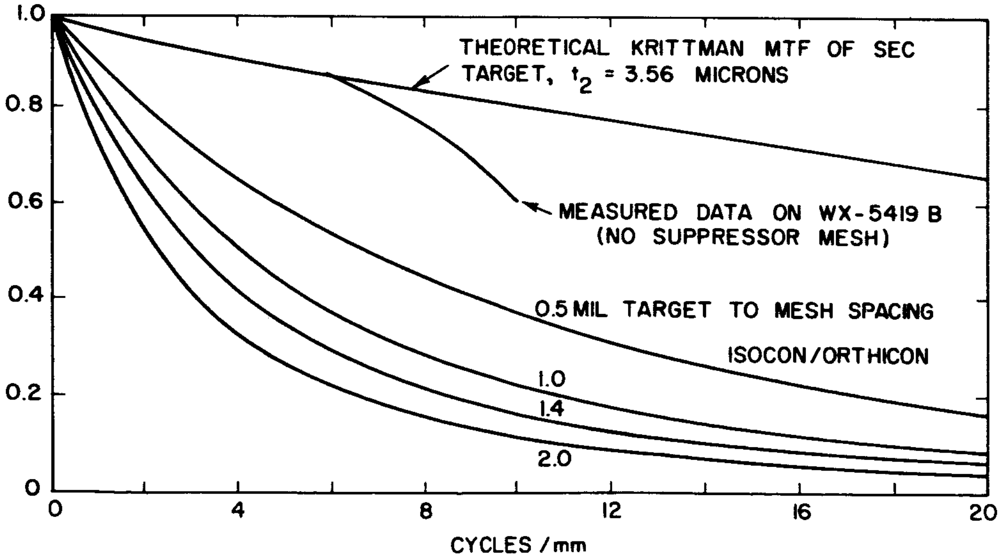

Figure 1.-Modulation transfer functions.

Photometric Transfer Function

The transfer function shown in Figure 2 illustrates the basic photometric characteristics of the SEC tube.

The 33 x 33 micron element size is used because the 50 micron square image element goal would be better served with some oversampling in both axes, assuming that data storage and transmission limits are not very restrictive in the application. A raster of 750 scans lines with 750 samples per line on the 25mm square target yields the 33 micron image element size.

Photoelectrons per image element is the input variable, so that photocathode quantum efficiency is not involved at this point.

The threshold performance is determined by the preamplifier noise which dominates approximately the first 5% of the useful exposure range. After an exposure of 63 photoelectrons per element is reached the shot noise of the input photoelectrons exceeds the preamplifier noise.

The transfer function is nearly linear with a slight reduction in gain

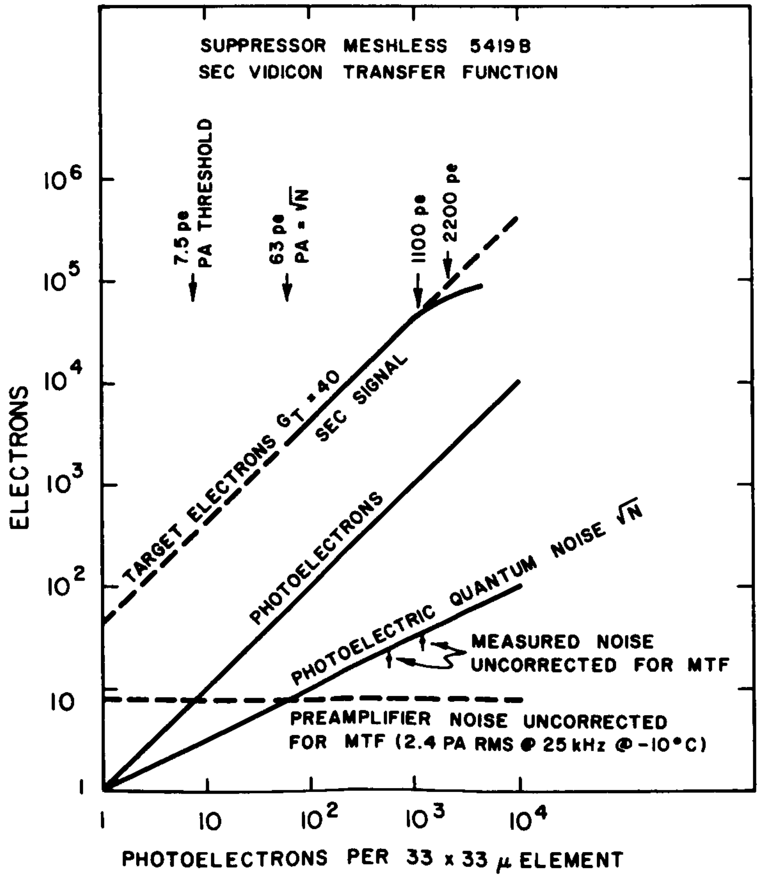

Figure 2.-SEC photoelectric transfer function.

as the full target conditions are approached. "Full target," the point where further exposure would best be recorded on an additional frame, is in the range of 1000 to 2000 photoelectrons per element.

The measured noise is less than the calculated quantum noise but it is not corrected for MTF. Correction for MTF is estimated to not quite double the noise at this element size, indicating that the performance closely approaches the quantum noise limit.

Since the threshold performance depends directly on the preamplifier and the preamplifier characteristics in turn dicate the readout rate, some comment on the preamplifier employed is in order.

Preamplifier

The SEC vidicon noise consists of the preamplifier noise and the quantum noise in the image. The preamplifier noise expressed in photoelectrons is

$$\frac{N_a}{(G)\ (MTF)}$$

where G is the SEC target gain. The preamp noise, N_a, consists of the shot noise in the channel current of the field effect transistor, the thermal (Johnson) noise in the resistors of the input network, and excess noise associated with gate leakage of the input transistor.

Figure 3 schematically illustrates the preamplifier employed at Princeton with the SEC tube. Its function is to measure the charge due to stored electrons on each image element. The first stage is a selected low noise junction field effect transistor (FET). Since the input FET is intrinsically a voltage sensitive device the ratio of the signal charge to total shunt capacitance is a key parameter.

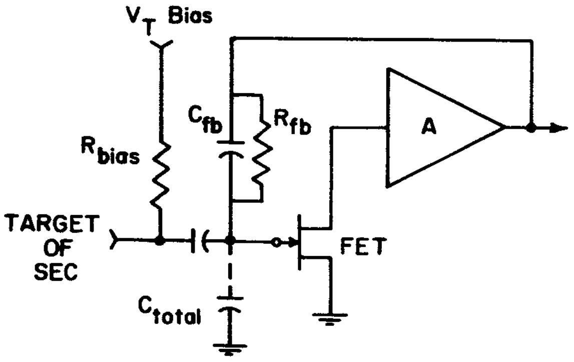

PERFORMANCE AT ELEMENT TIME OF
20 uSEC (25 KHZ) & Ta = 10°C.

NOISE TARGET ELECTRONS: 300
REFERRED TO PHOTOCATHODE: 7.5pe

PREAMPLIFIER NOISE CONTRIBUTIONS:

FET SHOT	174e
BIAS RESISTOR THERMAL	167e
"EXCESS"(FET LEAKAGE)	177e
RMS SUM	300e

SHUNT CAPACITANCE:

SEC TARGET & LEAD	40pf
FET	10pf
TOTAL	50pf

FET: I = 7 MA
Gm = 13.4 MA/V
SELECTED 2N4392

SHOT NOISE FIGURE OF MERIT FOR INPUT FET $= \frac{gm}{C_{TOTAL}} I^{\frac{1}{2}}$

Figure 3. -Preamplifier employed with SEC tube.

The channel current shot noise referred to the input of the preamplifier is calculated as follows:

$$N_c = \frac{C}{gm} \frac{\sqrt{N}}{\Delta t}$$

$$= \frac{C}{gm} \sqrt{N} \; (2 \Delta f)$$

where C is the total shunt capacitance to ground at the preamplifier input, gm is the trans-conductance of the FET, N is the number of channel electrons per element dwell time, Δt is the readout dwell time per element, and Δf is the corresponding readout bandwidth. This may be expressed in terms of the FET channel current:

$$N_c = \frac{C}{gm} \sqrt{\frac{I}{qe \, \Delta t}} = \frac{C}{gm} \sqrt{\frac{2 \, \Delta f \; I}{qe}} \quad \text{electrons/ half cycle}$$

The thermal noise current of a resistor is

$$i_n = \sqrt{\frac{4 \; kT \, \Delta f}{R}}$$

where $k = 1.372 \times 10^{-23}$ joules/°K

and T = temperature , °K

A half cycle of bandwidth is equal to $\frac{1}{2 \, \Delta f}$ seconds. The number of electrons per half cycle is

$$N_R = \sqrt{\frac{\dfrac{4 \; kT \, \Delta f}{4 \; (\Delta f)^2 \; R}}{qe}} = \sqrt{\frac{\dfrac{kT}{\Delta f \quad R}}{qe}}$$

The total preamp noise in electrons per half cycle or dwell time is:

$$N_a = \sqrt{\frac{kT}{\Delta f \quad R \, (qe)^2} + \frac{2 \; I \, \Delta f}{qe} \left(\frac{C}{gm}\right)^2}$$

From this one notes that the input resistance should be as high as practical, the input capacitance of the FET and the input network should be as low as possible, the gm should be high, the channel current should be low, and there is an optimum frequency for minimum total noise.

For the latest SEC vidicon and preamplifier:

$G = 40$
$f = 25$ kHz
$C = 50 \times 10^{-12}$ Farads
$gm = 13.4 \times 10^{-3}$ amperes/volt
$I = 7 \times 10^{-3}$ amperes
$R = 2 \times 10^{8}$ ohms
$T = 260°K$
$k = 1.362 \times 10^{-23}$ Joules/°K
$qe = 1.6 \times 10^{-19}$ coulombs/electron

Solution of the preceding equation for these values yields N = 242 electrons/half cycle.

This compares favorably with the measured preamp noise of 300 electrons per half cycle. The additional measured noise is attributed to the gate leakage current of the FET in the preamplifier. Since the channel shot noise performance depends directly on the total shunt capacitance at the preamplifier input, the reduction in shunt capacitance that accompanied the removal of the suppressor mesh from the SEC tube fully offset the decrease in target gain of the coated target, leaving the net threshold performance unchanged.

Negative feedback via C_{fb} (Figure 3) is employed to stabilize the performance against device parameter drifts, but the design is such that C_{fb} is kept small in relation to C_{total} so as not to degrade the channel shot noise performance.

The bias and feedback resistors are of high value ($\sim 10^{8}$ ohms) to minimize their thermal noise contribution. Upper limits on resistor values are determined by the FET leakage current (especially if operation in a radiation environment is planned) and by the need to avoid low frequency shifts in the SEC target bias potential.

Cooling of the preamplifier down to -10°C improves the noise performance by reducing the thermal component of the FET leakage current. Further cooling does not help, presumably because surface leakage becomes the dominant FET leakage noise contributor. To date, insulated gate type field effect transistors have proven to be excessively noisy for application to preamplifiers of this type, so we have been unable to take advantage of their extremely low gate leakages.

The dependence of preamplifier performance upon readout rate or element dwell time is shown in Figure 4. The FET channel shot noise rises with the one half power of frequency or inversely as the one half power of dwell time, while the other noise contributions behave in a reciprocal manner. This leads to an optimum readout rate with an upper video frequency of 25 kHz corresponding to a dwell time of 20 microseconds per image element. The minimum noise point is not a sharp minimum because of the one half power dependence of the contributions. The minimum can be shifted somewhat higher in frequency by selecting FET's with good shot noise characteristics, while sacrificing leakage or "excess" noise characteristics; and conversely can be shifted downward in frequency by using opposite device selection criteria. The important point of Figure 5 is that standard broadcast type readout rates are entirely too fast for optimum threshold performance.

Image Isocon Signal to Noise Ratio

The image isocon has several sources of noise, most of which are proportional to the square root of the signal. The quantum noise in the charge pattern on the target expressed in photoelectrons is:

$$\frac{\sqrt{N\ M_T \left(\frac{G_T}{G_T-1}\right)}}{M_T}$$

where N is the number of photoelectrons emitted by the photocathode, M_T. is the target mesh transmission, G_T is the secondary emission gain at target mesh transmission and $\left(\frac{G_T}{G_T-1}\right)$ is the increase in noise due to the Poisson statistics associated with the secondary emission gain process. The beam noise, again expressed in photoelectrons, is:

$$\frac{\sqrt{N\ M_T G_T G_B M_F \left(\frac{G_B}{G_B-1}\right)}}{(MTF)\ (M_T G_T G_B M_F)}$$

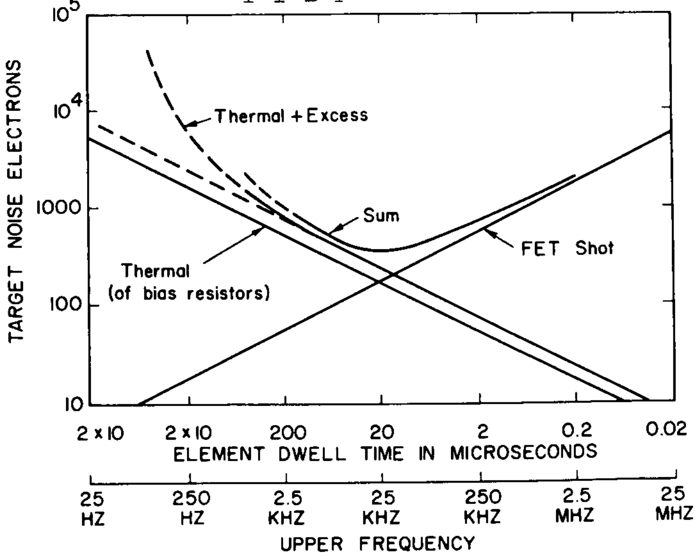

Figure 4.-SEC preamplifier performance against frequency.

G_B is the gain of the beam in scattered electrons per target electron and $\left(\frac{G_B}{G_B-1}\right)$ is the Poisson statistics increase in noise associated with the gain of the beam, G_B. This expression may be simplified to:

$$\sqrt{\frac{N}{M_T G_T M_F (G_B-1)\ (MTF)^2}}$$

The beam switching noise is:(1)

$$\overline{qn^2} = 2kTC_s$$

and in photoelectrons

$$= \frac{\sqrt{2kTC_s}}{M_T G_T}$$

For large values of "N" the beam switching noise can be neglected and the signal to noise ratio is

$$\frac{\sqrt{N}}{\sqrt{\frac{G_T}{M_T\ (G_T-1)} + \frac{1}{M_T G_T M_F\ (G_B-1)\ (MTF)^2}}}$$

An additional source of noise is the dark current. The dark current results from scattering from the field mesh, scattering in the dark portion of the image which is accentuated by target pulsing, and nominal adjustment of the separating aperture to keep from "clipping" off the lowest end of the dynamic range.

One notes that the isocon signal to noise ratio is independent of the scan rate and resultant video bandwidth. Equally important, it is proportional to the square root of the signal when the dark current is ignored. This "independence" of the readout rate may be of value in some applications such as solar astronomy where the data rate may be quite high.

Figure 5 shows the various noise components and the signal to noise ratio for an isocon with the following parameters:

Target Mesh Transmission	$M_T = 0.5$
Field Mesh Transmission	$M_F = 0.5$
Target Gain	$G_T = 4$

Beam Gain $G_B = 2$

Modulation Transfer Function

1 mil spacing (MTF) $MTF = 0.2$ at 19 c/mm (Figure 1)

$C_S = 0.875 \times 10^{-15}$ farad/element

$V = 1.6$ volts

These values yield a signal to noise ratio at 10 cycles/mm of $0.2\sqrt{N}$.

The peak signal is $Q = CV$

$$M_T G_T N = \frac{0.875 \times 10^{-15} \times 1.6}{1.6 \times 10^{-19}} = 8750$$

$$N = \frac{8750}{(0.5)\ (4)} = 4375$$

$$\text{The peak } S/N = 0.2\sqrt{4375} = 13.3$$

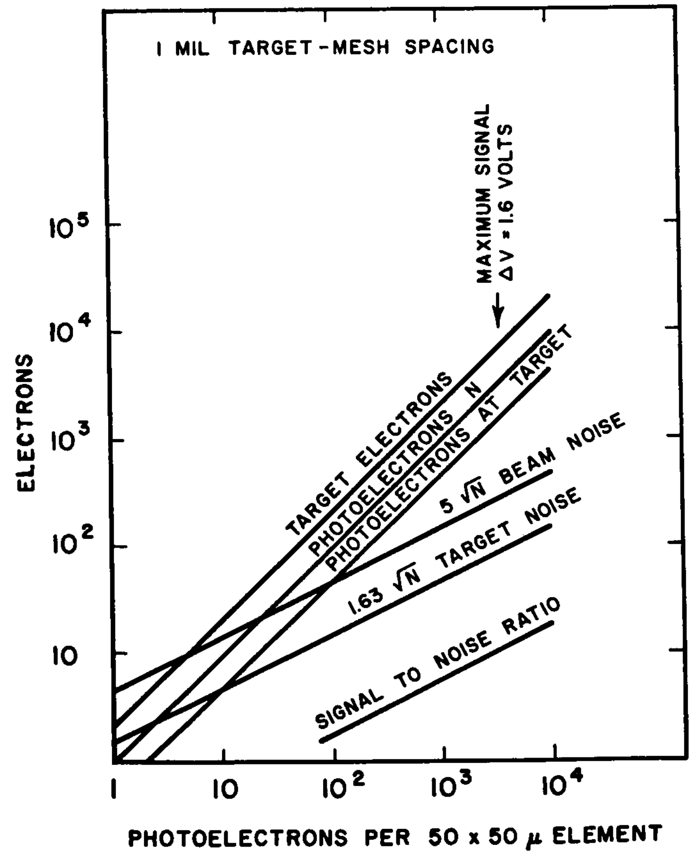

Figure 5. -Isocon transfer function.

The SEC vidicon would have a comparable S/N of

$$\frac{4375}{\sqrt{4375 + \left(\frac{7.5}{0.7}\right)^2}} = 67$$

However, the SEC vidicon saturates at about $\frac{1}{2}$ this signal so the peak signal to noise ratio in $\frac{1}{2}$ the exposure time would be 45 and computer summation of the two exposures would yield approximately 65.

Figure of Merit for Image Sensors

A perfect detector has a signal to noise ratio equal to the square root of the number of photons per image element

$$\frac{\text{Peak Signal}}{\text{RMS Noise}} = \sqrt{\text{No. of photons}}$$

In an actual detector the signal to noise is a function of several factors: preamplifier noise, quantum efficiency, and modulation transfer function (MTF) of the detector

$$\frac{\text{Peak Signal}}{\text{RMS Noise}} = \frac{\text{Signal}}{\sqrt{(\text{Noise}_1)^2 + \left(\frac{\text{Noise}_2}{\text{MTF}}\right)^2}}$$

where Noise_2 is any noise that is not filtered by the aperture response of the sensor such as preamplifier noise and beam noise.

A figure of merit for any sensor would be the ratio of the ideal signal to noise to the actual signal to noise ratio. This figure of merit will be a function of spatial frequency and magnitude of the incident photon signal. For a noiseless detector responsive to a fraction of the incident photons

$$\text{Figure of Merit} = \sqrt{\frac{Q_e \text{ No. Photons}}{\text{No. Photons}}} = \sqrt{Q_e}$$

where Q_e is the quantum efficiency defined as $\frac{\text{No. measurable events}}{\text{No. photons}}$.

The figures of merit for 103-0 photographic film, the SEC vidicon, and the image isocon are shown in Figure 6.

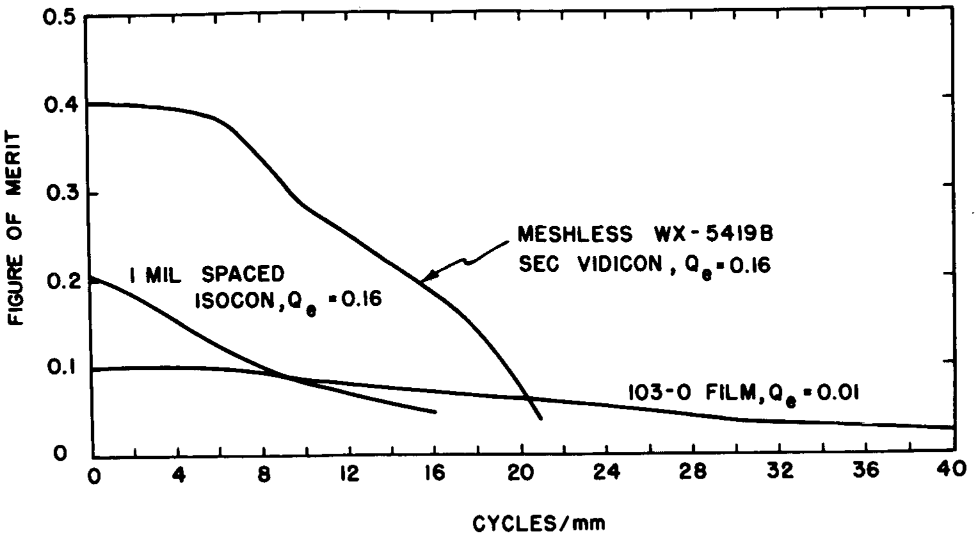

Figure 6.-Figures of merit for sensors.

A variation on this figure of merit would be its integral up to a given spatial frequency. This would then relate the figure of merit to the number of picture elements per unit area.

SEC Selection

The SEC vidicon tube being developed for the astronomy application is the WX-5419-B* which is about the size of a 3-inch image othicon. The tube employs magnetic focusing for both the reading and image sections. Since there are several more compact types of SEC tubes available, an explanation of why the 5419-B was originally selected for the astronomy application, and is still considered to be the optimum among the available types, is in order.

The major consideration is the size of the SEC storage target. For example, the diffraction limited imagery application requires that the sensor be used with a sufficiently long focal ratio so that the image tube's MTF does not significantly degrade the overall MTF. This is illustrated in Figure 7. By choosing the focal ratio so that the telescope MTF is zero at the spatial frequency where the sensor MTF has dropped to 0.5, the overall MTF is not seriously degraded by the sensor. For the SEC tube this occurs at about 10 cycles per mm spatial frequency at the target. The larger the target, the more half cycles or image elements can be included in the field of a given exposure. The 25mm square targets of the 5419-B provide a field of 500 x 500 image elements at the 10 cycles per mm limit. This is comparable in field coverage at equal MTF to a photographic film

---

*The Princeton version of this tube is the WX31718.

(e.g.,103 ag) only 12mm square. For many observations such as image field is adequate. It would require additional exposures to record objects or fields larger than 25 arc sec with a one meter diffraction limited telescope. For ground based observations where the seeing is rarely better than one arc second, the field coverage is about 8 arc minutes, also based on the matching criterion of Figure 2 . Since the 25mm square target of the 5419-B is the largest available, that tube is strongly favored on field coverage considerations.

Another parameter related to target size is photoelectron storage capacity, on a per element basis. A 50 micron square image element in the 5419-B target (corresponding to operating with spatial frequencies up to 10 cycles per mm) has a storage capacity of about 2500 photoelectrons, which corresponds to a photometric accuracy of two percent rms. Even assuming that smaller image elements might become feasible in the future by way of MTF or resolution improvement, the storage capacity would go down directly with the area of the smaller resolution elements and the photometric accuracy on a per element basis would decrease directly with the increase in limiting spatial frequency.

The point here is that the per element photometric accuracy attainable in a single exposure depends on the storage capacity of the target on a per element basis even if the effects of the MTF are ignored. Good photometry demands large target storage elements, or, alternatively, addition of successive "full target" exposures outside the camera tube.

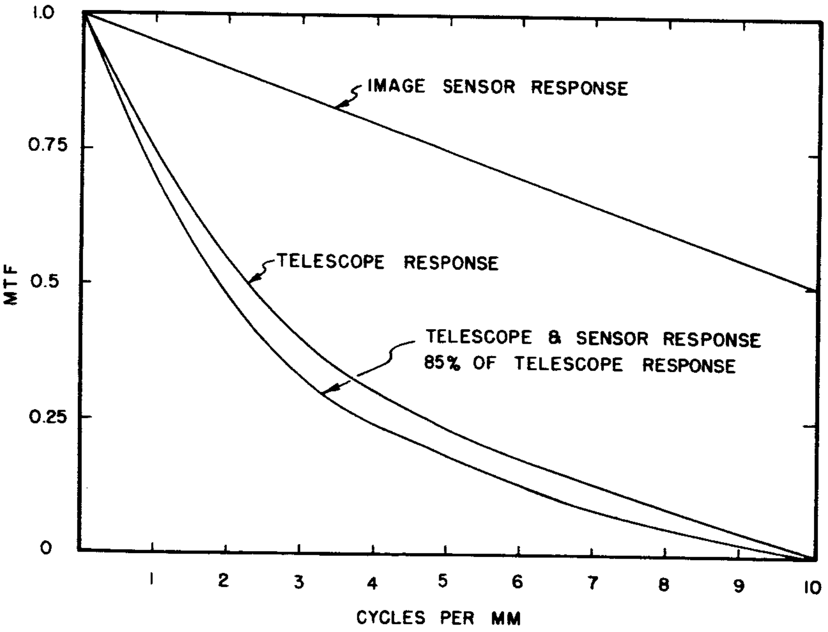

Figure 7.-Telescope and sensor MTF.

Certain aberrations in television tube performance can be neglected or readily calibrated out if the image element size is of the order of 50 microns. An example is "beam pulling", which is a displacement of the low velocity scanning beam by the potential gradient associated with the localized charge of the image.

Attempting to use the TV tubes at element sizes of 15 to 20 microns simply because the tubes have some response at the correspondingly high spatial frequencies leads to a cascading of problems such as low per element photoelectron storage, low MTF values, and aberrations such as beam pulling.

The conclusion is that pushing the TV tube resolution rapidly degrades its system effectiveness in the astronomical application, where most effective use of the light gathered by the telescope is the major consideration.

A secondary consideration in the selection of the 5419-B tube type is that its magnetically focused image section insures no significant degradation of MTF in the image section and also provides a flat input window which facilitates the system optical design and simplifies the attainment of a uv transmitting window.

Removal of Suppressor Mesh

A major advance in the SEC development program for the astronomy application was the removal of the suppressor mesh from the tube design. For many non-astronomy applications the suppressor mesh has been a necessary device to prevent destruction of the SEC target by "crossover", a destructive situation usually caused by overexposure of the tube leading to secondary emission charging of the scanned surface of the target to a potential sufficient to rupture the fragile insulating membrane. This is usually avoided by having the low potential suppressor mesh near the scanned surface of the target to limit the maximum potential the target surface can attain during a "crossover" situation.

The sequential operation of the tube in the astronomy application permits operating without the suppressor mesh. An advance in SEC target technology involving a coating of the scanned side of the target further insures safe operation.

The sequential operation employed is safe because the scanning beam is off when the photocathode is operating. There are no scanning electrons to generate secondaries at the scanned surface even if a portion is being overexposed by photoelectrons. The mesh behind the target, which in the case of a tube without a suppressor mesh is the field mesh, is kept at a low or zero potential during exposure, so that secondaries generated by primary photoelectrons cannot cause charging of the exit surface.

SEC target gains are lower by a factor of two with the coated target because the portion of the SEC target gain attributable to secondaries being collected by the mesh after their generation by a photoelectron is absent. That portion is known as the TSE component for transmission secondary emission. Only the basic SEC secondary electron conduction component of target gain remains. The SEC component depends on the initial electric field through the target supplied by the external target bias.

Three significant benefits are realized by removing the suppressor mesh from the 5419-B tube.

First, the threshold noise performance is helped considerably by the reduction in the shunt capacitance of the target to ground. This more than compensates for the loss of TSE gain inherent in meshless operation.

Second, the MTF of the tube is increased by 50 percent at 10 cycles per mm. We typically obtain 60 percent modulation at 10 square wave cycles per mm without the suppressor mesh, as opposed to 40 percent with the suppressor mesh.

Third, the problem of microphonic noise signals, which can be severe with slow scan readout operation, is intrinsically improved by removal of the suppressor. Further improvement resulted from a mechanical redesign of the target structure which was made feasible by the deletion of the suppressor mesh. The redesign also made the target more resistant to vibration damage.

Sequential Operation

For the astronomy application, where exposure time of the order of minutes and hours are common, the SEC tube is operated in a manner quite different from that employed in broadcast television operation.

In normal TV operation the image section of the SEC tube is continuously writing an image into the SEC storage target while the reading electron gun is continuously reading out the image that has been integrated in the brief frame or field interval since the beam last scanned its present location.

In the sequential operating modes used in the astronomy application the SEC tube is cycled through four modes. They are: PREPARE, EXPOSURE, STORE, and READOUT.

In the PREPARE mode the SEC storage target is normalized to make it suitable for exposure.

During the EXPOSURE mode the photocathode and image section are ON, integrating the incoming image into the SEC storage target.

After an exposure the tube can be put into the STORE mode where the photocathode and image section are OFF and the reading electron gun is also OFF. The integrated image stored in the SEC target will not degrade perceptibly after as many as 50 or more hours of storage.

During the READOUT mode the stored image is scanned out by the reading section's electron gun. During READOUT the photocathode and image section of the tube are OFF. Since the image section is OFF during the sequential mode type of readout, it is safe to have a high field mesh potential during READOUT. (It is also necessary to have had the mesh voltage low during the EXPOSE mode for complete safety during the subsequent READOUT especially if an uncoated SEC target is used.) The high reading beam decelerating field so obtained contributes greatly to the high MTF and low beam pulling characteristics of the suppressor meshless tubes.

The PREPARE mode consists of first flooding the photocathode with diffuse illumination while operating the reading beam with low field mesh voltage. This is followed by operating the reading gun <u>only</u>, first with low mesh voltage and, second, with the high readout mode mesh potential applied while adjusting the target bias upward to the desired level for the EXPOSE MODE.

An active PREPARE cycle of that sort is required to obliterate image charge patterns within the SEC target layer which are not neutralized by the readout beam which can only normalize the surface potential of the target. McMullan and Tower have previously reported in detail on the internal charge retention of the SEC target.(8)

Figure 8 illustrates the requirement for an active erase phase in the PREPARE cycle. The lower portion of the figure is a normal readout of a test pattern image. In our slow scan operation there is no residual image even on the second scan, that is, the reading beam completely recharges the target surface in one frame, the readout frame. However, if the target is then exposed to flat white illumination, a severe negative image of the previous pattern appears as shown in the middle portion of Figure 8.

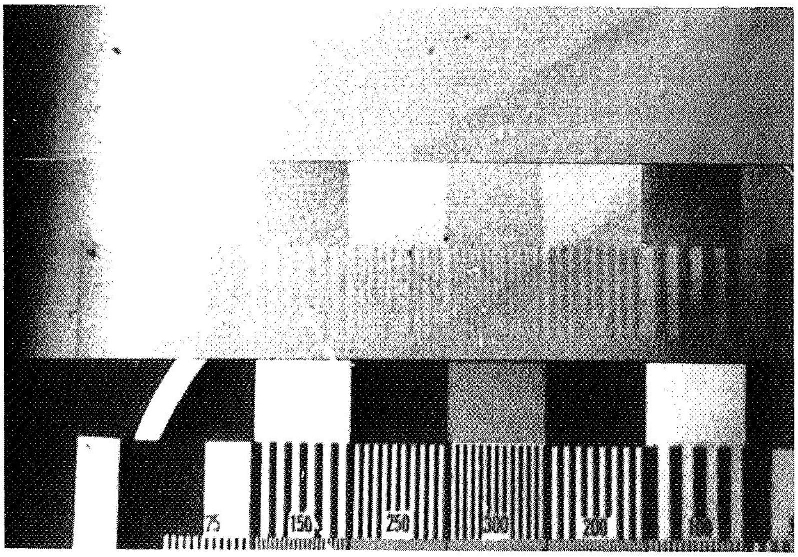

Figure 8.-Erase illustration.

The upper portion of the figure shows the image obtained from flat illumination after a PREPARE cycle has followed the test pattern image. Nothing of the test pattern can be seen in this case. (The shading and white marks in the upper portion of Figure 8 are photocathode and target irregularities of the developmental tube used for this test.)

Another requirement of sequential tube operation is that of "target pulsing". This is a procedure in which the target bias is raised approximately 0.5 volts above that used for the final PREPARE step and for EXPOSURE mode. If this were not done, the scanning electron beam would fail to land properly on those areas of the target that have received little or no exposure. The "target pulsing" bias insures that the scanning beam will land even in those portions of the target where the exposure was zero. Although "target pulsing" ensures that threshold level signals will not be compressed or lost in the readout process, it does give the video signal a rather uneven black or "zero exposure" level.

Signal Processing and Data Reduction

Figure 9 shows the type of video signals obtained from the SEC tube during sequential operation. The figure consists of oscilloscope traces of single lines of video signal scanned through the middle of the target area.

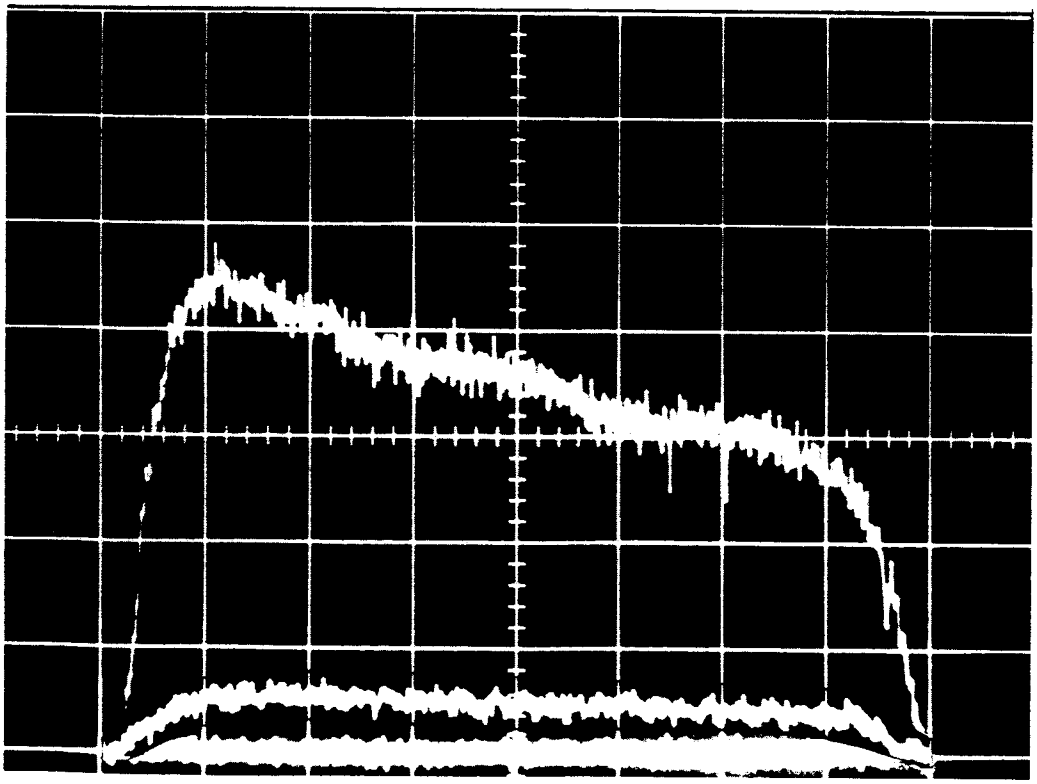

Figure 9.-Video signals.

The bottom trace of Figure 9 is the video signal with the scanning beam turned off. It is the electronic zero level and consists only of preamplifier noise.

The middle trace of Figure 9 is the signal obtained while reading out a zero exposure. This is the uneven zero level associated with the target pulsing needed to insure proper beam landing.

The upper trace of Figure 9 is the video obtained while reading out a uniform "full target" exposure. The increased noise due to the shot noise in the light flux of the exposure can be seen. The unevenness that appears as left to right shading is caused primarily by photocathode non-uniformity in the developmental tube used for these tests.

The video signal traces of Figure 9 serve to illustrate some of the basic data processing requirements for photometric application of the SEC tube to astronomy. The first data reduction step (after the video signal of an observational image has been digitized) is to subtract the uneven zero signal level from each data point. The zero signal level is quite stable and reproducible once the tube has been initially adjusted, so it is only necessary to have available as input data the signal obtained from one zero exposure test frame for a given observational run.

The second data reduction step is to normalize the observed data points by adjusting for the point by point sensitivity variations of the tube. The sensitivity data are obtained by subtracting the reference zero exposure data from a calibration exposure test frame made by exposing the tube to uniform illumination. This too need only be done on a periodic basis, perhaps a monthly calibration test exposure if the tube were employed as a sensor in most ground based observational programs.

After the input data have been zero corrected and normalized to cancel spatial sensitivity variations they are a close approximation to the output signal of a hypothetical, two-dimensional, integrating photomultiplier.

Further data reduction, depending on the application, can include correction for the MTF of the sensor or the optics and stacking of successive exposures of the same object to gain higher photometric accuracy.

Figure 10 is a block diagram of the processing of TV images currently undertaken at Princeton. The analog video signals from the readout of the TV tube are first recorded on an fm analog tape recorder. This step is included for two practical considerations in the Princeton work. One is that the subsequent digitizing hardware, partly because of economic considerations, cannot digitize the TV signals in real time. The analog tape recorder provides a convenient time base stretch of 16 to one, permitting the camera readout to remain at a rate that is consistent with optimum preamplifier performance and is also compatible with real time operator observation of the TV output image.

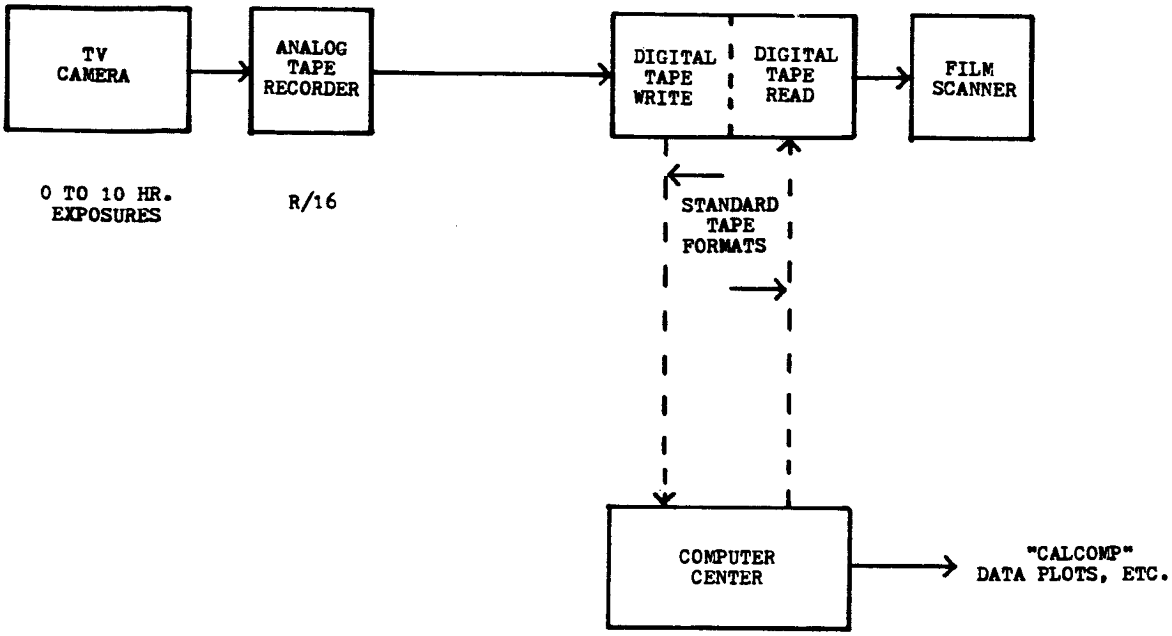

Figure 10.-TV image processing.

The second consideration is that only the analog recordings must be made during the actual observing session. The recorded images can be later (usually the following day) digitized for computer analysis.

The slowed down analog data is digitized, formatted and recorded onto standard 9 track 800 BPI computer input tapes. After processing in the computer, the image data may be displayed by a standard output device of the computer, such as "Calcomp" for spectral plots, or the computer output can be in the form of another digital tape containing the processed digital image. The same hardware that wrote the original digitized image tape can be used to read the computer output tape and to drive a film . scanning device for generation of high fidelity output images for visual inspection.

Figure 11 is a photograph of the film scanning device employed. The output film is placed on the rotating drum. A gas discharge lamp is advanced axially along the drum by a leadscrew arrangement exposing a helical track of 500 to 1000 lines per inch. The lamp is modulated by means of a digital to analog converter with the video signal from the digital tape. The digital data are clocked into the converter by means of a shaft encoder mechanically coupled to the rotating film drum.

The film scanner apparatus provides output images of sufficient quality so that there is essentially no degradation of the image by the output device. Although the film scanner is slow compared to a CRT display (the scanner takes about 15 minutes to scan a complete TV frame) its speed is of no consequence for this application, but the extremely high resolution (of the order of 400 TV lines at high contrast) and wide dynamic range are important in providing undegraded replicas of the computer processed TV image.

The film scanner is a modified color separation negative scanner used in the graphic arts industry. The digital form of the output video permits the use of a core memory in the digital tape reading hardware as an element to adjust the size and aspect ratio of the film scanner output image by adjustment of the clocking pulse used to strobe the digital image data into the digital to analog converter. The combination of the digital tape apparatus with the film scanner has proven to be an excellent image output system.

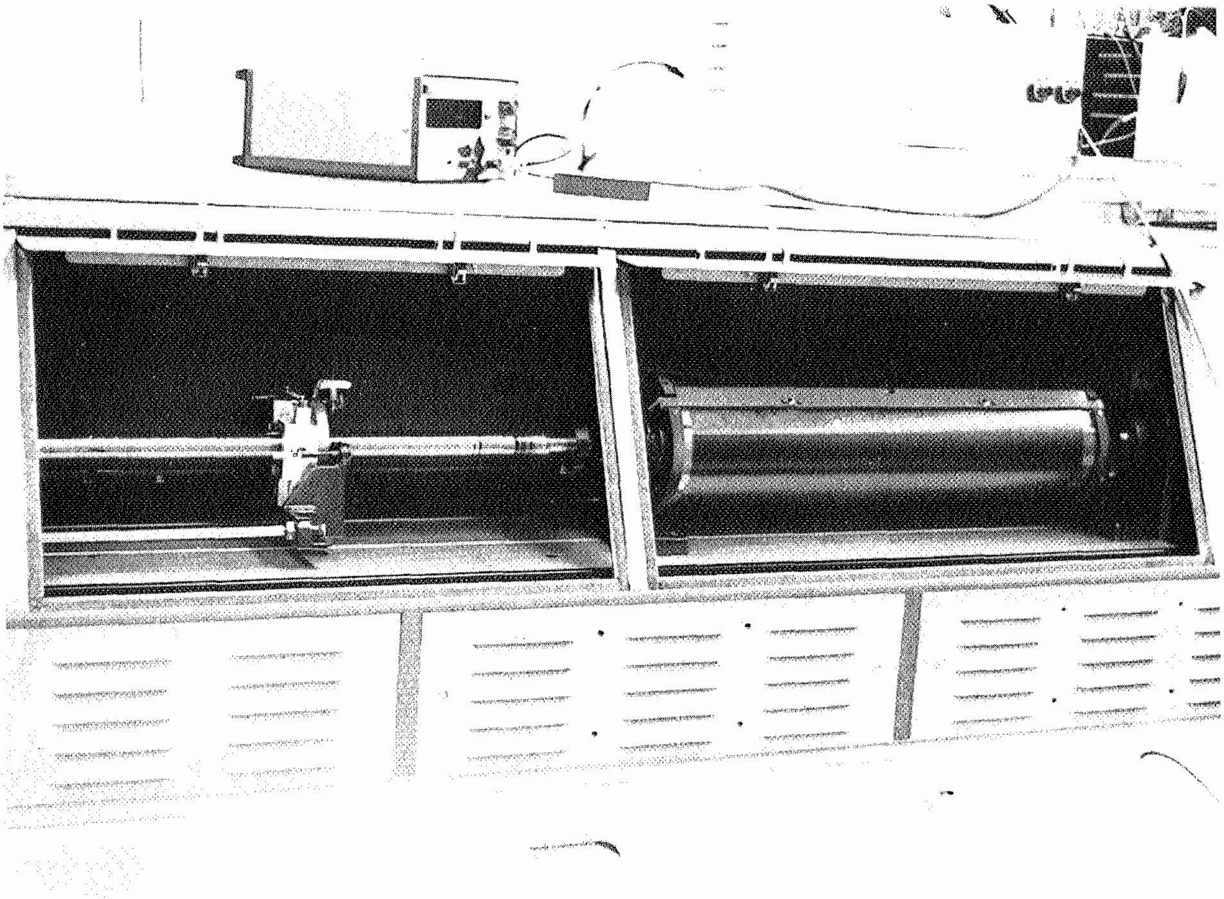

Figure 11. -Film scanner.

Long Exposure and Background Results

A capability for exposure periods of the order of ten hours is one of the primary sensor characteristics required for the astronomy application. Since the SEC target has sufficient resistivity to store an image change pattern for much longer than 10 hours without degradation, the limitation on integration period for the SEC tube is background effects in the image section. The limiting image section background is not thermionic emission from the photocathode, provided the photocathode is cooled below 10°C. The dark emission of comparable photocathodes in low noise photomultiplier tubes is lower by an order of magnitude than that required for 10 hour exposures without excessive background. Rather, the source of background in the SEC tube appears to be field emission associated with the high photocathode potential (-8kv) and related secondary effects. Accordingly, the tube development effort has included design and fabrication changes of the image section in order to get "quieter" tubes. It appears that bi-alkali photocathodes are intrinsically superior to S-20 varieties since no Cesium is employed in the image section. The lowering of the work function of image section components that have been exposed to Cesium while making S-20 photocathodes aggravates the background problem.

Figure 12 shows the background image formed after an 11.3 hour dark integration test at -10°C. Except for the hot spot in the upper left region of the image format, the background signal is approximately 20 percent of fullscale (200 photoelectrons per 33 micron square image element) over the balance of the image format. The hot spot, which filled to 50 percent of full scale, is correlated with an exceptionally sensitive region on the photocathode of the tube tested. Since the test tube is an engineering developmental "second class" type, it is reasonable to expect several better tubes to be obtained by selection from a production run of perhaps 20 tubes as opposed to the single tube assembly efforts used in the developmental work.

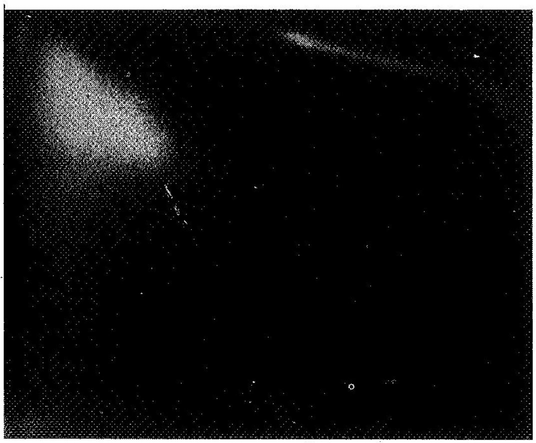

Figure 12. - Background from 11.3 hour dark integration.

The exposure of the photocathode to the illumination used during the PREPARE cycle does not degrade the long integration performance. This is attributed to the fact that even 10 hour integration does not require the extremely low photocathode background obtainable in some photomultiplier tubes which require protecting the photocathode from high illumination levels to achieve their extremely low background levels.

Figure 13 shows the image and video signals obtained with a 4.8 hour exposure of a mercury gas discharge source through an 8Å/mm spectrograph used to do stellar spectroscopy with the SEC tube. The exposure was extended to 4.8 hours by means of a dense filter in the light path. This is the longest exposure (as opposed to dark exposures for background tests) that we have made with the SEC tube. There is no sign of any reciprocity failure or other low intensity effects at this exposure duration. None were expected with the SEC sensor but the test served to confirm the expectation. The lines of mercury shown in Figure 13 are those at 3650.15Å and 3654.83Å and the pair at 3662.82Å/3663.27Å. The light continuum band of the image portion of Figure 13 is observatory dome light also coming through the entrance slit of the spectrograph. The intrinsically low background of the SEC tube at 4.8 hour exposure is evident in the dark unexposed portion of the image below the image of the spectrograph slit. This test was run at an ambient temperature of 15°C.

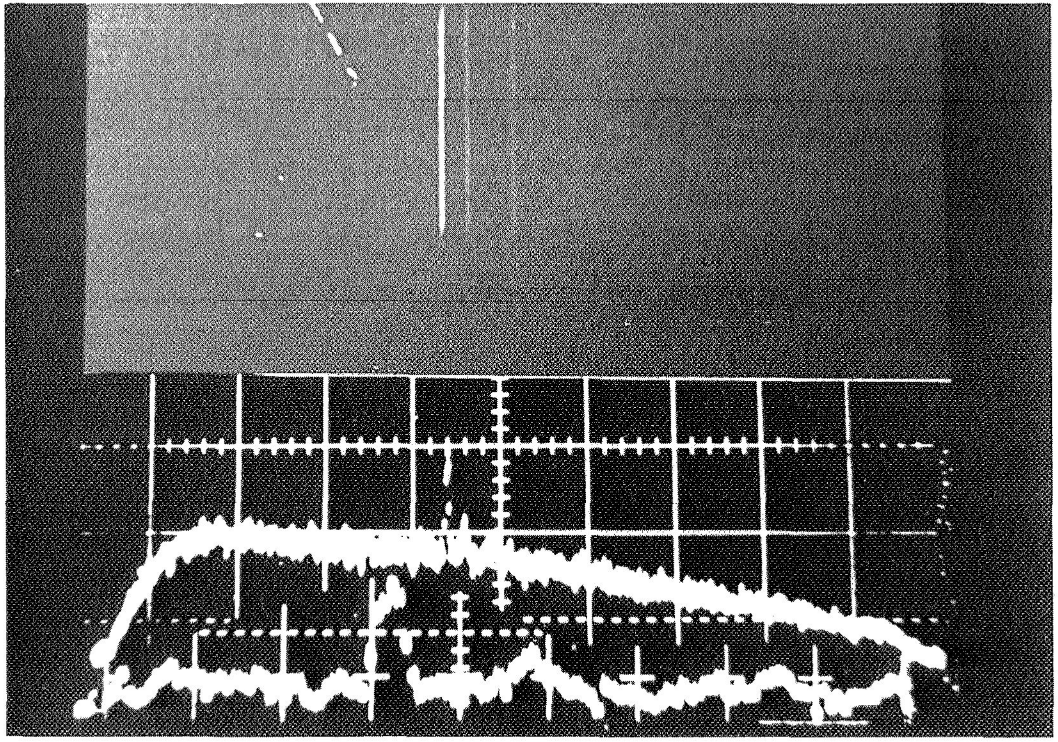

Figure 13.-4.8 hour exposure on mercury lines.

Addition of Frames

A method of extending the dynamic range of the SEC, either to obtain greater photometric accuracy or to be able to detect faint objects against a relatively bright background, is to add on a point by point basis two or more successive "full target" readouts of the same object. This can readily be done with the digitizing and computer data reduction methods discussed earlier.

Figure 14 shows video signals from a single full target exposure (single frame) and signals obtained by averaging four and nine successive exposures on the same test pattern. The noise in the white or fully exposed portions of the image is reduced as the number of frames averaged increases. The reduction for four frames averaged is, as expected for shot noise, about two to one. The reduction for nine frames averaged is not the expected three to one but appears to be more nearly 2.5 to 1. This is attributed to fine scale SEC target irregularities commonly known as target grain. The grain is normally masked by the shot noise of the signal for single frames, but as the noise due to photoelectron shot noise is averaged down by stacking of successive frames the coherent target grain noise becomes apparent.

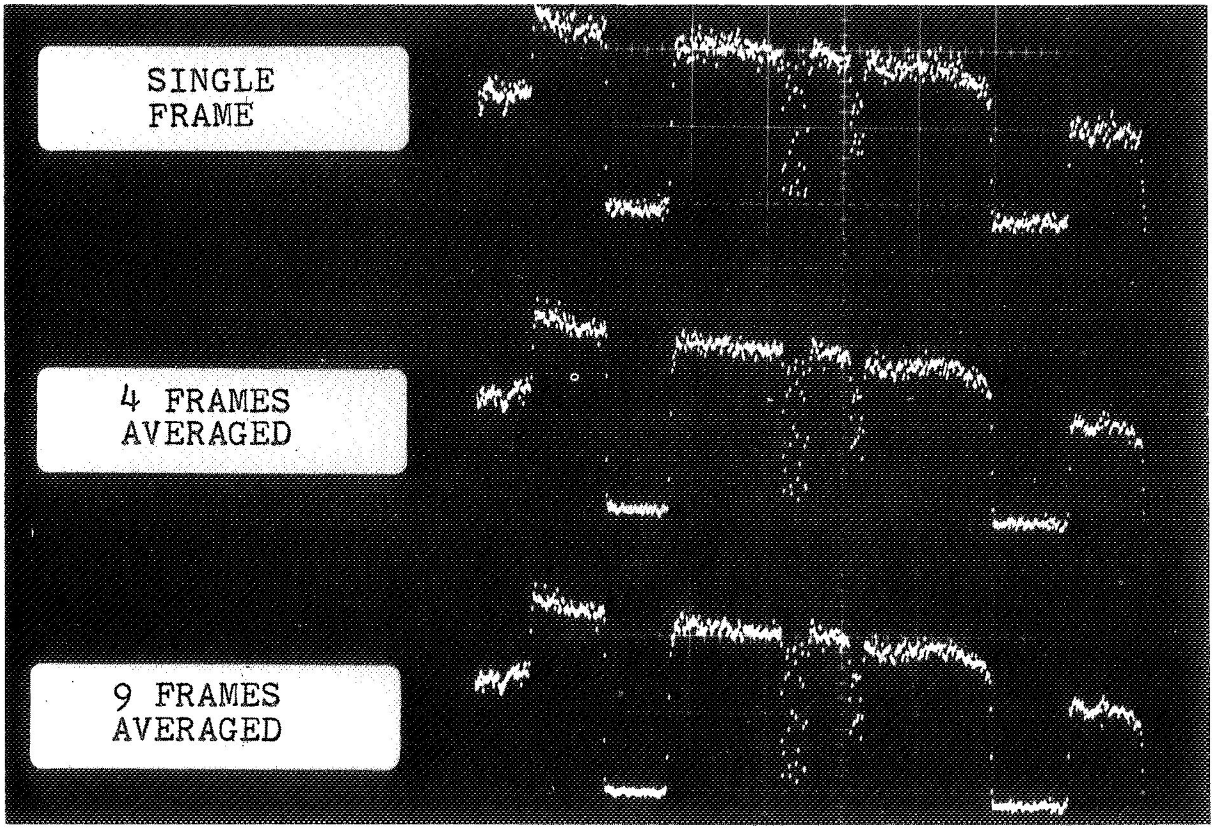

Figure 14.—Averaged video frame signals.

The noise in the black portions of the traces of Figure 14 consists entirely of preamplifier noise which is much less than the photoelectron shot noise and averages down as the square root of the number of frames as expected.

Application to Stellar Spectroscopy

The SEC tube has been used with an 8Å/mm spectrograph on the 36" reflector at Princeton University Observatory by Dr. Benjamin Taylor to observe H and K absorption and emission spectral details of cool stars.

Figure 15 shows the TV image of the spectrum of ξ BooÅ centered about 3950Å. The lower portion of Figure 15 is the same spectrum as the upper TV image but it has been enlarged 2 to 1 in dispersion and 5.1 normal to the dispersion by the digitally controlled film scanner to better illustrate the details.

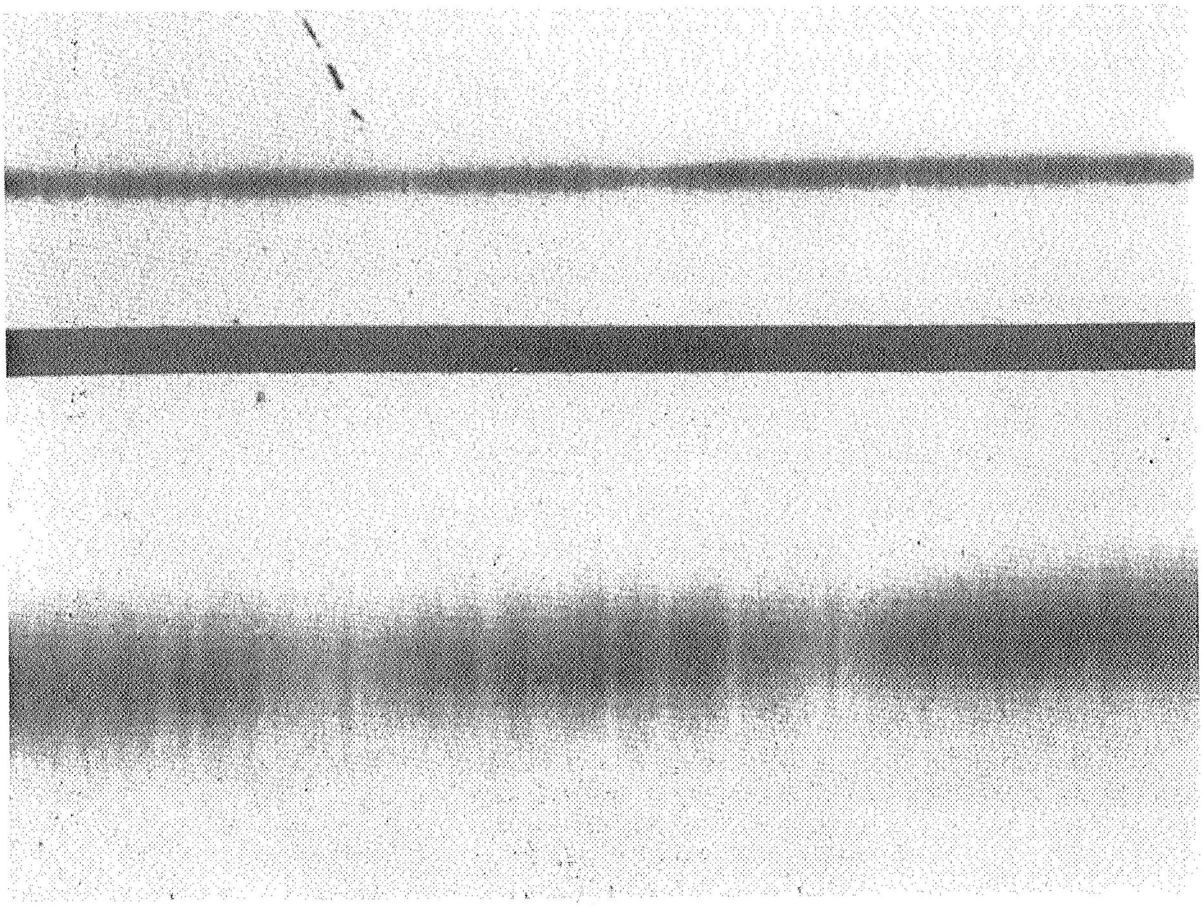

Figure 15.-TV spectra of ξ Boo Å.

Figure 16 is a Calcomp output from the computer after the spectral data of Figure 15 have been processed. The processing included zero subtraction, calibration for tube sensitivity variations, and averaging of the twenty television scan lines on which the spectrum appeared. The emission features in the center of the absorption bands can be clearly seen. (The wavelength scale is increasing to the right.)

Target Aging

There has been some concern about the life characteristics of the SEC target. Experience has indicated that the target gain does change somewhat, especially during the early hours (first 100) of the tube use.

Figure 17 is a TV image of a portion of the solar spectrum taken with the spectrograph-TV combination discussed previously. The dark streak of reduced target gain is the result of about 50 exposures with a total duration of 30 hours for stellar spectroscopy. The target gain reduction was of the order of 5 to 10 percent. The tube has since regained nearly all of the original loss in a few months. It appears that the problem of target aging can be circumvented by periodic calibration of the SEC tubes, which is readily done with the digital data handling methods. Further target development is also expected to alleviate the problem.

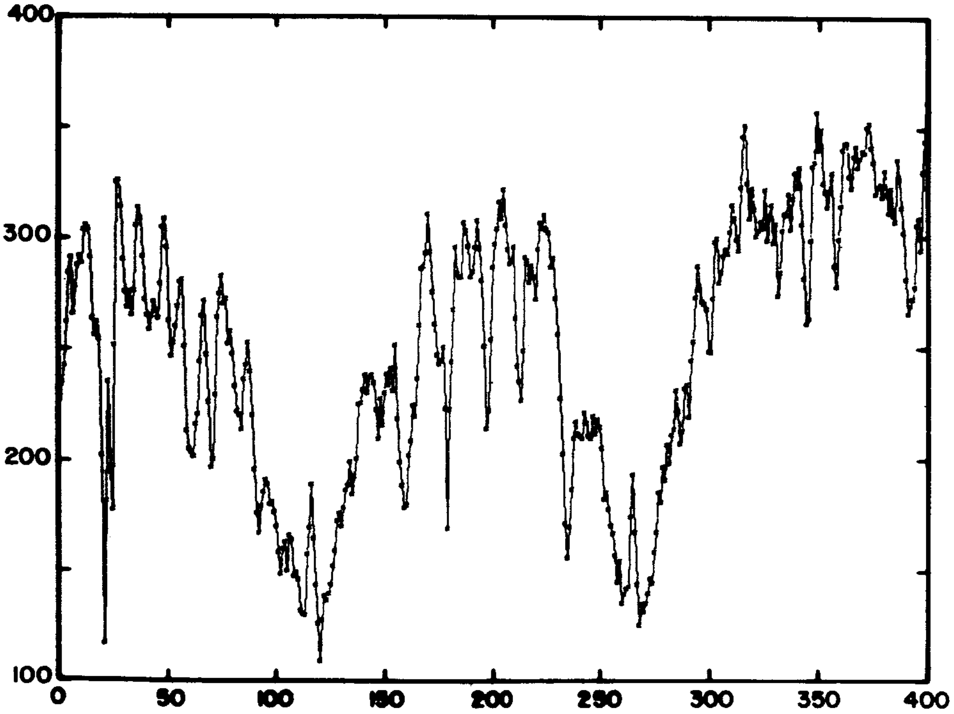

Figure 16. - Calcomp of data reduced TV spectrum.

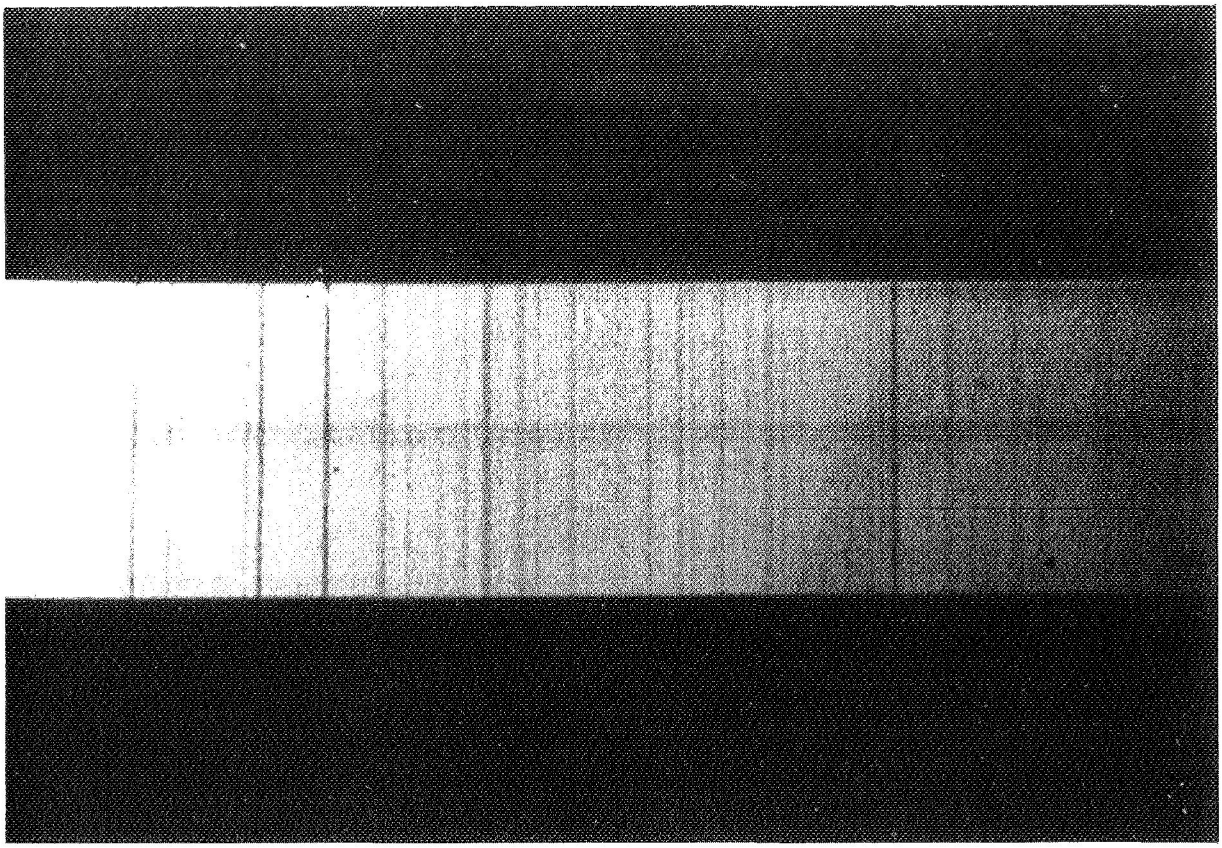

Figure 17.-TV solar spectrum.

Other Applications

Figure 18 is a TV image of the binary Gamma Leo which has a separation of 4.4 seconds of arc. The image of the Princeton 36-inch reflector was magnified to f/200 for this TV photo. Comatic distortion due to misalignment of the secondary mirror is readily apparent. It is planned to use the SEC/TV camera as a real time display at f/200 as a telescope alignment tool.

Future plans include the digital processing and enhancement of close binary star images taken at long focal ratios with the TV camera as a means of measuring the actual separations.

Figure 18.-Gamma Leo Binary at f/200.

REFERENCES

1. Beurle, R.L., Proc. Institute Elect. Engrs. 110, 1350 (1963).

2. Cope, A.D., Leudicke, E. "The Development of Camera Tubes for Recording Astrometric Images", Advances in Electronics and Electron Physics, Vol. 22A, pp. 175-188.

3. Flory, L.E., Pike, W.S., Morgan, J.M., Boyer, L.A. "A Programmable Integrating Television System for Use with Stratoscope", Advances in Electronics and Electron Physics, Vol. 22B, pp. 885-902.

4. Flory, L.E., Pike, W.S., Morgan, J.M., Boyer, L.A. "The Stratoscope II Television System", Journal of the SMPTE, Vol. 73, No. 1. Jan. 1964.

5. Krittmann, I.M. "Resolution of Electrostatic Storage Targets", IEEE Transactions on Electron Devices, Vol. 10, November, 1963.

6. Leudicke, E., Cope, A.D., Flory, L.E. "Astronomical Image-Integration System using a Television Camera Tube", Applied Optics, Vol. 3, No. 6 June 1964.

7. Lowrance, J., Zucchino, P. "Integrating Television Sensors for Space Astronomy", Advances in Electronics and Electron Physics, Vol. 26, 1969.

8. McMullan, D., Towler, G.O. "Some Properties of SEC Targets", Vol. 28A. Advances in Electron Physics, Academic Press.

Page intentionally left blank

SEC VIDICONS AS DETECTORS IN DIGITIZED PHOTOMETRIC IMAGE-FORMING SYSTEMS FOR ASTRONOMICAL OBSERVATIONS FROM THE GROUND AND SATELLITES*

G. E. Brueckner
E. O. Hulburt Center for Space Research
Naval Research Laboratory, Washington, D. C.

B. J. Tucker
Electro-Mechanical Research Corporation
Princeton, New Jersey

ABSTRACT

Two image-forming photometric systems using SEC vidicons are being constructed: (1) A digitized SEC vidicon system designed to map and measure the intensity of the outer solar corona from an OSO spacecraft, and (2) A digitized SEC vidicon system designed to measure absorption line polarization in the visible spectrum of the sun and to map solar magnetic fields. The advantages of the SEC vidicon over other detectors for these applications are discussed, including integration and storage of low-light level pictures in system (1) and high accuracy differential measurements in system (2). The limitations of SEC vidicons and the various noise sources are discussed and the first laboratory test results are shown.

---

*Supported by NASA funds.

ORBITING CORONAGRAPH

Brief Description of the Coronal Scene to be Observed by the Instrument - The first instrument we want to describe is a white light coronagraph to be flown on NASA's Orbiting Solar Observatory OSO-H. Koomen and Tousey have flown external occulted photographic coronagraphs on sounding rockets. The stray-light in this instrument could be reduced to be smaller than 10^{-10} of the sun's disc intensity. The field of view reaches from 3 to 10 solar radii. Almost each flight showed the range scale corona with straight coronal streamers having a small contrast from 3% to 10% to the electron scattering coronal background (Figure 1). Although geometric relationships between the streamers and active centers on the sun could be established, we are far from understanding the development and motion of the streamers. All pictures show straight streamers; no curvature could ever be seen. It seems strange that the streamers show a rigid rotation with the sun. In order to determine rotational effects of the streamers, two rockets within a time interval of 24 hours have been flown on 16 April and 17 April 1969. The surprising and disappointing result was that development effects within this time period dominate the rotational changes. It is obvious that one needs observations over a longer time period, but also with higher time resolution, in order to separate development effects from rotational effects. Photoelectric satellite observations are necessary because each rocket flight covers only 5 minutes.

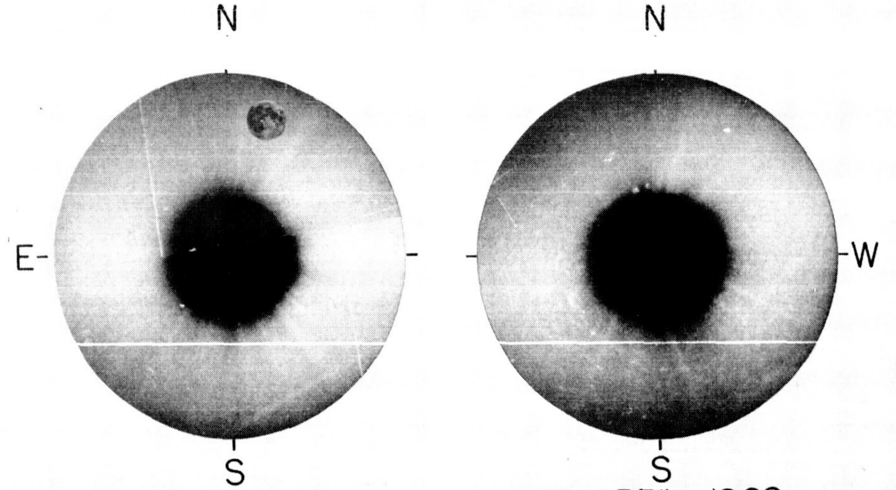

16 APRIL 1969
1620 UT

17 APRIL 1969
1645 UT

SOLAR CORONA RECORDED SUCCESSIVE DAYS.

Figure 1.-The solar corona photographed from a sounding rocket on successive days.

Brief Description of the Optical Arrangement - The imaging system of the coronagraph is an external occulted Lyot coronagraph (Figure 2). Two occulting discs (1) in front of the objective lens (2) provide a complete shadowing of (2) by direct sunlight in order to reduce stray-light produced by (2). The objective lens (2) images the coronal scene in the first image plane (3), where another occulting disc (4) stops all residual stray-light from the solar disc, imaged by (2) in this image plane. A field lens (5) images the objective lens into the plane (6), where an aperture stop (7) occults all diffracted stray-light produced at the edges of the objective lens. A relay lens (8) images the coronal scene on the photographic film plane (or the image tube). In the case of the orbiting coronagraph, the central portion of the image obscured by the occulting discs (1) will contain an attenuated image of the solar disc fed in by an auxiliary optical path (9) for calibration and alignment purposes. A polarizer (orbiting coronagraph only) was placed in direct contact with the fiber optics faceplate of the SEC tube. This polarizer consists of subsequent annular zones, where the direction of $\bar{E}$ vector is annular and radial to determine the polarization of the coronal scene at the boundaries of these zones.

Detection System Requirements - In the case of the orbiting coronagraph, the photographic film has to be replaced by a photoelectric detector. The following conditions have to be fulfilled by this system:

a. It has to be able to detect low light level signals. The intensity of the solar corona in the film plane of the coronagraph is 8×10^{-5} foot candle.

b. The minimum resolution has been determined to be 256 x 256 picture elements in order to place at least two readings on a narrow streamer.

c. The read out signal of each picture element should have a signal to noise level not less than 70:1 in order to record the weak contrast of the streamers.

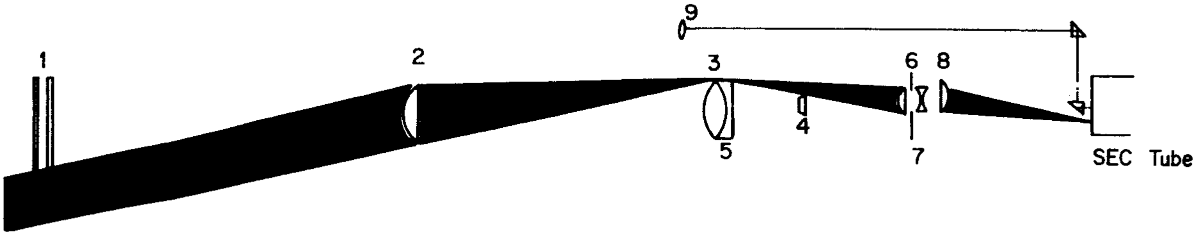

Figure 2.-External occulted Lyot coronagraph.

d. The photometric system has to be adapted to the very slow recording rate of the OSO tape recorder, which allows for this experiment to store only 25 8-bit words per second. To store the entire picture of 65536 words takes 43 minutes.

A point by point scanning system like a mechanical scanner and a photomultiplier or an electronic scanner with a photomultiplier does not fulfill these conditions. In order to achieve a signal to noise ratio of at least 70:1, each picture element needs an integration time of 0.4 second because of the low intensity of 1.3 x 10^4 photoelectrons per picture element per second. But the telemetry requires a storage rate of 25 p.e. per second. We have shown above that each available space in the telemetry has to be used in order to store at least one image per solar orbit. One would have to integrate using 10 photomultipliers simultaneously in order to match the low intensity to the given sample time of the recorder. The mechanical optical difficulties do not allow this solution.

The SEC vidicon overcomes all those problems because it can be used not only as an integration device for all picture elements simultaneously but also as a long time storage device for the electronic charge distribution on the target, provided we find a solution to read out the target very slowly over a period of 43 minutes without destroying the remaining charge distribution on the target. We have solved this problem by operating the SEC vidicon during the read out phase in a "beam pulsed mode". The read out beam is switched on by a positive voltage on grid No. 1 only for 2 microseconds to replace the charge of one picture element on the target without destroying the charge distribution of the remaining picture elements.

SEC Vidicon Systems Consideration - Three major constraints apply in the design of the solar coronagraph. These are: physical size, the unit must fit within the confines of the 4 x 4 x 20" sail experiment outline; power, a severe constraint since the OSO spacecraft has a limited power generation system; data rate, a severe limitation since the OSO telemeter allocation can accommodate only 200 bits per second.

Spacial resolution required is 256 elements per line and 256 lines per raster, causing a raster containing some 65,000 picture elements. Because the scene detail of interest is very low contrast streamers, it is essential that the ratio of signal to noise in signal ratio be as high as possible and, therefore, that exposure to the scene always be kept at a maximum. In order to make the effective quantitization noise level negligible, the video data are encoded to 8 bits (one part in 256), but only 7-bits are transmitted due to other considerations. It is desirable to observe the progress of the streamer across the scene with a time resolution not to exceed 5 minutes per raster.

Data generation rate is 1/5 raster per minute times 1/60 minutes per second equals 1/600 rasters per second. Since each raster contains some 65,000 words (elements), the word rate must be (1/600) (65,000) $\approx$ 100 words per second, and if each word is 8 bits, the data rate is 800 bits per second which equals the total OSO data capacity.

The problem then becomes how to retain the useful information for an 800-bit-per-second source while transmitting this information through a 200-bit-per-second link. The solution is the use of some sort of data compression with effective ratio of 4 to 1.

A great problem with data compressors is that data rate of generation is not constant but occurs in spurts necessitating buffering. Standard data buffering is prohibitive for use on the OSO spacecraft for reasons of size, weight, and power. The image tube itself, however, may act as a take-up buffer for the data system.

The SEC vidicon is uniquely qualified for this role because of the information storage and retrieval characteristics of the SEC target. Access to the information stored on a target element may be made in less than a microsecond but may be stored without degradation for many hours. This sort of operation is very similar to a core memory, but instead of storing one binary bit, it stores a number equal to the SNR with 1σ confidence. No other known camera tube can meet the requirements of quick access, long-term storage, and dynamic range.

The White Light Coronagraph Data Handling System is as depicted by block diagram (Figure 3).

The spacecraft power comes up either on command or as available; the power system, in turn, initiates a master clock which, after being started, gains synchronizing control of the power system itself. This enables power distribution to be made to the remainder of the system.

When the master clock is started, a programmer is enabled for operation as required from the spacecraft. The spacecraft applies two kinds of signals to the programmer, these being the programming commands which are normally stored in the spacecraft and are not changed except by ground command and the spacecraft data handling system status signals.

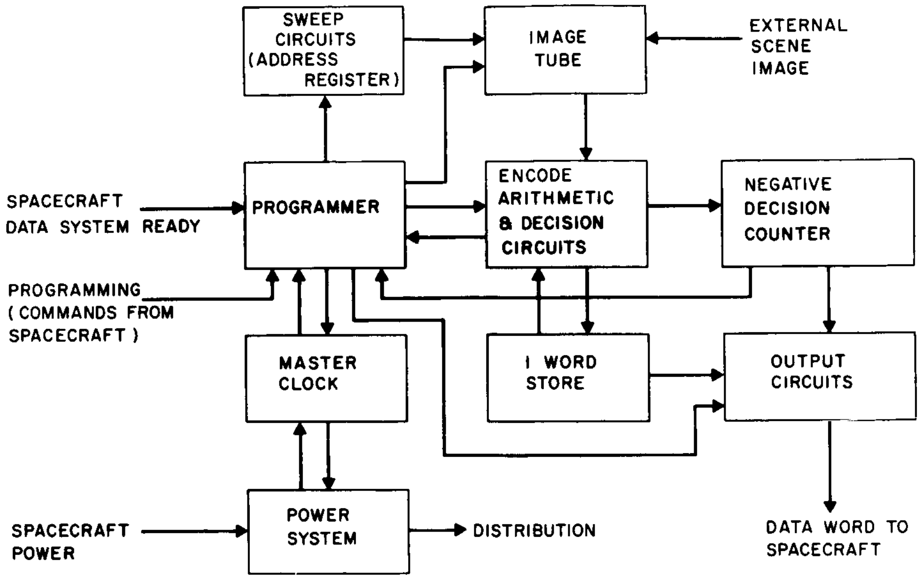

Figure 3.-Orbiting solar coronagraph, electronic system block diagram.

Upon receipt of a data system ready signal from the spacecraft, the programmer initiates a series of commands. The first of these causes an image stored on the camera tube (actually one element) to be encoded. When this intensity point is encoded, the signal enters decision-making circuits where the newly encoded signal is compared with the last intensity signal sent. A decision is made as to whether the newly encoded signal is redundant; then a negative decision pulse is sent to a negative decision counter and also a pulse is sent back to the programmer with the meaning to index to a new position (spacial address) since this position and value need not be transmitted. The programmer initiates a new address to the camera tube via the sweep circuits. This encoding and decision-making process continues until either: (a) 127 negative decisions have been encountered; (b) new data are detected; or (c) the television frame is completed. If a total of 127 negative decisions (adjacent redundant elements) have been recorded in the negative decision counter, the previously stored information data are resent and the negative decision counter reset. If new data had been encountered at any new element other than the element transmitted, then two things would occur; a pulse train representing the number of adjacent negative decisions encountered before the new data would be sent to the spacecraft and, following this, a pulse train representing the word "stored" would be transmitted and the value of the newly encoded data would be stored. If the television frame had come to an end, a unique synchronizing pulse train would have been sent to the spacecraft and the data system circuits would have been reset to zero.

In order to avoid negative compression ratios (effective compressions less than one) adjacent non-redundant information is transmitted without addressing data. This feature causes the requirement for a flag bit to be added to each transmitted word to identify whether the newly transmitted work is run-length data (number of negative data decisions) or intensity data.

With this type system, several popular compression schemes can be accommodated. The white light coronagraph system has incorporated a floating variable aperture zero-order predictor. The aperture is selectable by ground command and encoding resolution is 8 bits in this power system. Compression ratios of over five have been experienced with dynamic ranges transmitted of about 30 db.

Total power required is derived from the spacecraft and amounts to about 7 watts taken from the raw power bus.

System weight is about 12 pounds and volume required is 320 cubic inches, contained in a shape 4 inches by 4 inches by 20 inches.

Construction is by the mother board system, whereby small printed circuit boards containing the integrated circuit flat packs are mounted on a larger PC board. Electronic density is about 10 flat packs per cubic inch, which is less than that which is possible with large scale integration, but much more than standard high density card mounting.

Reliability is achieved through extensive use of redundancy, by the use of highest quality components available, by extensive quality control and other control programs, and by extensive testing.

REAL TIME SOLAR MAGNETOGRAPH

Magnetic Field in the Solar Atmosphere and Zeeman Splitting of Fraunhofer Lines - The second instrument which is now under construction at the Naval Research Laboratory (NRL) and at Electro-Mechanical Research Inc. (EMR) is a digitized solar magnetograph. The Westinghouse SEC vidicon No. WX30654 is used as a receiver. This instrument is not a flight instrument.

Mapping magnetic fields of the sun's atmosphere requires measurement of small intensity differences caused by the polarization of Zeeman splitted absorption lines in the solar spectrum. Because the thermal broadening of the lines exceeds the Zeeman splitting for fields below 1,000 gauss, those fields can be made visible only by isolating the left and right hand circular polarized σ components in case of the longitudinal Zeeman effect, or one can make visible transverse magnetic fields by measuring the linear polarization of the σ and π components. In any case, the measurement of small intensity differences requires low signal to noise ratios. The band-pass locations are shown in Figure 4 and the magnitudes of the effects to be measured are shown in Figure 5. We have calculated the calibration curves for longitudinal and transverse Zeeman effect by assuming a band-pass width of 0.13A. In order to detect longitudinal fields of 10 gauss, or transverse fields of 100 gauss, our signal to noise ratio has to be better than 2 x 10^{-3}.

In order to map the magnetic fields in regions of the sun, conventional magnetographs raster those regions point by point. The tremendous information loss makes those instruments very slow. Figure 6 compares the speed of different types of magnetographs.

Spectroheliograph type magnetographs make use of the two dimensional image they can get through the narrow slit, but the ratio of slit length to slit height is very high. The use of photographic techniques in connection with those instruments produces nice pictures of magnetic field distributions, but in order to obtain quantitative results one has to go through a tedious reduction process. The calibration curves shown in Figure 5 are not linear. Therefore, it is necessary to transform the measured polarization values point by point into magnetic field strength values.

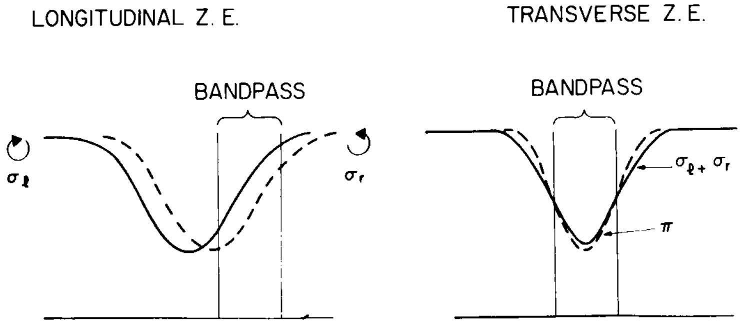

Fe I 5250Å BANDPASS 50mÅ

$P_V = 0.05 \times H_{\parallel} \quad 0 \leq H_{\parallel} \leq 500$

$P_Q = 7.5 \times 10^{-5} \times H_{\perp}^2 \quad 0 \leq H_{\perp} \leq 1000$

Figure 4.-Bandpass location for measurement of longitudinal and transverse Zeeman effect.

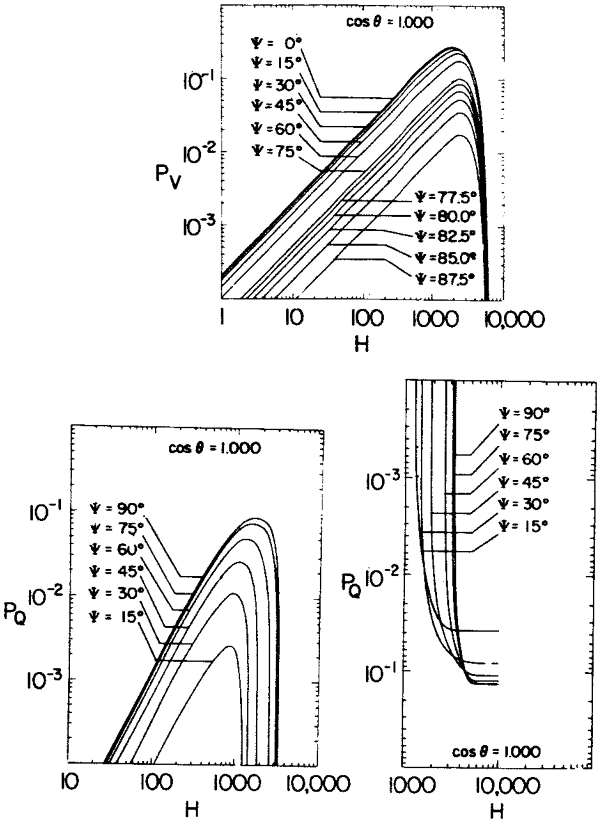

Figure 5. - Circular and linear polarization of the 5250A absorption line in the solar spectrum as function of magnetic field strength. The inclination of the field to the line of sight is the parameter (band width, 0.13A).

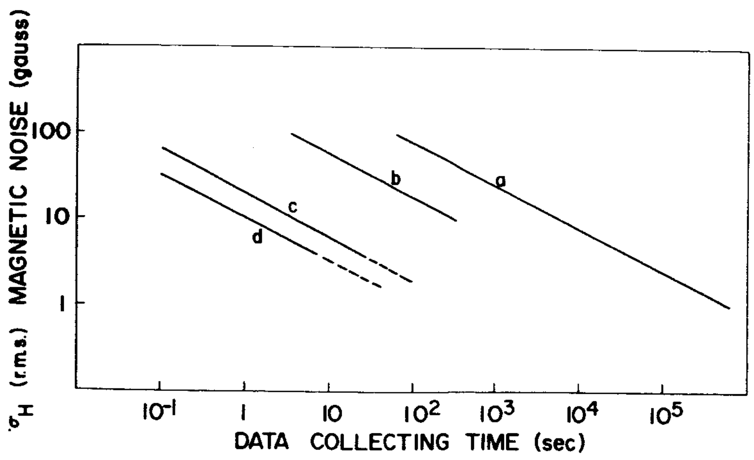

Figure 6.-Speed of different types of magnetographs: longitudinal field; area, 120 x 120 arc sec ^{2}; spatial resolution, 1 x 1 arc sec ^{2}; telescope aperture, 30 cm; 5250.2 A (g=3, band width, 1/6 A). a, Babcock type; b, Leighton, Michard spectroheliograph type (photographic); c, two-dimensional photoelectric (SEC) vidicon tube, noise limited; d, two-dimensional photoelectric (photon noise limited).

Brief Description of the Imaging Solar Magnetograph - This background leads to the design of our magnetograph, which uses a birefringent filter to obtain a two dimensional image of an area on the sun with a narrow band-pass of 1/8Å. We have to optimize the optical arrangement in such a way that the signal to noise ratio introduced by the receiving image tube is not compromised by the number of picture elements, as will be shown later. But at the same time a very high spatial resolution is required. The instrument we have built has a field of view of 5 x 5 arc minutes with spatial resolution of 2.5 x 2.5 arc seconds and an optional field of view of 2 x 2 arc minutes with a spatial resolution of 1 x 1 arc second. Using the large SEC vidicon No. WX30654 because of its larger target storage capacity compared with the tube used in the OSO coronagraph, we hope to obtain a signal to noise ratio of 150 to 1 for each single image element. The advantage of this type of instrument is the simultaneous integration of all picture elements. The limiting factor, however, is still the signal to noise ratio introduced by the tube's target storage capacity, because the intensity of the scene at the faceplate of the SEC vidicon is still higher than the number of equivalent photoelectrons which can be stored on the target.

Figure 7 shows the optical arrangement. A 30 cm Cassegrain telescope provides a 3 cm diameter solar image. The small field of view of 5 x 5 arc minutes is collimated through the polarization analyzer and the birefringent filter (band-pass, 0.13Å). A relay lens system images the monochromatic solar scene onto the faceplate of the SEC vidicon. Calibration of the instrument will be done by introducing artificial polarization.

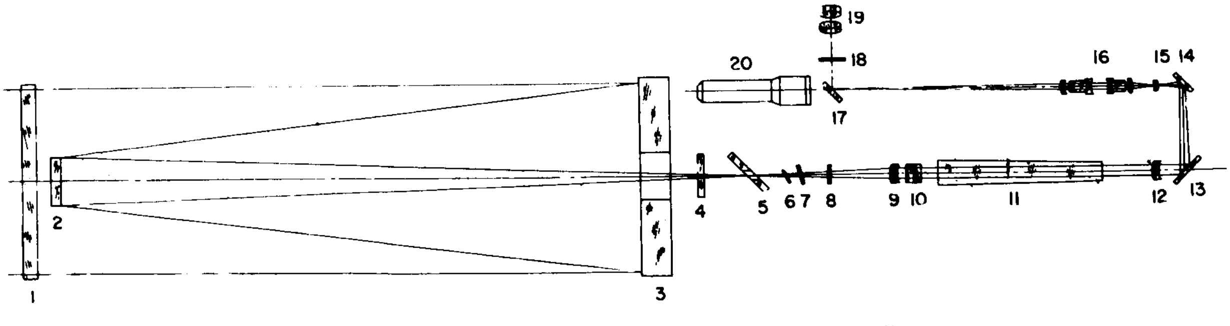

1. heat reflection filter, halfwidth 300 A
2. Cassegrain mirror
3. primary mirror
4. fused silica window
5. field of view aperture stop, auxiliary mirror
6. instrumental polarization compensation
7. calibration plate
8. λ/4 plate for L.Z.E. calibration
9. collimator lens
10. polarization analyser

11. birefringent filter
12. collimator lens
13,14. folding mirrors
15. field lens
16. relay lens
17. flip-in mirror for eyepiece monitoring,
18. reticle
19. eyepiece
20. SEC vidicon

Figure 7.-Real time solar magnetograph, optics schematic.

SEC Vidicon System Consideration - Electrical operating parameters for the computerized TV are very similar to those of the coronagraph; however, since the unit is confined to earth operation, constraints such as volume, weight, and power are not important. Of prime importance is signal to noise ratio, and all other parameters must be compromised in favor of signal to noise ratio. In order to achieve this, the 40 mm SEC vidicon has been selected, principally in order to achieve higher target elemental electron storage capacity.

Scanning density is about 45 TV lines per cm, and it would be expected that an elemental signal to noise in signal ratio of greater than 150 could be achieved.

The electronic system is depicted by the block diagrams of Figure 8 and Figure 9.

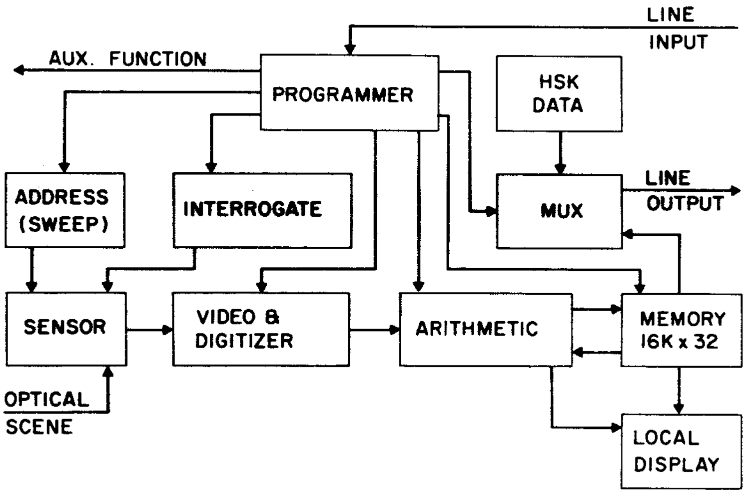

Figure 8.-Real time solar magnetograph tower unit, electronic block diagram.

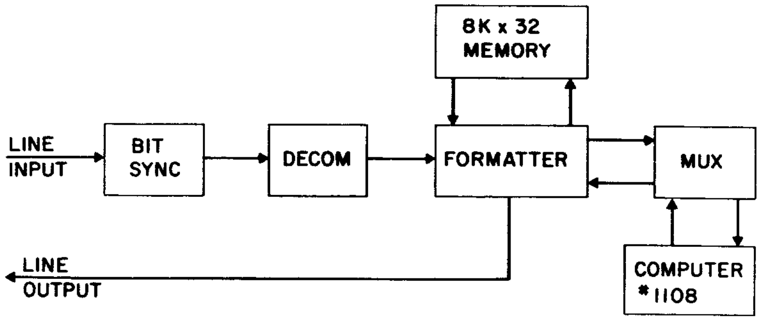

Figure 9.-Real time solar magnetograph receiver/formatter unit, electronic block diagram.

Again, as in the coronagraph, the camera tube is a part of the data system rather than an independent variable. A particular part of the scene is addressed by the programmer via sweep circuits. At the appropriate time, the SEC target is interrogated, and the stored information read, digitized, and held in a register. At the completion of this function, the programmer calls up from memory past history of the address in question, adds the new information and places the new number back at its assigned location in the core memory. This process repeats until the entire data frame is read into the core memory, at which time several options are available. Some of these options are: (1) the data field may re-cycle with the sensor input either on or off, (2) a sensor polarizing data field may be executed, (3) this portion of the data system may stop awaiting some external event, such as changing of the KDP voltage, indexing the birefringent filter, data dump, etc.

Two KDP crystals in front of the birefringent filter act as a polarization analyzer. Discrete voltage level combinations applied to those crystals result in different phase shifts of the analyzer combination, which are $-\lambda/4, 0, +\lambda/4$ and $+\lambda/2$. The target of the SEC vidicon is exposed to light of one of the specific phase shifts of the analyzer, which is controlled by the programmer. After readout, digitization and dump into one half of the memory, the programmer switches the analyzer into another phase shift. The target is then exposed to this opposite polarized scene which is digitized and dumped into the other half of the core memory. Subsequent images of the same analyzer phase shift can be added in the memory to enhance the signal to noise ratio.

The contents of the memory can be displayed as an analog image in rapid sequence on an oscilloscope screen and reloaded into the memory. This allows a quick visual evaluation of the image quality, which is determined by the seeing characteristics of the atmosphere during target exposure. Unwanted images can be disposed immediately and replaced by new exposures.

At convenient intervals, housekeeping data such as filter settings, local time, etc. must be added to the data stream so that identification can be made. This is accomplished by a conventional digital multiplexer.

A Receiver/Formatter unit is located at the computer central located some 10,000 feet away from the observatory tower. Since the signals from the tower have been serialized for transmission through a coaxial cable, a means must be provided for recovering the original reference. This is accomplished by use of a bit synchronizer. A de-commutator is used to group convenient numbers of bits for parallel presentation to the Formatter. The Formatter performs the function of controlling the 8KX32 memory where a complete data frame may be placed while awaiting time on the computer. This step is necessary because the computer is time shared via the multiplexer, and entry cannot be guaranteed at any specific time.

THEORETICAL AND TEST RESULTS

Noise Sources in a SEC Vidicon Electronic System - Errors which are normally present, or potentially present in a differential television digital photometer utilizing an SEC vidicon are as illustrated by Figure 10.

First transfer stage in the series is the photo-cathode quantum conversion efficiency, QE. In the model used, photon noise, N_{np}, is depicted as being added along with a noiseless photon stream. Certainly, the goal of any photometer is to measure with sufficient accuracy to the point where the statistics of the photons themselves determine the measurement accuracy. However, such is often not the case.

The transfer stage marked A_t, the SEC vidicon target, depicts one input to the target as being photoelectrons from the photo-cathode. Since the quantum efficiency is on the order of 10% for visible energy, photoelectron statistics will

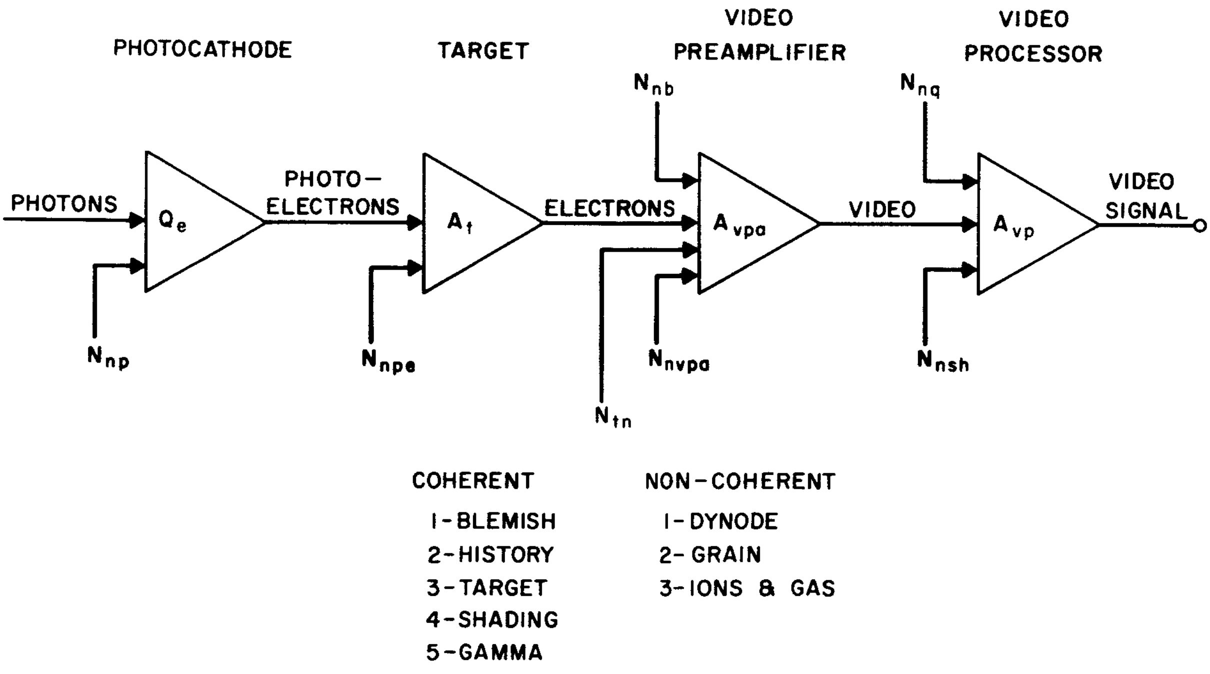

Figure 10.-Error sources of a SEC vidicon photometric system.

normally determine the ultimate in noise performance. The model again depicts the noiseless photoelectron stream accompanied by a noise source shown feeding into A_t labeled N_{npe}.

A_{vpa} represents the video pre-amplifier which is often the noise dominant factor for low signal levels. Into the video pre-amplifier, it can be seen that a number of noise electrons are added corresponding to the beam noise, N_{nb}. Another group is added as the video pre-amplifier equivalent noise, N_{nvpa}, and a rather large number of error sources are grouped under the title N_{nt}, target noise.

Video pre-amplifier noise, N_{nvpa}, is caused principally by the shot noise in the first amplifying element. The state of the art is such today that this noise component amounts to the order of 1000 electrons/sample as the uncertainty.

The electron scanning beam noise, N_{nb}, has two components, shot and spacial. Shot noise is normally not a significant factor for SEC vidicon systems because of the relatively high target gain; however, scanning beam spacial noise due to noise in the deflection system must be guarded against.

A large group of error or noise sources is illustrated as N_{tn}. These sources can be roughly grouped as coherent and non-coherent noise.

Coherent elements consist of blemishes which are defects within the target, history which is either burned in or unerased reproductions of images which have previously been present, Moiré patterns due principally to the field and suppressor meshes, shading which can cover a multitude of errors including photo-cathode and target nonuniformities to beam landing errors, and gamma, while not strictly a noise, nevertheless causes an upper limit on exposure.

Non-coherent sources of error include dynode noise which is added because of the amplifying process, grain which often increases with use, thereby setting the useful lifetime, and ion and gas noise. Ions and gas can cause several faults ranging from photo-cathode poisoning to charge flooding to irreversible target damage. Photo-cathode voltage level also causes noise, both in apparent target gain and in target amplifier statistics. These noise components for the most part are determined in manufacturing; however, some degree of control can be effected in all.

Additional noise components are added in the video processing system indicated by N_{nq} and N_{nsh}. N_{nq}, the quantization noise, can be made any arbitrary level by sufficient quantization levels in favor of speed or some other parameter. N_{nsh} is the sample and hold noise which has the same constraints as N_{nq}.

Other noise signals are not considered here, since the purpose of this paper is to consider only the photometer. One observation is made, however, with regard to digitized vs analog systems and that is that digitized signals can be transmitted to any arbitrary degree of accuracy, whereas analog transmission is severely limited.

Equivalent Photoelectron Target Storage Capacity - Target gain increases with polarization voltage in a manner similar to the curve of Figure 11. This curve was obtained experimentally from a type WX30691, but the curve is typical of all Westinghouse SEC vidicons evaluated. Numerically, the gain varies as the 1.6 power of target voltage.

From this curve, it would seem that all one has to do in order to get to the point of photoelectron counting is to increase target voltage. However, increased target gain is not without penalty. At higher target voltages, nonuniformities become much more pronounced, blemishes become objectionable, secondary redistribution occurs, and the target becomes sticky. This stickiness is usually caused by the onset of conduction band gain and occurs in the region of 20 volts across the target. One advantage besides higher gain is obtained from higher target voltage operation - beam landing errors become less significant, especially at low signal levels.

The maximum number of electrons which can be stored while maintaining unity gamma is normally 3.9×10^9 per cm^2 referred to the face-piece, and at a target voltage of 10.

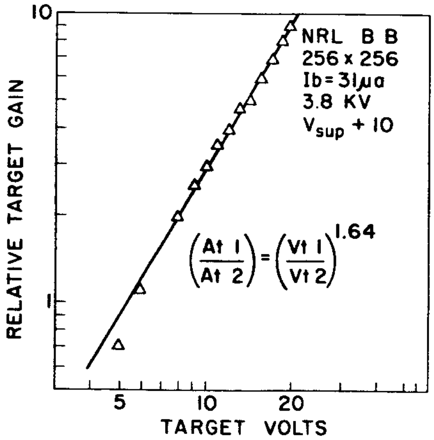

Figure 11. -Relative target gain as a function of target voltage.

It can be shown that target capacity is about 50 pf/cm^2 referred to the face-piece at zero target volts and increases to about 100 pf/cm^2 at 30 volts. Combining the effects of target capacitance sensitivity to voltage and target gain sensitivity to voltage, and assuming reasonable values of absolute target gain, i.e., 60 at 10V, an expression for storage capacity for photoelectrons can be derived:

$$N_{pe_{max}} = (1.9)\ (10^8)\ V_t^{-0.6} + (6.7)\ (10^6)\ V^{0.4} \qquad (1)$$

This equation is plotted as Figure 12. Significance of this parameter is that the photoelectron statistics along with video pre-amplifier noise determine total noise performance.

Signal to Noise Ratio of SEC Vidicons - The signal to noise ratio (SNR) can be defined as the ratio of the difference between two means (signal) to the total uncertainty in the signal. It can be shown that the standard deviation of mean difference is simply the square root of the sums of variances, i.e.

$$\sigma = \sqrt{\sigma 1^2 + \sigma 2^2 + \cdots}$$

Very often in SEC vidicon camera systems only two noise sources dominate all others. These sources are the shot noise in the photoelectron stream, N_{npe}, and video pre-amplifier equivalent noise, N_{nvpa}. When only these two sources

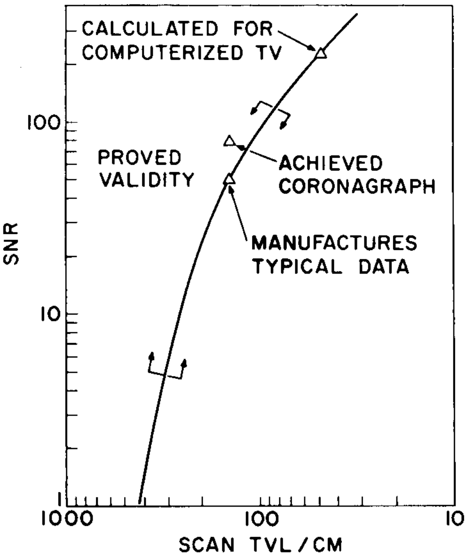

Figure 12.-Photoelectron storage as function of target voltage.

are considered and both are referred to the video pre-amplifier input, the total electron noise is

$$N_n = \sqrt{\left(A_t \sqrt{\frac{N_{pe}}{E}}\right)^2 + (N_{nvpa})^2}$$

Total usable signal referred to this same location is

$$N_s = A_t \frac{N_{pe}}{E}$$

therefore, the maximum signal to noise ratio can be expressed as

$$SNR_{max} = \frac{A_t \dfrac{N_{pe}}{E}}{\sqrt{\left(A_t \dfrac{N_{pe}}{E}\right)^2 + (N_{nvpa})^2}} \qquad (2)$$

where E is the total number of elements represented by the total number of photoelectrons, N_{pe}. Of course, if more convenient, N_{pe} can be replaced by N_pQE where N_p is the total number of photons contained in E elements.

It is pointed out that SNR in Eqn. (2) is also the dynamic range when N_{pe} is at maximum. Maximum signal to noise ratio will occur at an input level just at saturation, i.e., N_{pe} 6.2×10^7 photoelectrons/cm^2.

A difference in signal intensity between two areas can be expressed as

$$\frac{N_{pe}}{E}_1 - \frac{N_{pe}}{E}_2$$

If the modulation m is defined as the difference in intensities divided by the sum, then

$$m \doteq \frac{\dfrac{N_{pe}}{E}_1 - \dfrac{N_{pe}}{E}_2}{\dfrac{N_{pe}}{E}_1 + \dfrac{N_{pe}}{E}_2} = \frac{\Delta \dfrac{N_{pe}}{E}}{\dfrac{2N_{pe}}{E}}$$

When $\frac{N_{pe}}{E}$ is the mean density, the total signal S is expressed by

$$S = m \frac{2N_{pe}}{E} \qquad (3)$$

and the total noise N_n for the approximation under discussion

$$N_n = \sqrt{\left(A_t\sqrt{\frac{N_{pe}}{E}}\ _1\right)^2 + \left(A_t\sqrt{\frac{N_{pe}}{E}}\ _2\right)^2 + (N_{nvpa})^2}$$

or if $N_{pe1} \approx N_{pe2}$ and averages taken

$$N_n = \sqrt{2\left(A_t\sqrt{\frac{N_{pe}}{E}}\right)^2 + (N_{nvpa})^2}$$

then the signal to noise ratio at the video pre-amplifier input

$$SNR = \frac{m\ 2\ \frac{N_{pe}}{E}\ A_t}{\sqrt{2\left(A_t\sqrt{\frac{N_{pe}}{E}}\right)^2 + (N_{nvpa})^2}} \qquad (4)$$

Often it is advantageous to replace the quantity E, total number of resolution elements per cm^2, by a one dimensional quantity f, corresponding to elements per centimeter. Then $E = f^2$ and

$$SNR = \frac{m \qquad 2\ N_{pe}\ A_t}{f^2\sqrt{2\left(A_t\sqrt{\frac{N_{pe}}{f^2}}\right)^2 + (N_{nvpa})^2}}$$

or rearranging and combining with the effects of target gain sensitivity to voltage:

$$SNR = \frac{2\ m\ N_{pe}}{f\sqrt{2\ N_{pe} + f^2\left(\frac{N_{nvpa}}{1.5\ V_t^{1.6}}\right)^2}} \qquad (5)$$

For high signal values equation (5) for much of the range in f reduces to

$$SNR_h \approx \frac{m\,2\,N_{pe}}{\sqrt{f\,2\,N_{pe}}} = \frac{m}{f}\sqrt{2\,N_{pe}} \qquad (6)$$

The comment has been made that, for a fixed scene, the value of m varies f^{-2} for values of m .5.

Therefore

$$SNR_h \propto \sqrt{\frac{N_{pe}}{f^3}}$$

and for low signals

$$SNR_\ell \approx \frac{3\,m\,N_{pe}\,V_t^{1.6}}{f^2\,N_{nvpa}} \qquad (7)$$

and as above

$$SNR_\ell \propto \frac{N_{pe}\,V_t^{1.6}}{f^4\,N_{nvpa}}$$

One interesting and not so obvious result of equation (5) is that the SNR_{max} goes through a peak generally in the area of ten volts. The position of this peak is a function of scanning resolution and video pre-amplifier noise performance.

System noise in signal has been measured both by reduction of Polaroid pictures and by a statistics-taking machine. Figure 13 is a plot of one of these series of measurements. In this case the ratio of elemental signal to noise in signal reached a value of 80 at the upper extremity of the unity gamma region of the transfer function. The noise in signal value remained constant within 20% when the noise value was calculated along a TV horizontal line, along a TV vertical line, or on a single TV element over a series of TV frames.

A fixed spacial noise pattern is encountered at about 50 cycles per centimeter. This noise is a strong function of focussing and aligning fields and is therefore considered to be some sort of Moiré fringe pattern off the suppressor mesh.

Equation (5) has been plotted in Figure 14 for maximum signal to noise ratio as a function of scanning resolution. The general validity of this curve has been proved to scanning densities of 80 TV lines per cm, and no reason has been found to doubt its extension to even lower densities.

The curve has been plotted based on manufacturers typical data for standard 30 frame per second analog systems. The data points listed are based on digital television systems with asynchronous scan or incremental sweep with pulse beam operation.

In summary, the SEC vidicons have been found to be superior to any other sensor type in the role of a component within a data system. They are predictable, have good statistics, can store data indefinitely which can be accessed in less than one microsecond, have good signal to noise ratios, and have a large range of unity gamma. They are somewhat fragile both from the mechanical and overload viewpoints, have generally adequate but not spectacular life. Better aperture response is a definite requirement, and greater target storage capacity would be beneficial.

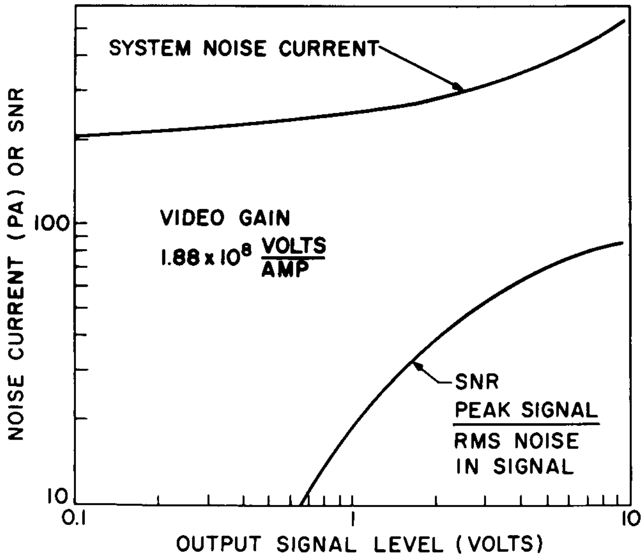

Figure 13. -Noise current and SNR as function of output signal level. NRL BB system noise performance over selected area of 10 adjacent elements. $V_t = +10$; $V_s = +10$; 256 x 256 picture elements; $I_b = 31\ \mu a$.

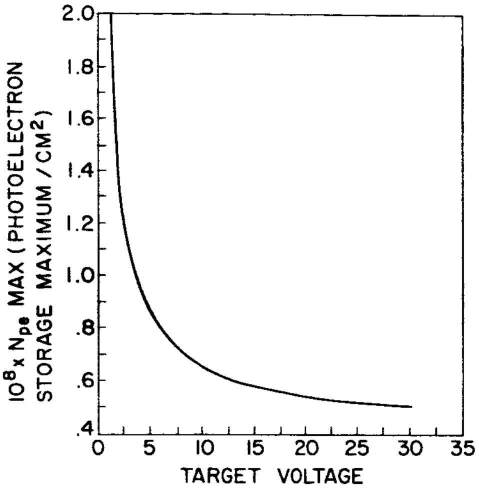

Figure 14. -SNR as function of scanning resolution.

Page intentionally left blank

AN IMAGE PHOTON COUNTING SYSTEM FOR OPTICAL ASTRONOMY

A. Boksenberg
Physics Department, University College London

The fundamental limitation in detecting radiation at very low levels is, of course, due to the quantum nature of the radiation itself. The information contained in an optical image can be expressed as the spatial and temporal variation in number of photons. The problem of detecting and recording such an image is then essentially one of counting the number of photons in each image element.

In the use of a photoelectronic image detector it is obviously desirable that the information present in the liberated photoelectrons is not degraded in the further processing that enables them to be recorded. More specifically, the properties required of an ideal astronomical detector are:

1. Every photon be recorded with equal weight and in a noise-free fashion.
2. All spatial information contained in the image be retained.
3. The information storage capacity be infinite.

No device having these properties actually exists and none probably ever will. However, currently available image intensifiers are indeed capable of registering single photoelectron events. For spectrum detection, for example, if photographic film is used as the recording medium, the overlapping of recorded scintillations can be avoided by moving the film perpendicular to the dispersion direction, so obtaining as large a storage capacity as desired. An automatic optical "spot counter" would replace the microdensitometer for readout and potentially has the advantage of discriminating against film fog and large noise scintillations.

Photon event counting by television recording rather than photography is a logical extension of the technique and, apart from ease of data handling, allows the spectrum to be continuously monitored while integrating. Thus, a system comprising an image intensifier optically coupled with a continuously scanning television camera would act as a multi-channel photon counter having comparable properties to a vast bank of photomultipliers. Image integration could be done conveniently by digital scaling in a computer.

Several advantages are to be gained from this image photon recording technique over conventional methods of recording:

1. Spatial resolution - In the conventional use of an intensifier, the image is integrated on film fundamentally as a pattern of overlapping, variously sized scintillations. Since only the presence of a scintillation is true information, resolution can be markedly improved simply by recording only the central position of each scintillation, irrespective of size.

2. Storage capacity - As a consequence of the use of a computer, storage capacity, for practical purposes, is unlimited.

3. Background noise - Bright noise scintillations, which are given a disproportionally high weight in conventional recording, can now be rejected by discriminating against scintillations occurring above a defined threshold in brightness. Amplifier noise can be similarly rejected by the use of a low threshold discriminator.

Evidently, this system promises to approach the desired ideal. Since it is essentially photon noise limited, image quality is independent of image scale. In the instance of spectrometry, this allows the use of fixed dispersion optics and the definition of spectral resolution in the computer according to signal-to-noise requirements.

The elements of such a system, currently in development at University College London in collaboration with the Rutherford High Energy Laboratory, are shown in Figure 1. The cascade intensifier is the natural choice for this application since, of the available types, it is well known to have the most favorable scintillation brightness distribution for event counting, this distribution being sharply peaked. A three-stage integral tube, developed by McGee at Imperial College, London, and now to be manufactured by E.M.I. Electronics Limited, is operated at a gain giving about 10^7 photons per photoelectron scintillation. The limiting resolution of this intensifier is typically 55 lp/mm. The Plumbicon is a suitable camera tube for registering the scintillations and is simple and compact; here it can be thought of as a buffer store acting between the intensifier and the computer. A blue sensitive Plumbicon is used to provide a match to the P11 phosphor of the intensifier. The coupling lens has been designed by Wynne at Imperial College, London, and is optimized for the P11 phosphor and the camera tube response. It will deliver about 10^5 photons from the intensifier within a 20-micron diameter spot on the camera tube. The respective fields are 35 mm and 21 mm in diameter. The bias illumination is needed to improve beam-acceptance for weak scintillations by building up the target potential to about 1 volt between readouts. The video signals are fed to a special signal processor and anticoincidence buffer store. It is proposed that this perform the following tasks:

(a) reject all scintillations having an integrated brightness (as detected in one frame) above and below certain threshold levels defined by the brightness distributions measured for signal and noise events

(b) locate the position of the apparent center of each photon scintillation

(c) correct for the effect of beam pulling

(d) encode the position of the true center of each photon scintillation

(e) store the positions of all photon events occurring in a given frame

(f) compare these positions with those recorded in the next frame and count coincidences once only

(g) pass all unique events to the computer store

The signal processor, operating in hardware terms, is needed because of the rate limitation that would be imposed if all processing were done by programming the computer (a D.E.C. PDP-8). The anticoincidence function is included to avoid counting, in a subsequent frame, scintillations which have appeared within a millisecond or so of the reading beam reaching them and are still decaying after the beam has moved on.

Figure 2 indicates the proposed scanning format and expected signals for a simple case considered initially: 1000 channels in a linear spectrum array intended for coarse spectral resolution (about 5 Å) over the optical region for the faintest sources accessible to the 150-inch Anglo-Australian Telescope. The decay time (to 10 percent) of the intensifier and camera tube combination is expected to be in the region of 5 milliseconds and the frame scan time will be typically 10 milliseconds. Special scan coils having low inductance and self-capacitance are being provided by E.M.I. Electronics Limited to allow digital scanning at the necessary rate. The maximum rate of randomly addressing and accumulating counts in the PDP-8 core memory, initially processed and labelled in the interface unit, is

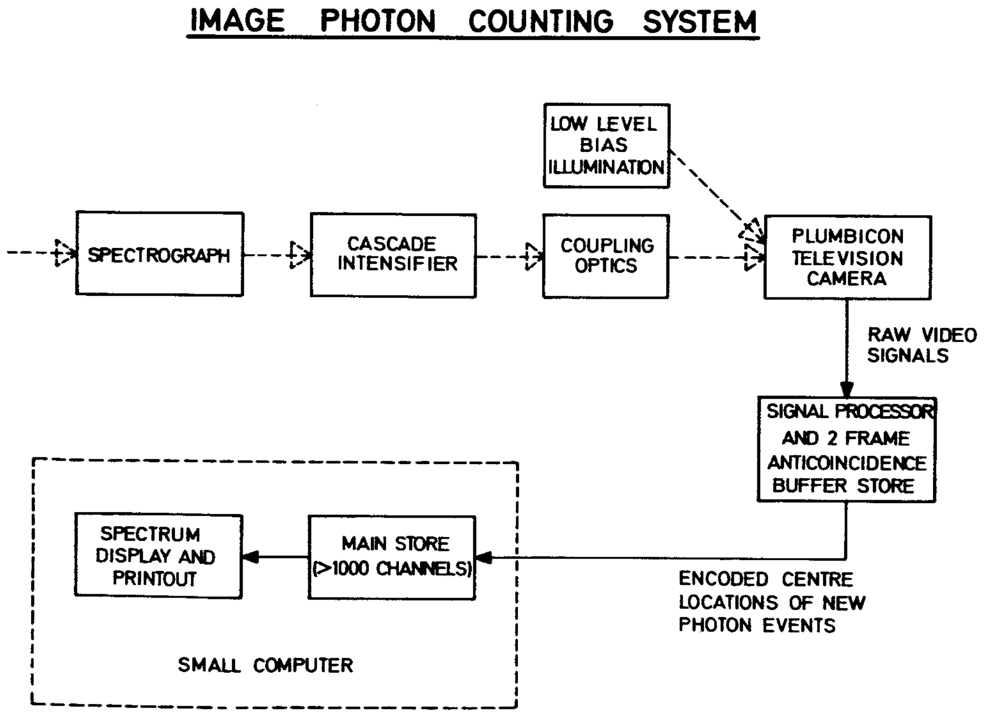

Figure 1.- Elements of an image photon counting system for optical astronomy.

6.7×10^5 sec^{-1} and does not present a limitation in the application under consideration. The core memory will be purged as necessary, through disk onto tape, to give any required storage capacity per channel. As an added facility, the available number of memory locations allows time-resolved spectra to be acquired with a resolution of 10 milliseconds or so.

Subsequent applications of the system will be:

(a) the recording of a two dimensionally arrayed echelle spectrum for high resolution studies

(b) multistar field photometry

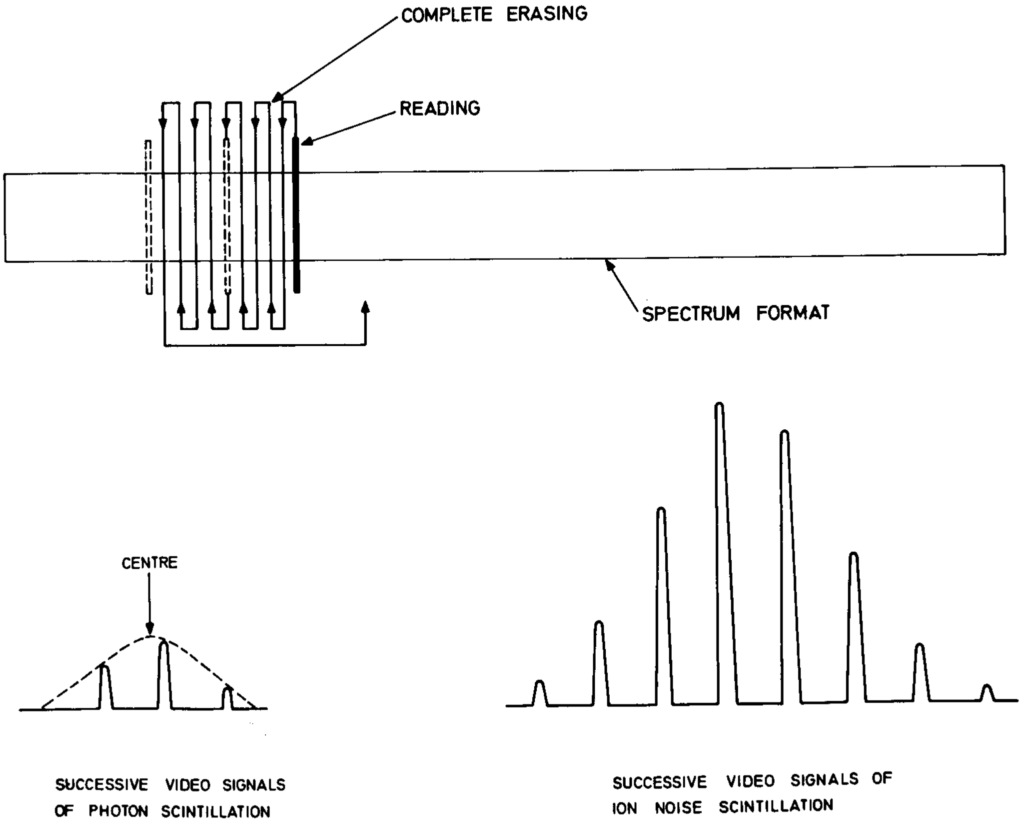

SCHEMATIC ILLUSTRATION OF CAMERA FRAMING SEQUENCE AND SIGNAL CHARACTERISTICS

SUCCESSIVE VIDEO SIGNALS OF PHOTON SCINTILLATION

SUCCESSIVE VIDEO SIGNALS OF ION NOISE SCINTILLATION

Figure 2. - Proposed scanning format and expected signals for reading a one-dimensional spectrum.

Several tests were made with various devices before beginning the present development. Figures 3(a), (b), and (c) show photographically recorded photon scintillations obtained with a four-stage cascade intensifier (courtesy of E.M.I. Electronics Limited) for increasing exposures taken to the point of film saturation. The scintillations are about 40 microns in diameter. Figure 4 shows photon and bright ion noise scintillations registered with a low gain fiber-optic coupled cascade intensifier and a standard isocon camera (courtesy of English Electric Valve Company Limited) and Figure 5 shows only photon scintillations registered with a high gain intensifier and a standard vidicon camera (courtesy of E.M.I. Electronics Limited). No processing of the type described above was carried out in these examples.

In conclusion, it should be stated that the discussion given here is not intended to imply that the image photon counting technique is critically dependent on the actual use of the main components identified for the current development. To a degree, these components were selected on the basis of availability and cost and would not be necessarily chosen if such considerations did not apply. For example, a more compact system than the one described could be assembled with a fiber optically coupled intensifier and camera tube. Rather, this paper presents an approach that shifts the emphasis from the detailed photometric performance of the photoelectronic devices themselves to the real-time data processing of the fundamental signals delivered ultimately by the primary photocathode in the system with the aim of correcting for the inherent deficiencies of the devices used.

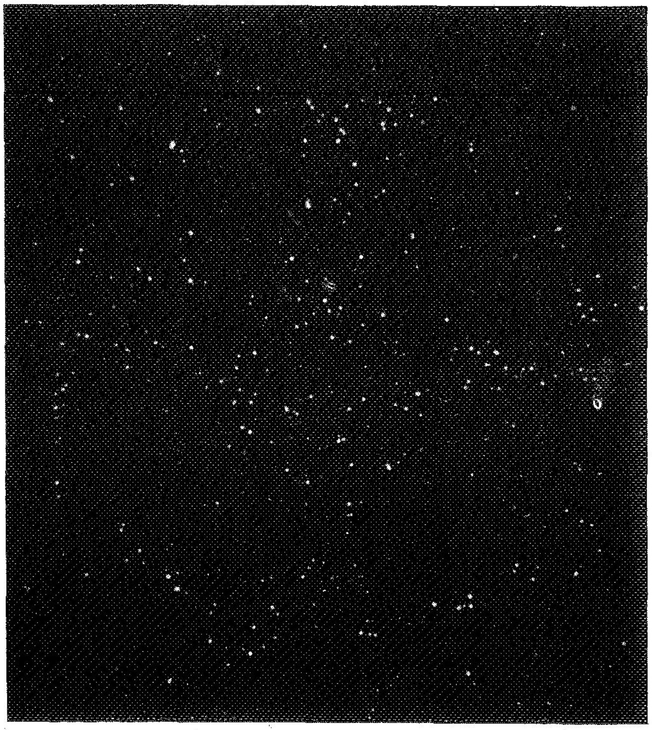

(a) Early exposure.

Figure 3.-Progressive photographic exposures of photon scintillations obtained with an E.M.I. four-stage cascade intensifier.

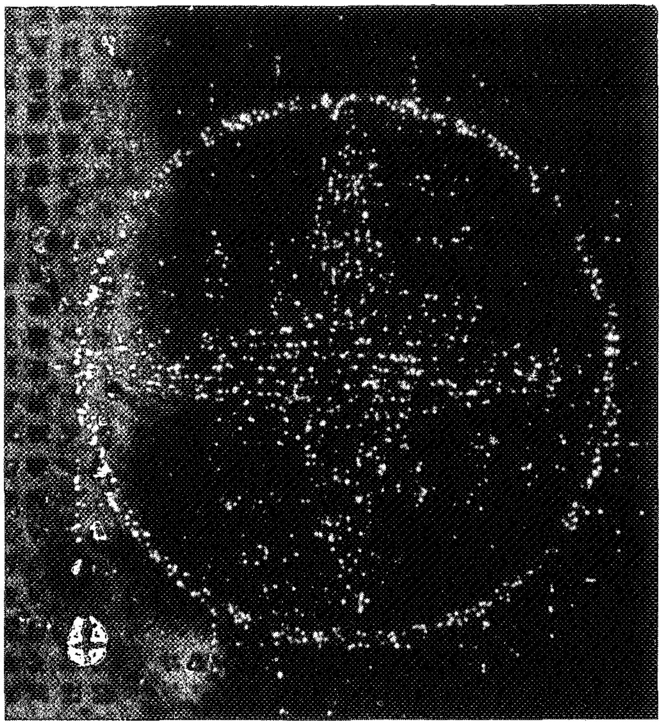

(b) Intermediate exposure.

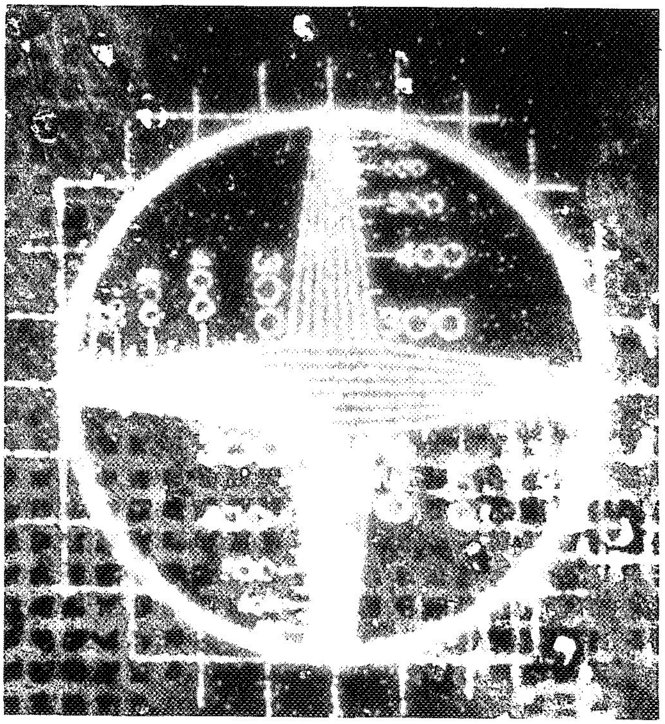

(c) Late exposure.

Figure 3. -Concluded.

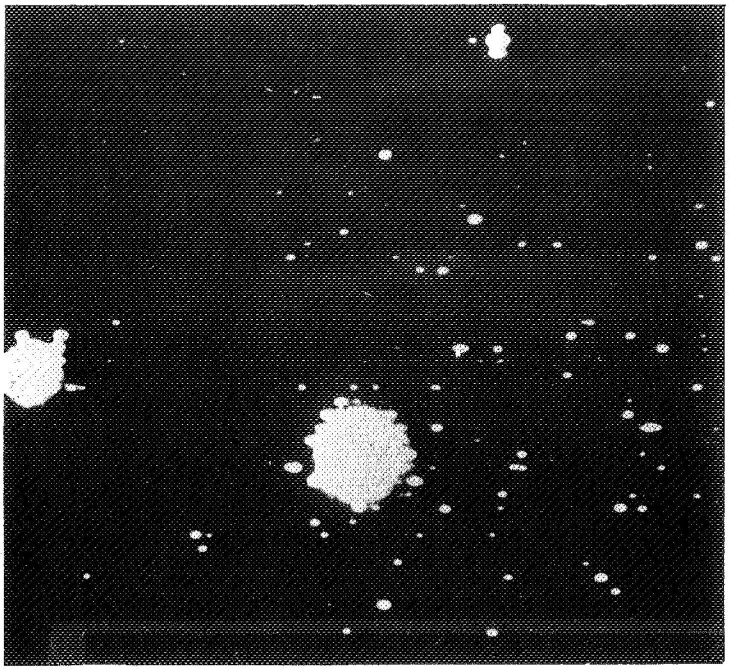

Figure 4. - Photon and ion-noise scintillations obtained with a low-gain EEV fiber-optic coupled intensifier lens coupled to an EEV isocon.

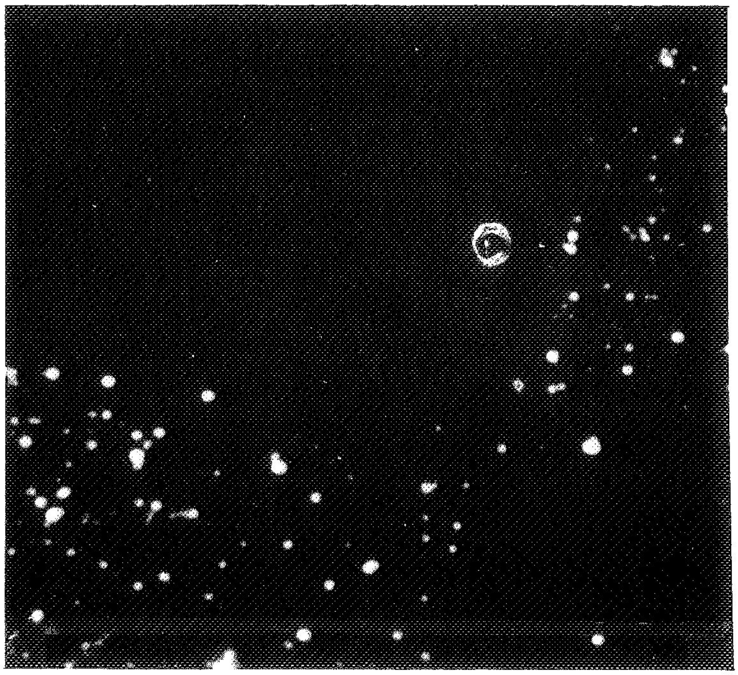

Figure 5. - Photon scintillations obtained with an E. M. I. four-stage intensifier lens coupled to an E. M. I. vidicon.

SINGLE PHOTOELECTRON RECORDING BY AN IMAGE INTENSIFIER TV CAMERA SYSTEM*

S. B. Mende

Lockheed Palo Alto Research Laboratory
Palo Alto, California

In the detection of images multichannel systems are fundamentally more efficient than are single channel systems such as photoelectric photometers. However, most multichannel systems have serious deficiencies associated with their storage component element where the information is accumulated during the exposure. For example, photographic plates, TV tube targets, have fundamental limitations as regards to dynamic range-retaining capability and linearity, whereas the electronic methods of recording signals from photomultipliers have such advantages that in many applications the use of scanning photometers is preferred to the multichannel methods.

With recent advances in image intensifiers and television cameras, it became possible to construct a multichannel system which is capable of recording the photoelectron events electronically. At the Lockheed Palo Alto Research Laboratories for the spectrophotometric investigation of atmospheric emission phenomena a very sensitive television camera was constructed by combining a plumbicon camera with a very high gain four-stage image intensifier. The image intensifier gain could be made sufficiently high that the resulting Image Intensifier Plumbicon Camera (IIPC) could be operated to record electronically the position of occurrence of individual photoelectron quanta.

---

*This paper was not presented to the Symposium because of the author's absence from the country.

If each photoelectron could be recognized from the electrical signals and recorded in a digital fashion, then we would have a very efficient image detector combined with a near perfect store with almost infinite capacity. In the simplest case, the combination of the IIPC and a magnetic video recorder provides a very large store in the form of magnetic tape storage. More sophisticated systems would eventually convert the video into digital information and use digital-computer-type storage techniques.

The fundamental restriction to this scheme of photoelectron recording is the inability to handle very large rates of photons; however, in the detection of faint images there are a number of applications where this is not an important limitation, as, for example, in high-resolution spectroscopy or in the detection of nuclear scintillation events where the counting rate is usually well within the range of the system.

The purpose of the present discussion is to give a critical review of the performance of the system in view of the photoelectron counting application.

There are a number of image intensifier TV camera combinations described in the literature, as, for example, the one by Scourfield and Parsons (ref. 1). A system using a plumbicon camera for image intensifier coupling is described by Taylor et al. (ref. 2). None of these, however, discusses the single photoelectron recording efficiency of such a system.

DESCRIPTION OF SYSTEM

The IIPC is shown schematically in Figure 1. The primary optics collects the image and focuses it on the photocathode of the four-stage EMI image intensifier (type EMI 9694) (ref. 3). The image tube is focused by a magnetic field generated by the axial solenoid. The focusing field is variable continuously from 200 to 450 g; this permits the focusing of the image intensifier at any applied electrostatic field. Mounted transverse coils are located on the outside of the focusing coil saddle (not shown in Fig. 1) which serve the purpose of centering the image in the image tube.

The television camera (Cohu Electronics 3207 series plumbicon camera) is coupled via two lenses face to face with one conjugate at infinity for each. The 85-mm Nikkor SC F/1.5 lens forms a virtual image which is then imaged on the plumbicon target by a 50-mm F/0.95 Schneider TV-Xenon. The combination, therefore, produces the required linear demagnification of 1.7 and produces a fairly high light collection efficiency at a moderate cost. This demagnification defines the useful area on the image intensifier as 27 by 20.5 mm (34-mm diagonal image).

The lens coupling permits the effective magnetic shielding of the TV camera from the image intensifier field. This is accomplished essentially by the magnetic material of the TV camera deflection yoke in combination with the field compensating coil. The magnetic material forms an open-ended cylinder around the plumbicon providing effective isolation for the entire length of the tube with the exception of the open end near to the lens. The compensating coil is merely used to null the field in the proximity of this open end. This compensating coil is connected in series with the focusing field of the intensifier magnet with a suitable adjusting shunt. The arrangement allows the exact compensation of the magnetic field for all focus currents and, therefore, the adjustment of the intensifier focusing field to any value without affecting the TV camera focus.

The TV camera is operated at the standard 525 interlaced scanning rate and the video is recorded on a helical-scan Ampex VR7500 video recorder on 1-inch-wide magnetic tape. The system was designed using the latest commercially available techniques as of 1968 and, whenever possible, with economy in mind. The inconvenience caused by

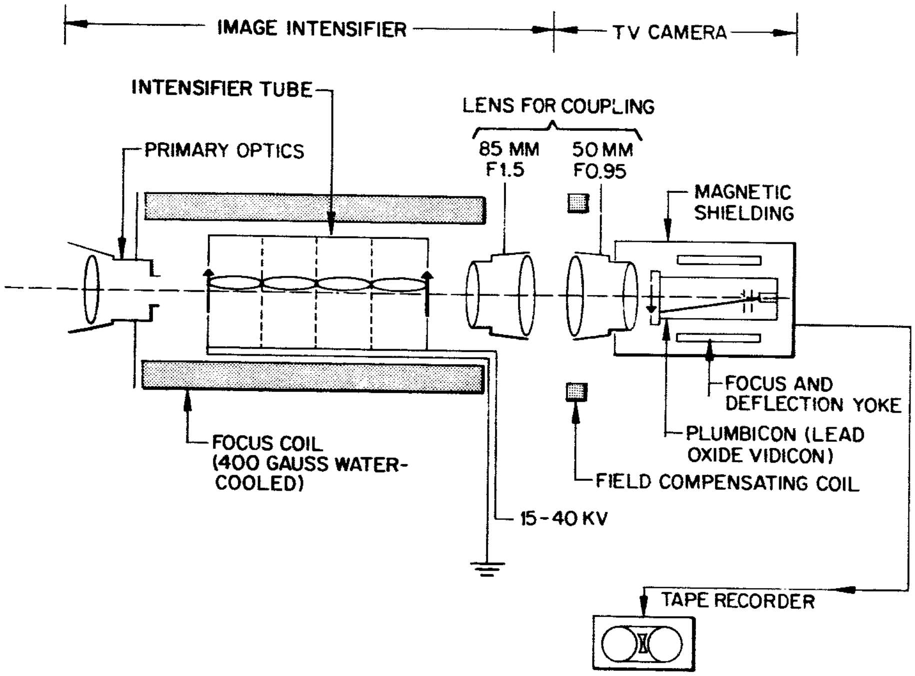

Figure 1. - The Lockheed image intensifier plumbicon camera (IIPC).

the use of the magnetically focused image tube is justified because magnetic image tubes give superior performance in regard to field uniformity, low distortion, and resolution (25 line pairs per millimeter after four stages of image amplification). The electromagnetic solenoid focusing permitted the operation of the tube at a wide range of operating voltages from 15 kV (daylight operation) to 38 kV (photoelectron counting).

The use of the plumbicon tube rather than the vidicon can be justified on a number of grounds such as superior spectral match in the blue of the P11 phosphor, negligible dark current, fast response (less than 15 percent for the third frame), larger field and, therefore, more efficient optical coupling, and a gamma close to unity (ref. 4).

GENERAL PERFORMANCE OF THE SYSTEM

A high-contrast test pattern was imaged on the photocathode and the light level was adjusted until the saturation level was reached on the tape recorder. Recordings of the image were made at various operating voltages from 20 to 38 kV at 2-kV increments. The result was replayed and a series of photographs were taken of the TV monitor (Fig. 2). A line from the top third of the picture was displayed on a line-selector oscilloscope and it is shown in Figure 3.

The series of pictures in Figure 2 shows how the image tube gain is related to the picture quality because the storage capacity of the TV tube is filled up by smaller and smaller currents of light quanta per frame. Note that the picture at the higher image tube gain was produced by a much fainter light source. Each camera exposure was 1/50 sec long. Similar photographs have been published for image intensifier film camera systems (ref. 5). The photographs in Figure 2 were taken with the aid of the TV camera, videorecorder, and TV monitor system in addition to that of the image intensifier. Although the distinction is arbitrary, it can be said that between 20 and 30 kV the IIPC system operates as a conventional television system of very high sensitivity and at 30 kV and higher the system operates in the photoelectron counting mode. We shall focus our attention chiefly on the latter method of operation.

The same conclusion can be drawn from Figure 3. At 20 kV the image is represented by a continuous video wave. It can be observed that even at these low voltages the amplifier noise (noise in the dark areas) is very much less than the quantum fluctuations in the image (noise in the white areas). As the voltage increases, the fluctuations in the white areas grow, and at about 26 kV one can distinguish peaks caused by the incidence of bright scintillations due to discrete events

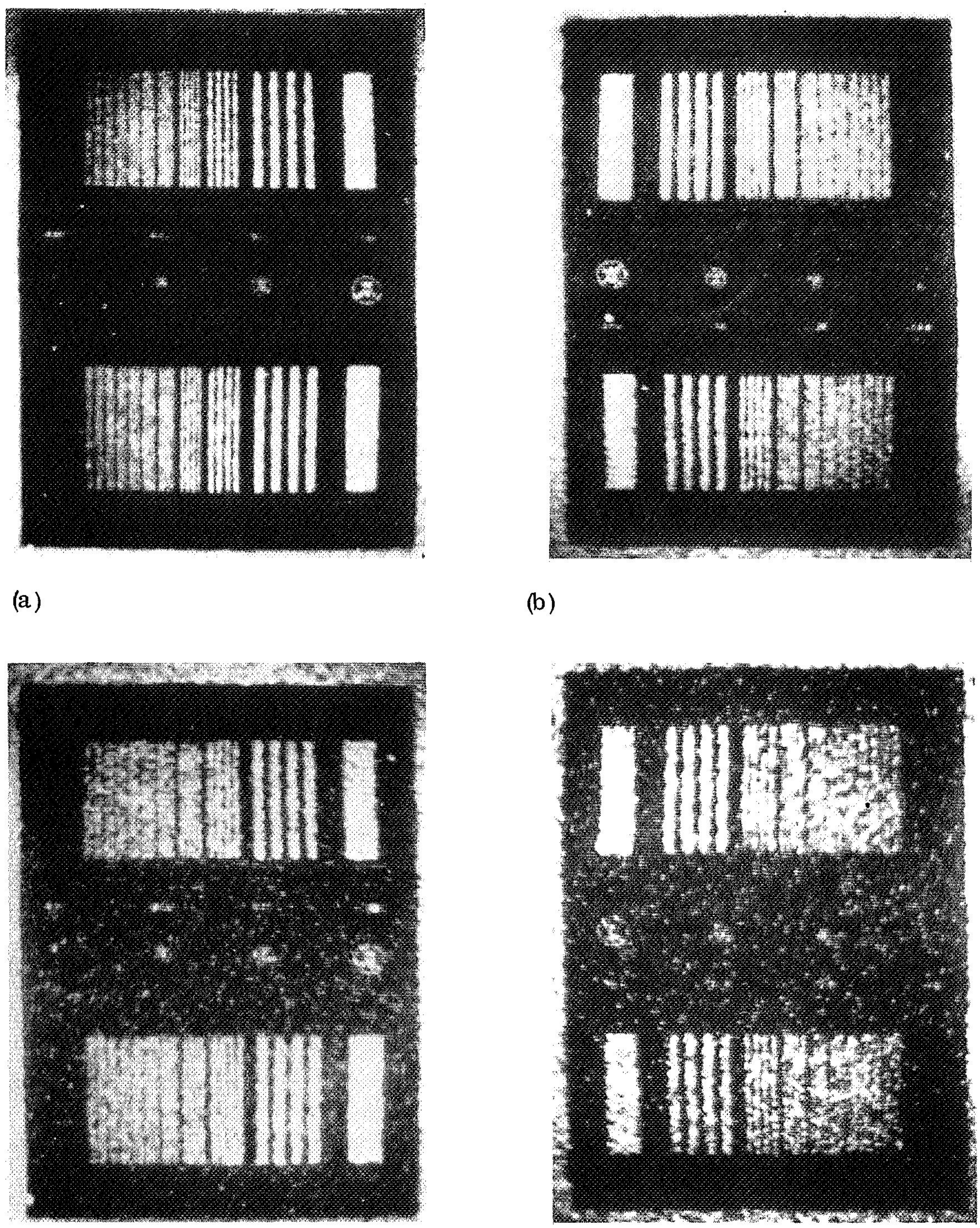

(a)

(b)

(c)

(d)

Figure 2. -Resolution test pattern viewed by the IIPC. Photographs of the TV monitor while replaying video recordings. TV camera is run at 525 lines, 2:1 interlace, and 60 fields per second. Photographic camera exposed for 1/25th second. (a) Image tube blue light photon gain of 10^4. (b) Image tube blue light photon gain of $7x10^4$. (c) Image tube blue light photon gain of $2x10^5$. (d) Image tube blue light photon gain of $7x10^5$.

(e) Image tube blue light photon gain of 1.5x10^6.

Figure 2. - Concluded.

while the continuous image decreases.

The modulation transfer function (MTF) of the system is shown in Figure 4. The limiting resolution was measured visually by independent observers and, under optimum condition, it was about 550 TV lines. Although the resolution is not outstanding, it should be noted that a 100 by 100 system is equivalent to 10^4 channels of conventional photoelectron counters.

The blue light photon gain of the image intensifier tube was 10^5 at 27 kV and 10^6 at 36 kV. The image intensifier had a very low background dark emission count of less than 200 electrons sec^{-1} cm^{-2}. The ion count was less than 3 sec^{-1} for the entire photocathode. The ions show up as very bright scintillations in Figure 2.

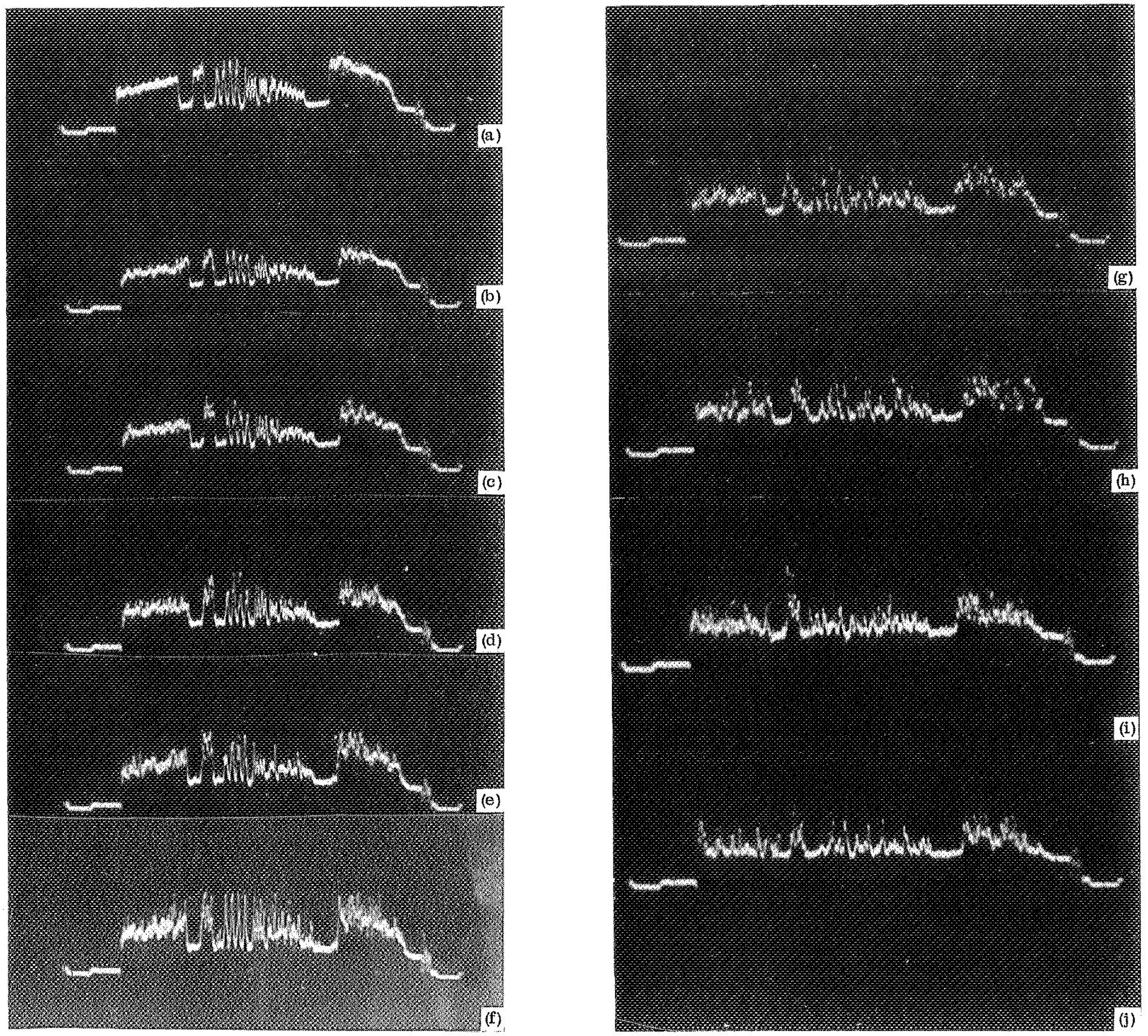

Figure 3. -Line selector oscilloscope photographs of test pattern shown in Figure 2. (a) Image tube gain of 5 x 10^3. (b) Image tube gain of 10^4. (c) Image tube gain of 3 x 10^4. (d) Image tube gain of 7 x 10^4. (e) Image tube gain of x 10^4. (f) Image tube gain of 2 x 10^5. (g) Image tube gain of 4 x 10^5. (h) Image tube gain of 7 x 10^5. (i) Image tube gain of 1.0 x 10^6. (j) Image tube gain of 1.5 x 10^6.

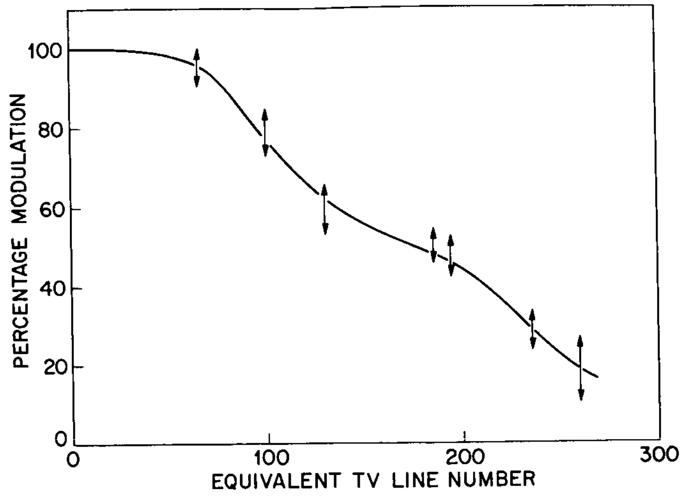

Figure 4. -Modulation transfer function of IIPC system operating image tube gain of 10^4. Visual resolution limit is in excess of 500 TV lines.

STATISTICAL PERFORMANCE

In the proposed application, the recognition of single photoelectron events is desired. The simplest way in which such a system could operate would be by use of an amplitude discriminator which rejects unwanted small noise signals and allows only the counting of the larger photoelectron signal events. It is, therefore, essential to investigate the pulse height distribution produced by the image intensifier and plumbicon camera systems.

Some previous experimental work on image intensifier pulse output distribution was done on EMI cascade image intensifiers. Reynolds (ref. 6) used a tube with P16 phosphor and obtained a fairly good pulse height distribution with distinct peak. The results of Randall (ref. 7), who used a tube with P11 phosphor, suggest that the output pulse distribution is not peaked and the most frequently occurring pulses are of the smallest amplitude. In our P11 tube, however, visual examination of the output phosphor with a microscope tended to suggest that the single electron pulses were of rather similar size and a peaked distribution was expected. The image tube pulse height analysis experiment setup is shown in Figure 5.

A calibrated (traceable to NBS standards) radioactive C14 with phospher source was used in combination with a green 5577A of 22A equivalent bandwidth. The total input was estimated as 3.5×10^5 photons cm^{-2} sec^{-1} on the photocathode. This pulse rate was several hundred times higher than tube background. The output of the image tube was focused by the relay lenses into a microscope objective. This microscope was used as a spot analyzer with an aperture and a photomultiplier in the position of the eyepiece. This aperture, combined with the magnification of the optics, defined the active area on the output phosphor. There was a beam splitter in the microscope and an auxiliary eyepiece permitting visual control of the focusing of the aperture on the output phosphor of the tube.

In order to explain the electronics setup, one has to consider the fact that the pulses from scintillation of the P11 output phosphors are relatively slow since they are in the millisecond range and, therefore, are too slow to be analyzed with conventional pulse height analyzers. During a scintillation event, the count rate in the photomultiplier rises to a peak and then returns slowly to background level. It is the "pulse height distribution" of this maximum counting rate which represents the image tube distribution.

To simplify the situation and to permit the use of automatic electronic pulse height analyzers, the following system (Fig. 5) was adopted. The photomultiplier current was amplified by an amplifier whose RC time constant limited the higher frequencies and thereby smoothed out the photomultiplier current acting as a ratemeter. Whenever a scintillation fell on the active area, a slow pulse was produced whose rise time was also limited by the same RC time constant.

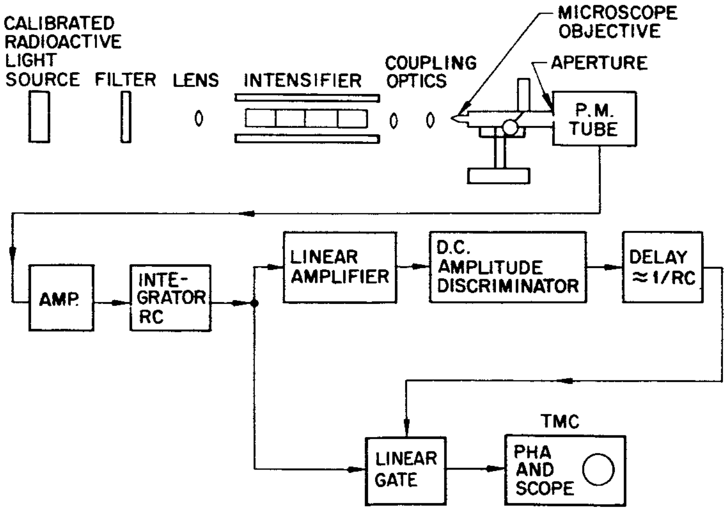

Figure 5.-Emperimental setup for image tube pulse height distribution measuring.

An amplitude discriminator was used to facilitate the recognition of the start of a scintillation and an adjustable delay timer was used to select the time of occurrence of the peak of the phosphor scintillation. This had to be set up for the peak and the setting depended on the previously mentioned RC time constant. A linear gate was used to gate out the peak portion of the scintillation pulse. The gate pulse duration was less than 1 u sec.

The setting up was quite critical and the RC time constant had to be selected for optimum performance. High time constant gave scintillation pulse pileup whereas low time constant did not give sufficient discrimination against background noise which was partly by dynode pulses and partly by the low-level uniform time-independent glow of the output phosphor. This latter contribution was also quantized by the photomultiplier and it could also show up as noise fluctuations. To confirm that only real scintillations were counted, each setting up was checked by defocusing the microscope, and it was observed that the counting stopped, showing that only well focused events which fell on the aperture gave rise to counts. The counting was repeated several times with the light source covered and uncovered at various intensifier voltages. Typical pulse height spectra are presented in Figure 6.

It can be seen from Figure 6 that the peak of the pulse spectrum is well resolved at higher voltages. The second smaller peak in the pulse spectrum was caused by dynode pulses and fluctuations and noise in the photomultiplier electronics. The output of the pulse height analyzer was read out numerically each time, and the total number of pulses was computed.

By taking a reasonable lower limit for the real phosphor scintillations as the minimum between the two peaks, one can arrive at a counting rate. This was 50 pulses $\sec^{-1}$ for the area of the aperture. After conversion for the magnifications, etc., the output pulse rate was $2.2 \times 10^4 \pm 0.4$ pulses $\mathrm{cm}^{-2}\ \sec^{-1}$. Hence, the overall image tube efficiency at 5577A is

$$\frac{2.2 \times 10^4}{3.5 \times 10^5} = 6.2 \pm 1.5 \text{ percent}$$

The photocathode efficiency at green 5577A was measured independently and it was found to be 9 ± 1 percent. This was an EMI low dark current type S-20 cathode (ref. 3). The measurement shows that the image-tube part of the system is about 70% efficient.

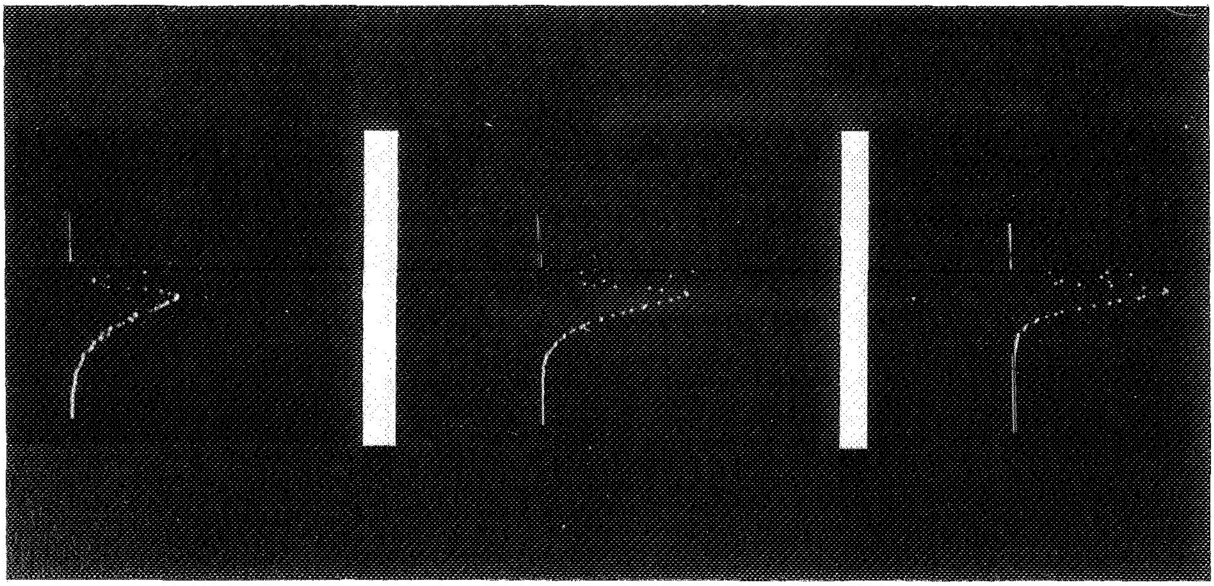

Figure 6. -Pulse height distribution from four-stage image intensifier with P11 phosphors. From left to right, image intensifier voltage is 32 kV, 35 kV, and 37 kV. Gain is approximately 10^6 at 37 kV.

ATTEMPT TO DETERMINE THE STATISTICAL PERFORMANCE OF THE COMPLETE SYSTEM

After it was established that the image intensifier produces a reasonable pulse height distribution, the pulse height distribution of the complete intensifier plumbicon system was examined. The setup is shown in Figure 7. A short 5-usec-duration interval was selected from a scan line and the video signal during this interval was pulse-height analyzed. This interval was selected in every third frame to avoid counting the same pulse twice.

The result of the experiment was rather discouraging (Fig. 8). Even at 38 kV there was no distinct peak of the pulse distribution. In the following discussions several possible reasons will be given why the inclusion of the plumbicon TV camera produces this apparent inefficiency.

In order to check the absolute pulse height recording efficiency, a photographic test was carried out. A known amount of illumination was allowed to fall on the IIPC first photocathode from the calibrated radioactive source through a known transmission. The illumination was calculated to be 4.8×10^3 photons of blue (4278A) light within the area of the illuminated spot.

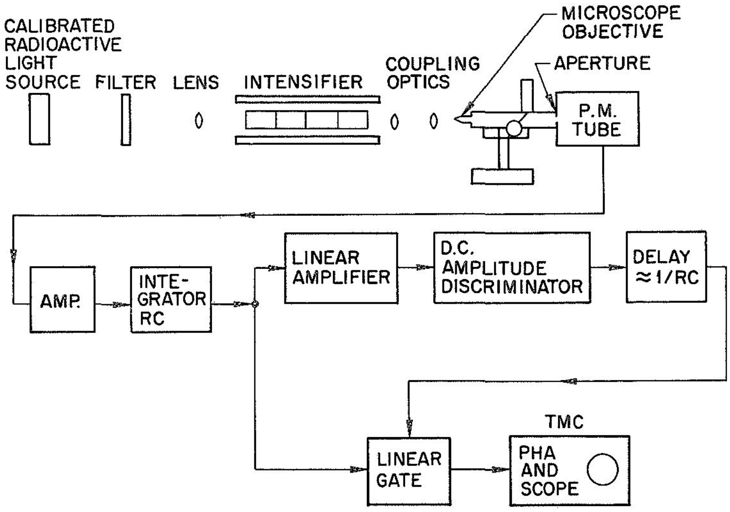

Figure 7.-Experimental setup to attempt determination of statistical performance of complete system.

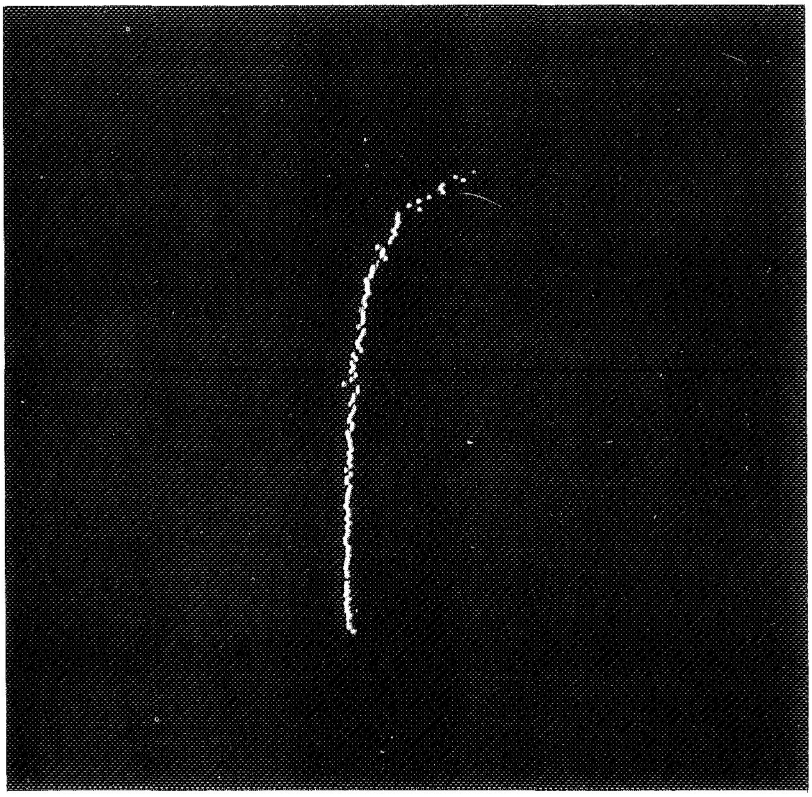

Figure 8.-Apparent pulse height distribution from single electron pulses with IIPC system as set up in Figure 7. Image tube run at maximum gain.

Photographs were taken of the TV monitor for 1/4-sec duration and the pulses were counted within the illuminated area. After the background was subtracted, the pulse rate was found to be 640 pulses sec^{-1}. As measured independently the photocathode efficiency was 22% in the blue. Hence, the efficiency of the image intensifier TV camera recording system, exclusive of the photocathode, was found to be 60%. This was regarded as being in fairly satisfactory agreement with the image tube efficiency and, therefore, it contradicted the pulse height distribution as measured in the previous test.

EFFECT OF SCINTILLATION SPOT SIZE ON PULSE HEIGHT DISTRIBUTION

Because of the resolution limitations in the image tube, coupling optics, and plumbicon target layer, the scanning beam in the plumbicon tube sees a fairly broad diffuse spot representing a scintillation. Such an intensity profile is shown in Figure 9(a). The scanning line is represented by width w. The scintillation, with center x_o distance away from the center of the scan line, is represented by the spread function $T(x_1)$. The signal generated at the instance of scanning $S(x_o)$ is represented by the shaded overlapping area. The magnitude of the signal $S(x_o)$ is dependent on the position x_o of the center of the scintillation as

$$S(x_o) = \int_{-w/2}^{w/2} (x_1 - x_o)\ dx_1$$

or

$$S(x_o) = \int_{-\infty}^{\infty} T(x_o - x)\ A(x)\ dx$$

where $$A(x) = 1 \quad \text{if } -\frac{W}{2}\ x\ \frac{W}{2}$$

and elsewhere

$$A(x) = 0$$

The function $S(x_0)$ is represented in Figure 9(b). If all the input pulses were the same in magnitude and the output pulses were pulse-height analyzed, the channel denoted by ds would be activated only if the center of the scintillation falls in the distance domain denoted by (x_0). Since the location of the scintillations is random, all values of x_0 are equally probable. The frequency of pulses occurring in channel s is proportional to x_0. Figure 9(c) shows x_0 plotted as a histogram. This is the pulse height distribution caused by such a system for input scintillations of equal brightness.

In order to obtain the pulse height distribution of our system, the function T(x) has to be found from the modulation transfer function of the system by Fourier transformation, In our case the modulation transfer was approximated by an analytical function of the form

$$e^{-x^2/z^2}$$

because it gives a simple Fourier transform of the form

$$e^{-\pi^2 a^2 x^2}$$

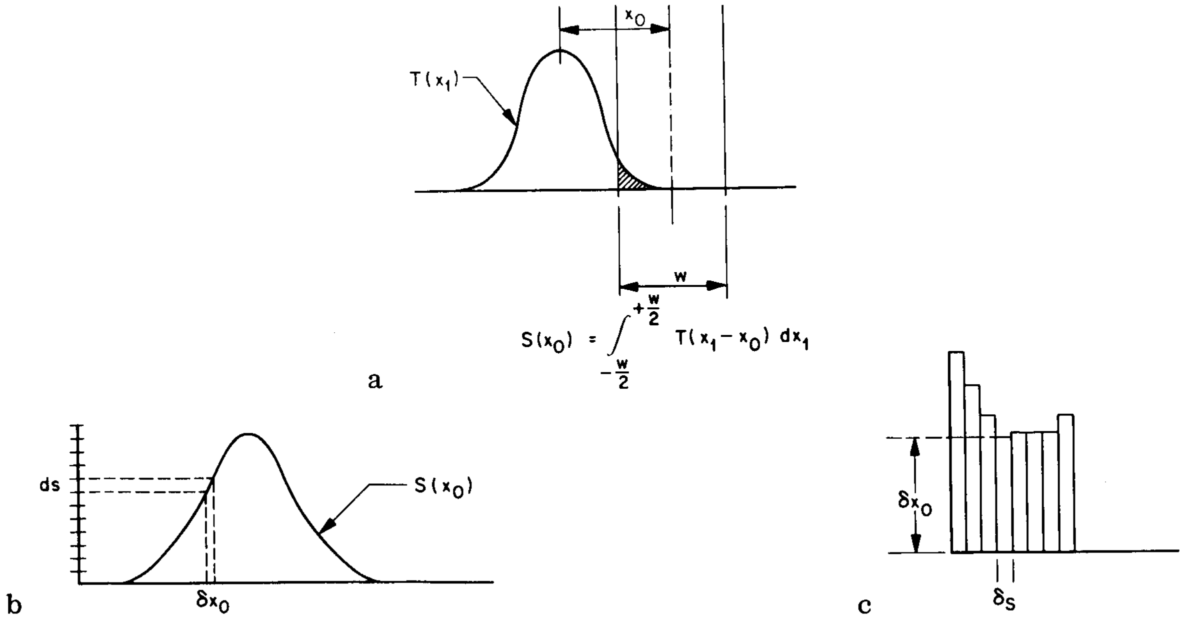

Figure 9.-Effect of scintillation spot size, spatial extent on the pulse height distribution. (a) Light distribution $T(x_1)$ and the width of the television line. (b) Signal produced from equal-magnitude scintillations as a function of distance X_0 of their centers from the TV line. (c) Resulting pulse height distribution for equal-brightness pulses occurring at random locations.

The function

$$\int_{-\infty}^{+\infty} T(x')\ A(x - x')\ dx'$$

was computed from numerical tables, and the resultant histogram is shown in Figure 10(a) as $p_2(n)$.

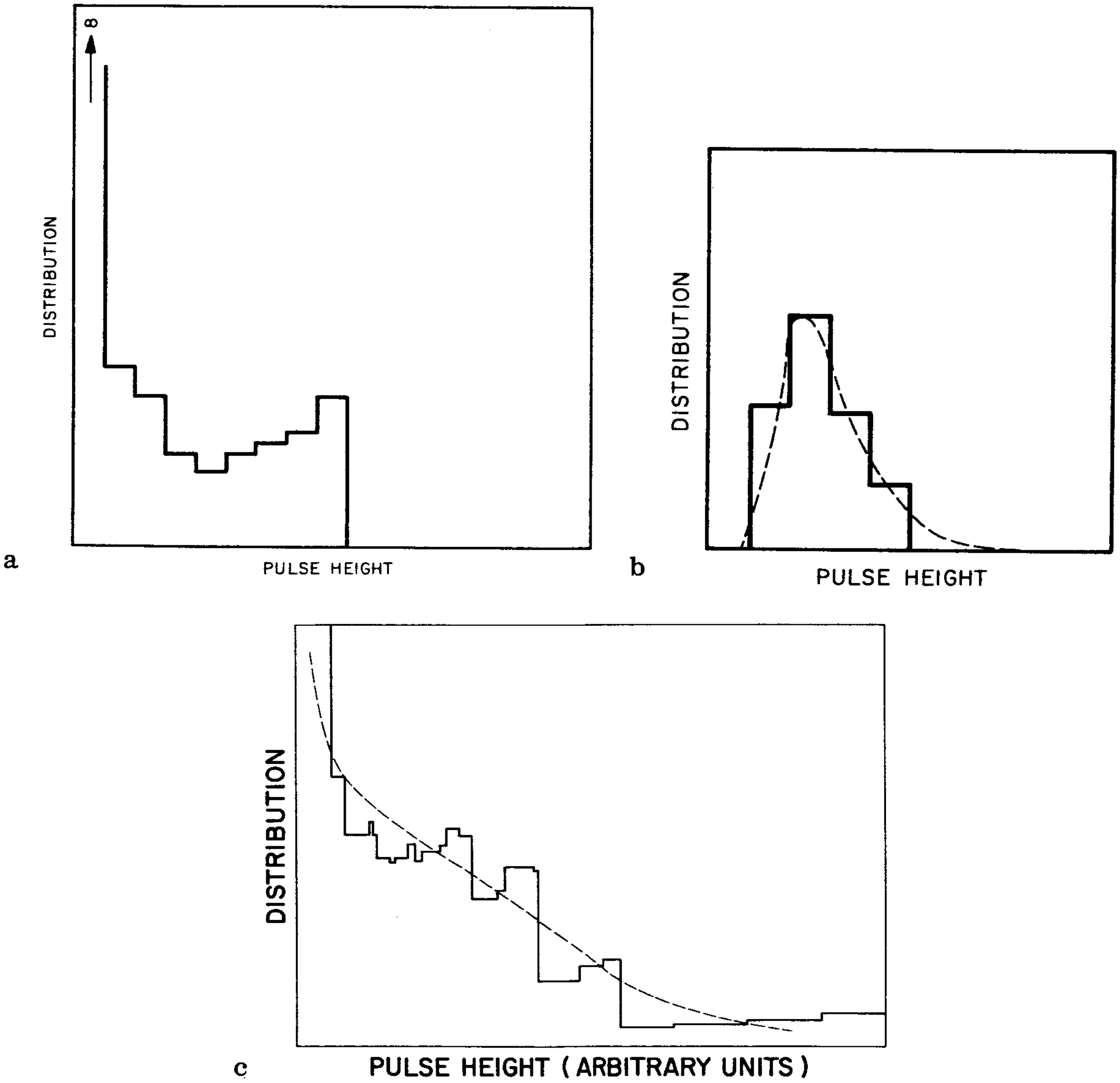

Figure 10.-Pulse height distributions. (a) Distribution derived from modulation transfer of e^{-x^2/a^2} type. (b) Simplified image tube pulse height distribution. (c) Combined resultant pulse height distribution from (a) and (b).

In order to simplify the calculations, the image tube pulse height distribution is represented by a simple histogram $p_1(n)$ (Fig. 10(b)). The convolution of the two histograms was computed by using the formula

$$p_3(n) = \sum_{n_1=0}^{\infty} p_1(n_1)\, p_2 \frac{n}{n_1}$$

The resultant histogram is shown in Figure 10(c). If the two distributions used had more resolution, a smoother resultant distribution would have been expected. As an illustration, a broken curve is drawn in Figure 10 to show that the resultant distribution for large pulse height resolution is expected to be a monotonously decreasing distribution with no distinct peak at any point. This agrees fairly well with the observed distribution of Figure 8.

The above description was given to show the importance of modulation transfer of the system and its effect on the pulse height distribution. In a pulse counting system it would be necessary to minimize this difficulty and two methods are suggested. The first one is simply the improvement of the system modulation transfer characteristics which can be accomplished by mismatching the resolution characteristics of the system with the number of scan lines; i.e., each scan line has to be much wider than the system aperture spread function $T(x_1)$. Since this is obtained by the Fourier transformation of the modulation transfer, one can express this same condition in terms of the modulation transfer function itself. The MTF, therefore, has to be close to unity everywhere within the equivalent bandwidths as expressed in scan lines per picture height. This can be achieved in the present system by using a different scanning format in which the line number is reduced from the present standard 525 to a lower value.

Since the modulation transfer is limited mainly by the coupling optics and image tube combination, the proposed modification would improve the situation. Naturally, the improvement would be achieved at the expense of resolution. In systems where the resolution is limited by the scanning tube because of the finite width of the scanning beam, it is necessary to supplement the reduction of lines by changing the profile of the scanning beam itself. This can be done by adding a very fast a.c. waveform to the vertical scan, thereby stretching the beam profile out in the vertical direction perpendicular to the scan lines. In this way, the area which is covered by the scanning beam is widened to the desired line width without changing the beam focus. For rather different purposes, this type of scanning method was discussed previously by Nozawa (ref. 8) and Mende (ref. 9).

The second possibility involves digital techniques and calls for the recognition of the two pulses in adjacent lines due to one photoelectron. By use of digital computers which can handle a whole frame, corrections could be made for spillover from one adjacent TV line into the other.

LIMITATIONS DUE TO HIGH VELOCITY BEAM ELECTRONS IN THE PLUMBICON

It was noticed in connection with other low-velocity scanned TV tubes when they were operated in a single frame mode that,if a single exposure was taken in the first frame, only the brightest portions were scanned by the scanning electron beam (refs. 9 to 11). This phenomenon was explained (ref. 10) to be due to the high-velocity electrons in the beam which charge the target negative in the quiescent state during the absence of any light image. Hence, the image in the first frame has to overcome this negative potential and charge the target positive by a substantial amount before any signal generation takes place. Vidicons with their strong dark current should not exhibit this property; however, other tubes, including image orthicon, SEC vidicon, and the plumbicon with their lower dark current, show the same phenomenon quite strongly. It does not affect the operation of these tubes when dealing with time stationary images, and the tubes are scanned repeatedly.

In our applications the photoelectron scintillations are all transient images lasting for a single frame only and, therefore, show the above effect. There is a very adverse effect on the system because the magnitude of the pulses in the video depends on the period while the spot was in complete darkness prior to the arrival of the scintillation. It also means that at a higher image brightness when there are a larger n umber of scintillations the scintillations are also larger because of the charge built up by the general stray light, phosphor persistence, etc. on the tube target prior to the arrival of the scintillation. This effect is fairly evident in Figure 3.

A method to minimize this adverse effect was outlined by Mende (ref. 9) and termed "bias illumination." We followed this technique and placed a faint small light bulb between the two coupling lenses. This flooded the plumbicon target with a uniform faint glow. The brightness was adjusted so that it was insufficient to cause a detectable signal current by itself. The scintillations which were now superimposed on this faint glow appeared much brighter and more uniform and independent of their frequency of occurrence. For satisfactory operation of the system, the bias illumination technique is essential and most tests concerning pulse counting were conducted using this technique.

THE LAG OR DECAY CHARACTERISTICS OF THE IMAGE INTENSIFIER PLUMBICON CAMERA SYSTEM

Since the various decay characteristics have a very important effect on the apparent pulse resolution of the system, a brief discussion is given of those characteristics.

The phosphors of the image tube are all of the P11 type. The decay time of an image tube scintillation is, therefore, the combination of the phosphors in the four stages of the image tube, and it is of the order of several milliseconds. The TV system has a scan rate which is equivalent to 60 fields per second; i.e., the duration of a field is 16 msec. The plumbicon camera's photoconductive and capacitive lags are exceptionally good, and less than 10% signal was measured for the third field (second frame). Hence, the plumbicon and the P11 phosphor tube are good matches in regard to signal decay properties.

At low voltages where the statistical noise of the signal is relatively small, the lag characteristics of the complete IIPC were measured. It was found that the whole system had a residual signal of less than 20% for the third field. Therefore, as defined for a conventional TV camera, the IIPC has very good time resolving capabilities.

Unfortunately, the decay from the last few percent (5%) level to zero is considerably slower. If a steady bright image is allowed to remain on the tube for some time and then is quickly removed, the decay for the last few percent takes several seconds, and even then a very faint image (too faint to measure its amplitude) will persist on the monitor for minutes. This very persistent temporary "burn in" is a property of the image tube phosphors and so far no remedy has been found. Fortunately, the burnt in image produces very little video signal and one may be able to discriminate against it electronically. From a reexamination of Figure 2 it can be seen that the scintillations in the white areas occur on a continuous pedestal whereas in the black area the signal returns to the true zero line.

Because of this effect when viewing a stationary object, the apparent picture often contains more information than is contained by the statistics of the discrete events within the observation time. This long persistence can integrate the signal for many frames, thereby superimposing the discrete scintillations on a faint image instead of a dark background. This can create a hazard in interpreting the detection efficiency of TV systems by giving the appearance of high system efficiency.

Figure 11 is presented to show the decay properties of individual scintillations. The video lines shown in the figure are the same lines taken from subsequent fields. One can see that the pulses at times take three frames to decay completely, and at other times one frame is sufficient. This is fairly well understood and this is caused to a lesser extent by the variation of position of the pulse with respect to the TV lines, and to a larger extent by the timing at which the scintillation is initiated with respect to the time when the point is rescanned. The phosphor has a persistence of a few milliseconds and a scintillation may persist into the next TV frame if the scintillation is initiated just before the scanning beam touches the point. In this case the pulse will produce response in the third field. This effect also presents another difficulty in obtaining good pulse height resolution.

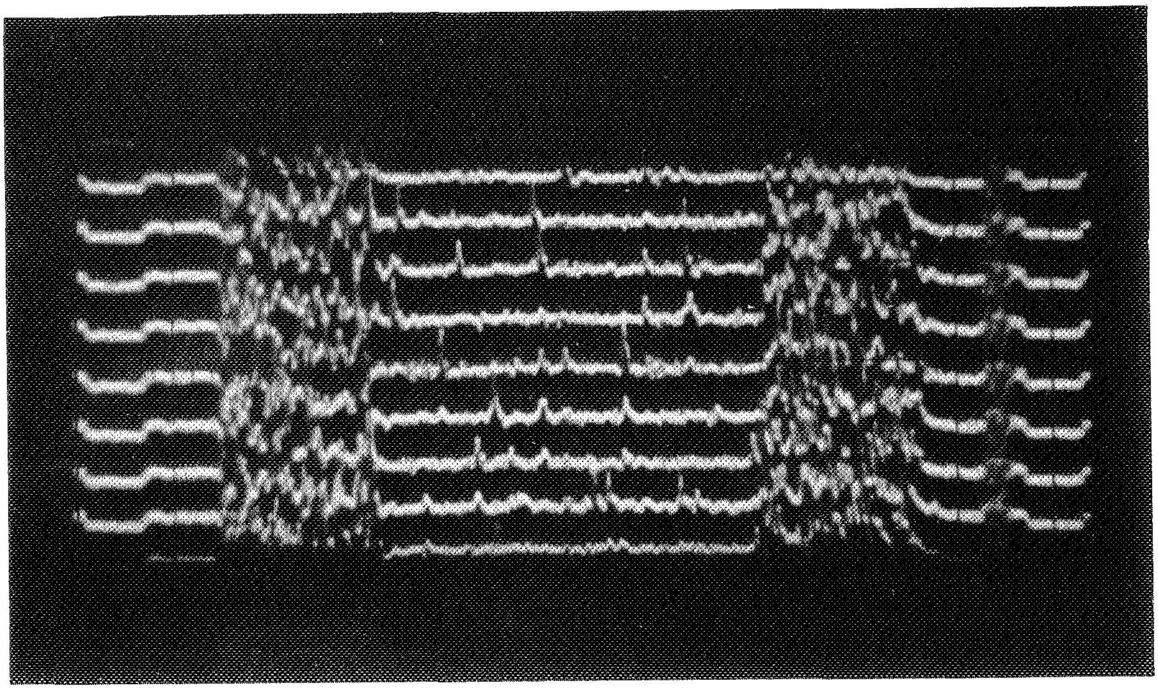

Figure 11.-A TV line from consecutive TV frames is displayed showing decay properties of individual scintillations.

DISCUSSION

The properties of the image intensifier TV camera system were discussed in some detail. The main conclusions are that this camera system concept works fairly well as a detector of single photoelectrons. There are, however, major obstacles in using it as a quantitative photoelectron counting device. These problems come from the fact that TV systems work by generating equal samples (lines and frames) both spatially and temporally, whereas photoelectrons occur as random events. Because of the practical deficiencies of the system, the photoelectron events are not infinitely small in extent either spatially or temporally (resolution and decay time, etc.) and, therefore, when the TV system generates its samples, there is a large probability that a single scintillation is divided and parts of it are picked up in adjacent samples.

To overcome this fundamental difficulty one has either to minimize the extent in space and time of the photoelectron events (improved resolution, faster response) or to increase the size of the TV samples (fewer scan lines, slower scanning). Alternatively, one can devise electronic methods for the recognition of the photoelectron event and search for spillovers into the adjacent samples. Once the signal due to one event is located in all adjacent samples (lines or frames), a summation can be carried out and the total video due to a single photoelectron can be found. The design description of such an electronic method is beyond the scope of this work, but, at the time of this writing, a design is in progress to construct a system which digitizes the video signal for computer processing and which will permit the application of all these corrections as part of the data handling program.

REFERENCES

1. Scourfield, M.W.J.; and Parsons, N.R., "An Image Intensifier-Vidicon System for Auroral Cinematography," Planet. Space Sci., Vol. 17, pp. 75-81, 1969.

2. Taylor, D.G.; Petley, C.H.; and Freeman, K.G., "Television at Low Light-Levels by Coupling an Image Intensifier to a Plumbicon," Advances in Electronics and Electron Phys., Academic Press, Vol. 28B, pp. 837-849, 1969.

3. Randall, R.P., "Dark Current Scintillations of Cascade Image Intensifiers," Advances in Electronics and Electron Phys., Academic Press, Vol. 28B, pp. 713-724, 1969.

4. deHaahn, E.F.; Van der Drift, A.; and Schampers, P.P.M., "The Plumbicon a new Television Camera Tube," Phillips Tech. Rev., Vol. 25, pp. 133-151, 1963-64.

5. Reynolds, G., "Sensitivity of an Image Intensifier Film System," Applied Optics, Vol. 5, p. 577, 1966.

6. Reynolds, G., "Secondary Electron Multiplication in Image Intensifier Dynode Structures," IEEE Transactions on Nuclear Science NS-13, pp. 81-87, 1966.

7. Randall, R.P., "Operating Characteristics of a Four Stage Cascade Image Intensifier," Advances in Electronics and Electron Physics, Academic Press, Vol. 22A, pp. 87-99, 1966.

8. Nozawa, Y., "A Digital Television System for Satellite Borne Ultraviolet Photometer", Advances in Electronics and Electron Phys., Vol. 22B, Academic Press, 1966, pp. 865-873.

9. Mende, S.B., "A Low Light Level Slow Scan TV Camera for Satellite Application," Proc. IEEE, Vol. 57, pp. 281-291, 1969.

10. Barton, G.G., Jr., "The Image Orthicon" in Proc. Image Intensifier Symp., Fort Belvoir, Va., October 1961; NASA SP-2, 1962, pp. 173-177.

11. Beyer, R.R.; Green, M.W.; and Goetze, G.W., "Point Source Imaging with the SEC Target," Advances in Electronics and Electron Physics, Vol. 22A, Academic Press, 1966, pp. 251-260.

Page intentionally left blank

AN APPLICATION OF THE SILICON VIDICON TO ASTRONOMICAL PHOTOMETRY

J. A. Westphal
Division of Geological Sciences
California Institute of Technology

and

T. B. McCord
Planetary Astronomy Laboratory
Department of Earth and Planetary Science
Massachusetts Institute of Technology

ABSTRACT

A diode matrix silicon vidicon is being adapted for astronomical photometry. Our tests have shown that, by moderate cooling, the diode dark current can be essentially eliminated. Difficulties with back lighting from the read gun filament presently limit exposure-readout times to about 10 seconds, however, mechanical modifications of the tube will remove this difficulty. The wide spectral range, combined with exact linearity, large dynamic range and high quantum efficiency will make this device extremely useful for planetary and stellar photometry.

A summary of some work which the authors have been doing with the silicon diode target vidicon will now be presented. (For a detailed description of this device see reference 1.) This device has the advantage of a wide spectral response (from 3000 A to about 12,000 A), with high quantum efficiency and wide dynamic range. It also has a linear response function, is very rugged, and has long-term photometric stability.

Since the target consists of approximately 6×10^5 individual diodes which, in principal, are independently readable, a major problem in our application is to handle this much data. To be able to utilize the potential dynamic range of more than 10^3 in these devices of necessity requires digitization and digital recording of the signals. Since, within our budget capabilities, we can handle only relatively slow data rates we have been testing these vidicons in a slow scan readout model.

Two major difficulties have been encountered in slow scan readout (≈ 100 seconds/frame). The first is the discharge of the target due to diode leakage. Fortunately, this is a strong function of temperature and by cooling the tube to < -20°C we seem to have removed this difficulty. A further difficulty is exposure of the target from the back by light from the heater of the reading gun. This is not a basic difficulty since mechanical changes in the gun structure can be made to block the light. By operating the heater at reduced power levels we have, with a cooled tube, been able to store images with no detectable degradation for more than 10 seconds. At the present time the only obvious limit to storage time is the back lighting from the heater. We hope to have tubes in the near future which are much less prone to this problem.

Our interest in these tubes is based on the following properties:

1. Sensitivity from < 3000 Å to at least 12,000 Å with quantum efficiencies greater than 50 percent over most of this range.

2. A dynamic range of greater than 10^3.

3. The output is a linear function of light flux; i.e., gamma is one.

4. The tube is mechanically stable and very rugged also because of the details of the processing; particularly with the newer tubes, the responsivity of the target is very stable in time.

5. The potential for long integration times (> 100 seconds) and sufficiently long readout times to allow use of inexpensive compact digital recording.

6. High spatial resolution on the target (≈ 15 microns) with discrete, defined sampling locations.

It is clear that a device with these properties will allow two-dimensional photometry of the moon, planets, galaxies and star fields with unprecedented accuracy and speed. Recording of one-dimensional data like spectra will also be improved, particularly if larger targets are produced. Since the system is linear, subtraction of large sky backgrounds is possible. This potentiality is very attractive for star finding purposes during daytime infrared observations with large telescopes.

REFERENCE

1. Crowell, M. H., et al., Bell System Tech. J., 48, 1969, p. 1481.

MICROCHANNEL INTENSIFIER VIDICON FOR FAR-UV IMAGING

George R. Carruthers
E. O. Hulbert Center for Space Research
Naval Research Laboratory
Washington, D.C. 20390

The vidicon camera tube and its associated camera chain electronics have an advantage, in comparison with the image orthicon and the SEC vidicon, of considerably greater simplicity. Many vidicon cameras have been used in space missions, such as Ranger, Mariner, and Surveyor. However, the vidicon is much less sensitive than other pickup tubes presently in use for low-light-level television, and in order to use the vidicon for low-light-level imaging the optical image must be intensified before input to the vidicon.

Until recently, the necessary amplification required the use of a two- or three-stage image intensifier. However, the availability of microchannel plates now makes possible equivalent gains using only a single-stage intensifier.

Presently under development at the Naval Research Laboratory are such single-stage intensifiers which use, in addition to the microchannel plate, front-surface alkali-halide photocathodes and have the collecting optics an integral part of the image tube. These latter two features have been previously used with electronographic recording for far-ultraviolet stellar spectroscopy and imaging (1-3).

Figure 1 is a diagram of the NRL microchannel intensifier-vidicon camera, components of which are discussed in more detail below. Incoming light is imaged by the Schmidt optical system onto an opaque alkali-halide photocathode, which is deposited on the focal surface. Electrons emitted by the photocathode, which is maintained at a high negative voltage, are accelerated toward the primary mirror, which is maintained at ground potential, and are simultaneously focused by an axial magnetic field produced by the surrounding magnet. The electron image is formed on the front face of the microchannel plate; this image is preserved while the incident electrons are multiplied in passing through the microchannel plate. These amplified electrons are then re-imaged onto a phosphor screen using a conventional electromagnetic imaging section. Light emitted by the phosphor is then conducted by fiber optics to the photosensitive surface of a conventional vidicon camera tube.

Schmidt Optical System

The Schmidt optical system has advantages in astronomical photography in that it provides wide field of view, with uniform illumination and image quality over the whole field. Some design parameters for Schmidt systems (4) are shown in Figure 2.

For a given corrector plate diameter and mirror diameter, the linear size of the field is independent of focal ratio. Therefore, these diameters should be selected so that the angular field of view is then determined by the focal length. It is seen that, in general, the television tube limits the field of view which can be covered. For example, a 2"-aperture Schmidt system is more than adequate to cover the input of a 1" vidicon; to obtain full use of larger Schmidt systems requires the use of larger pickup tubes. The present NRL breadboard camera system has a corrector plate clear aperture of 2.85 inches and a primary mirror diameter of 5 inches, giving a field of view with linear diameter of 1.25 inches (20° at f/1.0; 10° at f/2.0). This optical system was originally designed for electronographic recording on 35mm film. However, with a 1" vidicon having a maximum image diagonal of 0.75 inch, Figure 2 indicates that the corrector plate diameter could be increased to nearly 4 inches without introducing nonuniformities into the image illumination in the field of view accepted by the vidicon.

The Schmidt corrector plate is made of ultraviolet-transmitting material chosen according to the wavelength range to be covered. For example, a LiF corrector plate will transmit

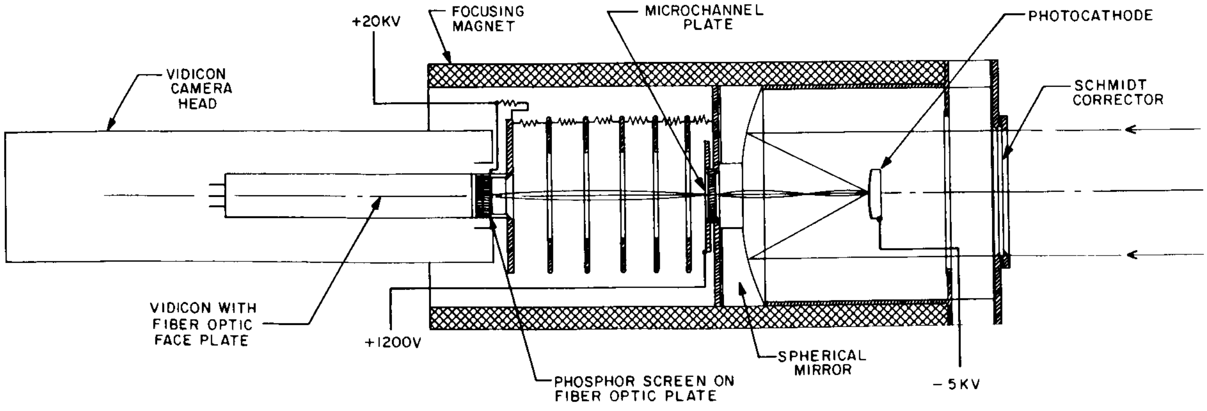

Figure 1.-Diagram of microchannel intensifier-vidicon camera.

wavelengths as short as 1050A. However, MgF_2 (short wavelength limit 1150A) may be chosen if the camera will be subject to a large cumulative dose of particle radiation (as in the Van Allen belts), since this material suffers far less transmission loss (due to color center formation) than does LiF for an equal radiation dose. CaF_2, with a short wavelength limit of 1230A, might be chosen if it is desired to exclude the Lyman-α line at 1216A, which is very strongly emitted by the geocorona.

Photocathode

At the focus of the Schmidt optical system, the image is produced on a front-surface (opaque) alkali-halide photosurface (as in Refs. 1-3). These photocathodes have very high quantum yields for photoemission in the far ultraviolet, often exceeding 50% near 1000A. In addition, they are totally insensitive to visible and near-ultraviolet radiation and can be exposed to dry air without loss in sensitivity. Figure 3 shows overall detection efficiencies (electrons per incident photon) for typical Schmidt systems using various alkali-halide photocathodes, various corrector plate materials, and with the primary mirror coated with aluminum plus an overcoat of MgF_2.

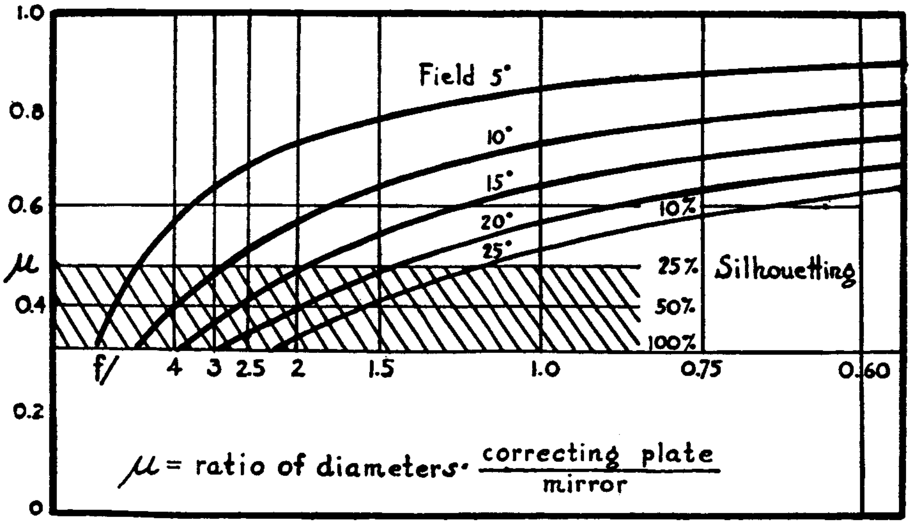

Figure 2.-Design parameters for Schmidt optical systems.

Microchannel Plates

The channel multiplier first described by Wiley and Hendee (5) is basically a tube of semiconducting glass, the inside surface of which is a good secondary emitter. When a voltage is applied along the length of the tube, an electron entering one end of the tube and colliding with the wall emits secondaries which, in turn, are multiplied in successive wall collisions as they move down the tube. Total gains of up to 10^5 are possible in such channel multipliers, and when a curved channel is used (6) to eliminate ion feed-back, gains up to 10^9 are obtainable. Microchannel plates consist of large numbers of very small straight channel multipliers, enabling image information to be preserved as well as the electron current to be amplified. The resolution in the output image is determined by the size and spacing of the channels. Microchannel plates are now available with resolution comparable to the finest available fiber optics. However, the very high-resolution microchannel plates are classified, and a "need to know" must be demonstrated in order to procure them. The image amplification can be as high as 10^5, limited by ion feedback. A typical range of operation is between 10^3 and 10^4. Figure 4 shows the gain vs. voltage for a typical microchannel plate in which the channels have length/diameter ratio of 60 (7). The curve shown is for an electron input energy of 5 KV; however, we have found very little effect of input electron energy on the amplification, even when the input electrons have less than 1 KV energy. Presumably, as long as the incident electron is energetic enough to produce secondaries, the total amplification should be essentially unaffected.

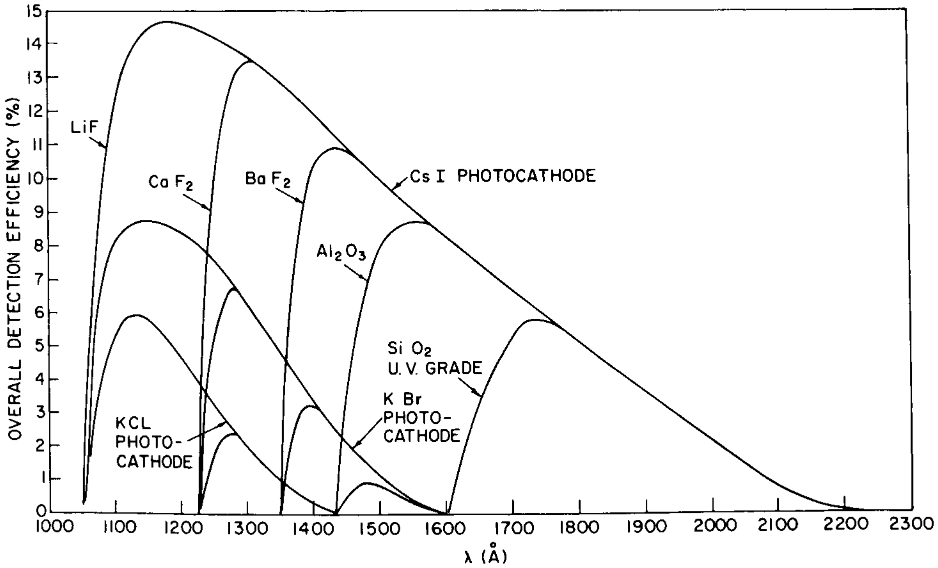

Figure 3.-Typical values of overall detection efficiency vs. wavelength for Schmidt systems using various photocathode and corrector-plate materials.

In an image intensifier consisting of a photocathode, microchannel plate, and phosphor screen (deposited on a fiber-optic output plate, for coupling to a fiber-optic input television tube) one also obtains a gain of about 50 in the phosphor screen conversion of electron energy to visible light (assuming the electrons emerging from the microchannel plate to be accelerated to 15-20 KV energy before striking the phosphor screen). Therefore, a typical overall gain of about 5 x 10^5 is obtained. As shown in Figure 5, this raises the typical limiting sensitivity of a vidicon to greater than that of an image orthicon, or of a SEC vidicon preceded by a single-stage image intensifier, and makes it nearly equivalent to an intensifer image orthicon (essentially photon-limited, i.e. capable of detecting single photoelectrons). A SEC vidicon using the microchannel intensifier would certainly be photon-limited.

Phosphor Screen and Vidicon

The amplified electrons emerging from the output face of the microchannel plate are accelerated to 20 KV energy and magnetically focused onto the phosphor screen, which is deposited on a fiber-optic plate. Magnetic rather than proximity focusing is used in order to insure that the maximum possible resolution is obtained (limited only by the system components themselves). The phosphor is type P4 or P11 settled from a slurry and is aluminized with a floated film of evaporated aluminum. The fiber optic plate consists of fibers of 6 to 8 micron diameter and is 0.25 inch thick (in order to safely withstand a potential difference of 20 KV across it). The fiber-optic vidicon, presently an RCA C23112, is placed in

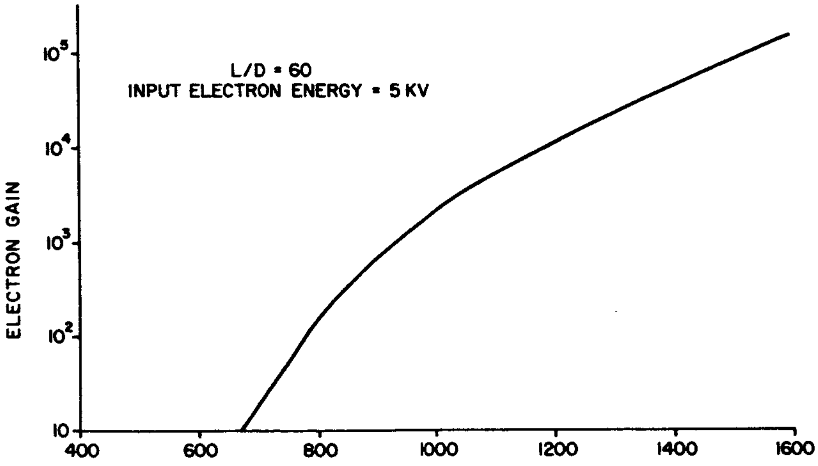

Figure 4. -Gain vs. voltage for a typical microchannel plate.

contact with the outside face of this plate. The camera head, which is part of the Fairchild TCS-950 camera system, is not modified except for the front pre-amplifier, which in this case is mounted to the side of the vidicon rather than concentrically around and in front of it, to allow the faceplate of the vidicon to be brought in contact with the fiber-optic output of the intensifier.

Applications

This system can be used for astronomical observations which otherwise would require the use of image orthicons or isocons or intensifier SEC vidicons. Other advantages are that the optical system is an integral part of the image intensifier and that the vidicon is a commercially available "off the shelf" visible-sensitive type. The ultraviolet-sensitive intensifier, on the other hand, utilizes alkali-halide photocathodes which can be prepared as required in a vacuum evaporator, and can be exposed to dry air without loss in sensitivity. The microchannel plate can also be exposed to air. Therefore, the intensifier can be of open construction and demountable, allowing photocathodes, corrector plates, etc. to be easily changed and any internal adjustments, such as focusing of the Schmidt optics, to be easily made.

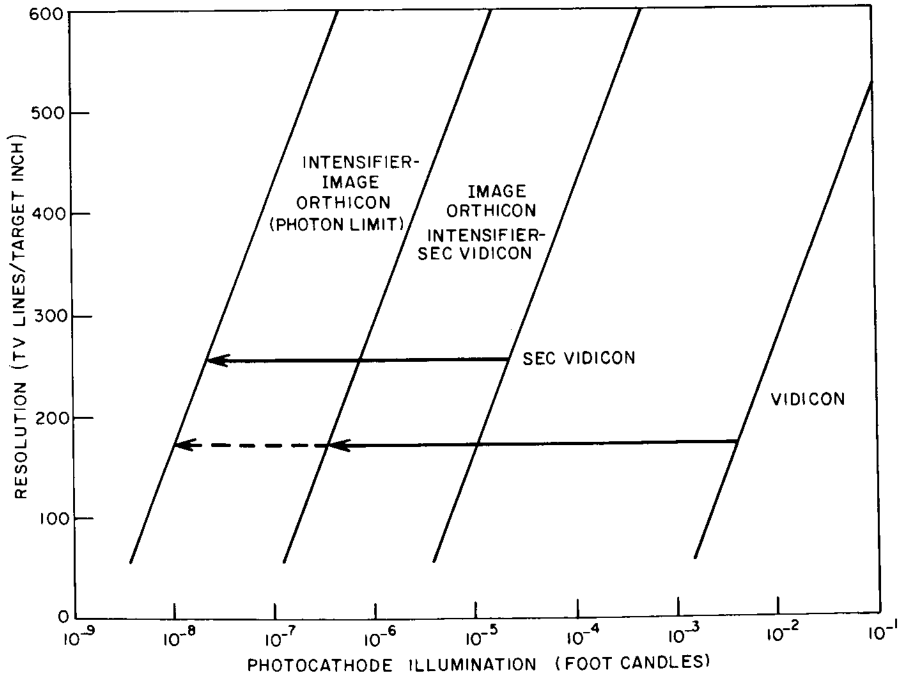

Figure 5.- Typical sensitivities for low-level television sensors; arrows illustrate the increased performance attainable with microchannel intensifier.

The astronomical applications of this instrument include, in addition to the starfield photography demonstrated by the OAO-Celescope experiment, far-ultraviolet imaging of aurorae and airglow. Here, to an even greater extent than in starfield photography, a wide field of view is of great utility. Also, a large aperture ratio (such as f/1.0) is helpful in the study of diffuse sources.

Another application in which far-ultraviolet television could be used to advantage would be to search for volcanic gas emissions from the Moon, using a camera on board a spacecraft in lunar orbit. Here, the object of the search is the far-ultraviolet absorption of the volcanic gases (H_2O, CO_2, CH_4, etc.) against the background of solar ultraviolet radiation reflected from the lunar surface. Since the majority of solar ultraviolet radiation in the ultraviolet below 1600A is in the Lyman-α line at 1216A, gases having high absorptivity at this wavelength (H_2O, CH_4) would be readily detected. Davis (8) has estimated, from OAO-Celescope observations, a lunar reflectivity of about 0.1% near Lyman-α, which would provide adequate background for use with the presently described system.

The UV-absorption technique of detection has the advantage that "point" sources of gas can be observed from great distances, whereas other detection instruments (mass spectrometers, etc.) would have to be quite close to the source. The escaping gas would probably be totally undetectable in visible light unless the mass flow rate was extremely high (such that the eruption would be revealed by suspended dust, condensation, etc.). The camera could also be used to track spacecraft, such as the Lunar Excursion Module, during the powered phase of their flight, as the exhaust plume would be observed as a dark cloud spreading out behind the spacecraft.

This work is being supported by the Naval Electronic Systems Command.

REFERENCES

1. Carruthers, G.R., in Small Rocket Instrumentation Techniques, Amsterdam: North Holland Publishing Co., 1969, pp. 168.

2. Carruthers, G.R., Applied Optics, 8, 1969, pp. 633-638.

3. Henry, R.C., and G.R. Carruthers, Bull. Am. Astron. Soc., 2, No. 2, 1970, pp. 198.

4. Paul, H.E., in Amateur Telescope Making, Bk. III, ed. A.G. Ingalls (Kingsport, Tenn.: Scientific American, Inc.), 1959, pp. 325.

5. Wiley, W.C., and C.F. Hendee, IRE Trans. Nucl. Sci. NS-9, 1962, pp. 103.

6. Evans, D.S., Rev. Sci. Inst., 36, 1965, pp. 375.

7. Adams, J., Electro-Optical Systems Design, 1, No. 3, 1969, pp. 46.

8. Davis, R.J., private communication, 1969.

THE RESPONSE OF PHOSPHOR OUTPUT IMAGE INTENSIFIERS TO SINGLE PHOTON INPUTS

JOHN McNALL

LLOYD ROBINSON

E. JOSEPH WAMPLER

Lick Observatory, Board of Studies in Astronomy and Astrophysics

University of California, Santa Cruz

ABSTRACT

The development of a multichannel spectrophotometer for faint optical sources has required an investigation of the single-photon response of image intensifiers. Tests of intensifiers with fiber optics faceplates show that it should be possible to construct a spectrophotometer that uses the storage properties of the output phosphor to provide pulse-counting operation in several hundred simultaneous channels.

I. INTRODUCTION

The recent declassification of low dark-current, moderately high-resolution image intensifiers with fiber optics faceplates will have a profound impact on astronomy. For the first time simple, rugged, and relatively inexpensive tubes are available to the general user. These tubes are rapidly finding application in spectrographs (Beardsley, DeJonge, Haring, and Hansen 1969) and in direct photography (Lynds 1970).

At Lick Observatory, in addition to the more conventional uses just described, we are attempting to construct an electronic pulse-counting spectrophotometer using the output phosphor of the last stage of a multistage intensifier as a temporary storage element in order to obtain simultaneous multichannel operation. An ideal phosphor storage element would be one that, when excited by an input photoelectron, would release photons at regularly spaced intervals, t_1, for some definite period, t_2. It is clear that under these circumstances it would not be necessary to continuously monitor the output phosphor in order to determine the flux of input photoelectrons, since it would be only necessary to detect one output photon for each input photoelectron. This means that, using an image dissector, a number of output elements could be monitored with very little loss of information. The number of such elements that could be simultaneously monitored is given by:

$$n = \mathcal{E} G \qquad (1)$$

where $\mathcal{E}$ is the efficiency for detecting output photons and G is the number of output photons per input photoelectron.

Because real tubes do not have ideal phosphors it is important to know the phosphor characteristics of actual tubes when designing a spectrometer. Studies of electron multiplication in image intensifiers have been reported by Reynolds (1966a, b) and the time response of multistage image intensifiers using P-20 phosphors was investigated by Flam (1969). The results of those experiments show that although transmission secondary emission tubes show exponential output pulse-height distributions, cascaded image intensifiers using phosphor-photocathode multiplying stages show a more nearly Poisson output distribution. Increasing the number of stages increases the observed decay time at the output phosphor.

Our measurements of the response of several 40 mm Varo[1] image intensifiers to single photoelectron inputs allow us to extend the results reported by others. Because our data have convinced us that it is possible to construct a spectrophotometer that can simultaneously count in several hundred channels, we have decided to publish the results of these tests in the hope that the data will be useful to others who are interested in multichannel devices.

II. TESTING PROCEDURE

The experimental set-up is shown schematically in Figure 1. One, two, or three 40 mm Varo image tubes were placed in an expandable oil box with a 1-inch-thick quartz entrance window. The photocathode of the first tube was operated at a high negative potential while the output phosphor was operated at ground potential. An oil box was used to eliminate corona at the voltages required (up to 40 KV for 3 tubes). A mask with a central hole 0.008-inch in diameter was placed in contact with the input fiber optics plate and a mask with 0.014-inch aperture was used at the output plate to delineate the image of the input aperture and reduce the amount of "dark" or background light that would ordinarily be detected. An ITT FW-130 photomultiplier with a 0.35-inch effective photocathode diameter was mounted behind the output aperture with a small drop of immersion oil acting as a light pipe between the image tube and the photomultiplier.

The input aperture was illuminated by pulsing a Monsanto MV 10A gallium arsenide phosphide light-emitting diode with 1 μsec, 50 mA pulses. With the tube located approximately 3 feet from the diode, only about 5% of the diode

---

[1] Varo, Inc., Garland, Texas

light flashes produced a response from the image intensifier. We assume that under these conditions most of the signals that we measured were indeed produced by single photoelectron events. The output of the FW-130 was fed to a fast amplifier/discriminator and then to a 100 MHz scaler. The gain of the FW-130 was sufficiently high that most of the single photoelectrons released from its photocathode could be detected. We estimate that roughly 5% of the photons released by the output phosphor of the image tube were detected by the photomultiplier. A small computer (PDP 8/I) was connected so that it could trigger the light emitting diode as well as start, stop, read, and reset the counter.

III. EXPERIMENTAL RESULTS

Figure 2 gives a plot of counting rate as a function of time for two- and three-stage intensifier chains. The first two tubes of the chain were operated at voltages up to 15 KV, while in the three-tube chain the last tube was operated at half this voltage. The curve was determined by using a computer program that measured the background rate, then flashed the light source and then determined the shape of the decay curve. After a delay of a few seconds the test was repeated until adequate statistics were built up. To measure the decay shape for times longer than 100 msec, the

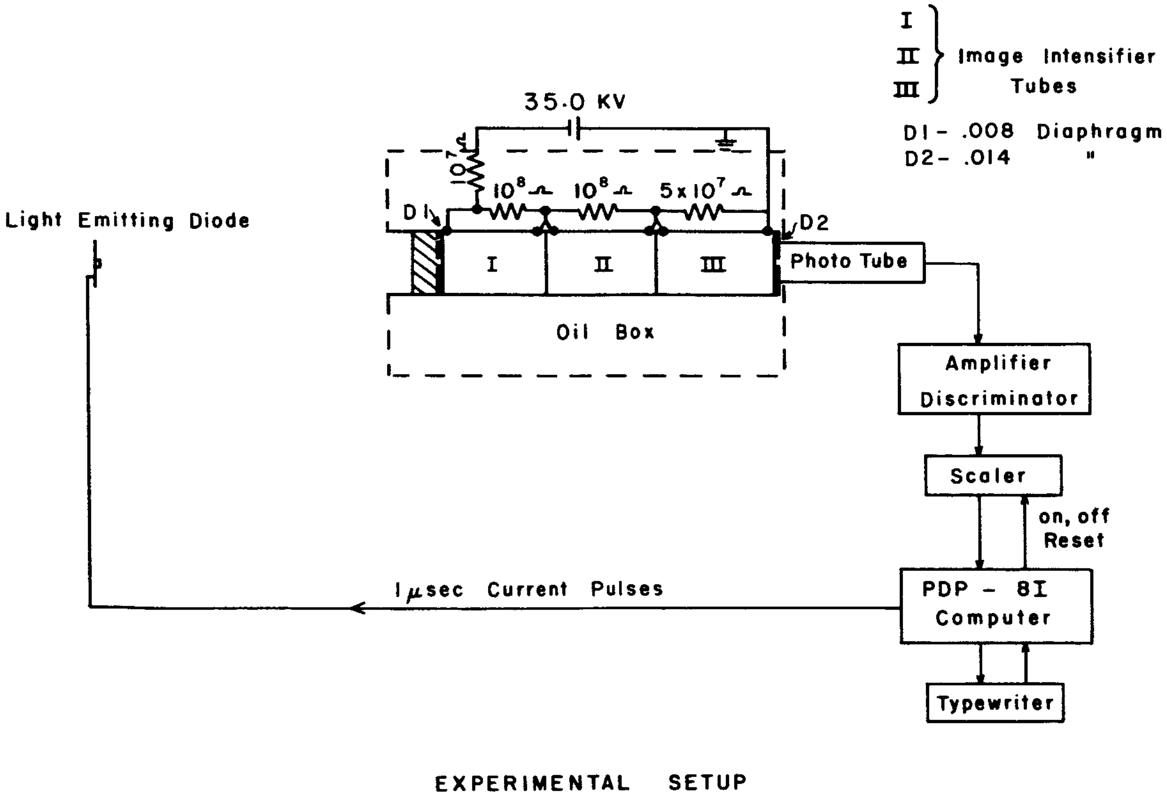

Figure 1. -Block diagram of the experimental arrangement.

light was rapidly flashed as many as 1000 times. Tests made by varying the flashing rate indicated that the decay rate did not change as the number of light flashes increased. It is clear from this plot that after about 10 msec the phosphor decay law is approximately of the form:

$$I(t) \propto t^{-\beta} \tag{2}$$

The exponent increases from approximately unity 10 msec after the light flash to approximately 2 after a delay of several minutes. It should be recognized that the impulse response function for this three-stage intensifier is the convolution of the impulse response function for the last stage with the first two stages (Flam 1969). The observed power law decay curve is not unusual, for often sums of exponentials and inverse power laws with exponents between about 0.2 and 3 are used to describe empirical phosphor decay curves (Leverenz 1950).

Our empirical power law decay curves can be used to calculate the fraction of total counts seen after any given interval of time. Figure 3 shows integral decay curves for 1-, 2-, and 3-stage image intensifiers. These curves were checked experimentally by the computer test set-up. The experimental and calculated results were found to be in good agreement. It has been our experience that the characteristics of the decay curve show little

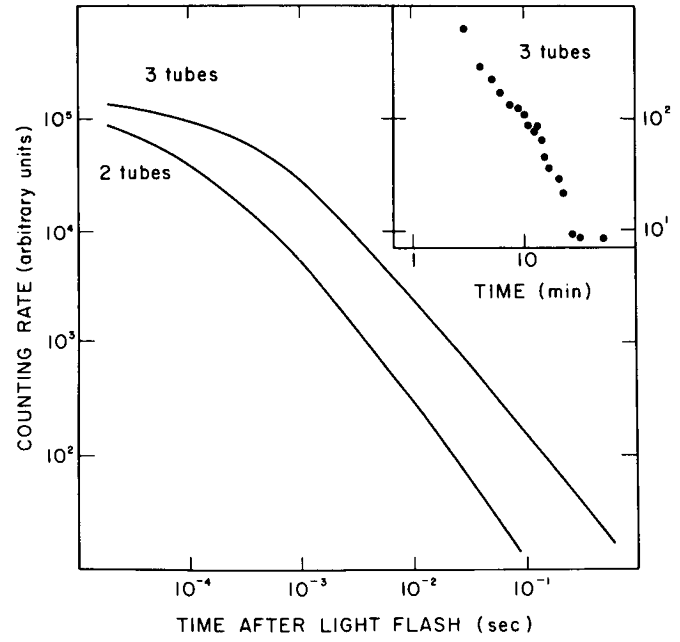

Figure 2.-Count rate vs time for 2- and 3-stage image intensifier systems with short pulses of low level illumination. The boxed curve is the delay curve for 3 tubes following a 5 minute exposure to a light source that produced about 103 primary photoelectrons per second.

variation with voltage, and we have not been able to detect any changes with temperature for temperatures between 10°C and 25°C. It should be emphasized that our observed decay curves were obtained with extremely low input illumination; in fact, we believe that they are representative of the intensifier response function for a single input photoelectron.

One of the primary goals of this experiment was to determine the "pulse-height distribution" (the distribution of the number of detected photons per primary photoelectron) at very low light levels. This was done with a computer program that measured the dark current, flashed the diode and recorded the number of counts for a specified time interval (usually 5 msec), and then waited for a time interval sufficiently long for the residual phosphor glow to be insignificant (usually 50 msec) before repeating the tests. From Figure 3 it can be seen that fully 50% of the output quanta are released within 5 msec of the light flash and the residual glow after 50 msec is quite low. Measurements made by counting for 200 msec after the light flash gave a gain distribution in good agreement with the 5 msec distribution after correcting for the lost counts.

A major source of error in these very low intensity measurements was the correction for dark current. It is easily seen that if $P_\ell(n)$ is the probability of n counts due to the light, $P_b(n)$ is the probability of obtaining n background counts, and $P_m(n)$ is the measured probability then

$$P_m(n) = \sum_{k=0}^{n} P_\ell(n-k)P_b(k). \qquad (3)$$

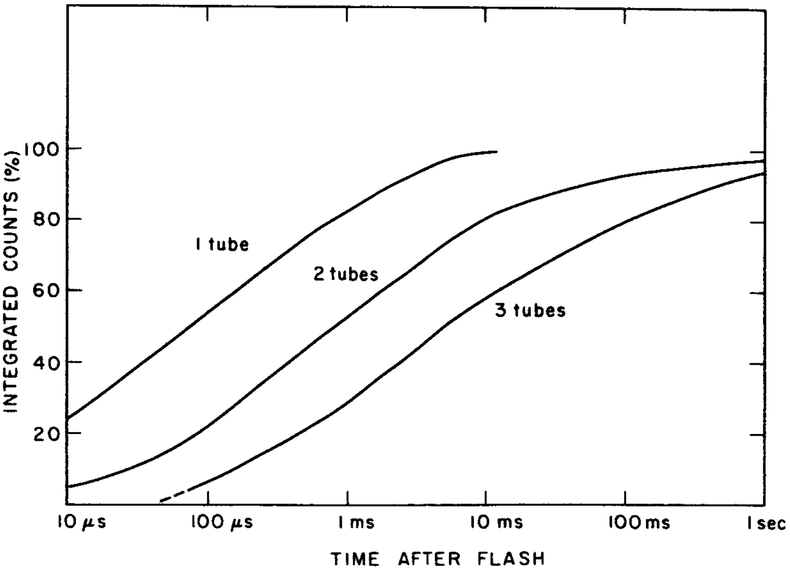

Figure 3.-Total accumulated count as a function of time after emission of a single photoelectron for 1-, 2-, and 3-stage intensifiers.

Since $P_m(n)$ and $P_b(k)$ are obtained from measurement, $P_\ell(n)$ can in principal be determined by an iterative process using equation (3). The determination of $P_\ell(0)$ is particularly simple since it is given by

$$P_\ell(0) = P_m(0)/P_b(0). \tag{4}$$

However, for the higher terms it was found that the error increased very rapidly unless $P_b(k) \ll 1$ for $k > 0$.

Although for the earlier runs the light intensity was adjusted so that $P_\ell(0)$ was greater than 95% (fewer than 5% of the diode flashes were actually detected), it was found that this restriction could be relaxed somewhat without significantly modifying the shape of the pulse-height distribution. In Figure 4 we have plotted the pulse-height distribution with the brightness of the diode adjusted so that 12% of the diode flashes produced a detected response from the image tube. Assuming

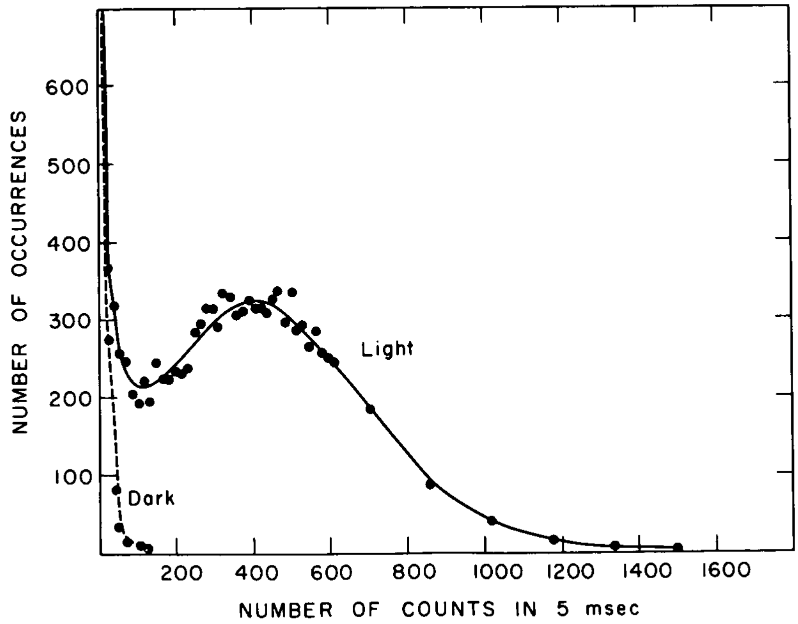

Figure 4.-Pulse-height distribution for a 3-stage image intensifier using the experimental arrangement of Fig. 1. The data show the number of photons detected by a photo-multiplier within 5 msec of the emission of a single photoelectron from the first photocathode of the image intensifier. The broken curve indicates the distribution of counts seen with no input light. The shape of the curve is similar to those of the curves calculated by Lombard and Martin (1961) for the pulse-height distribution from an electron multiplier assuming a Poisson distribution at each stage. At least part of the tail at high amplitude is due to the presence of a small percentage of multiple photoelectron inputs. The position of the peak depends on the gain of the image intensifier chain. For these data an overall voltage of 35 kV was used.

a Poisson distribution for the input events we expect that approximately 94% of the detected events were produced by single photoelectrons. A background distribution was measured at the same time and the plotted data were obtained by subtracting 88%(= 100%-12%) of the background from the raw count data. This curve is the result one would expect if it had been possible to ignore all events in which no photoelectron was emitted. Each count in the plotted distribution includes some remaining contribution from the background and therefore the peak in the distribution actually produced by input events is lower by the number of counts due to the background. Because a 5 msec window was used for the gain distribution shown in Figure 4, the actual pulse-height distribution is the observed distribution multiplied by approximately a factor of two.

The number of channels that can usefully be employed before the loss of information caused by the sampling procedure of the image dissector becomes important depends not only on the gain as given in equation (1) but also on the statistics of the photoemission process of the image intensifier chain. Although it would be possible to predict the performance of the device from the measured properties of the intensifier as shown in Figure 2 and 4, it is somewhat more reassuring to actually measure the degradation of the measurement precision caused by the sampling procedure and the statistical nature of the image tube amplification.

In order to investigate the precision of measurements made with the intensifier, the tube was continuously illuminated by a weak source. The output of the intensifier was then sampled for a period of 4 μsec once every 500 μsec and the average of the counting rate was recorded for repeated 200 sec counting periods. The results should simulate the behaviour of a single channel of a simultaneous multichannel photometer. With the light intensity adjusted to produce an average of 100, 1000, 2350, and 8600 primary photoelectrons to the intensifier during each 200 sec time interval, the fluctuations in the total count could be explained almost entirely by the randomness expected for the small number of primary photoelectrons.

Linearity tests have shown that when using a 0.008-inch-diameter input aperture the gain of the three-tube chain is essentially linear from less than one input photoelectron per second to more than 5×10^3 input photoelectrons per second. However, caution must be taken in extrapolating this result to spot sizes that are equal to the resolution capability of the tube, for a 0.008-inch aperture is easily resolved by a three-tube chain.

DeVeny (1970), using photographic photometry and a Westinghouse WL-30677 image intensifier, reports very large differences in sensitivity over the output screen. We have not found such large differences and feel that we can make corrections for those that exist in our tubes.

A low light level TV tube (such as an SEC camera tube or a silicon intensifier camera tube) could be used to record the output scintillations. Although this procedure has the advantage of using all the information produced by the image tube, commercially available targets for TV-type detectors are noisy and have very limited dynamic range. Also the SEC target must be carefully protected from excessive photocurrent to prevent it from being burned.

A second alternative is to use an image dissector to record the output scintillations. An image dissector can be made very stable because it is essentially a photomultiplier with a small, deflectable input aperture. Because it is a multiplying phototube it is nearly an ideal detector, but it can view only one information element at a time, and light from other elements is not detected. It must therefore rely on the persistence of the image tube phosphor to act as a memory element.

IV. CONCLUSIONS

Measurements of stability, linearity and statistical precision of output vs input light intensity on three Varo image tubes indicate that it is feasible to construct a multichannel photometer using such tubes. The use of a small-aperture image dissector to repetitively scan the information stored on the output phosphor of the image tube should allow direct digital readout into several hundred channels. Use of a small on-line digital computer may be necessary to allow immediate correction for any spatial non-uniformities of the image tube or phosphor response.

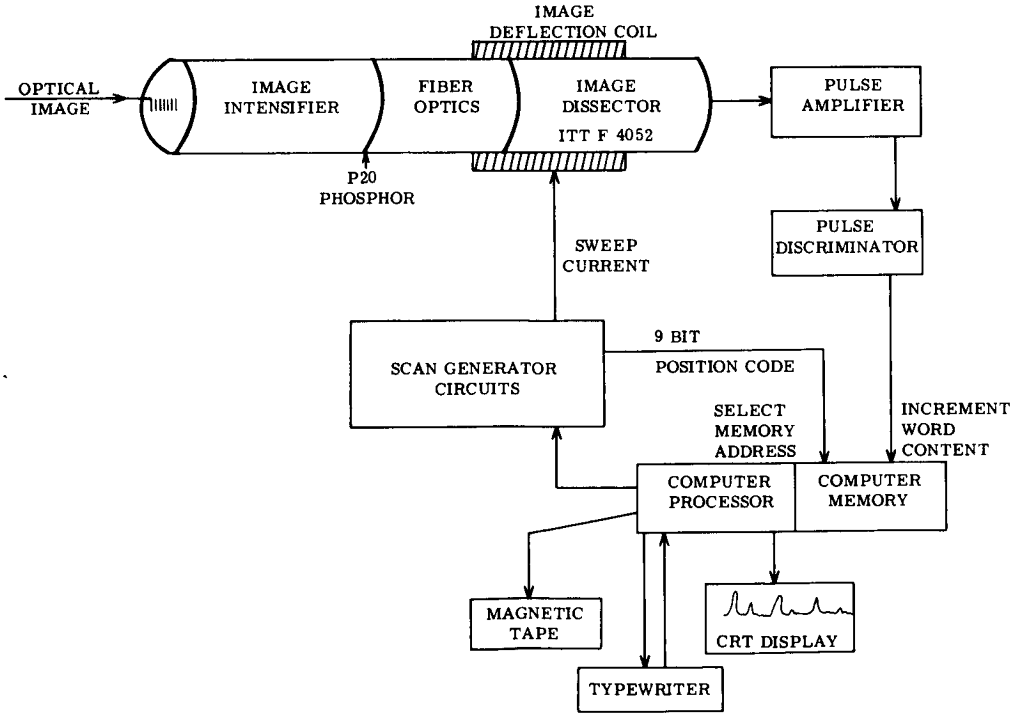

IMAGE TUBE OPTICAL SCANNER

Figure 5.-Experimental arrangement for test of image-scanner electronics system.

APPENDIX

A preliminary test of a combined image-tube image-dissector was made using the experimental arrangement shown in Fig. 5. An optical pattern was transmitted to the photo cathode of the image-intensifier by placing a mask on the fiber-optic entrance face. The mask had 4 mil. diameter holes spaced at 100 mil. intervals. The image dissector was swept with a period of 2 ms, and the resulting output distribution was stored in 512 computer words or "channels".

Fig. 6 shows a CRT display of the data collected in two 1-hour exposures, the first with a faint light falling on the mask, the second with no light. The narrow peaks are due to light passing through holes in the mask. A "continuum" is seen because the mask was constructed of translucent plastic. The large bump at the center is believed due to ion emission in one or more of the image tubes. The counting rate under this bump fell by a factor of 10 during the first 48 hours after the image tubes were turned on. Fig. 7 shows the difference between the light and dark patterns. The shape of the curve is almost identical with one obtained in a 5 minute exposure with higher light intensity. The two large irregularities in the "continuum" curve are due to the presence of small pieces of opaque material accidently left attached to the mask.

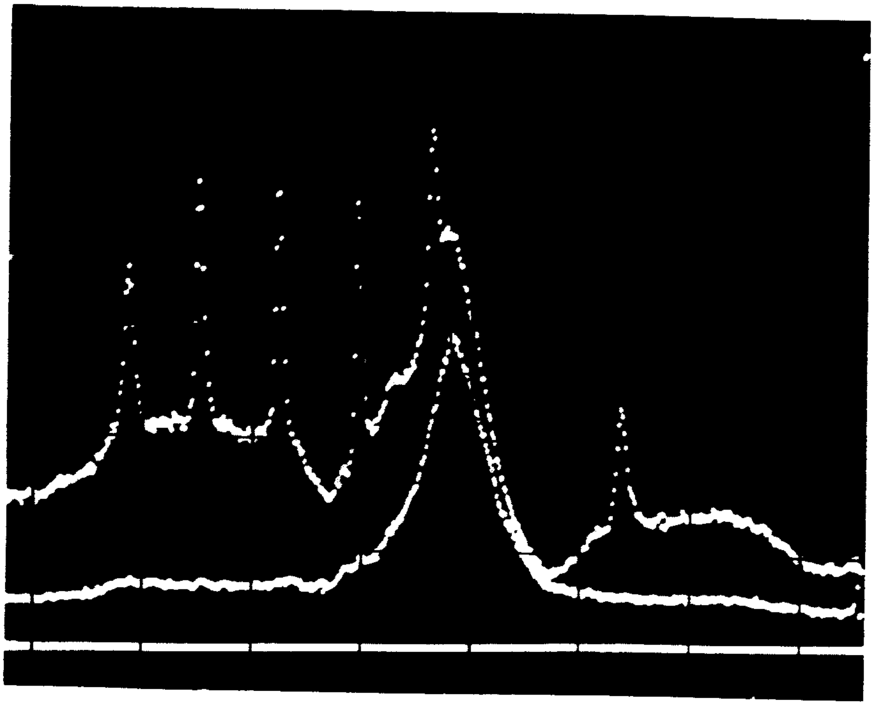

Figure 6.-Pulse count distribution from two 1-hour runs. The upper curve had light intensity sufficient to produce less than 1 photoelectron per channel per sec. The lower curve was due to dark current at room temperature. Full scale on the display is 10^4 counts.

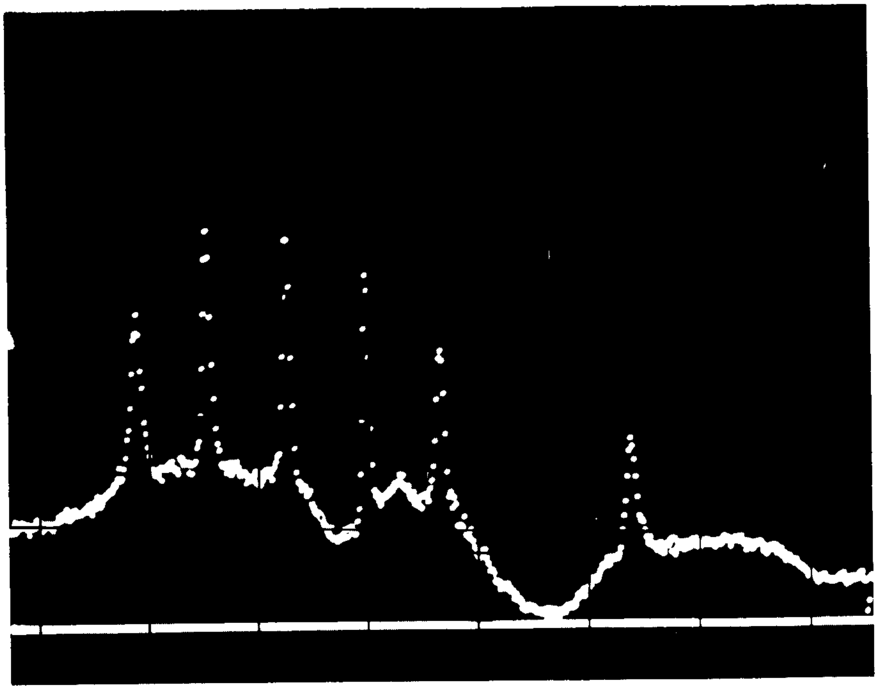

Figure 7.-Count distribution obtained by subtraction of the two curves of Figure 6.

The image dissector had a slit width of 4 mils. This, combined with holes in the mask, should have resulted in peaks of 8 mils full width, which corresponds to 4 or 5 channels. The narrowest observed peak is at least 9 channels wide. The reason for the discrepancy is not known, but we believe that more careful focusing of the image dissector tube will produce improved results.

To obtain an idea of the overall counting efficiency, an opaque mask with an 8 mil aperture was placed in front of an ITT FW-130 photomultiplier. A count rate of 2 x 10^5 counts per hour was obtained using the same light intensity as that used for the run shown in Fig. 6. The total counts recorded under each peak in Fig. 7 is about 3 x 10^4. If we assume quantum efficiencies for the photo tube and for the image intensifier are equal, this means that about 0.6 photons were detected for each photo electron released by the image intensifier photo-cathode.

It should be noted that (except for the two irregularities noted above) the continuum shown in Fig. 7 changes by less than a factor of 2 over the area scanned, indicating a reasonably uniform response over the face of the image intensifier tube.

The variance of 31 points in the continuum just to the right of the right hand peak was calculated and found to be in reasonable agreement with the value expected from the input shot noise.

ACKNOWLEDGEMENTS

We would like to thank Mr. Edward Eberhardt of ITT for much advice and encouragement, Mr. Grady Stowe of Varo for his help in obtaining low dark current image tubes, and Dr. William Burke for several helpful discussions.

This project was supported, in part, by NASA Grant NGL 05-061-008 and NSF Grant GP 6310 to Lick Observatory, and by NASA Contract NAS 5-1348 to the University of Wisconsin.

REFERENCES

Beardsley, W.R., DeJonge, J.K., Haring, D.J., and Hansen, J.R. 1969, Pub. of the Allegheny Obs. 11, 1.

DeVeny, J.B. 1970, Pub. A.S.P. 82, 142.

Flam, R.P. 1969, I.E.E.E. Proceedings 57, 2152.

Leverenz, H.W. 1950, Electrical Engineers Handbook, 4th ed., H. Penderand and K. McIllwain, eds. (New York: Wiley) 20.

Lombard, F.J., and Martin, F. 1961, Rev. of Sci. Instr. 32, 200.

Lynds, C.R. 1970, Ap.J. Letters, 159, L151.

Reynolds, G.T. 1966a, I.E.E.E. Trans. on Nuclear Science 13, 81.

________ 1966b, Adv. in Electronics and Electron Physics 22A, 71.

Page intentionally left blank

AN ELECTRICAL READOUT TUBE FOR ASTRONOMICAL SPECTROSCOPY

Jay Burns
Lindheimer Astronomical Research Center
Northwestern University, Evanston, Illinois

This paper describes the general features of an electrical readout image tube designed specifically for use on the LARC Coude spectrograph. This tube incorporates some unconventional features and is presented to illustrate how the special requirements of astronomical spectroscopy may be used advantageously to relax certain constraints ordinarily placed on image tube design by the shadow of television requirements. The two principal characteristics of astronomical spectroscopy that lead to novelty in the present design are the essentially one-dimensional nature of a spectrum and the freedom the astronomer has to read out his stored image slowly at some time after the exposure is made.

The tube to be described was designed to be an electronic substitute for the 103a emulsion in taking spectra. That is, the tube has been designed to replace this or similar photographic plates on a spectrograph originally designed for such plates, hence minimum requirements for resolution, information storage capacity, image stability, photometric linearity, and dynamic range were dictated a priori by the corresponding properties of the plate though it was expected that many of these values could be improved on in the tube. The spectrograph itself has a 3-meter focal length, a first order dispersion of 3Å/mm, and a measured resolution of 0.04Å at 4000Å. Therefore it has an instrumental width of approximately 13 microns and is fairly well matched to 103 or Spectroscopic Type I and II emulsions. The spectrograph uses standard 10" long plates and one requirement for the image tube was to be able to record substantially this full spectrum at a single exposure.

Image Section

The target of choice for most astronomical applications involving long integration and storage times is the SEC/TSE target(1-4), and this target was chosen for the present tube because it is capable of image storage for at least 24 hours without degradation and has a high internal gain together with a high information storage capacity. Sufficient internal gain was required so the readout could register as little as one photoelectron per resolution element of diameter 16 microns. The capacitance of the SEC target depends somewhat upon its operating conditions, but a good design center value is 200pf./cm^2, and the corresponding target surface potential sensitivity is 0.3 millivolts/electron/resolution element. A gain of 50-100 is therefore needed to produce a target sensitivity of the order of 15-30 mv./electron which is about what is needed to avoid special readout problems.

Conventional electrostatic or magnetic focusing did not appear attractive for a tube which is to record nearly a full 10" length of spectrum. Both of these methods suffer in several respects by comparison with proximity focus as image size grows beyond 3 to 4 inches. The requirement of a flat photocathode becomes difficult and expensive to meet with fiberoptic faceplates in large electrostatically focused tubes while size, weight, and power requirements pose problems with large magnetically focused tubes. Proximity focusing, on the other hand, is a simple and compact solution to large tube focusing. Moreover, it is relatively tolerant of small misalignments of tube parts, and it is easily adapted to cylindrical shaping of a long photocathode to conform to the focal plane curvature of certain types of spectrographs. It also gives images with a high degree of magnetic rigidity or resistance to shift or defocusing by weak, changing external magnetic fields such as the earth's field when a tube is used on the telescope. Elaborate magnetic shielding or field cancellation coils are therefore unnecessary with proximity focused tubes.

Proximity focusing suffers from two disadvantages. It is generally necessary to process the photocathode "externally" in a side chamber of a large vacuum system, to transfer it to the tube body, and to perform the final sealing operation all in very good vacuum. Secondly, the high electric field strengths required for good resolution lead to problems with enhanced tube backgrounds. Techniques for external photocathode processing have been developed successfully and no longer present formidable difficulties. Photocathodes processed this way have very high uniformity, which would be a good reason for using external processing in large tubes even if it were not dictated by proximity focusing.

The enhanced background problem has two facets. Contributions due to cold field emission can be reduced to negligible proportions by careful design of feedthroughs and internal tube hardware and by external photocathode processing which avoids the presence of excess alkali metal in the tube that would lower the work functions of any rough microscopic protrusions or edges. The other contribution to background is field-enhanced thermionic emission from the photocathode. The Schottky enhancement factor may be written exp $[4.4\sqrt{E}/T]$ where E is the electric field strength in volts/cm. and T is the absolute temperature. This factor is the ratio of field-enhanced thermionic emission to ordinary thermionic emission. For field strengths of the magnitude employed in the present tube design the enhancement factor is a little more than 25. It is therefore often necessary to cool the tube to reduce enhanced emission to the level of ordinary thermionic emission, but the need for cooling depends a great deal upon type of photosurface employed and upon the limitation set by background emission for a given spectroscopic problem so no generalizations will be attempted here. It may be remarked, however, that a $20^{\circ}C$ temperature reduction is generally sufficient to cancel the effect of a 25-fold field enhancement in a Cs-Sb photocathode.

A simple approximate relation between the size of a resolution element, δ, the photocathode-to-target spacing, d, and the accelerating voltage, V_a, can be written

$$\delta \approx \frac{d}{\sqrt{V_a}} \qquad (1)$$

This expression includes effects of averaging over the angular and energy distributions of photoelectrons in an approximate way to sufficient accuracy for present purposes. Taking $\delta = 16\mu$ and $V_a = 6400$ volts, a good design-center value for an SEC target, the required separation $d \approx 1.3$mm and the field strength $E \approx 50{,}000$ volts/cm. Notice that the required separation is not inconveniently small. Mechanical distortion of the thin SEC membrane under the electrostatic force is not expected to be a problem in a spectroscopic tube in which the target has a long, narrow shape, being supported in the present design by a plate with a slot 10" long and only a few millimeters wide. The small amount of bowing of the membrane that occurs neither defocuses nor distorts the image to any significant degree in a proximity focused tube.

Readout

A variety of readout methods are possible, some conventional, others not. In view of the long time available for readout and the requirement for a high degree of positional accuracy in reading the image, mechanical scanning of the reading beam was chosen. This method, shown schematically in Figure 1, uses a very simple electron gun, basically a small, low voltage gun with only minimal focusing properties that floods a fine slit about 10μ wide located close to the target. The reading beam is defined by this slit, and the entire gun-slit assembly is arranged to be moved along the target mechanically by means of a bellows drive. This insures positive, precise location of the reading beam and eliminates shading, beam landing errors, and other problems associated with electrical scanning. It also eliminates the need for suppressor and field meshes since the slit plate functions as a suppressor grid. Mechanical scan by cam drive also permits linearization of spectrograph dispersion or linear wavenumber readout, etc.

To avoid the inconvenience of having to move a single gun over a distance as long as 10", an array of several guns is used side by side with a corresponding decrease in the length of movement required to scan the whole plate. Readout methods that employ return beams allow all guns in the array to read simultaneously; in capacitive discharge readout (as in the Vidicon) only one gun reads at a time, and the array of guns may be sequentially switched or the scanning motion may be repeated several times.

Readout methods may be put into two main categories according to whether they measure the charge supplied to a picture element by the reading beam in recharging it to some reference potential or whether they actually measure surface potential variations over the target surface. The charge measuring methods are the ones commonly used and they will be discussed first.

Capacitive discharge readout can be performed slowly to permit reduction of video bandwidth to whatever value is necessary to maximize the signal-to-noise ratio with a given amplifier. It is possible to take as long as several seconds to read a single picture element in this tube; consequently synchronous detection or the use of a vibrating reed electrometer become possible. It appears, however, that detection of single photoelectrons by capacitive discharge readout requires a target gain somewhat larger than the SEC target can give, so this simple method of readout will not give the ultimate sensitivity desired.

A second mode of charge readout makes use of the fact that as the target surface approaches cathode potential under the action of the reading beam electrons are repelled by the target and return to the slit plate (Fig.2). If the slit plate is a microchannel plate operated in the pulse saturation mode, it becomes a simple matter to detect the time at which the picture element reaches cathode potential. The time lapse between the start of readout of a given element and the onset of beam return therefore measures the total charge that was stored in that picture element of the target. In this readout method the lowest energy electrons in the beam are the first to return and be detected. Since the low limit on electron energy is fairly definite, in contrast with the high energy "tail" of the energy distribution, this method should appreciably reduce the effects of energy spread in the beam upon readout accuracy. This method of readout appears capable of achieving the ultimate sensitivity, namely detection of single photoelectrons with the SEC target.

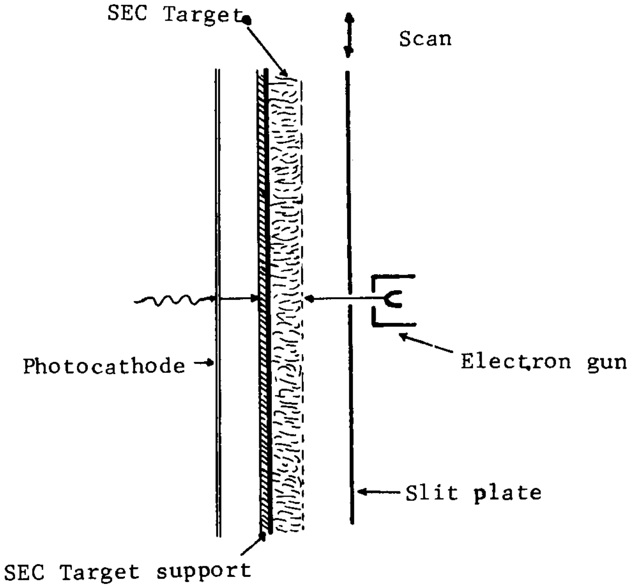

Figure 1.-Schematic illustration of capacitive readout with mechanical scan.

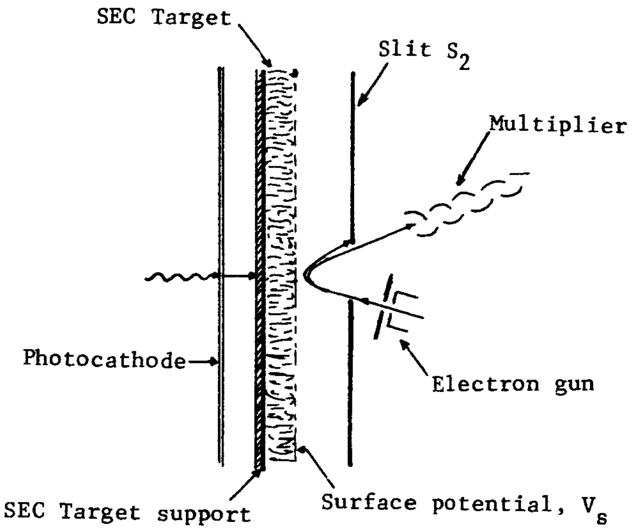

Figure 2. -Return beam readout or time-of-flight readout.

Two methods will be mentioned that actually read target surface potentials directly without erasing the image by recharging the target during readout as the above methods do. The first of these will be termed deflection modulation and is shown schematically in Fig. 3. In this method the electron beam is incident upon the target from an angle to the target normal with the plane of the incident beam parallel to the lengths of the spectral lines in order to avoid deflection of the beam by potential gradients that lie along the dispersion direction of the spectrogram. The energy spread and finite size of the incident beam give rise to a distribution of trajectories lying within the limits shown in Fig. 3, and the surface potential in the vicinity of the region of closest approach of the beam determines how much of the return beam is intercepted by the half-slit, S_2, and how much is transmitted to the multiplier behind S_2. It is clear from the figure that the current entering the multiplier depends upon V_s, and a detailed analysis shows that the method is capable of measuring surface potential variations as small as 10 millivolts.

A closely related method may be termed aberration modulation. It makes use of the aberrations of a saddle-field electron lens (e.g., an einzel lens) established in the plane of the slit placed close to the target, very much as in Fig. 3 but with a closer target-slit separation. These aberrations deflect the return beam through an angle that depends among other things upon the potential of the target surface. Since the aberrations, hence the return beam deflection, are very sensitive to the influence of the nearby target surface potential upon the exact shape of the lens, it is possible to determine V_s from deflections of the return beam partially intercepted by a half-slit as in the deflection modulation scheme.

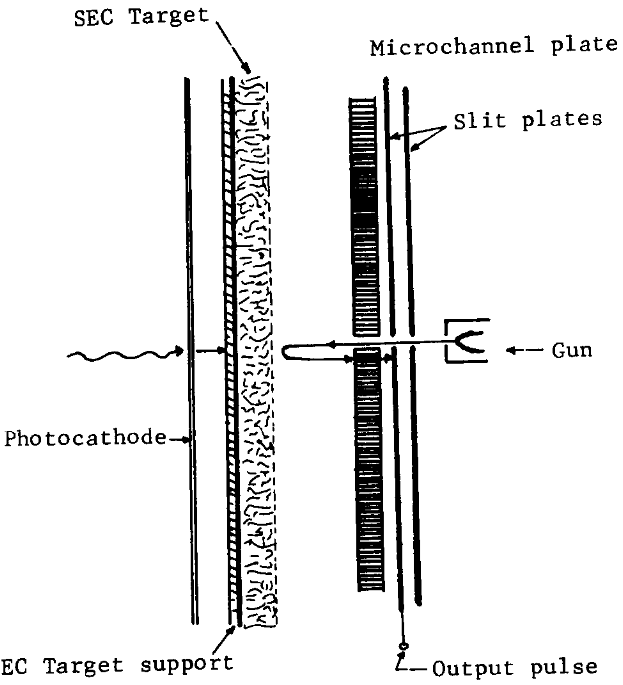

Figure 3.-Deflection modulation readout.

Another non-erasing method of determining target surface potential measures the time of flight of a charged particle (ion) during its turn-around path between a slit and the target. Low velocity ions should be used to obtain reasonably long times of flight of the order of fractions of a microsecond for energies of a few ev, and alkali metal ions in small numbers may be generated thermionically from a suitable indirectly heated Zeolite cathode(5). The ion gun may therefore be virtually as simple as the electron gun in Fig. 1. Figure 2 shows the time-of-flight method schematically with a microchannel plate to detect arrival of the returned ions. In operation the gun grid (normally at cutoff) would be pulsed with a fast rise-time pulse to give a short burst of ions, and the same grid pulse would trigger the timing ramp in a time-to-amplitude converter. The pulse from the microchannel plate that signals arrival of the first ion would stop the TAC.

The chief drawback of this method is the high order of timing accuracy required to achieve good sensitivity. For example, a typical readout sensitivity would be a few tenths of a microsecond per volt change in target surface potential. Therefore, in order to read single photoelectron events that give 15-30 millivolt target potential shifts in the SEC target, time resolution of the order of 5-10 nanoseconds is required.

To summarize the readout situation, the destructive readout methods are simpler with capacitive discharge being the simplest of all but limited in sensitivity. The return beam method that measures charging time seems to best combine sensitivity and relative simplicity and is the method being used initially in this tube design.

REFERENCES

1. Goetze, G.W., in "Adv. in Electronics and Electron Physics," ed. by McGee, J.D., McMullan, D., and Kahan, E., Vol. 22A, p. 219. Academic Press, N.Y. (1966).

2. Boerio, A.H., Beyer, R.R., and Goetze, G.W., ibid. p. 229.

3. Beyer, R.R., Green, M., and Goetze, G.W., ibid. p. 251.

4. Filby, R.S., Mende, S.B., and Twiddy, N.D., ibid. p. 273.

5. Mandel, L., Brit.J.Appl.Phys. 10, 233 (1959).

Page intentionally left blank

VIDEO DATA PROCESSING FOR THE CELESCOPE EXPERIMENT*

R. J. Davis, W. A. Deutschman, K. Haramundanis, Y. Nozawa,
and K. O'Neill

Smithsonian Astrophysical Observatory, Cambridge, Massachusetts

ABSTRACT

Smithsonian's Celescope experiment, operated in NASA's Orbiting Astronomical Observatory, produces video data from which we reconstruct the ultraviolet brightnesses of stars and other objects contained in the pictures. As described in another paper in this symposium (Nozawa, Davis, Deutschman, Haramundanis, and O'Neill), Celescope produces video data in digital form. This is essentially the form in which these data are delivered to SAO; each picture is accompanied by engineering data required for its analysis. As the first step in our processing, we separate noise and background from the signal and combine adjacent signal elements to derive a total signal amplitude and raster position for each object within the picture. The next step converts the signal amplitude and raster position into ultraviolet intensity and true position in spacecraft coordinates by use of calibration data obtained before launch. We then convert spacecraft coordinates into celestial coordinates and match the observed objects with stars from an identification catalog or with objects such as calibration-lamp images created by the Celescope experiment. Finally, the results are reviewed for consistency and accuracy before they are published as a catalog of ultraviolet brightnesses and of identifications with known stars.

INTRODUCTION

The Celescope Experiment of the Smithsonian Astrophysical Observatory (SAO), operated in NASA's Orbiting Astronomical Observatory (OAO), produces video data from which we reconstruct ultraviolet brightnesses of stars and other objects contained in the pictures. As described in another paper in this symposium (1), Celescope produces video data in digital form. This is essentially the form in which these data are delivered to us; each picture is accompanied by engineering data required for its analysis. Normally, our data reduction proceeds from digital magnetic tapes produced for us by NASA and compatible with our CDC 6400 computer. An alternative source of video data, faster but less complete, is analog magnetic tapes (containing these same

---

*This research has been supported in part by Contract NAS 5-1535 from the National Aeronautics and Space Administration.

digital data, but in raw telemetered form). These analog tapes are produced by Smithsonian's Data-Handling Equipment (DHE) directly from telemetry signals furnished to us by NASA.

CELESCOPE DATA REDUCTION

The reduction system for Celescope observational data contains a series of computer programs supplemented by human intervention at certain points to augment decisions made by the programs. Intermediate products of the reductions are made available for use in subsidiary studies.

A flow chart of the reduction system is shown in Figure 1. Magnetic tape, random-access magnetic disk, punched cards, and computer-controlled cathode-ray-tube devices are all utilized in the reduction system.

Preprocessing

Before reduction can begin, the two forms of incoming data, analog and digital tapes, are treated by a set of preprocessing programs (known collectively as Phase 0) that standardize the picture format and display for checking

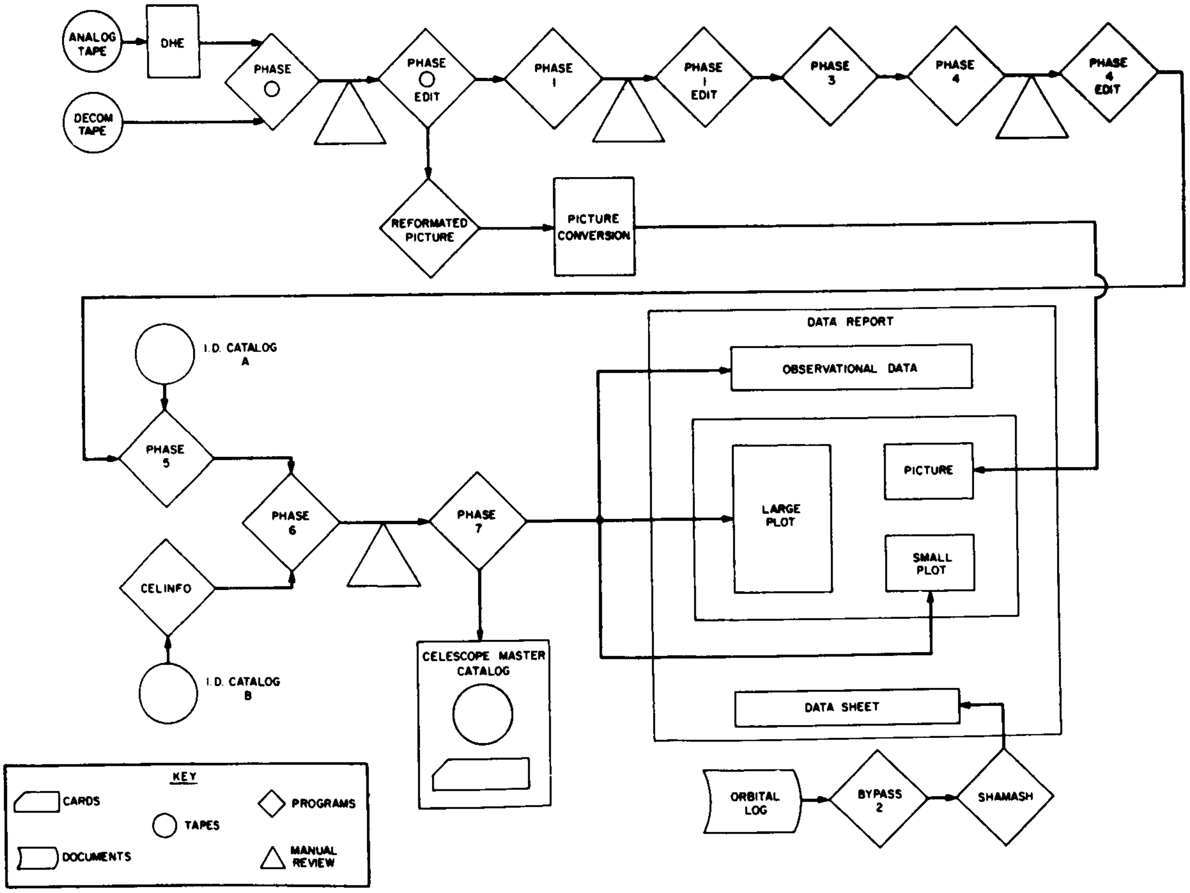

Figure 1.-Celescope data flow.

the descriptive picture headers and a printer-shaded one-page presentation of each picture. Analog tapes must be preprocessed on a tape converter (the DHE) before processing by the CDC 6400; digital tapes supplied by NASA (DECOM or decommutated tapes) are preprocessed directly on the SAO CDC 6400.

Evaluation

Successfully preprocessed pictures are displayed for evaluation. Evaluation consists of determining picture quality and matching each picture with its descriptive header as obtained from field-team orbital log forms. Data in the headers contain the equatorial coordinates of the field center (at epoch of date), exposure time, and various experiment parameters needed in the reduction. During evaluation, a "quality code" is attached to each picture and retained as part of the descriptive header for that picture.

An editing program eliminates irreducible frames at the request of the user and corrects errors in the descriptive headers. Output from the editing program goes in three directions: 1) into the data stream for reduction, 2) into the SAO Celescope Tape Archive, and 3) into a (non-SAO) computer that reconstructs the digital picture on a cathode-ray-tube display that is photographed for a permanent record.

Poor-quality data may be processed for special purposes and in some cases may be improved before entry into the main reduction system. A special program recognizes single-line data losses and replaces each intensity in such a line with the average of the lines immediately preceding and following. A group of lines containing bad data is set to zero and ignored for further processing. Pictures altered in such a manner are assigned a nonzero quality code.

Data Reduction

Entry into the reduction system occurs when a picture is processed by Phase 1, the principal reduction program, which separates signal from noise. The first step in this program computes, on the basis of frequency-distribution counts, the "level of significance" for the entire picture. (Figure 2 contains a histogram of such a count.) All points greater than or equal to this level are considered to be signal; all others are considered to be noise. The average of all noise points in each 16×16 element box is the computed background for the box. The program next subtracts the background from each signal point, associates all contiguous points into objects, and for each object, adds the signal points to compute the intensity of the object (the quantity sigma (Σ)), determines the center of the object relative to its location in the picture raster (k, ℓ), and assigns it a permanent identification number.

In areas of exceptionally high or anomalous background, the program computes star intensities (Σ) that cannot be correctly reduced by subsequent steps in the reduction. The program automatically flags all such objects. The printed output from Phase 1 is checked to eliminate spurious objects and to separate clearly multiple objects. Any change to an object is automatically flagged by the editing program, which incorporates the change into the data tape. Output containing the background computed for each 16×16 element box is retained for supplementary studies.

Relative calibration is performed for each object by the next program in the data system, Phase 3, which converts the computed raster locations (k, ℓ) into spacecraft-centered coordinates (ζ, η) appropriate for conversion to equatorial (α, δ) coordinates and the signal (Σ) into logarithm of intensity (log I). (Refer to SAO Special Report No. 282 (2) for definitions of these.) The calibration tables used in the computations are those prepared by use of prelaunch laboratory data.

The next step in the reduction system is the automatic identification of "engineering objects," i. e., objects that are known to be in the picture, such as the calibrator lamp, its ghosts, and defects in the target. Each such object is identified in the program (Phase 4) within a window of fixed size and intensity. Objects at the edges of the field are identified either by their raster locations or by their distance from the center of the ζ, η coordinate system. Additionally, very faint objects whose intensities are questionable are flagged by this program.

The composite list of engineering and celestial objects is next plotted on a preliminary finding chart with a scale of 3 arcmin/mm, a scale close to that of the DM charts and the Bečvář Atlases. An enlarged plot containing object numbers and engineering identifications is plotted by the same program to

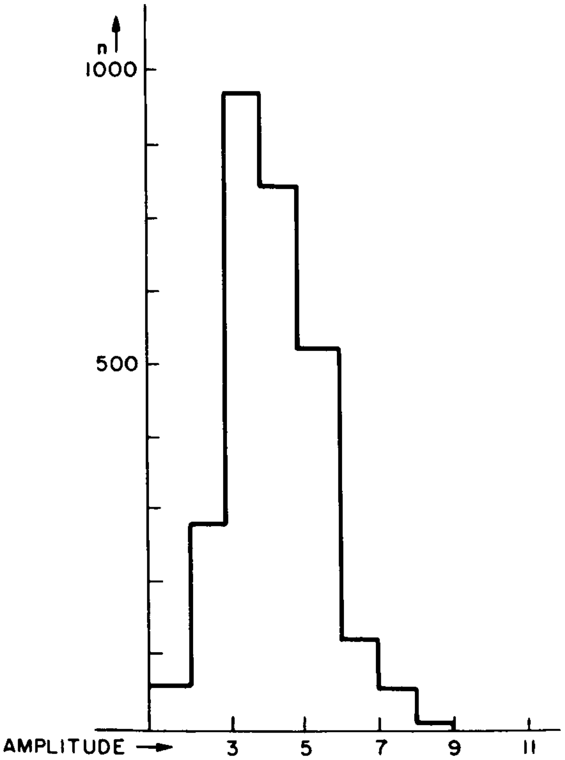

Figure 2.-Frequency count for typical picture (contact no. ɸ 3655, camera 1). For this frame, level of significance is nine.

accompany each finding chart. These plots are prepared directly from a plotter tape written on the CDC 6400 and plotted on a Calcomp drum plotter.

The Celescope Identification Catalog (the ID Catalog) utilized in the next three parts of the data-reduction system is a finding list of those objects most likely to be observed by the Celescope. It is used in two forms: one containing only positional information in a tape format packed specifically for random access by a pattern-recognition program, and the other containing additional information of astrophysical value (magnitudes, color indices, spectral types, luminosity classes, references to the literature, etc.).

Phase 5 processes the data one picture at a time. Input to the program are the ζ, η coordinates of each object (as computed in Phase 3), the equatorial coordinates (α_0, δ_0) of the field center (for epoch of date), and the roll (ρ) of the pointing. From the given field center, coordinates at epoch 1950.0 are computed and the short (random-access) form of the ID catalog is searched for all objects within a 1°5 radius of this point. Positions of all catalog objects are projected onto the satellite ζ, η coordinate system by gnomonic projection, appropriately scaled for each camera.

Phase 5 performs a configuration match and the solution of the equations

$$\zeta = A + B\zeta' + C\eta'$$

$$\eta = D + E\zeta' + F\eta'$$

where ζ, η are the observed coordinates of the object, ζ', η' are the calculated catalog coordinates, and A through F are plate constants for the picture, determined by least squares.

With an acceptable fit, an object positively identified by the program as identical with a catalog entry is given the coordinates of the catalog entry; all other objects receive coordinates computed from the plate constants for the picture and their original ζ, η coordinates. Phase 5 may fail to compute coordinates for objects if any one of the following occurs: there are fewer than four matches between observed and catalog objects, there is a radical imbalance of catalog versus observed objects, or the position given for the field center is incorrect. If Phase 5 fails, the plotted finding charts are used in the next step in the reduction system to hand-match against the appropriate Bečvář Atlas.

Phase 5 also computes the ultraviolet magnitudes U_n and the filter number (defined by camera number and η coordinate) and flags each object near the filter boundary.

The field centers from Phase 5 are input to a program that searches the master ID catalog for all astrophysical data within 1°5 of the field center and outputs these data in a form for merging with the observations.

The observations and the astrophysical data are merged by the next program in the data system, Phase 6, which outputs a list in order of increasing right ascension. A reviewer examines this list, verifies all identifications by a comparison with the appropriate DM chart and catalog, and adds, where necessary, data from the Henry Draper Catalogue (3) or the UBV Catalogue of the U.S. Naval Observatory (4). The final list prepared by the reviewer is checked by an astronomer who verifies ambiguous identifications and determines if the data are of publishable quality.

Data from the contact-by-contact list are filed as the data base to be used for compilation into the final Celescope observational catalog and may be run through a printing program to produce data reports periodically.

Currently under development is a recalibration program that can accept the final output of the reduction system, along with other intermediate outputs as deemed necessary, and recompute the ultraviolet magnitudes with improved algorithms and calibration data.

DISCUSSION

The greatest problems we have encountered in processing the video data from the Celescope experiment have been 1) proper separation of signal from noise in Phase 1, 2) proper compensation for changes in the calibration of the equipment during orbital operations, and 3) rapid processing of extremely large quantities of this type of data.

Figure 3 presents, in digital form, a portion of one of the Celescope pictures. The full picture contains 256 lines with 256 elements in each line. The purpose of the Phase 1 program is to remove signal from noise, to determine which signals represent portions of star-like objects, and to combine the signals from these stars into three numbers representing horizontal position (ℓ), vertical position (k), and total signal amplitude (Σ). Outlined in Figure 3 are those portions of the picture where the amplitude exceeds the significance level determined as explained in the preceding section. Phase 1 determines the background in this portion of the picture, subtracts this background from each signal element, and assembles contiguous points to determine k, ℓ, and Σ for each star. Figure 4 is that portion of the Phase 1 printout containing the star outlined in Figure 3. Only k, ℓ, Σ, and the identification number are passed on to subsequent phases of the data-processing system. Manual review of each "star" as presented in Phase 1 is required for removing certain types of spurious objects and for separating multiple stars. We are in the process of revising Phase 1 to incorporate those features of the review for which we have been able to specify algorithms.

Compensation for changes in the calibration of the equipment during orbital operations has been the greatest problem we have faced in the reduction of our data. The original computational system, which adjusted our measured ultraviolet stellar magnitudes by an amount indicated by changes in the signals from our calibrator lamp images, gave unexpectedly large residuals in the magnitudes of those stars we have observed more than once. We are attacking this problem by intercomparing and reviewing the observing conditions associated with our measurements of each multiply observed object in order to improve the calibration tables used for converting signal amplitude into stellar magnitude and to include the proper changes in these calibration tables to correct for the observed changes in system performance during our 16 months of orbital operation.

Finally, the sheer volume of data to be handled through our system has required us to develop a rather complex set of procedures for controlling and monitoring the flow of data. These procedures keep track of the processing status of each picture taken by Celescope and the location of all records related to each of these pictures. Our procedures also control the processing in such a manner as to ensure that those pictures most relevant to solving the calibration problem and those containing the greatest amount of astrophysical information are analyzed first. A great deal of cross referencing and computer processing is required to enable us to compile our data on both a picture-by-picture basis and a star-by-star basis.

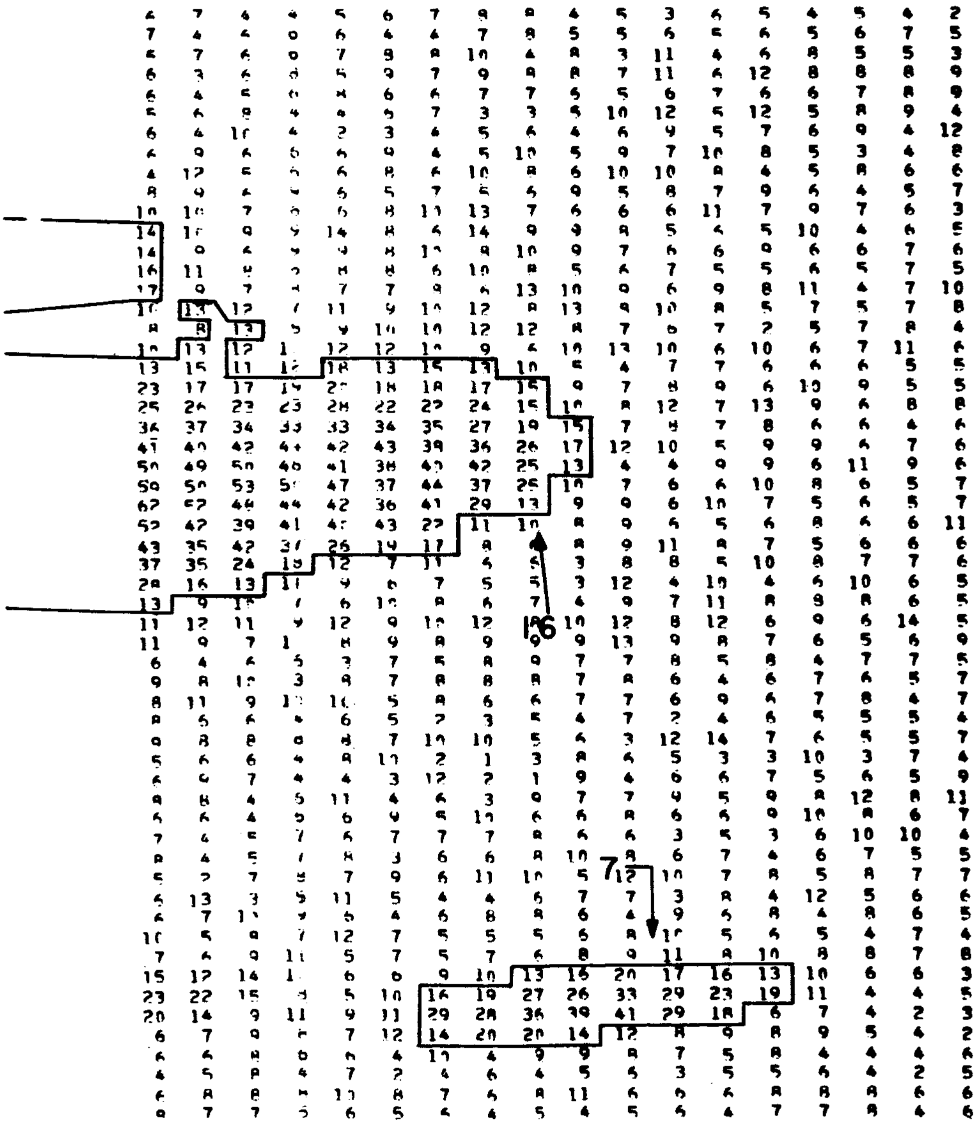

Figure 3. -Portion of the raw video signal from typical Celescope picture.

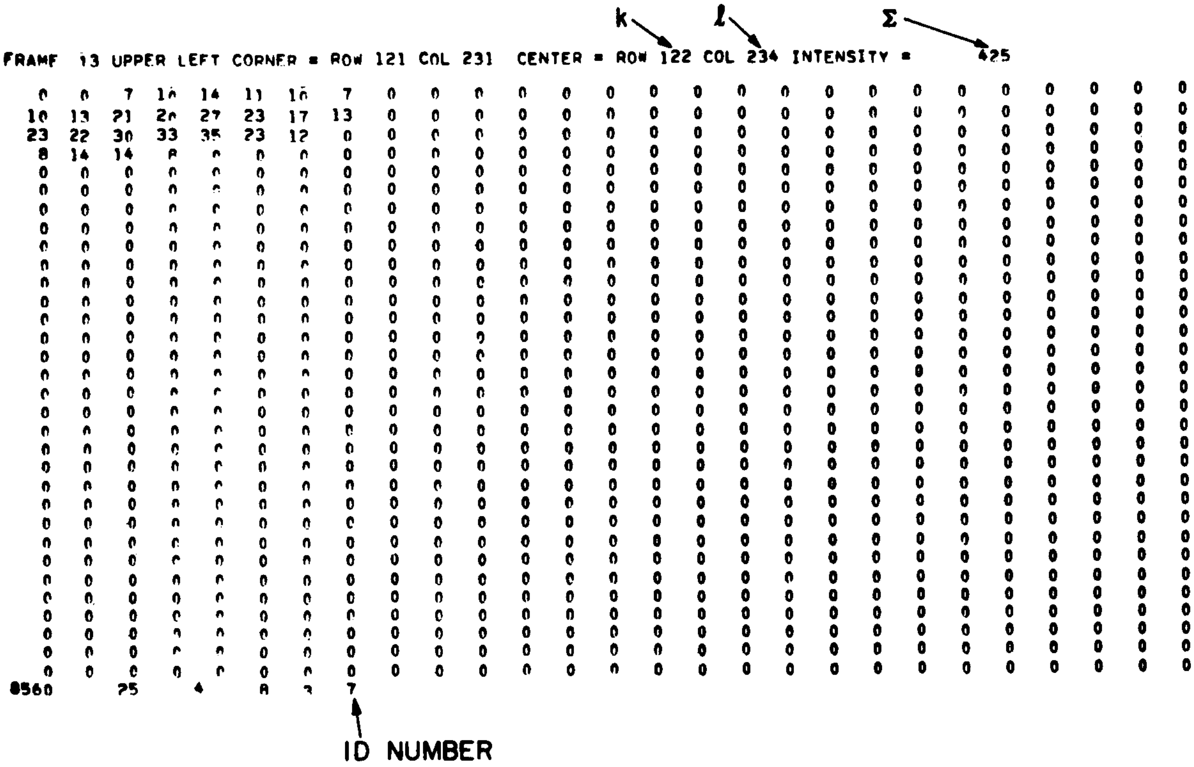

```
FRAMF  13 UPPER LEFT CORNER = ROW 121 COL 231  CENTER = ROW 122 COL 234 INTENSITY =    425

   0   0   7  10  14  11  10   7   0   0   0   0   0   0   0   0   0   0   0   0   0   0   0   0   0   0   0
  10  13  21  20  27  23  17  13   0   0   0   0   0   0   0   0   0   0   0   0   0   0   0   0   0   0   0
  23  22  30  33  35  23  12   0   0   0   0   0   0   0   0   0   0   0   0   0   0   0   0   0   0   0   0
   8  14  14   8   0   0   0   0   0   0   0   0   0   0   0   0   0   0   0   0   0   0   0   0   0   0   0
   0   0   0   0   0   0   0   0   0   0   0   0   0   0   0   0   0   0   0   0   0   0   0   0   0   0   0
   0   0   0   0   0   0   0   0   0   0   0   0   0   0   0   0   0   0   0   0   0   0   0   0   0   0   0
   0   0   0   0   0   0   0   0   0   0   0   0   0   0   0   0   0   0   0   0   0   0   0   0   0   0   0
   0   0   0   0   0   0   0   0   0   0   0   0   0   0   0   0   0   0   0   0   0   0   0   0   0   0   0
   0   0   0   0   0   0   0   0   0   0   0   0   0   0   0   0   0   0   0   0   0   0   0   0   0   0   0
   0   0   0   0   0   0   0   0   0   0   0   0   0   0   0   0   0   0   0   0   0   0   0   0   0   0   0
   0   0   0   0   0   0   0   0   0   0   0   0   0   0   0   0   0   0   0   0   0   0   0   0   0   0   0
   0   0   0   0   0   0   0   0   0   0   0   0   0   0   0   0   0   0   0   0   0   0   0   0   0   0   0
   0   0   0   0   0   0   0   0   0   0   0   0   0   0   0   0   0   0   0   0   0   0   0   0   0   0   0
   0   0   0   0   0   0   0   0   0   0   0   0   0   0   0   0   0   0   0   0   0   0   0   0   0   0   0
   0   0   0   0   0   0   0   0   0   0   0   0   0   0   0   0   0   0   0   0   0   0   0   0   0   0   0
   0   0   0   0   0   0   0   0   0   0   0   0   0   0   0   0   0   0   0   0   0   0   0   0   0   0   0
   0   0   0   0   0   0   0   0   0   0   0   0   0   0   0   0   0   0   0   0   0   0   0   0   0   0   0
   0   0   0   0   0   0   0   0   0   0   0   0   0   0   0   0   0   0   0   0   0   0   0   0   0   0   0
   0   0   0   0   0   0   0   0   0   0   0   0   0   0   0   0   0   0   0   0   0   0   0   0   0   0   0
   0   0   0   0   0   0   0   0   0   0   0   0   0   0   0   0   0   0   0   0   0   0   0   0   0   0   0
   0   0   0   0   0   0   0   0   0   0   0   0   0   0   0   0   0   0   0   0   0   0   0   0   0   0   0
   0   0   0   0   0   0   0   0   0   0   0   0   0   0   0   0   0   0   0   0   0   0   0   0   0   0   0
   0   0   0   0   0   0   0   0   0   0   0   0   0   0   0   0   0   0   0   0   0   0   0   0   0   0   0
   0   0   0   0   0   0   0   0   0   0   0   0   0   0   0   0   0   0   0   0   0   0   0   0   0   0   0
   0   0   0   0   0   0   0   0   0   0   0   0   0   0   0   0   0   0   0   0   0   0   0   0   0   0   0
   0   0   0   0   0   0   0   0   0   0   0   0   0   0   0   0   0   0   0   0   0   0   0   0   0   0   0
   0   0   0   0   0   0   0   0   0   0   0   0   0   0   0   0   0   0   0   0   0   0   0   0   0   0   0
   0   0   0   0   0   0   0   0   0   0   0   0   0   0   0   0   0   0   0   0   0   0   0   0   0   0   0
   0   0   0   0   0   0   0   0   0   0   0   0   0   0   0   0   0   0   0   0   0   0   0   0   0   0   0
   0   0   0   0   0   0   0   0   0   0   0   0   0   0   0   0   0   0   0   0   0   0   0   0   0   0   0
   0   0   0   0   0   0   0   0   0   0   0   0   0   0   0   0   0   0   0   0   0   0   0   0   0   0   0
   0   0   0   0   0   0   0   0   0   0   0   0   0   0   0   0   0   0   0   0   0   0   0   0   0   0   0
8560      25       4       8   3   7
```

Figure 4.-Corresponding portion of Phase 1 printout for the picture displayed in Figure 3.

REFERENCES

1. Nozawa, Y., Davis, R. J., Deutschman, W. A., Haramundanis, K., and O'Neill, K., Some Factors Affecting Accuracy of Space-Borne Astronomical Photometer, paper presented at this Symposium.

2. Davis, R. J., The Celescope Experiment, Smithsonian Astrophys. Obs. Special Report No. 282, 1968.

3. Cannon, A. J., and Pickering, E. C., Henry Draper Catalogue, Harvard Annals, Vols. 91-100, 1918-1936.

4. Blanco, V. M., Demers, S., Douglass, G. G., and Fitzgerald, M. P., Photoelectric Catalogue; Magnitudes and Colours of Stars in the U, V, B and U_C, B, V systems, Publications of the U.S. Naval Observatory, second series, Vol. 21, 1968, 772 pp.

DIGITAL IMAGE PROCESSING FOR THE RECTIFICATION OF TELEVISION CAMERA DISTORTIONS*

Thomas C. Rindfleisch

Jet Propulsion Laboratory
Pasadena, California 91103

ABSTRACT

All television systems introduce distortions into the imagery they record which influence the results of quantitative photometric and geometric measurements. Digital computer techniques provide a powerful approach to the calibration and rectification of these systematic effects. Non-linear as well as linear problems can be attacked with flexibility and precision. Methods which have been developed and applied for the removal of structured system noises and the correction of photometric, geometric, and resolution distortions in vidicon systems are briefly described. Examples are given of results derived primarily from the Mariner Mars 1969 television experiment.

Introduction

As all physically realizable instruments influence the data they collect, television cameras leave their signatures on the imagery they record. Scientific analyses of television photographs must be performed with the knowledge that the scene is observed through the camera's eye and any distortions introduced by the camera system processes potentially affect the results. The subject of this paper is the application of digital computer techniques to quantify and correct for video data distortions so that measurements and interpretations of the imagery can be based upon information as representative of the object scene as possible. This aspect of image processing represents but one of the several broad areas of application of digital methods to imagery, including camera system diagnostics, subjective detail enhancement, quantitative data rectification, and information extraction.

---

* This paper presents the results of one phase of research conducted at the Jet Propulsion Laboratory, California Institute of Technology, under contract number NAS 7-100, sponsored by the National Aeronautics and Space Administration.

The specific goal of the work to be discussed is the rectification of raw camera output data, using calibrated camera system performance characteristics, to produce photometrically and geometrically precise, high resolution imagery of the object scene. In approaching this problem, five major topics will be discussed including:

1. Encoding image information for the computer
2. Optimization of the system signal-to-noise properties
3. Calibration and correction of photometric distortions
4. Calibration and correction of geometric distortions
5. Calibration and restoration of image resolution

These classes of distortions are common to all camera systems, even though the physical mechanisms involved and the severity of particular types of distortion vary from sensor type to sensor type. Examples will be shown primarily illustrating the correction of distortions in vidicon television systems such as have flown on the Ranger, Surveyor, and Mariner spacecraft missions. All of this work was performed in the Image Processing Laboratory at the Jet Propulsion Laboratory using a general purpose computer, a specialized software system, and a high resolution film recorder and scanner.

Image Quantization

By their very natures, object scenes are continuous distributions of light intensities and digital computers are devices which manipulate discrete numbers. Two quantization processes are involved in converting a continuous image into an array of numbers on which the computer can perform various operations, each of which can cause serious artifacts in the processing results. The first quantization step is the two-dimensional spatial sampling of the image and the second is the binary encoding of each intensity sample. Because the major video distortions are introduced prior to the quantization procedure and because any distortions introduced in the quantization process itself are not reversible, it is important to observe certain criteria in encoding images for computer processing.

The vertical sampling of the image is generally the result of the line scanning of a raster and the horizontal sampling, the result of a subsequent periodic measurement of the one-dimensional scanned video signal. The effective density of these samples, in the image plane being scanned, must be high enough to satisfy the Nyquist sampling criterion, i.e., the sampling frequency in each direction must be at least twice the spatial frequency bandwidth in that direction. Physically this means that there must be at least two samples in a characteristic horizontal and vertical diameter of the system point spread function. This criterion guarantees that the discrete set of samples accurately describe the continuous image intensity distribution, even at points lying between the sample points. If this criterion is not satisfied (the data are aliased), then the actual behavior of the continuous image function between two sample points can deviate significantly from an interpolated estimate between those points and introduce spurious results in various geometric correction and enhancement filtering processes.

The binary encoding of each sampled intensity introduces an uncertainty in the quantized data which is related to the size of the intensity steps between encoding levels. In order to guarantee that the quantized image data are limited in their precision by the random noises of the image formation and camera sensor, a sufficient number of bits must be used to make the quantization noise insignificant. For a linear encoding to n bits of a signal such as the output of a vidicon camera with limited dynamic range V, the steps between encoding levels δV are

$$\delta V = V/2^n$$

The root-mean-square (rms) noise introduced by this encoding, σ_q, is

$$\sigma_q = \delta V/2\sqrt{3}$$

If the rms random noise at the output of the camera system is σ_r, a reasonable criterion for the number of bits required for the encoding is derived from requiring the quantization noise to be on the order of half the random noise

$$\sigma_q \lesssim \frac{1}{2} \sigma_r$$

The required number of bits is then

$$n \gtrsim \log_2 (\frac{V}{\sigma_r})-0.8$$

If the quantization noise dominates the random noise, the possibility of processing artifacts again arises. As the quantization interval becomes comparable to the image intensity fluctuations over a local area, the quantization noise becomes highly correlated with the signal. This appears as blocks of neighboring sample points having the same encoded intensity value, thereby introducing series of plateaus or contours in the encoded data. These correlated noises cause artifacts in enhancement filtering processes in addition to limiting measurement accuracy.

System Noise

The practical limit to all quantitative or photointerpretive measurements on a properly encoded image is the presence of noise. Enhancement processes such as to improve image resolution can sharpen features only at the expense of overall signal-to-noise ratio. For these reasons, one of the most important initial steps in digital image processing is the suppression of noise so that subsequent enhancement and restoration processing can be performed on maximum signal-to-noise ratio imagery to achieve optimized results.

Many noise sources exist in imaging systems ranging from random, wideband shot and thermal noises to highly structured periodic noises. Furthermore, in situations such as space photography, it is generally not possible to obtain multiple imagery in order to use frame averaging techniques. The precise separation of any noise from the composite video of a single frame must be based on one or more quantifiable characteristics of the noise signal of interest which distinguish it uniquely from the other video components. In most real situations one has only statistical information about the various components of the total video signal and thus, even in the theoretical limit, their separation is approximate. This is certainly the case in the data output of spacecraft video systems where the dominant signal represents a complex natural scene. The essence of video noise removal is to isolate and remove the various identifiable and characterizable noise components as rigorously as possible so as to do a minimum of damage to the actual video data. In most cases, the errors introduced to the real signal by the removal process, while small, vary from point to point and are impossible to measure meaningfully since very little is known in detail about the scene being photographed and the efficacy of removal is data dependent. In the following, the removal of three different types of structured noise will be described, including periodic, long-line, and spike noises.

Periodic Noise Removal - In electronic video systems, a common noise problem arises from the coupling of periodic signals related to the raster scan and data sampling drives into the low signal portions of the video handling electronics.

These noises are generally introduced when the video scene is represented by a one-dimensional temporal signal. Because of the periodicity of this type of noise, a useful method for characterizing it is in terms of a Fourier decomposition. A one-dimensional digital power spectrum of a test scene photographed by a Mariner Mars 1969 camera is shown in Figure 1. The power spectrum clearly shows a smoothly varying background decreasing in amplitude with increasing frequency and representing the true video spectrum on which is superimposed a number of narrow, abnormally large spikes. These spikes are the various components of the periodic noises present in the Mariner system and are related to multiples of the 2400 Hertz spacecraft power supply frequency.

For well designed systems, these periodic noises exhibit phase coherence over times long compared to the frame time of the camera. For this reason, when the two-dimensional image is reconstructed, the periodic noise appears as a two-dimensional pattern exhibiting periodicity not only along the scan lines, but perpendicular to them as well. If one computes a two-dimensional Fourier transform of a reconstructed picture, as shown in Figure 2, this two-dimensional structure becomes evident. Again the actual video signal spectrum appears as a noisy continuum falling off in amplitude toward high spatial frequencies and the noise components appear as well-defined two-dimensional spikes.

Because the noise as well as the scene exhibit two-dimensional correlation, a more precise removal can be achieved by filtering the noise from the two-dimensional Fourier space than from the one-dimensional space. This can be seen by considering the effects of one-dimensional filtering as observed in the two-dimensional transform space. Since the removal of a one-dimensional frequency component is

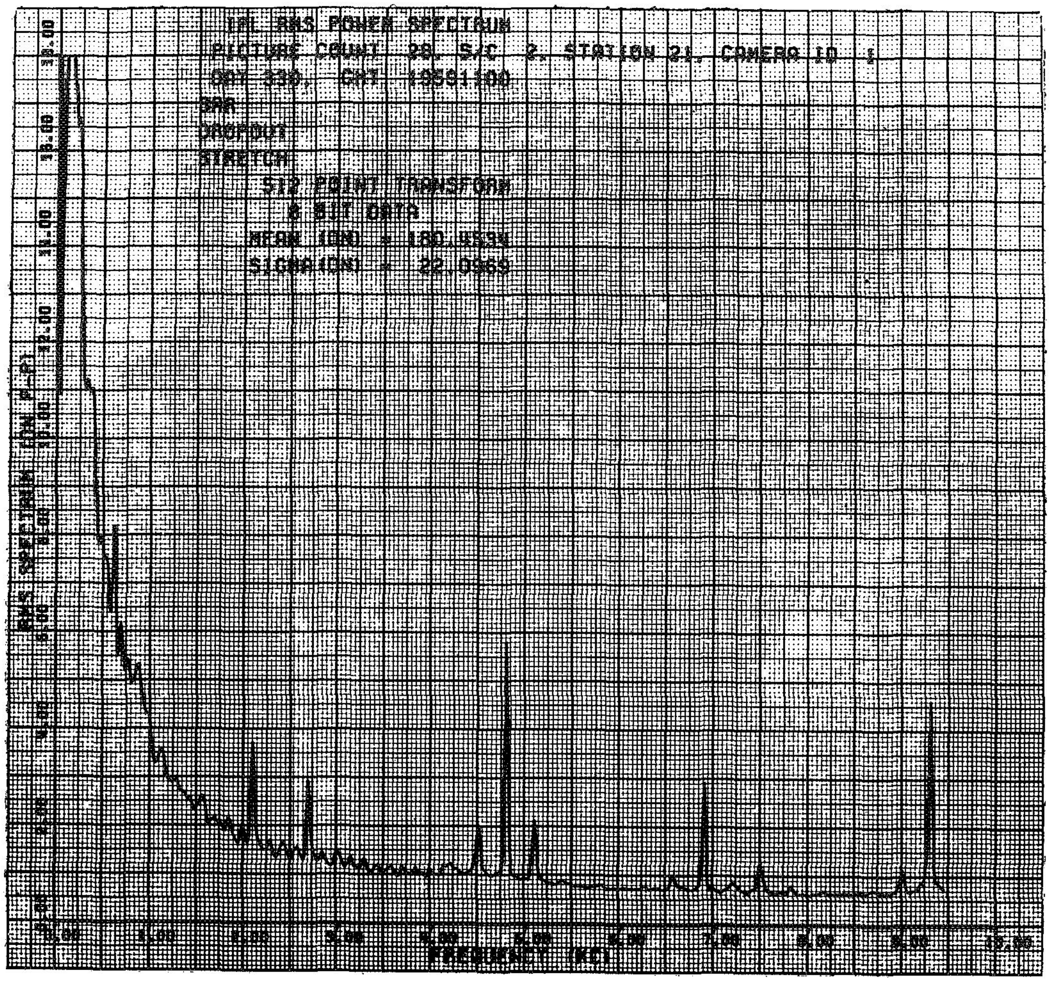

Figure 1.-Digitally computed Fourier power spectrum of test scene photographed by a Mariner Mars 1969 camera. The spectrum was computed from the one-dimensional scan output of the camera.

done irrespective of its vertical variation, the corresponding spectral components removed in two-dimensional frequency space lie in a vertical bar. Thus, since the noise component is contained in one spike along the bar, a large amount of video signal is unnecessarily removed.

Removing the two-dimensional spikes, one achieves a first order clean-up of the periodic noise components. By this method only the portion of the component spectral spikes can be isolated which protrude above the video spectrum continuum, without unduly removing the video signal. As can be seen in the power spectrum of Figure 1, the spikes clearly have skirts extending below the continuum. These skirts represent a subtle local modulation (generally amplitude modulation) of the basic noise pattern as might occur with amplitude dependence or saturation

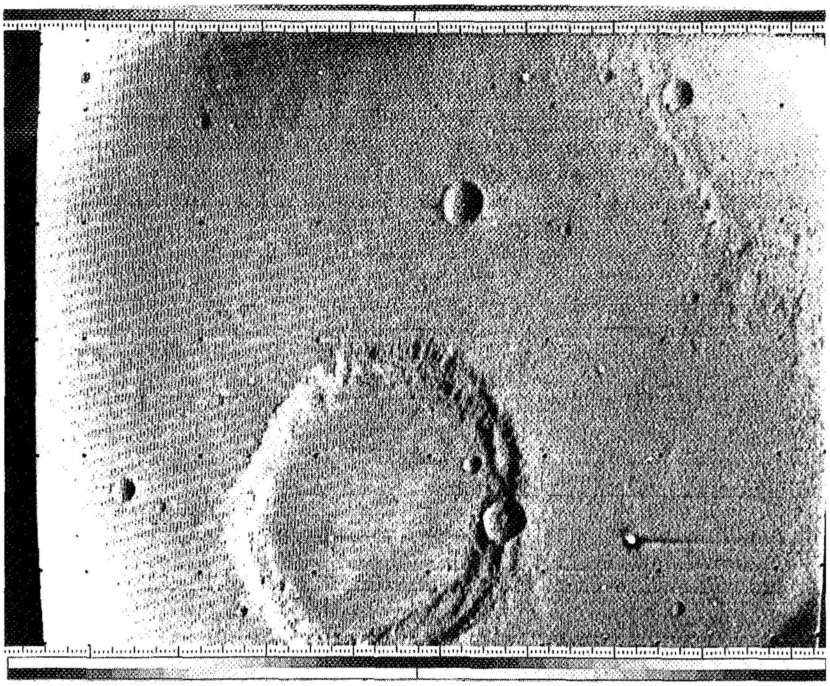

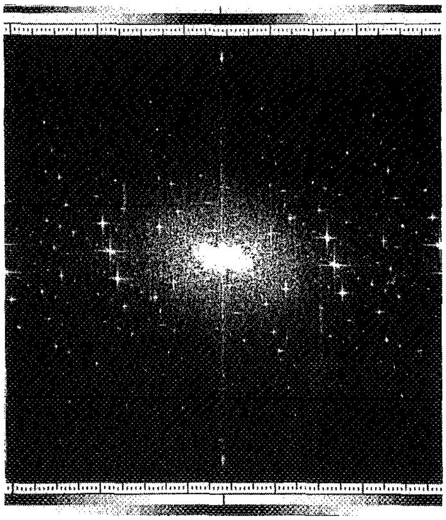

Figure 2.- The top picture is a raw photograph of Mars returned by a Mariner VI camera. Note the diagonal bands of periodic noise. The bottom picture is a digitally computed two-dimension Fourier spectrum of a portion of the top picture. The absolute spectrum amplitudes are displayed as gray levels increasing from black to white. The DC point of the spectrum is in the center of the bottom picture. Positive and negative horizontal spatial frequencies are above and below.

effects on the noise signal. These cannot be readily isolated by frequency space filtering. A more effective approach is to determine a local modulation coefficient for the idealized noise pattern derived from careful two-dimensional filtering. This coefficient is typically slowly varying relative to the resolution limits of the camera. The criterion which has been used for determining the local modulation coefficient is to minimize the variance of the noisy signal minus a variable fraction of the idealized noise pattern over a local region. If N_{ij} is the noisy image, n_{ij} is the idealized noise pattern, a_{ij} is the local modulation coefficient, and σ^2_{ij} is the "cleaned-up" signal variance for the local region of dimension M, the definition of local signal variance

$$\sigma^2_{ij} = \frac{1}{(M+1)^2} \sum_{k=-M/2}^{M/2} \sum_{l=-M/2}^{M/2} \left[(N_{i+k,j+l} - a_{ij} n_{i+k,j+l}) - (\langle N \rangle_{ij} - a_{ij} \langle n \rangle_{ij}) \right]^2$$

is used. The bracketted terms are average values defined for any matrix m_{ij} to be

$$\langle m \rangle_{ij} = \frac{1}{(M+1)^2} \sum_{k=-M/2}^{M/2} \sum_{l=-M/2}^{M/2} m_{i+k,j+l}$$

By using the minimization condition

$$\frac{d\sigma^2_{ij}}{da_{ij}} = 0$$

one derives the expression

$$a_{ij} = \frac{\left\langle \left[N_{ij} - \langle N \rangle_{ij} \right] \left[n_{ij} - \langle n \rangle_{ij} \right] \right\rangle}{\left\langle \left[n_{ij} - \langle n \rangle_{ij} \right]^2 \right\rangle}$$

which defines a modulation coefficient for each point in the picture in terms of the noisy image and the idealized noise pattern. The dimension M of the local area used to determine the coefficient a_{ij} for each point is chosen on the basis of the spatial frequency bandwidth appropriate for a_{ij}.

The results of applying these techniques to remove the periodic noise component from the Mariner VII picture shown in Figure 3 are apparent in Figure 4. The complicated periodic noises which were extracted are seen in Figure 5.

Long-Line Noises - A variety of mechanisms can produce long-line or streak noises in television images such as gain variations, line bunching, data outages, and analog tape recorder drop-outs. This type of noise, caused by drop-outs in the case of Mariner 1969, becomes apparent as horizontal streaks in Figure 4 with the removal of the periodic noise. The characteristic which distinguishes streak noises from the actual scene is their linear correlation along some particular direction and the lack of correlation in the perpendicular direction. This distinction is not complete, however, since linear features are common in natural scenes. The problems of data dependent noise removal are exemplified by this case since major damage to the true video signal may result in particular localized regions which contain scene components resembling the noise.

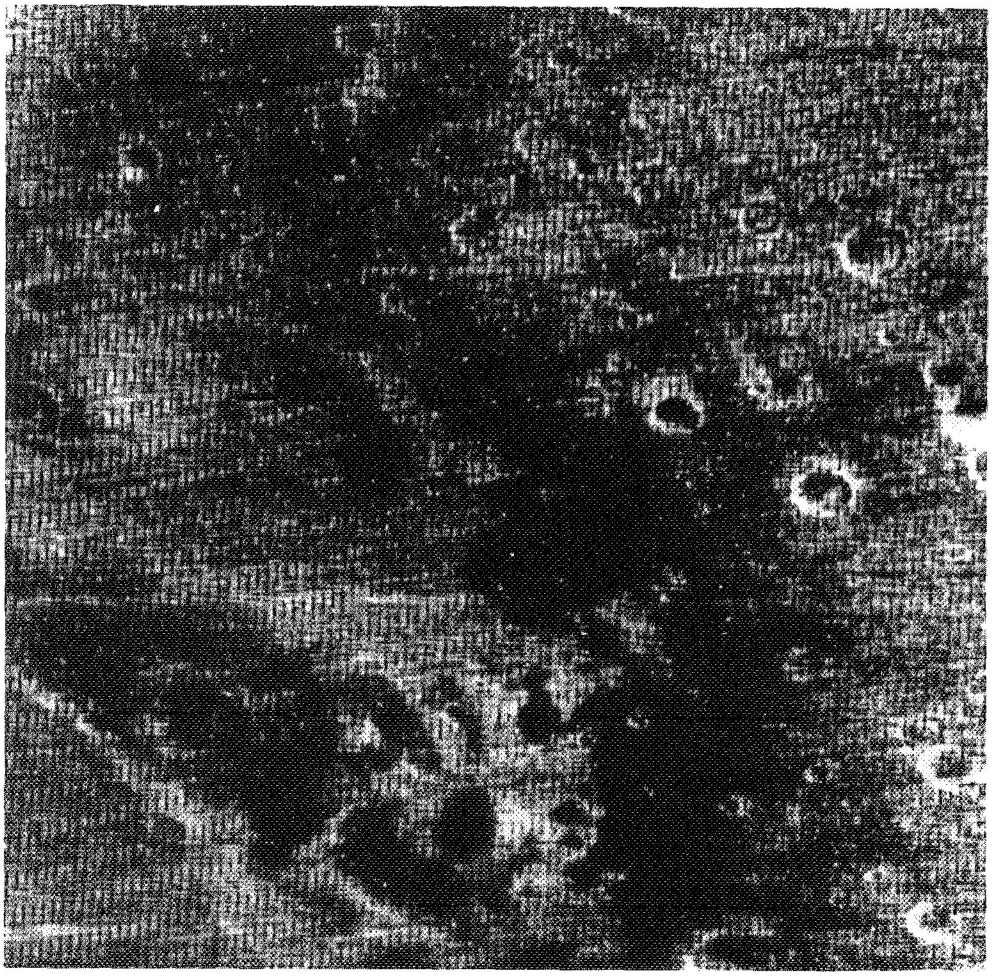

Figure 3.-A Mariner VII picture of Meridiani Sinus as received from the spacecraft and enlarged two times to make the noises apparent.

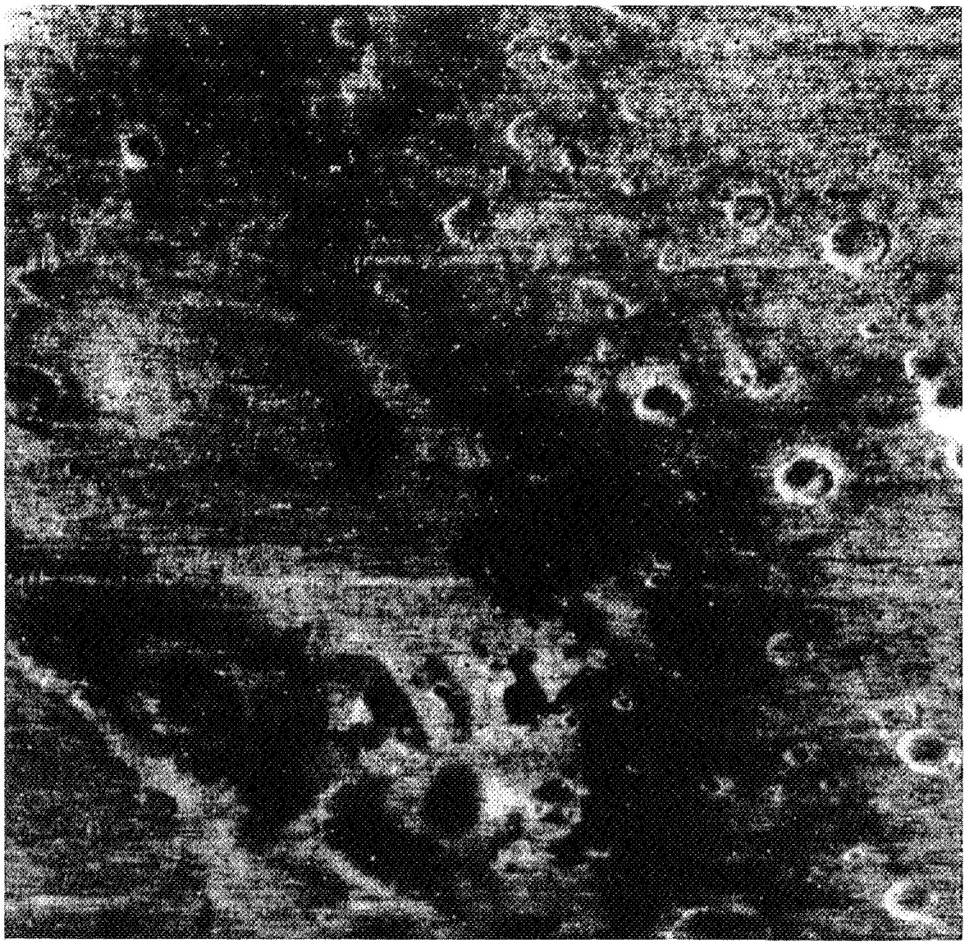

Figure 4.-The result of removing the periodic noises from Figure 3. Note the presence of horizontal streak noises at this point.

The technique developed to correct for these streak noises is to compare the local average intensity value of lines adjacent and parallel to the streaks with the average value of the streak itself and to apply a gain factor to account for any differences. A multiplicative rather than an additive correction is applied because the physical origin of the noise (magnetic tape drop-outs) is multiplicative. Since the correlation between points in a picture decreases with increasing separation, a linearly decreasing weight is applied to more distant local lines in determining the surrounding average. If N_{ij} is the noisy picture (j is the index along the direction of the streak noises) and G_{ij} is the corrective gain to be applied to the point (i,j), the expression

$$G_{ij} = \frac{\sum_{k=1}^{P} (P-k+1) \left[\langle N \rangle_{i+k,j} + \langle N \rangle_{i-k,j} \right]}{P(P+1) \langle N \rangle_{ij}}$$

is used where P is the number of adjacent lines above and below the streak and the average values are defined by

$$\langle N \rangle_{ij} = \frac{1}{Q+1} \sum_{k=-Q/2}^{Q/2} N_{i,j+k}$$

In this latter expression, Q is the low pass filter dimension along the direction of the streaks and is determined by the lengthwise correlation of the long-line noise. The dimension, P, is determined by the perpendicular correlation.

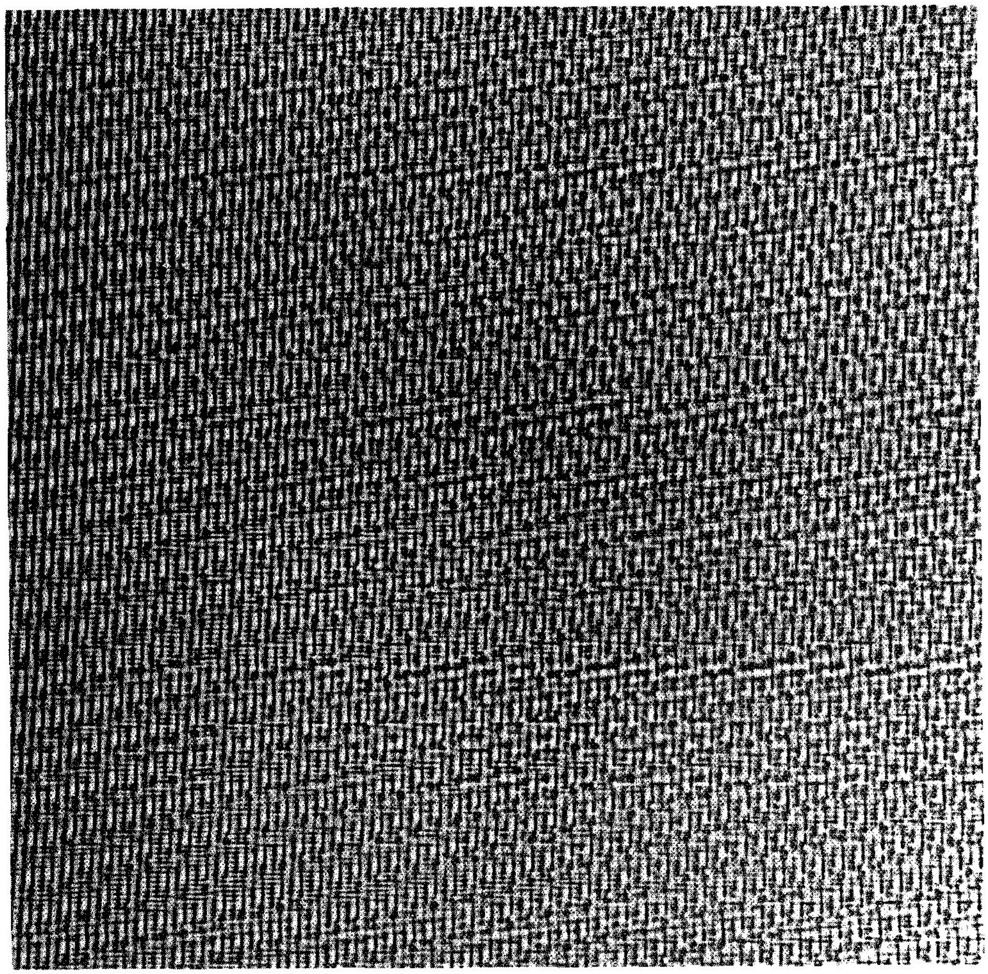

Figure 5.-The periodic noise pattern removed from Figure 3 to obtain Figure 4.

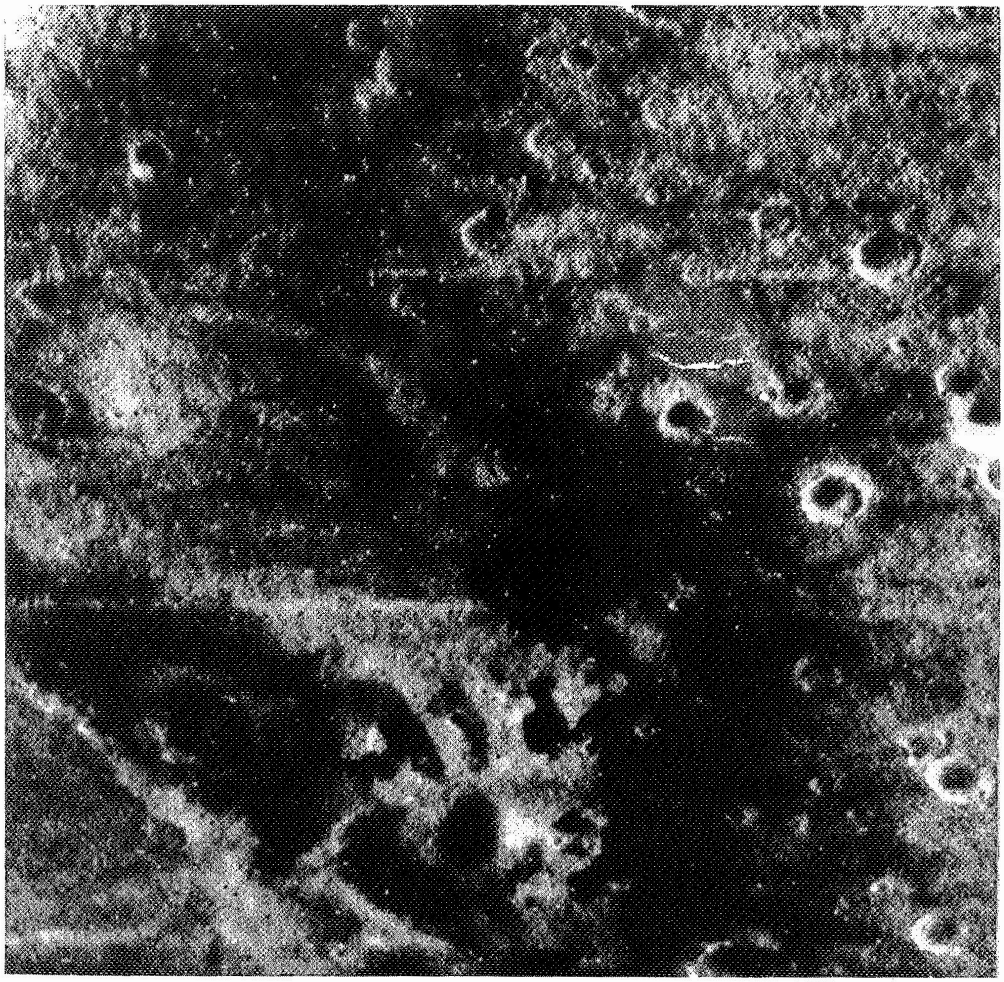

Figure 6.-The result of removing the streak noises from Figure 4. Note the presence of black and white spike noises scattered through the picture.

A further refinement was used in determining the numerator of the gain determining equation. The numerator was computed as shown but then a "majority rules" logic was applied so that terms deviating significantly from the average were eliminated from determining the average on a second pass. This algorithm is a refinement of the long-line filter described in reference 2.

The result of correcting for the streak noises in Figure 4 is shown in Figure 6. It should be emphasized that this correction is particularly data dependent and its effect, while closer to the truth in the large, may introduce artifacts in the small.

Isolated Spike Noises - The occurrence of a bit error in telemetering digital video data or the presence of sharp spikes of noise from the analog electronics can cause isolated picture elements to deviate significantly from the surrounding data. The removal of the periodic and streak noises illustrated in Figure 6 reveals an additional noise component consisting of black and white spikes. The characteristic which distinguishes these spike noises from the actual video is the fact that because of resolution limitations of a Nyquist sampled video system the picture element to picture element variation of the true signal is limited.

The logic used to remove spike noises is very simple. Each picture element is examined and if it is significantly above each of its neighbors or significantly below its neighbors it is replaced by the average neighboring intensity. The results of applying this correction to the remaining spike noises in Figure 6 is shown in Figure 7.

A comparison of Figures 3 and 7 shows a dramatic improvement in signal-to-noise ratio by using the digital computer to isolate and remove various structured noise components from the raw video. This type of processing, while preliminary to further restorative steps, of itself produces an enhancement which allows analysis of surface detail closer to the resolution limits of the camera system. Techniques for removing noises from video are of widely varying character and in some cases strongly video system and data dependent.

Photometric Distortions

Probably the most variable and complex properties of the various types of image sensors are those affecting the conversion of light intensity to electrical signal amplitude. The discussion here centers on the photometric properties of vidicon systems but is more broadly applicable to other types of sensors. Procedures for correcting for sensitivity non-uniformity, sensitivity non-linearity, and image retentivity as a function of wavelength and temperature have been developed. In a very real sense, each encoded sample or picture element intensity value, in the output image of a camera system, can be thought of as a reading of a tiny photometer with its own unique properties. The overall properties of sensor shading, spectral response, and dynamic range, as well as local blemishes, can be considered, to a good approximation, as a composite of the corresponding properties of many such discrete independent photometers positioned at each sample point of the image.

The correction procedure which is being applied to the Mariner 1969 photographs consists of calibrating each of these photometers and then applying the appropriate linearity or residual correction to the corresponding picture element in the experiment data. The positional and geometric stability of the image raster with time is very important here since as the picture raster is displaced the correspondence between picture elements in the image and physical position on the sensor surface changes. Particularly in areas of rapid spatial variation in photometric response, such as around blemishes or reseaux, a misalignment of this type between calibration and experiment data can cause large correction errors. Calibration is achieved by exposing the sensor to a series of test targets and then extracting the absolute and relative photometric properties of each sensor element from these test images.

Residual Image - The vidicon is a good example of an image sensor exhibiting memory or residual image effects. Each output image is actually a composite of the current exposure and the retained effects of previous exposures. The residual effects of any one exposure die out in time, but the rectification of photometric distortions for a given image requires the consideration of the effects of the immediate exposure history of the sensor. In the Mariner Mars 1969 calibration a very simple model for residual image was used. The net camera output $O_j(x,y)$ for a given exposure j was assumed to be a combination of the output $E_j(x,y)$ which would result if no residual effects were present and a fraction $b(x,y)$ of the previous total camera output,

$$O_j(x,y) = E_j(x,y) + b(x,y)\ O_{j-1}(x,y)$$

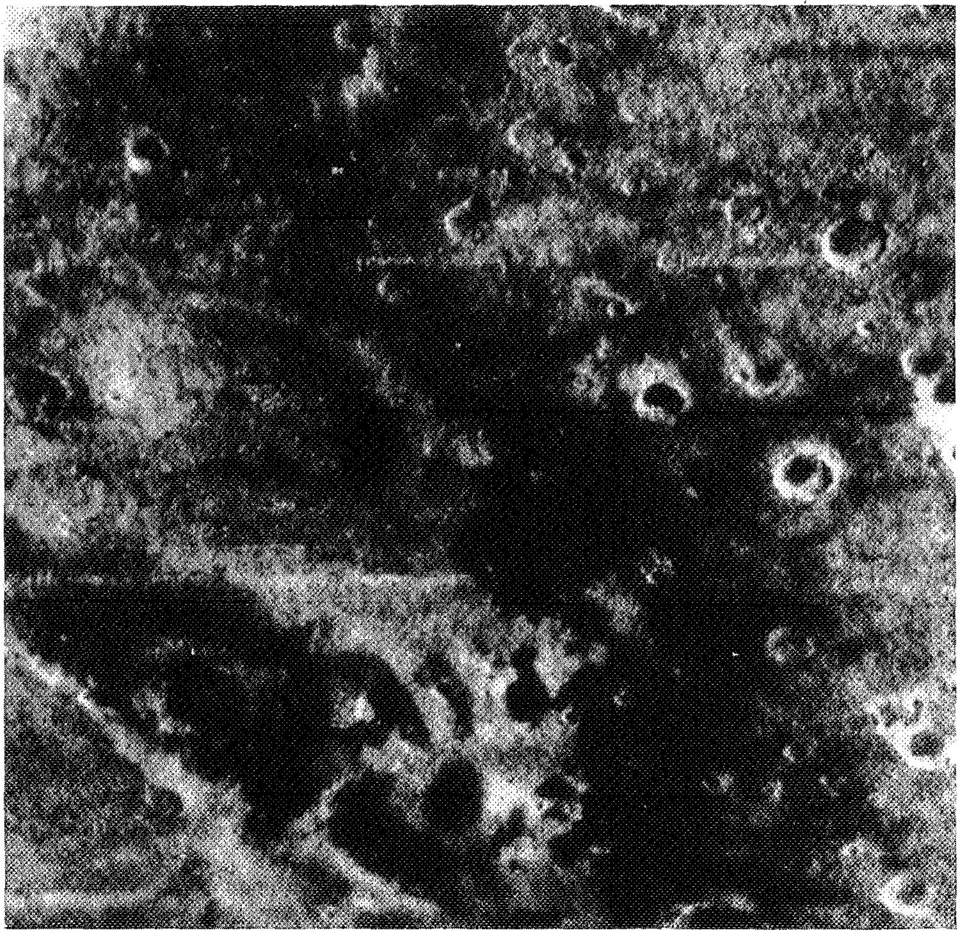

Figure 7.-The result of removing the black and white spike noises from Figure 6. Note in comparison with Figure 3 that objects of considerably higher resolution are discernable in Figure 7.

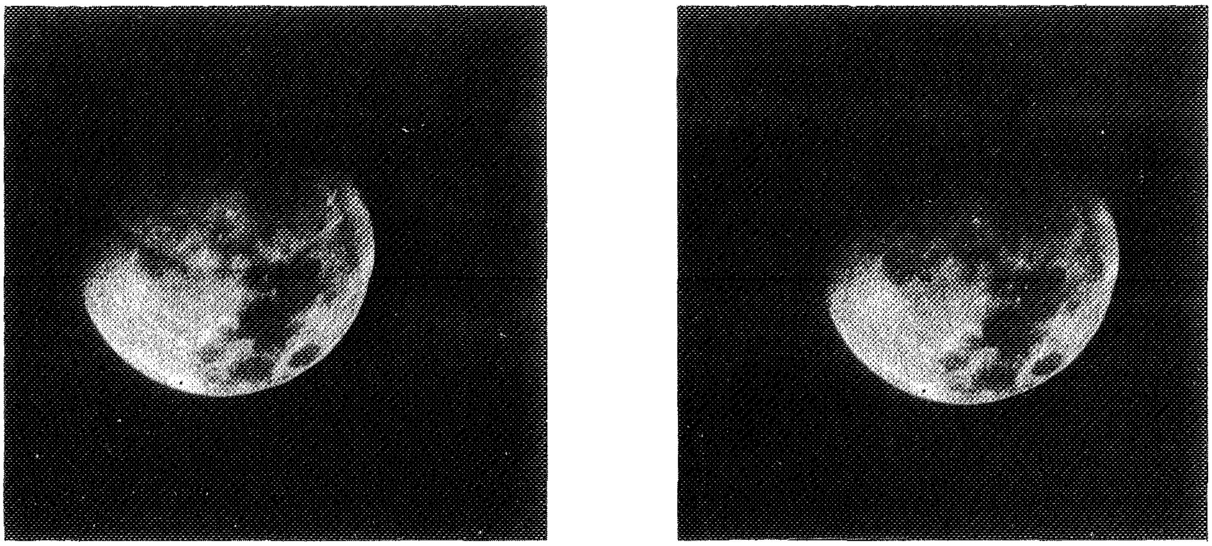

Figure 8.-The left picture is a raw photograph of the moon taken by a Mariner 1969 camera system and illustrates residual image from a prior exposure. The right picture is the result of removing the residual component by a linear combination with the previous exposure.

The residual coefficient, b, was measured as a function of position in the frame by exposing the camera to a gray wedge target constructed to produce varying gray level exposures over each local region of the sensor. The residual image coefficient was then determined by reexposing the target in a slightly displaced position and measuring the remaining gray step transitions from the previous exposure. In this way a residual image coefficient map was constructed as a function of position in the image format and by varying the operating conditions, as a function of temperature.

An example of applying this correction procedure is shown in Figure 8. An image of the moon taken with a Mariner 1969 camera is shown in Figure 8(a) containing a residual of the previous displaced exposure. The result of applying the above correction is shown in Figure 8(b). The residual image has been removed so as not to be visible in the print but a careful investigation shows the correction to be good to only several percent. The model used is only marginally adequate and the residual coefficient exhibits strong intensity dependence. Efforts to improve the technique are under way for the Mariner Mars 1971 mission.

Photometric Linearity - Vidicon systems have limited dynamic ranges and exhibit light transfer curves relating the camera output to input luminance level, similar to H & D curves for film systems. Because of various mechanisms causing nonuniform sensitivity in the tubes (oblique beam landing and blemishes), each point in the tube exhibits a unique light transfer curve. Appropriate curves are generated simultaneously for each point by sequentially exposing the camera to spatially uniform illuminations with varying intensities. Wavelength and tempera-

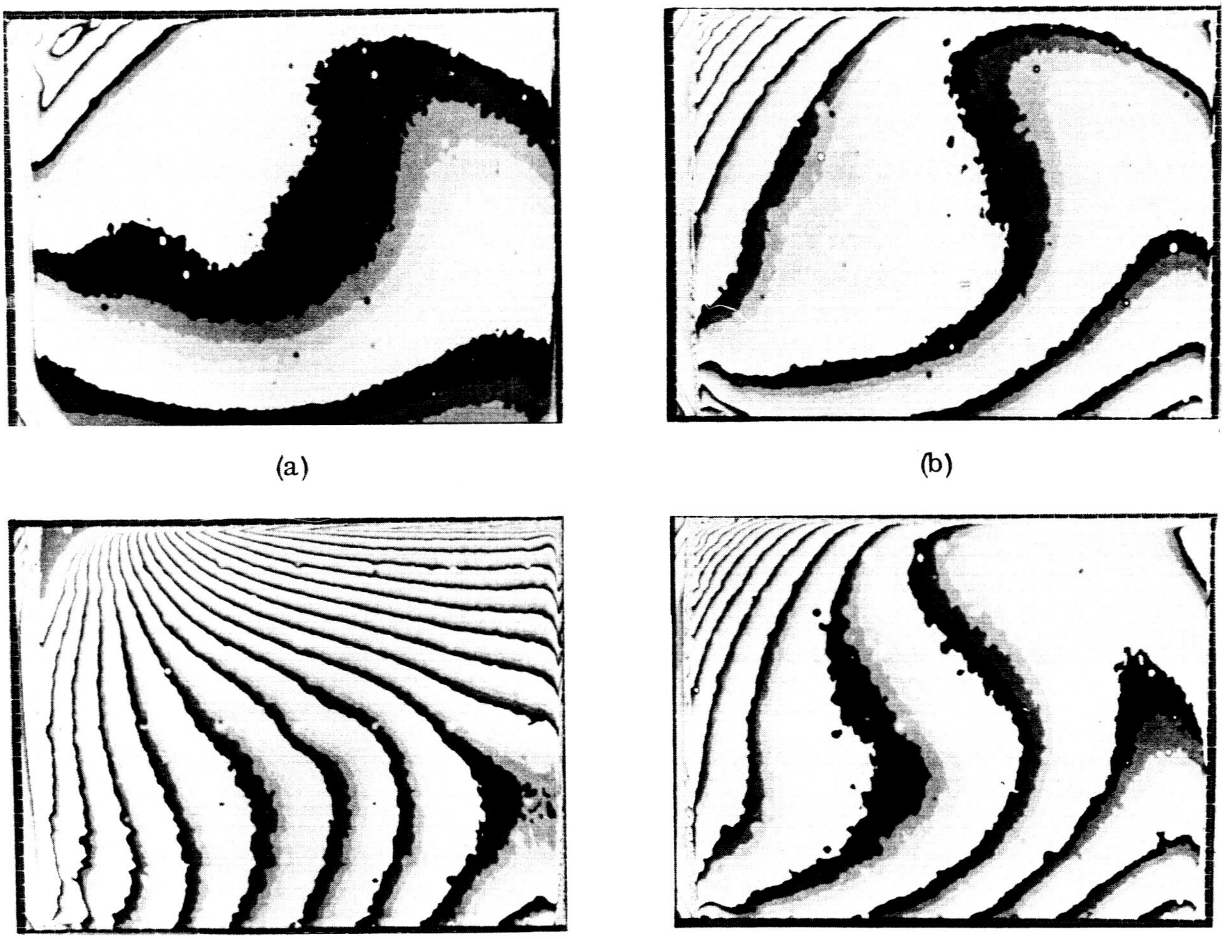

(a)

(b)

(c)

(d)

Figure 9.-A sequence of contoured flat field calibration frames from a Mariner 1969 camera system. Contouring was achieved by suppressing the five most significant bits of eight prior to display. The light levels are (a) 100 Foot-Lamberts, (b) 400 Foot-Lamberts, (c) 800 Foot-Lamberts, and (d) 1600 Foot-Lamberts.

ture dependence is determined by altering the spectral filtering of the light source and the operating temperature. The light transfer curve for each point in the image is stored on magnetic tape and is applied to correct the corresponding element in the actual experiment data. A sufficient number of points on each curve is measured to guarantee that a linearly interpolated correction produces adequate accuracy.

Contoured examples of four such flat field exposures are shown in Figures 9(a) through 9(d). The contours were generated by removing the five most significant bits from the eight bit calibration data thereby producing a "saw tooth" effect in the image display. The changing shapes of the contours with changing light levels is apparent and indicates a strong spatial dependence of the sensor light transfer properties. The presence of isolated blemishes and reseaux is also apparent.

Geometric Distortions

Geometric distortions in the output of an electronic imaging system arise in many ways and must be removed in order to measure the geometric shapes and relationships between objects in the scene, as well as to properly align calibration data with experiment data. This latter consideration is important, for example, in the alignment of photometric sensitivity data taken prior to flight with the data returned by a space mission, since a raster shift is typical once the device is removed from the earth's magnetic field. In Mariner class systems, shifts of the order of five to ten picture elements are common. In addition, small shifts from frame to frame due to electronic sweep variations can also occur.

The major sources of distortion in vidicon systems, apart from foreshortening due to oblique photography, are optical distortions, electronic raster sweep distortions, and raster shifts due to changes in the magnetic environment. A negligible effect in vidicon systems is mentioned only because it is important in other types of sensors and represents an interesting problem. This effect is called "beam bending" and arises because as the sensor charge image is read out and discharged small tangential electric fields are set up on the tube target which are a function of the recorded image intensity. These fields can cause a corresponding displacement of the readout electron beam, particularly for low energy electrons, and introduce an image dependent geometric distortion.

For the Mariner television experiment, the optical and electronic geometric distortions are characterized by measuring separately the overall system distortions and the frame to frame electronic distortion fluctuations. The system distortions are determined by measuring the relative displacements of the intersections of a precise grid target after being photographed by the system. The electronic distortions are determined by measuring the relative displacements of the images of reseaux in a pattern permanently deposited on the sensor tube target. This reseau pattern allows the frame to frame tracking of electronic changes. The corresponding stability problem in the case of optical distortions does not exist typically.

The correction for geometric distortions is then performed in two steps. Since the reseau pattern is permanently affixed to the tube and since the reseaux must not obscure a sizable portion of the image area, they are typically too sparse to determine, in detail, the electronic geometric distortions. The frame to frame electronic shifts as well as the shifts due to magnetic environment changes are, however, typically small and are largely simple translations in the raster. Thus, the reseaux are used to apply a small and largely homogeneous correction on a per frame basis to align the reseaux of a particular frame with those in the calibration grid target frame. The more detailed and precise system distortion correction is then applied to the result. Partially successful attempts have been made to automate, in the computer, the reseau detection and measurement procedure, on a per frame basis, to accommodate the overall correction process.

The actual application of the geometric distortion correction to the raw sampled output of the camera is conceptually the superposition of a new, non-uniform set of sample points on the raw data. The positions and local spacings of the new sample points are determined by linearly interpolating the distortion data derived from the calibration frames. Clearly the locations of the new sample points will not be commensurate with the uniform sampling of the raw camera output so that interpolation of the intensity data is required to determine the intensity values at the new sample locations. If the raw image was not Nyquist sampled, this interpolation process can severely degrade the corrected image resolution.

The result of photographing a grid target with a Mariner 1969 camera is shown in Figure 10(a). A significant pin-cushion distortion is evident. The result of applying the above correction is shown in Figure 10(b). The location corrections for points between the various grid target intersections were determined by linear interpolation.

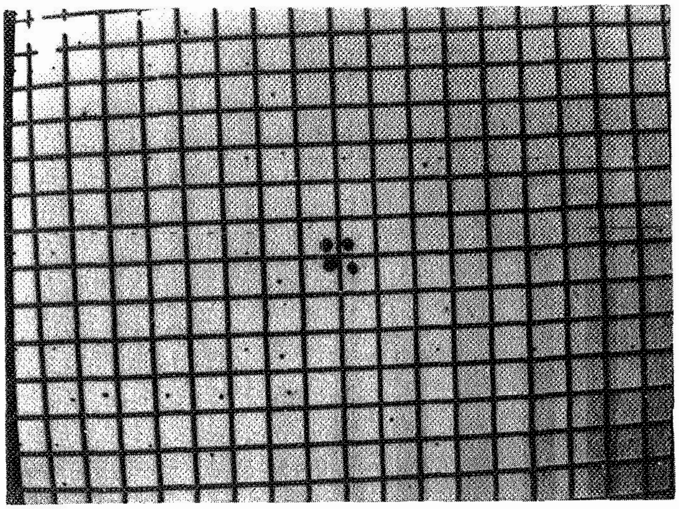

(a)

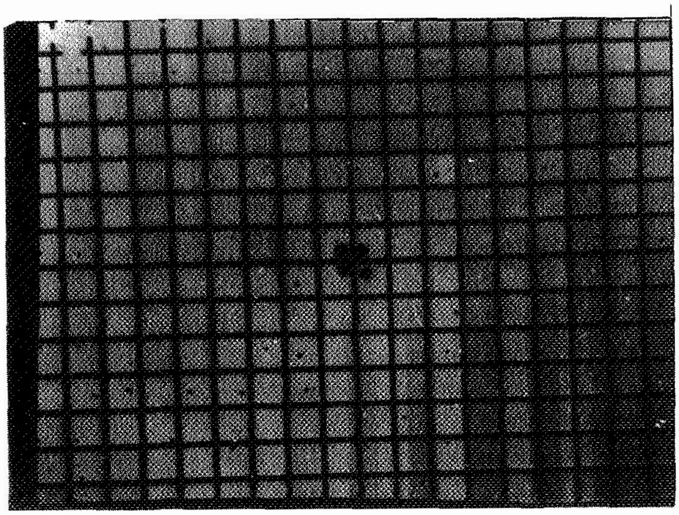

(b)

Figure 10.-Grid patterns. (a) Grid pattern photographed through a Mariner 1969 camera system exhibiting barrel distortion. (b) Result of computer correction of the distorted target.

Resolution Enhancement

The scale size of object scene detail visible through a television camera is limited, in a perfect system, by diffraction effects in the optics. This, of course, ignores the effects of atmospheric turbulence. For most systems this limit is not realized as the camera sensor system itself imposes resolution limitations which are dominant. In any case, the result is an apparent loss of contrast in small scene detail (small relative to the resolution of the system) or equivalently a broadening of the transitions between adjacent intensities in the camera output. These effects influence not only the visibility of scene detail for photointerpretive purposes but also photometric measurement accuracy on small detail.

If the camera system is linear or if the input scene is sufficiently low in contrast, the degradation in image resolution is describable in terms of an amplitude independent system point spread function. If the point spread function is furthermore independent of position in the image plane, such as for narrow angle systems, then the camera output, $O(x,y)$, can be written in terms of the object scene intensity distribution, $I(x,y)$, and the system point spread function, $S(x,y)$, by a simple convolution relation

$$O(x,y) = \int du \int dv \quad I(x+u,y+v) \; S(u,v)$$

This relation can be inverted using Fourier transformations to express the desired input scene in terms of the camera output

$$I(x,y) = \int du \int dv \quad O(x+u,y+v) \; F(u,v)$$

$F(x,y)$ is a correction filter related to the point spread function through the relation

$$F(x,y) = \mathfrak{F}^{-1}\left[\frac{1}{\mathfrak{F}\left[S(x,y)\right]^{*}}\right]$$

where $\mathfrak{F}[\;]$ is the Fourier transform operator.

This sequence of equations has a discrete counterpart appropriate to digital computation. The additional condition of Nyquist sampling must be imposed in the discrete case for validity.

The correction filter function F is a function only of the uniform camera point spread function and thus may be calibrated independently of the object scene. This is done for the Mariner 1969 experiment by measuring the modulation transfer function (MTF) or the Fourier transform of the point spread function rather than the point spread function directly. The reason is that for vidicon systems, in order to produce a sufficient output point spread amplitude to make reliable measurements for all spatial frequencies, the input must be so large as to drive the system into non-linear response. The MTF is measured by exposing the camera to spatial sine wave transmittance targets of various frequencies and orientations and extracting the sine wave amplitude degradation along the line scan and perpendicular to the line scan directions. These curves are then used to model the two-dimensional MTF function by assuming the contours of equal response are ellipses. The phase component of the MTF is ignored, not so much as justified as because the measurement of phase properties has not been possible. The resulting MTF is then used to generate the correction filter.

The correction filter is theoretically the reciprocal of the MTF function. For typical systems however, the response at high spatial frequencies becomes quite low so that gains in excess of ten at these frequencies are necessary. The addition of wideband noises within the system make this theoretical correction undesirable. Since the scene spectral components decrease in amplitude at high frequencies and add coherently and since the noise is essentially white and adds incoherently, any filter correction degrades the gross signal-to-noise ratio of the resulting image. Thus some criterion for suppressing the large high spatial frequency gains is necessary based on the competition between small feature and edge transition fidelity and degraded signal-to-noise ratio.

There are quantitative criteria for this trade-off and correction filter generation such as the Wiener-Hopf filtering technique. For many purposes,however, these are unacceptable since they are based on large scale statistical measures of error and in the small, produce less than optimum results. Adaptive filtering approaches, based on both large scale and small scale fidelity, are most desirable but are expensive in terms of computer time. Continued development in this area is under way.

For many purposes a simple trial and error solution to the problem is adequate. In Figure 11 a typical MTF curve is shown and labelled A . The theoretical correction filter based on this MTF is shown as curve B . By introducing an artificial truncation to the theoretical curve, such as shown in the dashed curves labelled C , the emphasis of high spatial frequency noise amplification can be controlled. A filter or series of filters consistent with the camera signal-to-noise properties, the typical scene spectral composition, and experiment measurement goals can be derived.

Examples of applying this type of truncated MTF correction to a Mariner Mars 1971 test scene are shown in Figures 12 through 14. The raw camera output is shown in Figure 12 and the results of resolution enhancements with gain truncations at 2.5 and 10.0 respectively, are shown in Figures 13 and 14. A comparison of these results show the most subjective improvement between Figure 12 and 13 with a slight additional sharpening in Figure 14 but a more significant increase in noise levels.

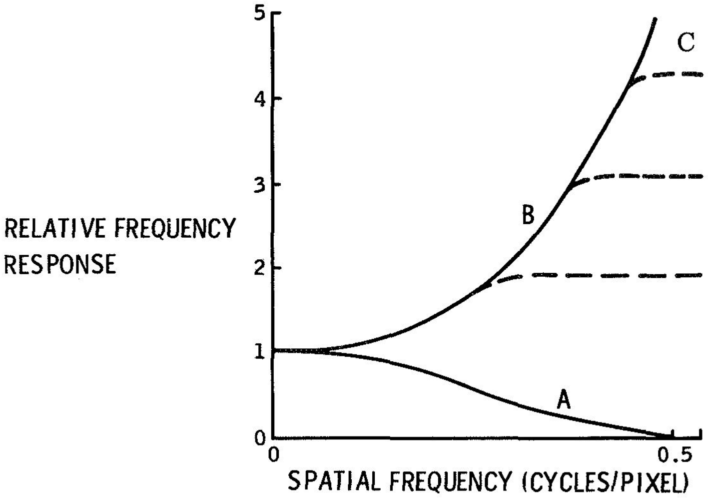

Figure 11.- Modulation transfer function and correction filter spectra. Curve A shows a typical modulation transfer function (MTF) for a vidicon system. Curve B shows the theoretical reciprocal correction filter function. Curves C (dashed) show various gain truncations of the theoretical correction curve used to minimize the signal-to-noise degradation caused by the enhancement process.

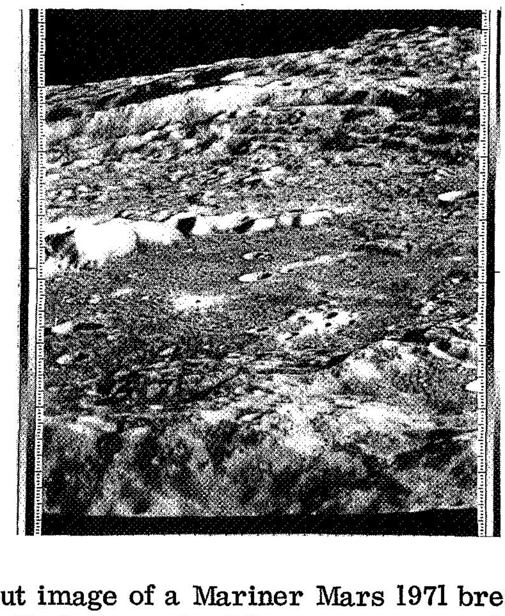

Figure 12. -Raw output image of a Mariner Mars 1971 breadboard television camera An Apollo 11 photograph of the moon was used as the test target.

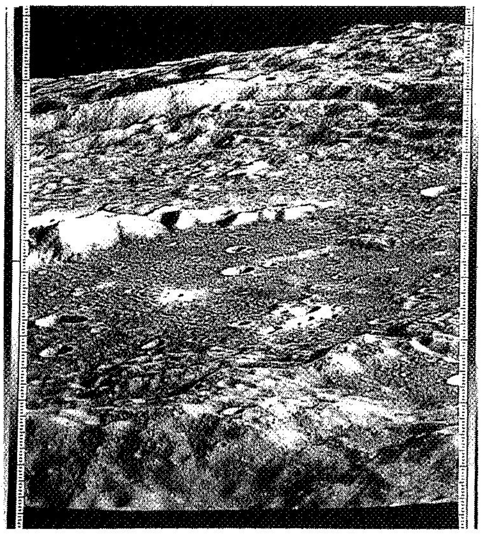

Figure 13. - High spatial frequency enhanced version of Figure 12 with a gain truncation of the correction filter spectrum at 2.5.

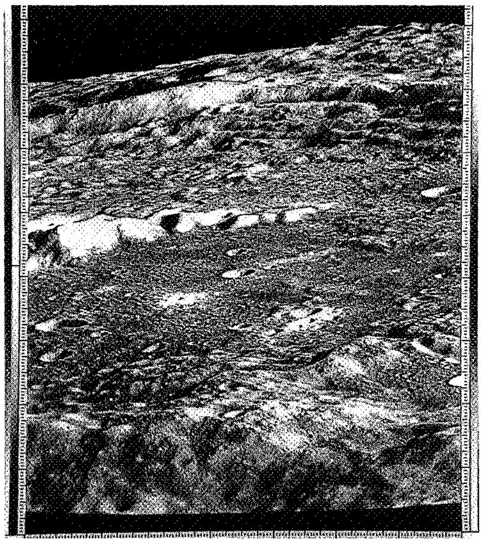

Figure 14. - High spatial frequency enhanced version of Figure 12 with a gain truncation of the correction filter spectrum at 10.0.

These corrections were applied as convolution filters with the kernels generated from the reciprocal MTF function rather than as direct frequency space filters. The reason is strictly one of economy. The convolution kernel matrix for these corrections needs be only on the order of 15 picture elements square and increased calculation speed is realized by matrix convolution rather than transformation. This trade-off is, of course, machine dependent. An example of the opposite trade-off is that of the previously discussed periodic noise filtering. In order to obtain sufficiently narrow frequency space bandpass characteristics, the convolution kernel would be prohibitively large thereby making direct transform space filtering the more economical approach.

Conclusion

The inherent physical limitations in camera system and sensor capabilities introduce significant distortions into the imagery which is recorded. Careful measurements on such imagery must take these effects into account. The digital computer is an extremely useful tool for this purpose offering precision and flexibility to solve non-linear as well as linear distortion problems in a highly controlled and reproducible manner. Techniques have been demonstrated and continue to be improved for the correction of camera system noise, photometric, geometric and resolution distortions. The application of digital image processing techniques makes possible quantitative scientific investigations using television imagery which would not be possible otherwise.

ACKNOWLEDGMENT

This work is the result of the collective contributions of many people, in addition to the author, in the areas of algorithm design, software development and applications, and hardware system development. Principally these people include F. Billingsley, R. Brandt, Dr. J. Dunne, H. Frieden, E. Johnson, Dr. R. Nathan, and W. Stromberg.

REFERENCES

1. Billingsley, F.C., "A Digital Image Processing Rationale," Journal of the Association for the Advancement of Medical Instrumentation, Vol. 3, No. 1, January 1969.

2. Nathan, R., "Digital Video-Data Handling," JPL TR 32-877, January 5, 1966.

IMAGE RESTORATION TECHNIQUES APPLIED TO ASTRONOMICAL PHOTOGRAPHY*

B.L. McGlamery
Visibility Laboratory
Scripps Institution of Oceanography
University of California, San Diego, California

INTRODUCTION

This paper deals with image processing techniques which can be used to process astronomical images whose principal degradation is caused by atmospheric turbulence. The purpose of the processing is to extract information from the degraded image or images which cannot be extracted by the unaided human visual system.

Previous results have demonstrated the feasibility of improving turbulence degraded images. An earlier paper (1) demonstrated the digital restoration of a short time exposure (5 milliseconds) image severely degraded by laboratory generated turbulence. In that experiment the complex optical transfer function, which specifies both amplitude attenuation and phase shift of the spatial frequencies, was obtained by photographing a reference point source placed near the object. Harris (2) has reported the improvement of a long time exposure (2 minutes) image in which the image was digitally restored by means of an analytic modulation transfer function which corrected only the attenuation of the spatial frequencies and did not correct for phase shifts. The phase shift correction was left to the effect of time averaging. A similar experiment using an analog method of processing has also been reported (3).

In many cases of practical interest the complex optical transfer function associated with a single image will not be available, nor will the time averaged phase shifts for a single image be negligible at all spatial frequencies of interest. Hence, methods of restoration other than those described above must be utilized. This paper will describe two such methods based on averaging techniques applied to multiple degraded images. The first method consists essentially of averaging the irradiance values of m images to decrease the phase shifts

---

* This paper was prepared under the sponsorship of the Advanced Research Projects Agency, ARPA order No. 1062, and was monitored by H. D. Newby, ETELE, Patrick AFB, Florida, under Contract No. F08606-68-C-0017.

associated with the resulting averaged optical transfer function. This method is of interest because it is easily implemented and is often suggested as a suitable means of processing. The addition of m images, each recorded over a period of T, is basically equivalent to averaging an image over a time of mT. Several investigators (4), (5), (6) have developed relationships between the physical properties of the atmosphere and the ensemble averaged optical transfer function, which has a zero phase component for isotropic turbulence. However, the length of time for a time averaged optical transfer function to approach the ensemble averaged optical transfer function has not been considered. This is an important question from the standpoint of image restoration and will be considered in this paper. The second method of processing is a method based on the averaging of the amplitude and phases of the Fourier transforms of the m degraded images. These two methods will be compared both theoretically and experimentally.

BASIC CONCEPTS

Assumptions

The following basic assumptions are used:

1) The object is invariant so that the differences between the multiple images are due only to the random changes of the turbulence.
2) The object is incoherently illuminated.
3) The degraded images are isoplanatic, which means that within a single image the point spread function is invariant over the image. This condition is necessary if Fourier techniques are to be utilized.
4) The turbulence is statistically stationary over the time the images are recorded.

Definitions and Notation

The undegraded image is the irradiance map of the geometrical optics image formed in the image plane of the optical system in the absence of turbulence. The degraded image is the irradiance map of the actual image in the presence of turbulence. The degraded image can be mathematically expressed as the convolution of the undegraded image and the point spread function associated with the combined effects of the turbulence and optical system. The Fourier transform of the point spread function is the optical transfer function. Let

$U(x,y)$ = the undegraded image irradiance map
$S_j(x,y)$ = the jth point spread function irradiance map
$D_j(x,y)$ = the jth degraded image irradiance map

A tilde ($\sim$) will be used to represent the Fourier transform, and (u,v) will be the transform or frequency domain coordinates. Thus

$\tilde{U}(u,v)$ = Fourier transform of $U(x,y)$
$\tilde{S}_j(u,v)$ = Fourier transform of $S_j(x,y)$
$\tilde{D}_j(u,v)$ = Fourier transform of $D_j(x,y)$

The Fourier transform is a complex quantity with amplitude, or modulus, of A and phase of φ. The subscripts U, S, and D will be used on A and φ to denote the image with which A and φ are associated. Expressing $\tilde{U}(u,v)$, $\tilde{S}_j(u,v)$, and $\tilde{D}_j(u,v)$ in terms of amplitude and phase gives

$$\tilde{U}(u,v) = A_U(u,v)\ e^{i\varphi_U(u,v)} \tag{1}$$

$$\tilde{S}_j(u,v) = A_{Sj}(u,v)\ e^{i\varphi_{Sj}(u,v)} \tag{2}$$

$$\tilde{D}_j(u,v) = A_{Dj}(u,v)\ e^{i\varphi_{Dj}(u,v)} \tag{3}$$

Now $D_j(x,y)$ is the convolution of $U(x,y)$ and $S_j(x,y)$,

$$D_j(x,y) = U(x,y) * S_j(x,y) \tag{4}$$

so that in the transform domain

$$\tilde{D}_j(u,v) = \tilde{U}(u,v)\ \tilde{S}_j(u,v) \tag{5}$$

In the amplitude and phase form Eq. 5 becomes

$$A_{Dj}(u,v)\ e^{i\varphi_{Dj}(u,v)} = A_U(u,v)\ A_{Sj}(u,v)\ e^{i\left[\varphi_U(u,v)\ +\ \varphi_{Sj}(u,v)\right]} \tag{6}$$

so that

$$\varphi_{Dj}(u,v) = \varphi_U(u,v) + \varphi_{Sj}(u,v) \tag{7}$$

$$A_{Dj}(u,v) = A_U(u,v)\ A_{Sj}(u,v) \tag{8}$$

The quantities $\varphi_{Sj}(u,v)$ and $A_{Sj}(u,v)$ are, respectively, the phase transfer function and modulation transfer function associated with the effect of the turbulence and optical system on the image. Together they constitute the optical transfer function. Because of the stochastic nature of the turbulence, $\varphi_{Sj}(u,v)$ and $A_{Sj}(u,v)$ are random variables as a function of j. In general the statistical properties of $\varphi_{Sj}(u,v)$ and $A_{Sj}(u,v)$ will vary as a function of the spatial frequency coordinates (u,v), since both phase shifts and amplitude attenuations increase with increasing spatial frequency. In this paper the averaging processes to be considered are done on each individual frequency, independent of other frequencies. Therefore the (u,v) functional relationships on all quantities will be dropped for notational simplification. It should be remembered, however, that all quantities discussed are functions of (u,v).

Since φ_{Sj} and A_{Sj} are random variables, φ_{Dj} and A_{Dj} are also random variables. The statistical properties of these parameters are of great interest. The following conventions for defining these statistical parameters will be used. The probability density function (PDF) of a variable x will be denoted by f(x). The statistical parameters will be assumed to be constant for all values of j. For example, the PDF of φ_{Dj} is denoted by $f(\varphi_D)$. For phase PDF's, means will be denoted by μ and standard deviations by σ. For amplitude PDF's, means will be denoted by ρ and standard deviations by α. Subscripts will be added to μ, σ, ρ, and α to indicate the associated parameter.

Statistical Properties

Little experimental data on the statistical properties of φ_S and A_S exist, but some reasonable assumptions can be made. The phase shift due to turbulence can have both positive and negative values and we assume that $f(\varphi_S)$ is Gaussian with a mean and standard deviation of μ_S and σ_S. Then, from Eq. 7, it follows that $f(\varphi_D)$ is also Gaussian with mean, μ_D, and standard deviation, σ_D, given by

$$\mu_D = \varphi_U + \mu_S \tag{9}$$

$$\sigma_D = \sigma_S \tag{10}$$

The values of A_S, which specify the attenuation of spatial frequencies, usually lie between unity and zero. Only in cases of extreme scintillation will A_S exceed unity. Assuming A_S always lies between unity and zero, then $f(A_S)$ must be non-Gaussian and in general can be expected to be non-symmetrical. The mean and standard deviation of $f(A_S)$ are defined as ρ_S and α_S, respectively. From Eq. 8 it follows that $f(A_D)$ has the same shape as $f(A_S)$ and a mean, ρ_D, and standard deviation, α_D, of

$$\rho_D = A_U \rho_S \tag{11}$$

$$\alpha_D = A_U \alpha_S \tag{12}$$

Restoration

Now, given m images from which m values of φ_{Dj} and A_{Dj} are computed at each spatial frequency, we wish to obtain good estimates of φ_U and A_U by some averaging process.

From Eqs. 9 and 11 we obtain

$$\varphi_U = \mu_D - \mu_S \tag{13}$$

$$A_U = \rho_D/\rho_S \tag{14}$$

In many applications both μ_S and ρ_S can be found from measurements on images of a known reference object, such as a star. Such images can be recorded independentl of the degraded images being processed if the statistical properties of the turbulence are the same for the two sets of images. For isotropic turbulence no measurement of μ_S is necessary since it is equal to zero. If μ_S and ρ_S are known, and if good estimates of μ_D and ρ_D can be made from the m degraded images, then from Eq. 12 and 13 good estimates of φ_U and A_U can be obtained and the image can

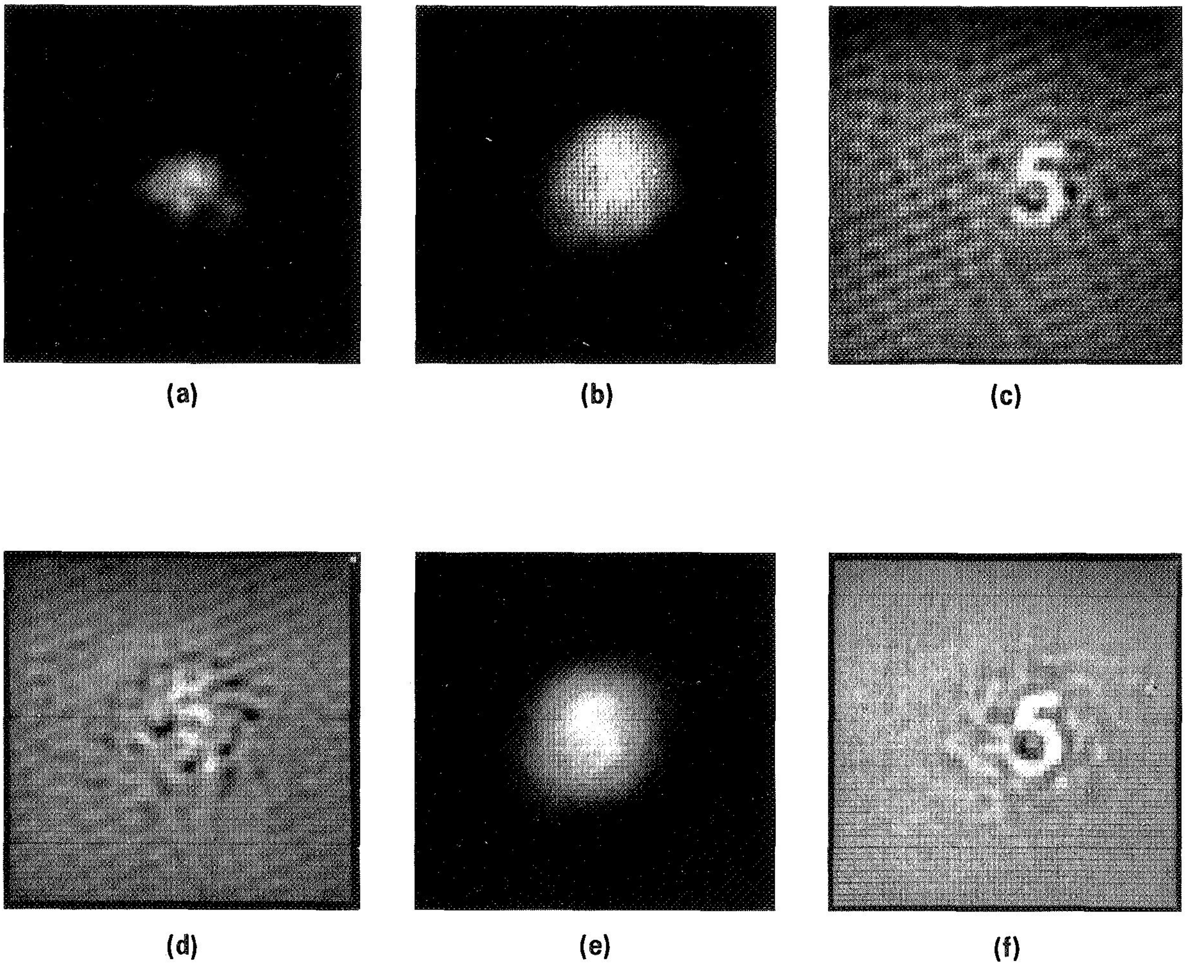

(a) (b) (c)

(d) (e) (f)

Figure 1.-Relative importance of amplitude and phase corrections. (a) Turbulence point spread function. (b) Degraded image. (c) Restoration of (b) using complex optical transfer function from (a). (d) Restoration using only modulus of OTF for correction. (e) Restoration using only phases of OTF for correction. (f) Image (e) Corrected with an analytic modulation transfer function.

be restored. The error involved in the estimate is a function of m, σ_S, α_S, and the method of estimation.

Relative Importance of Amplitude and Phase

While the degraded image must be corrected for both amplitude attenuations and phase shifts, experiments have shown that correction of the phase shifts presents the most difficult problem. This is illustrated in Fig. 1 for an image degraded by laboratory turbulence. Here it is shown that if the phase shifts are corrected then the amplitudes can be sufficiently corrected by use of an

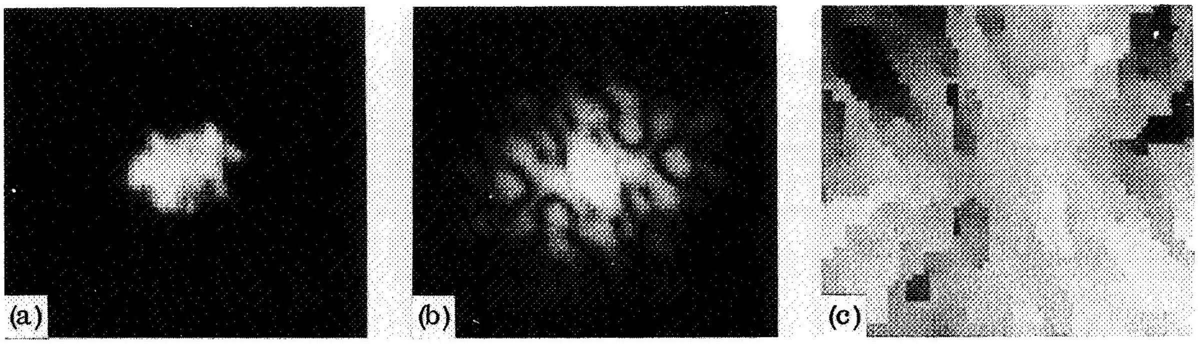

Figure 2. - Star image and its associated spectrums. (a) A Star image degraded by atmospheric turbulence photographed with the USAF Cloudcroft 48 in. diameter telescope, 1/60 second exposure time, by E. Tyson. The digitized picture element size is 0.23 arc seconds. (b) Modulus of the Fourier transform of (a). (c) Phase of the Fourier transform. Zero phase is midway in the brightness range.

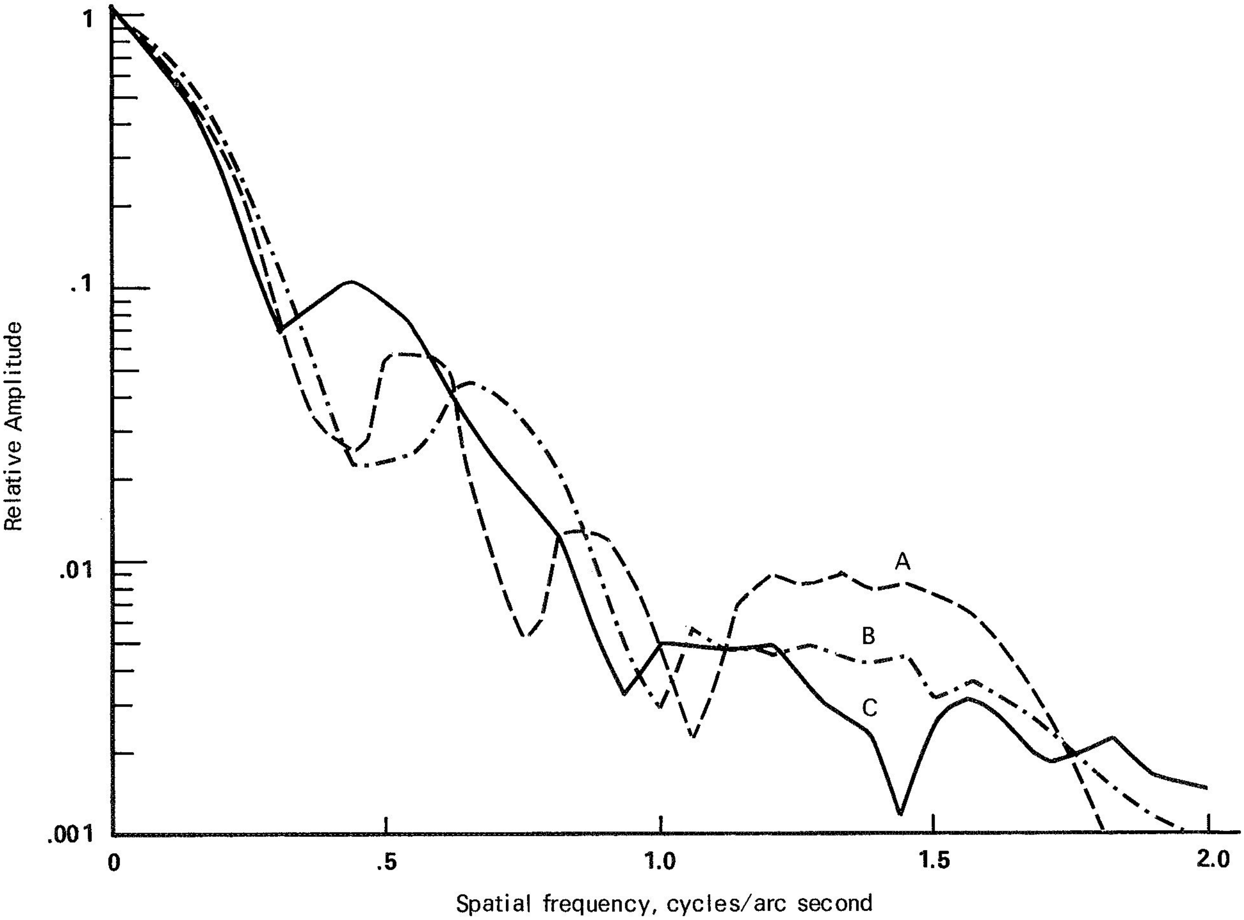

Figure 3. - Moduli of turbulence optical transfer functions. Curve A is a plot of the moduli along the center column from the center to the top of the modulus spectrum shown in Fig. 2. Curves B and C correspond to photographs of the same star taken a few moments later.

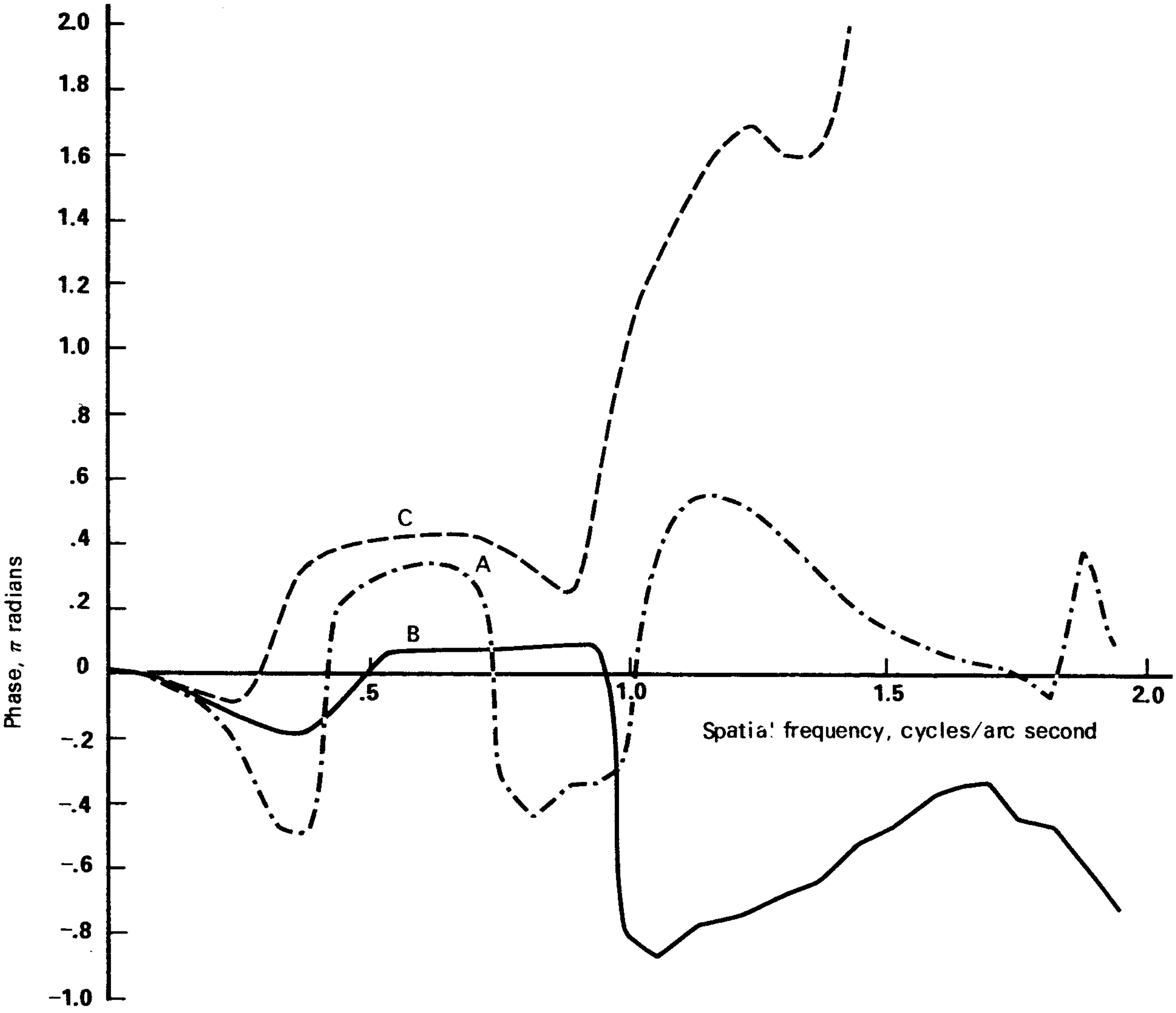

Figure 4.-Phases of turbulence optical transfer functions. Curve A is a plot of the phases along the center column from the center to the top of the phase spectrum shown in Fig. 2. Curves B and C correspond to photographs of the same star taken a few moments later.

analytic function chosen on a trial and error basis. However, if the amplitudes are corrected but significant phase shifts remain, the resulting image gives little indication as to the phase changes that are needed to correct the image. Figures 2 to 4 suggest the reason for this. Figure 2 shows a star image and its associated two dimensional amplitude and phase spectrums. Figures 3 and 4 show cross sectional plots of amplitude and phase for this star image and for two other images recorded moments later. The amplitude attenuations tend to monotonically decrease with frequency. However, the phases vary widely and often change sign. Thus, even for a single short exposure image the amplitudes can be reasonably corrected by choice of a proper analytic function but the phases cannot. Hence, the major emphasis in this paper will be on analyzing the effectiveness of the averaging techniques in restoring the phases of the spatial frequencies.

IMAGE IRRADIANCE AVERAGING

The Method

Beginning with m degraded images, the image irradiance averaging process is defined to consist of the following steps. Any necessary gray scale and geometric distortion corrections are made to each image. The images are registered by some means, such as superimposing centers of gravity, to eliminate gross image shifts. The average degraded image $\bar{D}(x,y)$ is computed from

$$\bar{D}(x,y) = \frac{1}{m} \sum_{j=1}^{m} D_j(x,y) \qquad (15)$$

The Fourier transform of $\bar{D}(x,y)$ is computed and is divided by an optical transfer function which corrects for the time averaged attenuation of the amplitudes and any average phase shifts due to statistically non-isotropic turbulence. For convenience we assume the turbulence is statistically isotropic so that the average phases do not require correction. After appropriate attenuation of those frequencies which are sensor noise dominated, the inverse transform is taken to produce the restored image.

Analysis of Method

We evaluate this method by considering the PDF of the amplitude and phases associated with the averaged image. The j th image can be expressed in terms of its Fourier transform $\tilde{D}_j(u,v)$ as

$$D_j(x,y) = \int_{-\infty}^{\infty}\int_{\infty}^{\infty} \tilde{D}_j(u,v)\, e^{-2\pi i(ux + vy)} du\, dv \qquad (16)$$

Using this expression for $D_j(x,y)$ in Eq. 15 and interchanging the order of the sum and integral gives

$$D(x,y) = \int_{-\infty}^{\infty}\int_{\infty}^{\infty} \left[\frac{1}{m} \sum_{j=1}^{M} \tilde{D}_j(u,v)\right] e^{-2\pi i(ux + vy)} du\, dv \qquad (17)$$

Equation 17 shows that averaging the irradiance values in the spatial domain is equivalent to averaging the complex Fourier coefficients in the frequency domain. We define the average of the Fourier coefficients as $\tilde{R}(u,v)$,

$$\tilde{R}(u,v) = \frac{1}{m} \sum_{j=1}^{M} \tilde{D}_j(u,v) \qquad (18)$$

The amplitude and phase of $\tilde{R}$ are A_R and φ_R.

Apart from the factor of $1/m$, $\tilde{R}$ is simply a sum of m vectors, each vector having the PDF associated with a single image. Considering only the problem of the restoration of phase, the effectiveness of the image irradiance method can be evaluated by considering the effectiveness of the sum m random vectors in estimating the mean phase of the probability density function of those phases. To make this evaluation, the PDF for $\tilde{R}$, $f(\tilde{R})$, is needed. Given the PDF for $\tilde{D}$, $f(\tilde{D})$, $f(\tilde{R})$ can be found by convolving $f(\tilde{D})$ with itself m times (7). Solution of the problem using this approach is difficult both theoretically and numerically. However, an approximate solution of sufficient accuracy is available. Before this solution is introduced, however, discussion of a simple example will be instructive.

Consider the sum of vectors with unity amplitude and phases having a Gaussian PDF. Such a distribution can have phases which lie outside of the 2π interval. For images degraded by atmospheric turbulence, phases ranging over an interval greater than 2π are physically justified. For example, suppose the degraded image could be viewed through a device which displayed a single sinusoidal component of the image so that one could see the wave pattern shift continuously as a function of time as a result of the changing turbulence. For sufficiently strong turbulence, excursions of a crest of this wave larger than a 2π interval is intuitively possible. For the vector representing this wave, a phase PDF extending beyond a 2π interval is feasible. However, for the purposes of vector addition only the principal value of phase is of interest. Therefore, a PDF constrained to a 2π interval is needed. Let $f(\varphi)$ be a Gaussian PDF and $f'(\varphi)$ be the associated constrained function. The constrained function is found by sliding all probability density which lies outside of the 2π interval into the interval and adding the displaced probability density to the density already within the interval. For a $-\pi$ to $+\pi$ interval this operation is described by

$$f'(\varphi) = \sum_{k=-\infty}^{\infty} f(\varphi + 2\pi k), \quad -\pi \le \varphi \le \pi \tag{19}$$

Figure 5 shows a comparison of $f(\varphi)$ and $f'(\varphi)$ for standard deviations of $\sigma = \pi/4$, $\pi/2$, and π. As σ is increased $f'(\varphi)$ begins to level out and is nearly flat at $\sigma = \pi$. A perfectly flat distribution corresponds to a random vector with a uniform phase distribution. A sum of vectors having a uniform phase distribution never has any preferred direction. Thus, as σ approaches π and higher values, the method of image irradiance averaging can be expected to be an ineffective method of estimating the no-turbulence phase.

An analytical solution to the problem of finding the PDF for the sum of m vectors can be found by using an approximation method given by Beckman (8). This method is based on the assumption that for sufficiently large m the sum of the X components and the sum of the Y components of the m vectors can be assumed to have Gaussian PDF's, $f(X)$ and $f(Y)$, by virtue of the Central Limit Theorem. Let the mean and variance of $f(X)$ be defined as a and v_1, and the mean and variance of $f(Y)$ be defined as b and v_2 so that

$$f(X) = \frac{1}{\sqrt{2\pi\, v_1}}\, e^{-\frac{(X-a)^2}{2v_1}} \tag{20}$$

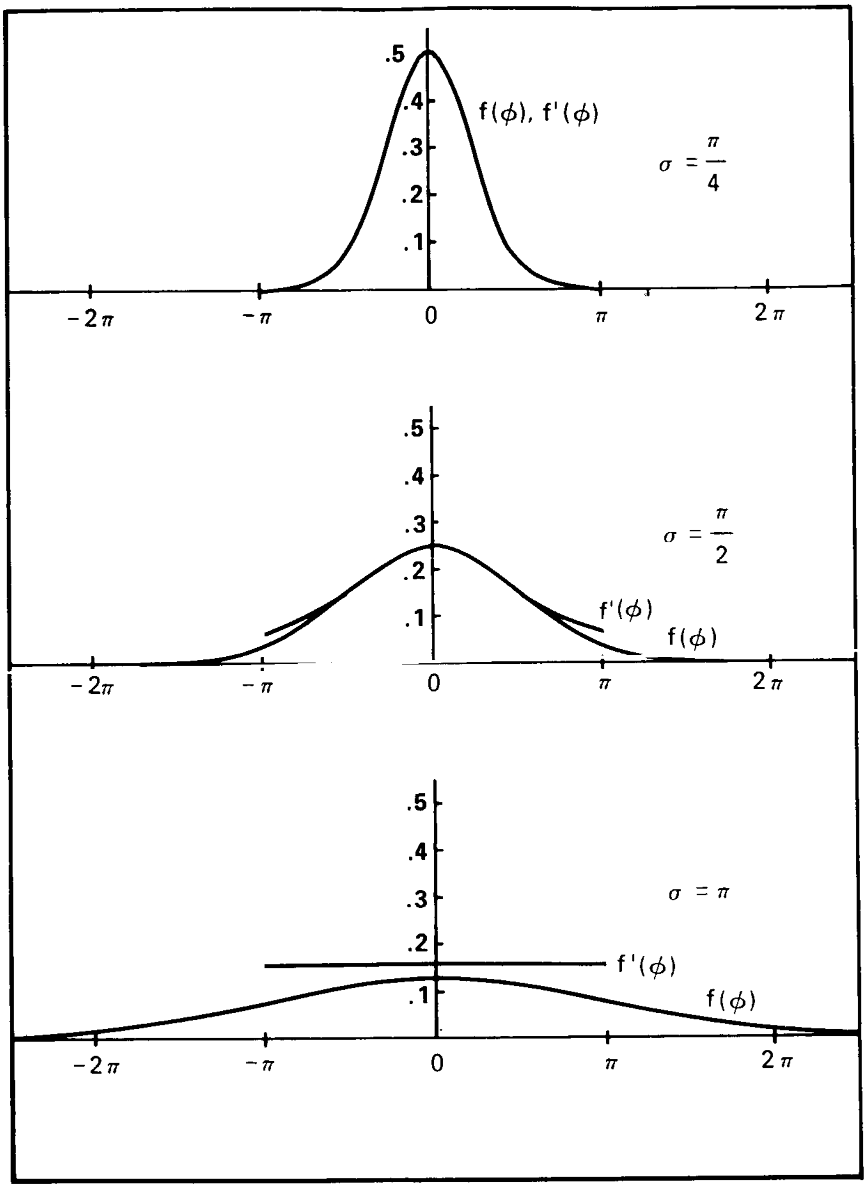

Figure 5. -Gaussian probability density functions, f(Φ), and the same functions constrained to the $-\pi$ to $+\pi$ interval.

$$f(Y) = \frac{1}{\sqrt{2\pi \, v_2}} \, e^{-\frac{(Y-b)^2}{2v_2}} \tag{21}$$

The parameters a, v_1, b, and v_2 are computed from a knowledge of $f(\tilde{D})$. Knowing f(X) and f(Y), $f(\tilde{R})$ can be formed from

$$f(\tilde{R}) = f(X,Y) = f(X)\, f(Y) \tag{22}$$

and the PDF in polar coordinates, $f(A_R, \varphi_R)$, is given by the transformation

$$f(A_R, \varphi_R) = A_R\, f(X)\, f(Y) \tag{23}$$

Substituting Eqs. 20 and 21 for f(X) and f(Y) into Eq. 23 and transforming X and Y according to $X = A_R \cos \varphi_R$ and $Y = A_R \sin \varphi_R$, $f(A_R, \varphi_R)$ can be expressed by

$$f(A_R, \varphi_R) = \frac{A_R}{2\pi\sqrt{v_1 v_2}} \exp\left[- \frac{(A_R \cos\varphi_R - a)^2}{2v_1} - \frac{(A_R \sin\varphi_R - b)^2}{2v_2} \right] \tag{24}$$

By integrating Eq. 24 over A_R from zero to infinity, $f(\varphi_R)$ can be obtained. By proper rotation of the coordinate axis the mean value of the Y component, b, can always be made zero. Beckman has performed the integration for $b = 0$ which yields

$$f(\varphi_R) = \frac{K \exp\left[-B^2(1+K^2)/2\right]}{2\pi(K^2\cos^2\varphi_R + \sin^2\varphi_R)} \left[1 + G\sqrt{\pi}\; e^{G^2} \;(1 + \operatorname{erf} G)\right] \tag{25}$$

where

$$K = \sqrt{\frac{v_2}{v_1}} \tag{26}$$

$$B = \frac{a}{\sqrt{v_1 + v_2}} \tag{27}$$

$$G = BK \cos \varphi_R \sqrt{\frac{1+K^2}{2(K^2\cos^2\varphi_R + \sin^2\varphi_R)}} \tag{28}$$

$$\operatorname{erf} G = \frac{2}{\sqrt{\pi}} \int_0^G e^{-t^2}\, dt \tag{29}$$

Now we assume that the single image probability density functions for the amplitude, $f(A_D)$, and phase, $f(\varphi_D)$, are known. Assuming that μ_D, σ_D, ρ_D, α_D are known and that $f(\varphi_D)$ is Gaussian, a, v_1, v_2 can be evaluated. The method is outlined in Appendix I. The results are:

$$a = \rho_D\, e^{-\frac{\sigma_D^2}{2}} \tag{30}$$

$$v_1 = \frac{\rho_D^2}{2m}\left[\left(1 - e^{-\sigma_D^2}\right)^2 + \frac{\alpha_D^2}{\rho_D^2}\left(1 + e^{-2\sigma_D^2}\right)\right] \tag{31}$$

$$v_2 = \frac{\rho_D^2}{2m}\left(1 - e^{-2\sigma_D^2}\right)\left(1 + \frac{\alpha_D^2}{\rho_D^2}\right) \tag{32}$$

Evaluation

The density function $f(\varphi_R)$, given by Eq. 25, has been evaluated for various values of its parameters and its standard deviation, σ_R, has been computed. While the formulas used are based on large m, comparison of σ_R computed by Beckman's method and σ_R computed by a Monte Carlo method shows very good agreement. For m = 1 the maximum error of Beckman's method is 18% and for m = 10 the error is negligible.

In Fig. 6 σ_R versus σ_D is plotted for various values of m. The quantity σ_D is a measure of the phase shifts induced in a single image at a given spatial frequency by the turbulence and σ_R is a measure of the phase shifts at the same spatial frequency after averaging the irradiance values of m images.

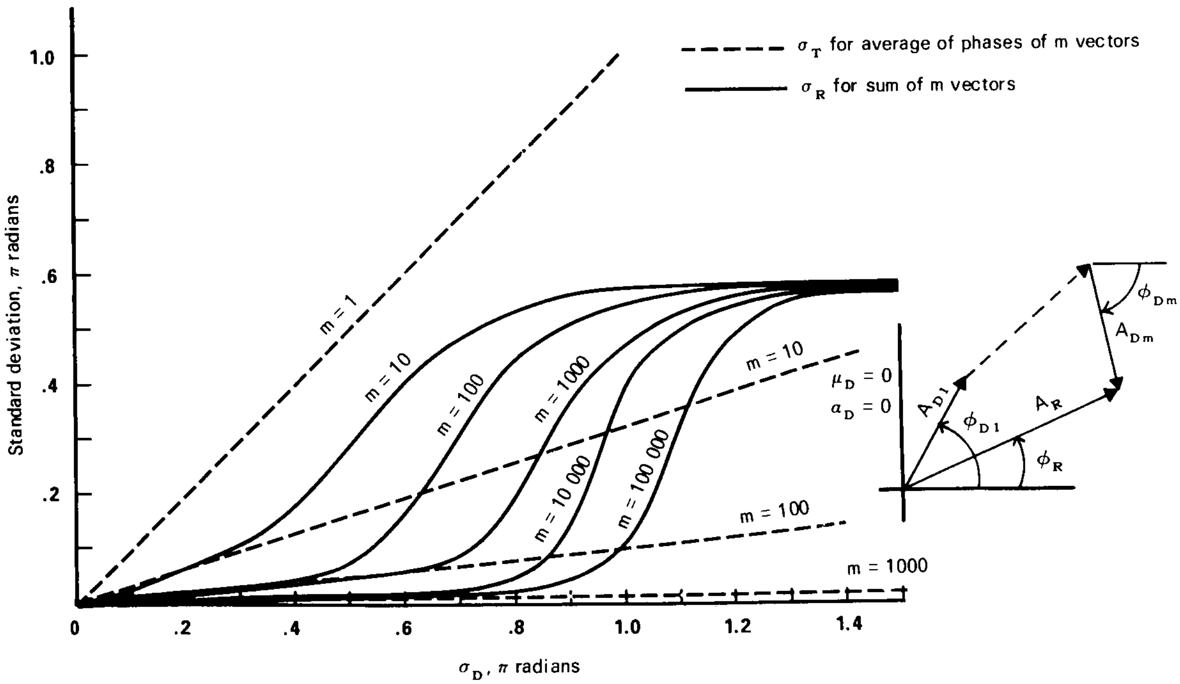

Figure 6.-Standard deviation of phase, σ_R, of the sum of m constant length vectors with phase standard deviation of σ_D(——) and standard deviation of phase, σ_T, of average of phases of m vectors with phase standard deviation of σ_D(---).

Therefore, effectiveness of the image irradiance averaging technique in reducing the phase shifts caused by turbulence can be judged by observing the reduction of σ_R from σ_D. For all values of m, σ_R is less than σ_D, indicating that reduction in phase shifts do occur as a result of the averaging. However, for sufficiently large σ_D, σ_R always saturates at a value of about $.58\pi$. The standard deviation of a uniform distribution of phases is $\pi/\sqrt{3} = .578\pi$. Therefore, at those values of σ_D and m where σ_R begins to saturate $f(\varphi_R)$ is beginning to approach a uniform distribution. At these values of σ_D and m the image irradiance averaging technique is ineffective in significantly reducing the phase shifts.

An important question is: how small must the phase shifts be to produce a good restored image? The answer depends upon the intended use of the restored picture. However, subjective experiments have provided the following guidelines: phase errors over the entire spectrum which have a standard deviation of $\sigma = 15^\circ$ or $\pi/12$ cause a perceptible but not dramatic change in the image, errors with $\sigma = 30^\circ$ or $\pi/6$ cause a very noticeable effect on the image and errors with $\sigma = 60^\circ$ or $\pi/3$ cause a very serious degradation of the image. On the basis that a high quality restoration is desired, let a phase error with standard deviation of $.1\pi$ be a requirement. In table I the values of σ_D and m_D which result in $\sigma_R = .1\pi$ have been tabulated. Thus, as σ_D increases, the number of images required for a good image rapidly increases and soon exceeds reasonable bounds.

The effect of varying amplitude on σ_R is shown in Fig. 7 where σ_R versus σ_D is shown for $m = 100$ and various values of a_D/ρ_D. Here it can be seen that, for a given m, increase of a_D/ρ_D requires a reduction of σ_D to maintain a constant σ_R.

The effect of sensor noise on the image irradiance method is now considered. Associated with each degraded image is a noise image, defined as $N_j(x,y)$ so that the j th recorded image, $D'(x,y)$, is given by

$$D_j'(x,y) = D_j(x,y) + N_j(x,y) \tag{33}$$

Table I.- σ_D and m for $\sigma_R = .1\pi$

σ_D	m
$.29\pi$	10
$.54\pi$	100
$.72\pi$	1,000
$.87\pi$	10,000
π	100,000
1.11π	1,000,000

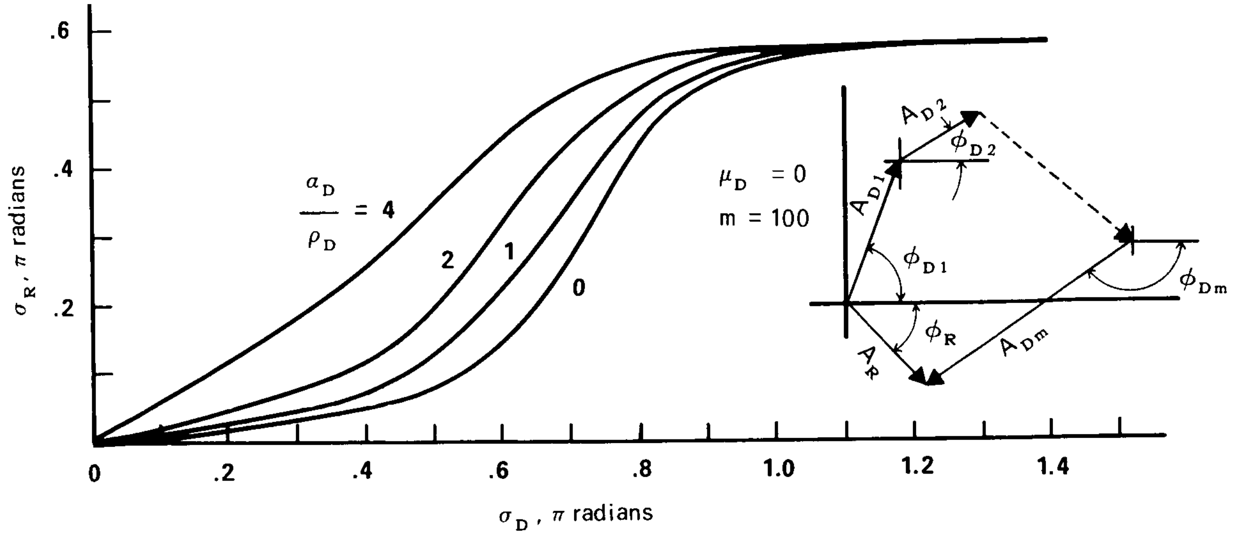

Figure 7.-Standard deviation of phase, σ_R, of sum of m vectors with amplitude mean of ρ_D, amplitude standard deviation of α_D, and phase standard deviation of σ_D.

The averaged recorded image, $\bar{D}'_j(x,y)$, can, in a manner similar to $D_j(x,y)$, be expressed in terms of the Fourier transform of $D_j(x,y)$ and $N_j(x,y)$,

$$\bar{D}'_j(x,y) = \frac{1}{m} \int_{-\infty}^{\infty}\int_{-\infty}^{\infty} \sum_{j=1}^{m} \left[\widetilde{D}_j(u,v) + \widetilde{N}_j(u,v) \right] e^{-2\pi i(ux+vy)}\, du\, dv \qquad (34)$$

Thus in the frequency domain there is a noise vector, $\widetilde{N}_j(u,v)$, added to each degraded image vector. Let α_N be the standard deviation of the amplitude of the noise vector. The variance of the amplitude for a single vector is α_N^2 and, for the averaged sum of m noise vectors is α_N^2/m. The variances for the X and Y components of the sum of m noise vectors α_{NX}^2 and α_{NY}^2 are then given by

$$\alpha_{NX}^2 = \frac{\alpha_N^2}{2m} \qquad (35)$$

$$\alpha_{NY}^2 = \frac{\alpha_N^2}{2m} \qquad (36)$$

The effect of the noise on the probability density function $f(A_R, \varphi_R)$ can be included by adding the noise variances α_{NX}^2 and α_{NY}^2 to the X and Y variances due to turbulence, v_1 and v_2, to obtain new X and Y variances, v_1' and v_2' ,

$$v_1' = v_1 + \alpha_{NX}^2 \tag{37}$$

$$v_2' = v_2 + \alpha_{NY}^2 \tag{38}$$

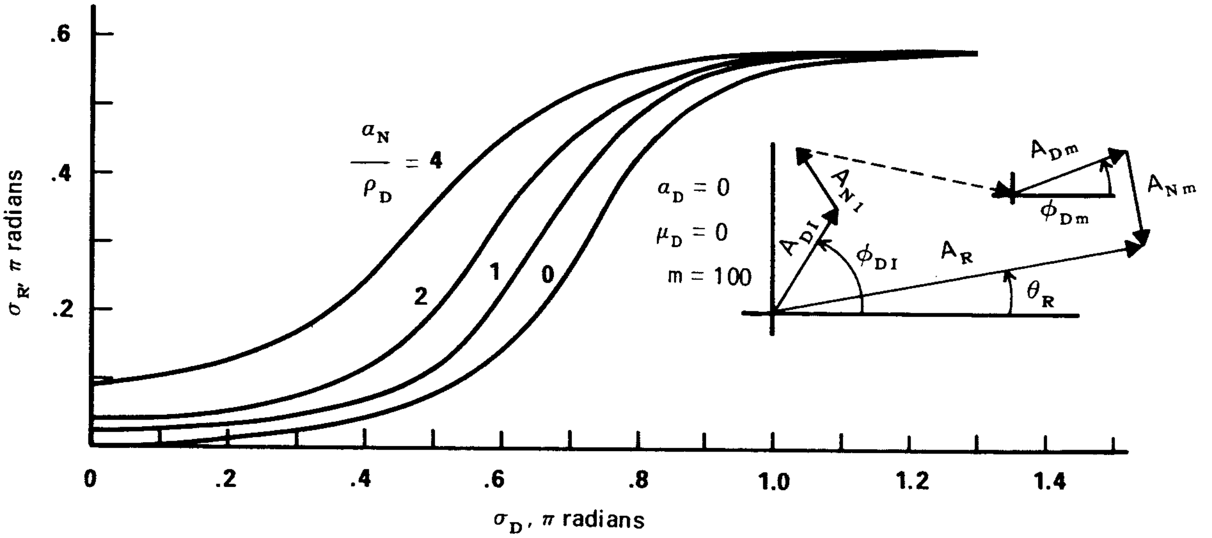

Figure 8. -Standard deviation of phase, σ_R, of sum of m vectors with constant amplitude of ρ_D, phase standard deviation of σ_D, plus the sum of m noise vectors with amplitude standard deviation of α_N.

The effect of sensor noise on the image irradiance averaging method is shown in Fig. 8 as σ_R versus σ_D for $m = 100$ and various values of α_N/ρ_D. As expected, sensor noise reduces the effectiveness of the method. For $\alpha_N/\rho_D = 1$ only a small decrease of σ_D is required to maintain $\sigma_R = .1\mu$, while for $\alpha_N/\rho_D = 4$ σ_D must be decreased to nearly zero.

Discussion

The quantity σ_R is obviously a complex function of many parameters, therefore no comprehensive statement can be made about the effectiveness of the image irradiance method for correcting turbulence degraded images. However, the relationship between σ_R, m, and σ_D demonstrated in Fig. 6 seems to be highly significant. From table I, 100,000 independent images are required to produce a σ_R of $.1\pi$ when σ_D is approximately π. The scanning and digital processing of this large number of images would be a difficult task. A more reasonable approach would be to do the averaging in the image plane of the telescope by use of a long time exposure. Removal of gross image shifts would be necessary to avoid an unnecessary increase of σ_D. Assuming a minimum time of .01 second for complete change of the turbulence, an exposure of 1000 seconds or 16.7

minutes would be required to obtain the necessary averaging. If σ_D increased to 1.1π then, from table I, 1,000,000 independent pictures would be required or an exposure time of 167 minutes. Thus it is clear that the use of the image averaging technique to reduce the phase shift of spatial frequencies is limited to those spatial frequencies whose phase shifts are on the order of π or less.

Another factor which can be expected to limit the image irradiance method to phase shifts of less than π is the sensor noise characteristics. The mean of the resultant vector sum amplitude, ρ_R, is identical to a as given in Eq. 30. This function decreases rapidly as a function of σ_D. At $\sigma_D = \pi$, $a = 7 \times 10^{-3}$, and, at $\sigma_D = 2\pi$, $a = 2 \times 10^{-9}$. Thus for σ_D between π and 2π, μ_R will drop below the noise level of most sensors.

Although phase statistics of the optical transfer function due to turbulence are scarce, phase shifts of π and greater are possible. For example, the spatial frequency of one cycle per arc second is shifted in phase by π for an image shift of .5 arc second. For $\lambda = .5$ micron a spatial frequency of 1 cycle per arc second is associated with pairs of points spaced 10 centimeters apart on the objective lens. Since image shifts of .5 arc second and greater are observed with 10 centimeter diameter telescopes, phases shifts of π and greater are possible. Therefore, the image irradiance averaging technique can be expected to be inadequate for restoring turbulence degraded images in many practical applications.

AMPLITUDE AND PHASE AVERAGING

The Method

The method of amplitude and phase averaging is defined as consisting of the following steps. Beginning with m images degraded by turbulence, any necessary gray scale and geometric distortion corrections are made so that the corrected images are a true representation of the irradiance maps that existed in the image plane of the optical system. These images are registered with respect to each other by some means, such as superimposing centers of gravity, in order to eliminate gross image shifts. A complex Fourier transform of each image is computed and is converted into the amplitude and phase form. The computed phases are initially constrained to the -π to +π interval but are converted to their true values by adding or subtracting multiples of 2π by some suitable criteria based on spectrum continuity requirements. Letting $\tilde{T}(u,v)$ represent the complex spectrum which will result from the amplitude and phase averaging technique, the phase and amplitude associated with $\tilde{T}(u,v)$ are, respectively, $\varphi_T(u,v)$ and $A_T(u,v)$. At each spatial frequency the average phase and amplitude are computed from

$$\varphi_T = \frac{1}{m} \sum_{j=1}^{m} \varphi_{Dj} \qquad (39)$$

$$A_T = \frac{1}{m} \sum_{j=1}^{m} A_{Dj} \qquad (40)$$

If the turbulence is non-isotropic, φ_T is then corrected by subtracting μ_S, according to Eq. 13. The quantity A_T is corrected by an averaged modulation transfer function, according to Eq. 14. The complex spectrum is then formed from the corrected amplitude and phases, appropriate attenuation of sensor noise dominated frequencies is made, and the inverse Fourier transform is taken to produce the restored image.

Analysis of Method

The effectiveness of the amplitude and phase averaging method can be judged by how closely φ_T and A_T approximate μ_D and ρ_D. Again we will consider mainly the problem of estimating the phases. In Eq. 13 we replace μ_D by φ_T to give φ_U', the estimated value of φ_U,

$$\varphi_U' = \varphi_T - \mu_S \tag{41}$$

Now φ_T is a sample mean and is a random variable (6) with mean, μ_T, and standard deviation, σ_T given by

$$\mu_T = \mu_D \tag{42}$$

$$\sigma_T = \frac{\sigma_D}{\sqrt{m}} \tag{43}$$

By use of Eq. 9 for μ_D, Eq. 42 can be written as

$$\mu_T = \varphi_U + \mu_S \tag{44}$$

Thus φ_T has a mean value equal to the desired value, φ_U, plus a shift due to non-isotropic turbulence. A computation of φ_T for a given set of images will result in a value equal to its mean plus an error, ϵ,

$$\varphi_T = \mu_T + \epsilon \tag{45}$$

where ϵ has a standard deviation given by Eq. 43. Combining Eqs. 45, 44, and 41 gives for φ_U'

$$\varphi_U' = \mu_T + \epsilon - \mu_S = \varphi_U + \epsilon \tag{46}$$

The restored phase is the desired phase plus an error which has a standard deviation of $\sigma_T = \sigma_D/\sqrt{m}$

Evaluation

In Fig. 3 σ_T versus σ_D is plotted for various values of m. Comparing σ_T to σ_R obtained by the image irradiance averaging method, the amplitude and phase technique is seen to be a much more effective method of processing.

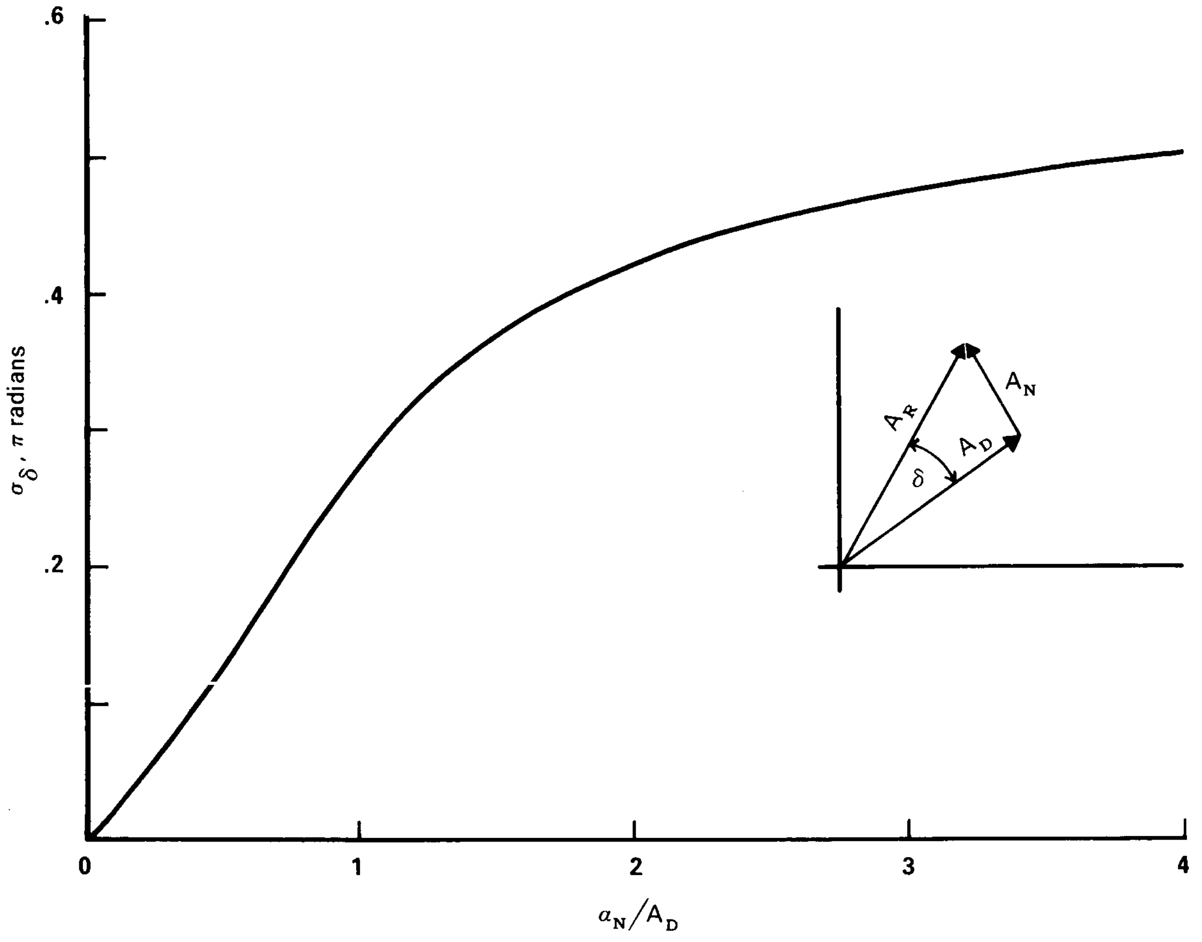

Figure 9.-Standard deviation of error phase caused by addition of a noise vector with standard deviation of α_N to a vector with amplitude A_D.

For example, for σ_D equal to π and $m = 100$, the phase averaging method results in a σ_T of $.1\pi$ while σ_R is greater than $.5\pi$ and near the value which corresponds to a uniform distribution.

Since the amplitude and phase averaging method is non-linear the effect of noise upon it is difficult to formulate exactly. However, an approximate evaluation can be made. For a single image the effect of noise is to modify the measured amplitude and phase, as shown in the vector diagram in Fig. 9. The resulting error phase, δ, has a probability density function, $f(\delta)$. This PDF can be evaluated from Eq. 25 if v_1 and v_2 are replaced by $\alpha_N^2/2$ and a is replaced by ρ_D. The standard deviation of $f(\delta)$, σ_δ, is shown in Fig. 9 as a function of the ratio α_N/A_D. Up to $\alpha_N/A_D = 1$ σ_δ is approximately linear. Above this σ_δ begins to saturate, suggesting that $f(\delta)$ is beginning to flatten. Figure 10 shows the shape of $f(\delta)$ for the same values of α_N/A_D. For α_N/A_D greater than unity $f(\delta)$ does begin to flatten out. The uniformly random component of the resultant phase seriously effects the phase averaging technique.

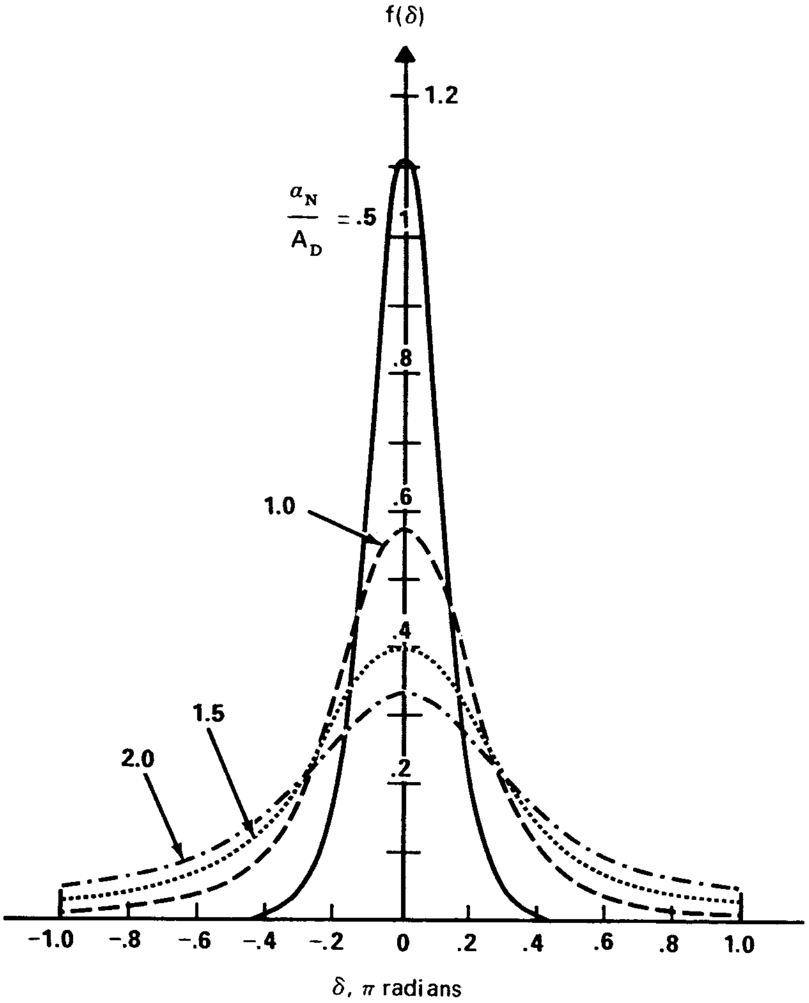

Figure 10. -Probability density function of error phase, 8 , caused by addition of a noise vector with a standard deviation of a_N to a vector with amplitude A_D.

The result of a Monte Carlo experiment which demonstrates this is shown in Fig. 11. Here it is shown that for $\alpha_N/A_D \geq .5$ significant errors occur in the computation of the average of m phases even for $\sigma_D = 0$ and the relative large value of $m = 100$. In comparison the phase errors for $\sigma_D = 0$, $m = 100$ which result from the image irradiance method are much smaller, as shown in Fig. 8. Thus the amplitude and phase averaging technique requires a frequency domain noise to signal ratio, α_N/A_D, of .5 or less to function effectively.

EXPERIMENTAL COMPARISON

The two methods of averaging have been compared in an experiment utilizing images degraded by laboratory turbulence. Details of the experimental setup have been described in a previous publication (1). Figure 12 shows six samples of the series of degraded images used in the experiment. The phase shifts of the spatial frequencies were relatively high; at a spatial frequency of 1 cycle per four picture elements the standard deviation of phase was approximately π. Figure 13 shows the results of applying the two averaging techniques for m = 4, m = 16, and m = 54 images. Here we see that the image averaging technique was ineffective in improving the image. This was expected because for $\sigma_D = \pi$ and m = 54 the standard deviation of phase after image averaging is nearly equal to that of a uniformly random vector, as can be deduced from Fig. 6. The amplitude and phase averaging method without the application of phase continuity was also ineffective since for $\sigma_D = \pi$ the constrained phase probability density function is nearly uniform, as shown in Fig. 5. The amplitude and phase averaging technique using phase continuity was successful, with the restored image improving as m increased. This result is consistent with the expected decrease of σ_T as a function of m .

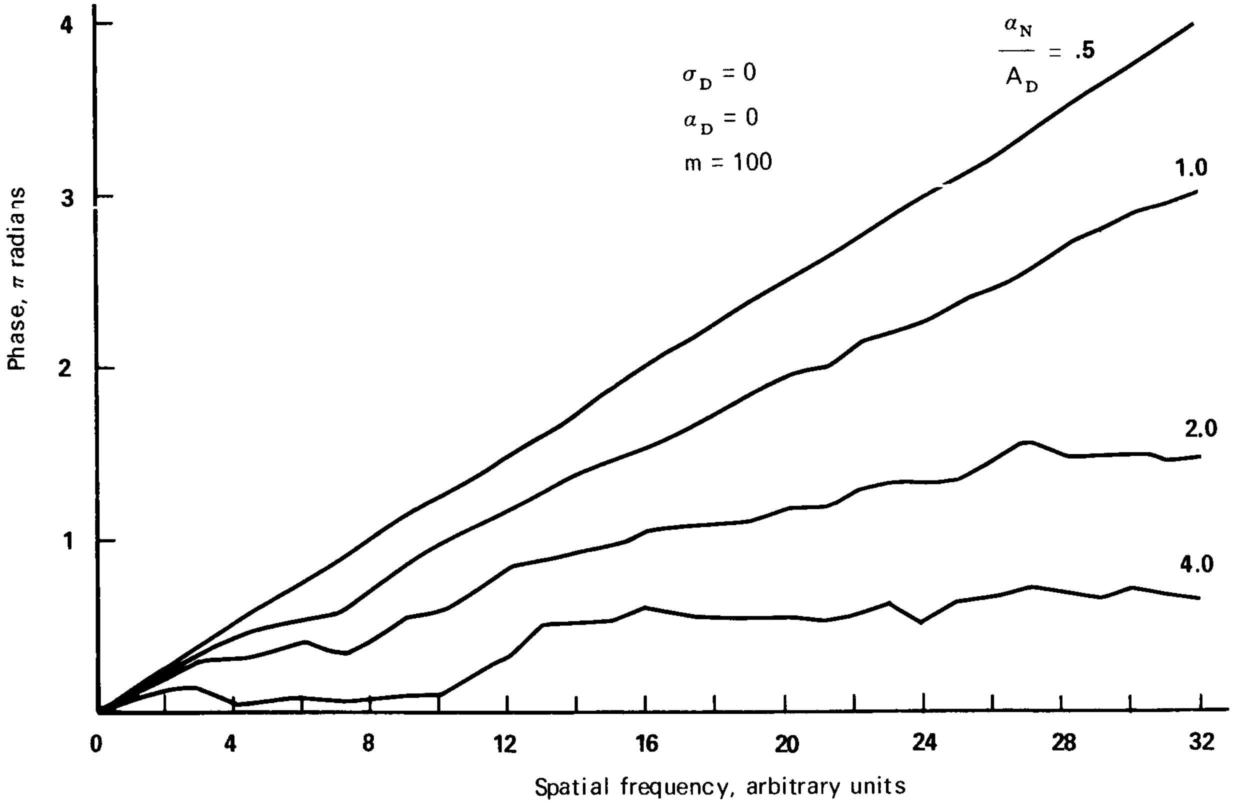

Figure 11.-Results of a Monte Carlo experiment showing the effects of noise on the phase averaging method. The initial noise-free complex spectrum had a constant amplitude A_D and a phase which increased linearly from zero to 4π radians at a frequency of 32. Gaussian white noise with amplitude standard deviation of α_N was added to the complex spectrum. The phase spectrum was computed and 100 such spectra were averaged, each with different noise, to give the results shown. The principal value of the difference between the plotted results and a uniform ramp with phase of 4π at a frequency of 32 is the phase error caused by the noise.

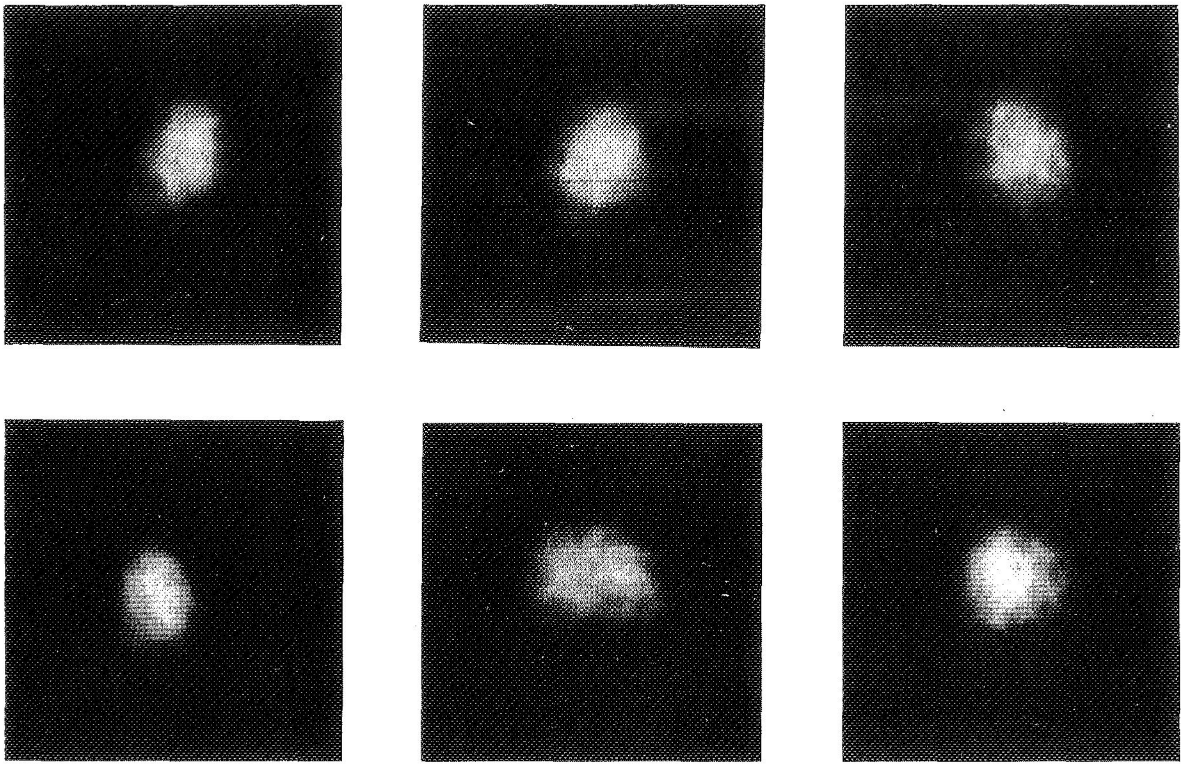

Figure 12.-Images degraded by laboratory generated turbulence.

APPLICATION TO ASTRONOMICAL PHOTOGRAPHS

The amplitude and phase averaging technique has been applied to objects photographed through natural atmospheric turbulence. One experiment was done on film recorded images of the Pegasus satellite taken with the USAF Cloudcroft 48 inch diameter telescope. The exposure time was 1/60 second. The other experiment was done on film recorded images of the planet Mercury taken with the Mount Wilson 100 inch diameter telescope, which was stopped to an effective diameter of 50 inches (10). The exposure time was 1/15 second. In both cases spatial frequencies needed to restore detail to the images were noise dominated so that no image improvement was obtained.

The above two examples are by no means representative of all types of objects which are of interest to users of ground based telescopes. However, the examples do indicate that sensor noise is a major problem with respect to image restoration. The replacement of film with a high quantum efficiency photoelectric sensor appears to be a necessary step in order to decrease noise. A signal to noise improvement of a factor of 10 may be possible here. Whether this step results in an adequate signal to noise ratio depends upon many factors: the spectral irradiance of the object, the spatial frequency spectrum of the object, the telescope entrance pupil diameter, the statistical properties of the turbulence-telescope optical transfer function, and the sensor spectral sensitivity and noise characteristics. Some of these factors are usually known. One of the key factors which is usually unknown is the statistical properties of the short exposure optical transfer function associated with the effect of the turbulence and optical system. From these statistical properties the short exposure and long exposure attenuation of the spatial frequency amplitudes can be estimated and the number of images needed to reduce the phase shifts can be estimated. Thus measurements of the statistical properties of the optical transfer function at the observing site should be a part of any program of image restoration using averaging techniques. Such measurements could easily be done with short exposure photographs of star images and the appropriate hardware and software for analyzing the images.

In many cases even improved sensors will not produce suitably low noise levels for short time exposures for the amplitude and phase averaging technique. In these cases increase of exposure time can be used to decrease noise. Because of dynamic range limitations, the sensor may saturate before a suitable length of time has been reached. In such cases the exposure time per image should be adjusted to prevent sensor saturation and multiple images recorded. These images would then be averaged digitally in groups to produce images for use in the amplitude and phase averaging method.

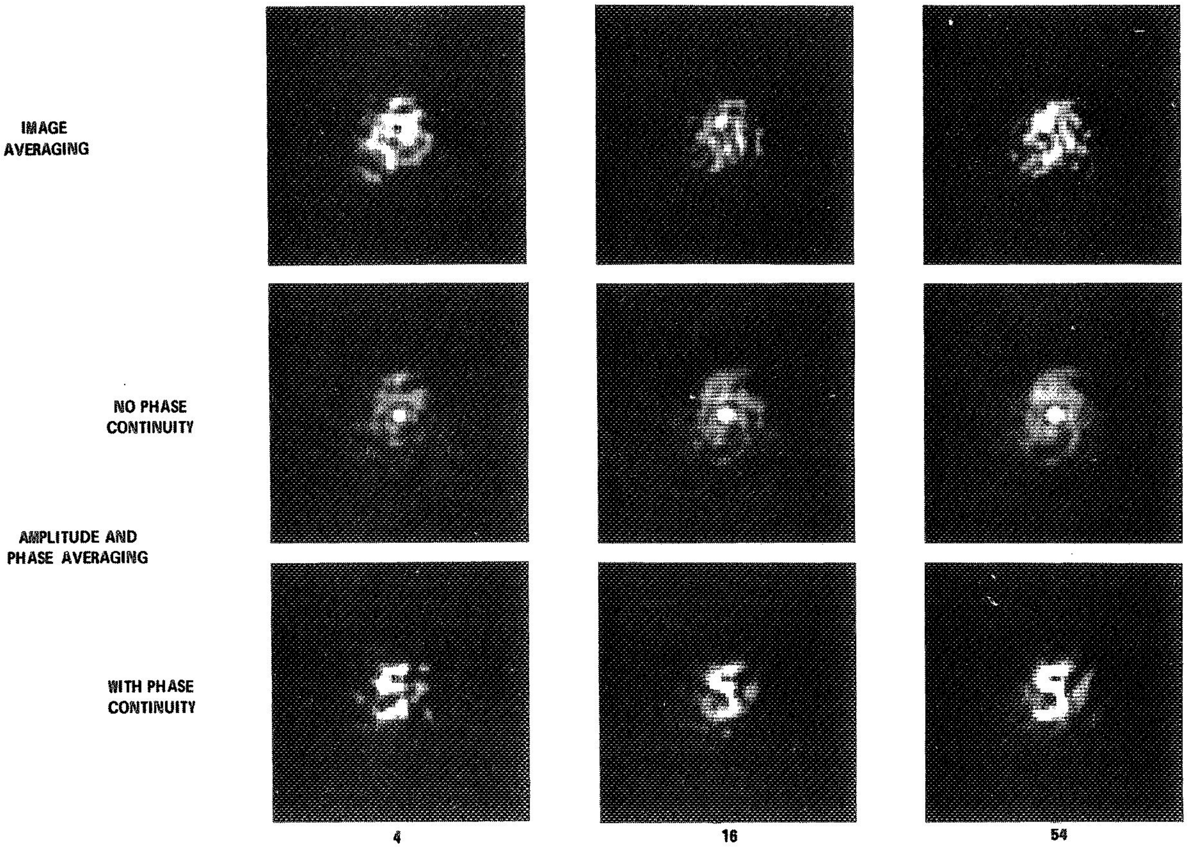

Figure 13.-Processing of images degraded by laboratory turbulence using averaging techniques. The number below each column is the number of images used in the processing. The original object was the numeral 5.

CONCLUSIONS

Theory and experimental results indicate that the amplitude and phase averaging of multiple images is a potentially useful method of improving turbulence degraded images and is superior to the method of image irradiance averaging. Feasibility of the method for specific applications depends on a variety of factors. Two of the most important factors are the statistical properties of the short exposure optical transfer function and the sensor noise characteristics. The signal to noise ratio in the spatial frequency domain must be on the order of 2 or above for the method to function correctly. Increase of the signal to noise ratio by use of high quantum efficiency sensors is a necessity.

ACKNOWLEDGEMENTS

Appreciation is expressed to Madison L. Myers for programming the image restoration operations and to W. Hadley Richardson for programming the probability density function analyses.

APPENDIX I

A brief outline of the derivation of the parameters a, s_1 and s_2 used in Eq. 25 is given here.

Given m vectors, each with amplitude A_j and phase φ_j, the X and Y components of the sum of these vectors is given by

$$X = \frac{1}{m} \sum_{j=1}^{m} A_j \cos \varphi_j \tag{1}$$

$$Y = \frac{1}{m} \sum_{j=1}^{m} A_j \sin \varphi_j \tag{2}$$

We assume that both X and Y are normally distributed and that the mean of Y is zero,

$$f(X) = \frac{1}{\sqrt{2\pi v_1}} e^{-\frac{(X-a)^2}{2v_1}} \tag{3}$$

$$f(Y) = \frac{1}{\sqrt{2\pi v_2}} e^{-\frac{Y^2}{2v_2}} \tag{4}$$

We want to determine a, v_1, and v_2 in terms of the statistical properties of A_j and φ_j.

Evaluation of a

We use the brackets $\langle\,\rangle$ to denote an ensemble average. If A_j and φ_j are independent then

$$a = \langle X\rangle = \frac{1}{m}\sum_{j=1}^{m}\langle A_j\rangle\langle\cos\varphi_j\rangle \tag{5}$$

If ρ is the mean of A_j then

$$\langle A_j\rangle = \rho \tag{6}$$

If φ_j has a Gaussian distribution of zero mean and standard deviation of σ then

$$\langle\cos\varphi_j\rangle = \frac{1}{\sigma\sqrt{2\pi}}\int_{-\infty}^{\infty}\cos\varphi\; e^{-\frac{\varphi^2}{2\sigma^2}}\,d\varphi$$

$$= e^{-\sigma^2/2} \tag{7}$$

Using Eqs. 6 and 7 in Eq. 5 gives

$$a = \rho\, e^{-\sigma^2/2} \tag{8}$$

Evaluation of v_1

The variance v_1 is given by

$$v_1 = \langle (X - X\ )^2\rangle$$

$$= \langle X^2\rangle - \langle X\rangle^2 \tag{9}$$

From Eq. 8 $\langle X^2\rangle$ can be evaluated,

$$\langle X\rangle^2 = a^2 = \rho^2\, e^{-\sigma^2} \tag{10}$$

By use of Eq. 1 $\langle X^2\rangle$ can be shown to be

$$\langle X^2\rangle = \frac{1}{m^2}\left[\sum_{j=1}^{m}\langle A_j^2\rangle\langle\cos^2\varphi_j\rangle + \sum_{\substack{j=1\\ j\neq k}}^{m}\sum_{k=1}^{m}\langle A_j\rangle\langle A_k\rangle\langle\cos\varphi_j\rangle\langle\cos\varphi_k\rangle\right] \tag{11}$$

where the assumption has been made that A_j, A_k, φ_j, and φ_k are all independent. In a manner analogous to Eq. 7, it can be shown that the first summation in the brackets of Eq. 11 is equal to

$$\frac{m\langle A_j^2\rangle}{2}\left(1+e^{-2\sigma^2}\right) \qquad (12)$$

If α^2 is the variance of A_j then it can be shown that

$$\langle A_j^2\rangle = \langle A\rangle^2 + \alpha^2 = \rho^2 + \alpha^2 \qquad (13)$$

The second summation within the brackets of Eq. 11 reduces to

$$(n^2-n)\,\langle A_j\rangle^2\, e^{-\sigma^2} \qquad (14)$$

Substituting Eq. 13 into Eq. 12, and Eqs. 12 and 14 for the terms in brackets in Eq. 11, and reducing and combining Eq. 11 and 10 in Eq. 9 give

$$s_1 = \frac{\rho^2}{2m}\left[\left(1-e^{-\sigma^2}\right)^2 + \frac{\alpha^2}{\rho^2}\left(1+e^{-2\sigma^2}\right)\right] \qquad (15)$$

Evaluation of s_2

Since the mean of Y is assumed to be zero, the variance v_2 is given by

$$v_2 = \langle Y^2\rangle \qquad (16)$$

By use of Eq. 2 $\langle Y^2\rangle$ can be shown to be

$$\langle Y^2\rangle = \frac{1}{m^2}\left[\sum_{j=1}^{m}\langle A_j^2\rangle\langle\sin^2\varphi_j\rangle + \sum_{j=1}^{m}\sum_{\substack{k=1\\ j\neq k}}^{m}\langle A_j\rangle\langle A_k\rangle\langle\sin\varphi_j\rangle\langle\sin\varphi_k\rangle\right] \qquad (17)$$

In a manner similar to Eq. 12 the first term in the brackets is

$$\frac{m\langle A_j^2\rangle}{2}\left(1-e^{-2\sigma^2}\right) \qquad (18)$$

The second term of Eq. 17 is zero since $\langle\sin\varphi_j\rangle$ is zero for the assumed distribution of φ_j. Substituting Eq. 13 for $\langle A_j^2\rangle$ into Eq. 18 and Eq. 18 into Eq. 17 and reducing gives s_2,

$$s_2 = \frac{\rho^2}{2m}\left(1+\frac{\alpha^2}{\rho^2}\right)\left(1-e^{-2\sigma^2}\right) \qquad (19)$$

REFERENCES

1. McGlamery, B. L., Restoration of Turbulence Degraded Images, J. Opt. Soc. Am. 57, 293 (1967).
2. Harris, J. L., Image Evaluation and Restoration, J. Opt. Soc. Am. 56, 569 (1966).
3. P. F. Mueller and G. O. Reynolds, Image Restoration by Removal of Random-Media Degradations, J. Opt. Soc. Am. 57, 1338 (1967).
4. R. E. Hufnagel and N. R. Stanley, J. Opt. Soc. Am. 54, 52 (1964).
5. Trabka, E. A., J. Opt. Soc. Am. 56, 128 (1966).
6. Fried, D. L., J. Opt. Soc. Am. 56, 1372 (1966).
7. Papoulis, A., Probability, Random Variables, and Stochastic Processes, McGraw Hill Book Co., New York, p. 189.
8. Beckman, P., Probability in Communication Engineering, Harcourt, Brace and World, Inc. , Chap. 4.
9. Hold, A., Statistical Theory with Engineering Applications, John Wiley and Sons, Inc., New York, p. 219.
10. B. C. Murray and J. A. Westphal, Investigations into Improvement of Astronomical Photography, Final Report, NSF Grant GP5113.

REAL TIME COMPUTER PROCESSING OF VIDEO IMAGES

T. J. Janssens and N. K. Baker
San Fernando Observatory
The Aerospace Corporation
El Segundo, California

E. E. Robbins
NASA Manned Space Center
Houston, Texas

Introduction

Origin of the technique - The technique of digitizing and computing with television images in real time grew out of a specific task; namely, the measurement of solar magnetic fields, and perhaps it is best to illustrate the technique by describing this particular measurement.

To measure solar magnetic fields by use of Zeeman splitting and polarization of a Fraunhoffer line requires the spectral isolation of light from just one wing of a magnetically sensitive line, detection and subtraction of the light intensities in right and left handed circular polarizations, and a scanning process which repeats this process for each point on the sun under investigation.

Figure of Merit for an Idealized Magnetograph - A high performance solar magnetograph would look at a large section of the sun with high spatial resolution, high sensitivity, and high temporal resolution.

If we let ΔB = the magnetic uncertainty
a = the area of resolution cell
T = the time for a scan
n = the number of resolution elements per scan,

then for an idealized point scanning photon-limited solar magnetograph, the ratio $n/(\Delta B)^2\, T\, a$ remains invariant with the magnetic uncertainty, ΔB, changing as the other three parameters are adjusted. The ratio depends only on the rate of photon detection per cell area and is proportional to the product $A \epsilon N$ where A is the area of the obective lens, ϵ is the overall efficiency and N is the number of data channels. Using the ratio as a figure of merit we have:

$$\text{Figure of merit} = \frac{n}{(\Delta B)^2 T\, a} \quad \alpha \quad A\,\epsilon\, N$$

which shows that for this idealized consideration the figure of merit is increased by enlarging the lens, raising the efficiency, or increasing the number of channels. This approach is an attempt to increase the effective number of channels.

The Scanning Mode - Consider three modes of scanning and their effective number of data channels for similar resolution and area of interest of 40,000 points. The most usual method is a point-by-point scan with an effective $N = 1$.

A method developed by R. B. Leighton involves simultaneous spectroheliogram pairs whose difference yields a picture of the magnetic fields. This slit scanning for this example has an effective $N = 200$ although in practice it may have N of about 1000.

The third method of scanning detects photons from all parts of the image simultaneously. This has an effective $N = 40{,}000$ but requires spectral isolation by use of a very narrow integrating detector such as film or a television type camera.

Detector and Data Processing Requirements - Use of film is impractical if one wishes to maximize the rate of photon detection because of the large quantities of film required and the difficulties with photographic subtraction, but with television other problems are encountered.

To maximize the photon detection rate, the television tube is scanned at a fast rate (standard TV rate) since the target of a camera tube can hold only a given number of photoelectrons before being read off.

The usual method of data processing is to digitize and store on magnetic tape for later analysis but here a problem arises. The video data rate is 4 million bytes per second compared with about 30,000 bytes per second for a typical magnetic tape recorder. Thus for a straightforward approach 133 tapes recorders would be required and since a reel of tape holds about 10^7 bytes, reels would be filled at the rate of one each $2\frac{1}{2}$ seconds or 14,400 tape reels in 10 hours.

Real Time Computation- This severe case of data poisoning could be solved by computing in real time since a great many frames are added and subtracted to give a resultant magnetic picture, but for a general purpose computer the memory size and speed would be prohibitive.

To solve the problem a very high speed arithmetic unit was combined with a digital magnetic disk used with parallel, sequential access instead of random access. The disk has 72 tracks and 131,000 bits per track, and rotates at 30 Hz.

Discription of the System

Organization - For convenience, the digital system shown in Fig. 1 is divided into three working areas:

1. A data gathering section where the raw data are collected as a 16-bit digitized array.
2. A display section where the data are reduced to 4 bits (8-16 gray levels).
3. A data storage section where two 16 bit frames, or four 8 bit frames, or 16 bit-bit frames can be stored temporarily.

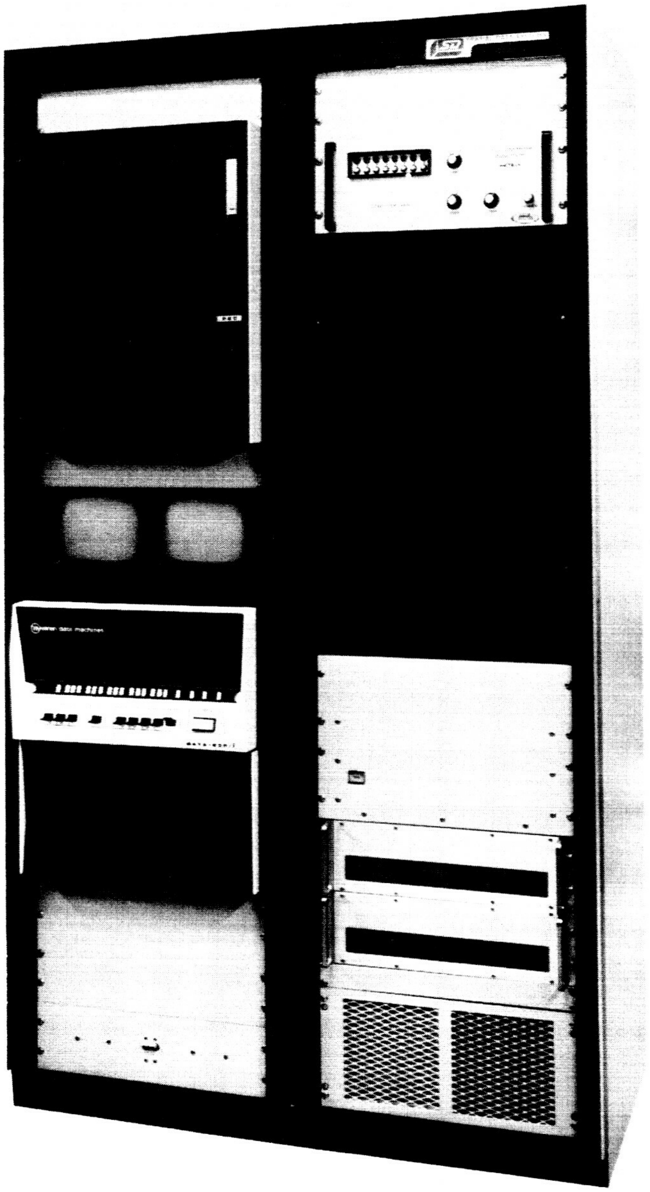

Figure 1.-Digital video processor. On the left is the ADC, high speed adder, and digital magnetic disk. On the right is the magnetic tape recorder, output displays, and general purpose computer. Now shown in the light pen.

Data Gathering - The data gathering area was designed to accept an analogue signal from a TV camera which was synchronized with the disk's rotation speed. This signal is digitized into 8 bits (256 levels) by a 4 megacycle convertor which is synchronized with the data flow of the disk. The output of the analogue to digital converter can be added to or subtracted from a previously stored array in the data gathering area of the disk and then stored, thereby erasing the previous image array. This operation is controlled by the disk interface controller which requires one instruction per frame whether to add or subtract the incoming image. It is operated on an interrupt basis by a small general purpose computer attached to the system.

After the completion of the data gathering mode, the system can be interrogated for information on the entire frame. At present, we can get the number of elements greater than a certain value, value of the nth largest element and mth smallest element, or the average value. The position of the element cannot be found in this interrogation mode.

For instance, the time to obtain the nth largest element in the array of 100,000 points is 0.5 second. This information is mainly used to set the levels for the display and to make distribution plots.

Display and Light Pen - In the display section, we have a variety of choices, ranging from arbitrary selection of 8 to 16 gray levels to automatic selection by the computer. The display can be in either a positive or negative mode, logarithmic or linear scaling. These display data are transferred to the display section of the disk and displayed to the operator. The 4 bit (16 gray levels) data is connected to a digital to analogue convertor and fed to two TV monitors which are synchronized to the disk. The operator can use a light pen on the monitor to select points or areas on which he wants more information, such as the numerical value of a specific point or position of the point. For areas, the operator can define rectangles or circles of various sizes in which he wants average values, maximum value, or minimum value.

The display section can also be used for graphic and alphanumeric display of the data, ranging from intensity plots on arbitrary cross sections of the picture to distribution plots of the entire frame.

Storage - The data storage area is used as an intermediate storage to free the data gathering area. From this area, the data can be transferred to permanent storage on tape. It can also be used to hold image correction data which the computer could use to correct the raw data for imperfections or shading in the TV camera.

Present Status - At the present writing the system is completed but with two remaining problems which are now being solved. One is recurrent failures of one of the digital components which has now been replaced and the other is switching the polarization of the image without hurting the image quality or registration. (NOTE - Successful operation began on July 17, 1970.)

Tests on multi-image enhancement (essentially 2 dimensional signal averaging) have shown that the noise is indeed Gaussian in nature and hence sensitivity does increase as $\sqrt{n}$ where n is the number of frames involved.

Possible Other Applications

General Considerations - Applications of real time computing on video images might include studies of 2 dimensional scenes especially where the measurement is of differences with certain variables such as wavelength (Doppler, color indices), polarization (synchroton, Zeeman), time (pulsations, sudden eruptions). Other applications capitalize on one or more of the special features, e.g., the ultrahigh speed processing, the two dimensional signal averaging, the real time computations by the general purpose computer, the immediate display with man-interface interaction, and the data compression.

We may symbolically characterize a scene to be studied as

$$Z = I(x,y,\lambda,p,t) + j(x,y,\ ,p,t)$$

where I = intensity of the object
x,y = spatial variables
λ = wavelength
p = polarization
t = time
j = perturbations from the detector, atmosphere, etc.

The two dimensions on the tube face are usually x and y but could be λ or some other variable. Most measurements would involve enhancement of differences due to variations in one or more variables while the effects of perturbations are minimized.

An Example - A simple illustration might be the search for an optical pulsar when its frequency is known but not its exact position. If a telescope equipped with image intensifier and television camera tube had its video taped output played back into this system and alternately add and subtract frames separated by half the pulsar's period, then when the phase was right only light coming from the pulsar should fail to cancel.

Another example might be two dimensional photon counting though this.would require additional preprocessing. The dimensions could be spatial or spectral.

Page intentionally left blank

IMAGE PROCESSING OF STRATOSCOPE PHOTOGRAPHS

R. E. Danielson

and

M. G. Tomasko

Princeton University Observatory
Princeton, New Jersey

INTRODUCTION

The existence of a stable instrumental profile (or point spread function) in diffraction limited balloon and orbital telescopes makes the photographs obtained by these instruments prime candidates for image restoration techniques. Moreover, the quality of imagery is uniform over the photograph, which is generally not the case for imagery with ground based telescopes. In the case of a non-solar space telescope, the instrumental profile is readily obtained by photographing a star.

Our interest in image restoration is primarily due to the necessity of processing Stratoscope II photographs in order to extract the maximum information from them. Similar restoration techniques will be required for orbital telescopes. In order to develop these techniques, we chose to process a few Stratoscope I photographs taken of sunspots over 10 years ago by a 12-inch balloon-borne telescope.

IMAGE QUALITY IN A DIFFRACTION LIMITED TELESCOPE

The monochromatic transfer function of an ideal diffraction limited telescope is shown in figure 1 (a) and the corresponding point spread function, the classical airy disk, is shown in figure 1 (b). However, a substantial reduction in the ideal transfer function occurs even in the case of excellent optical tolerances. For example, manufacturing errors equalling $\lambda/50$ rms on the surface of the primary mirror lead to a wavefront error of $\lambda/25$ rms. The corresponding reduction in the transfer function at half the limiting spatial frequency is about 6%. Other factors which have a similar or larger effect include focus errors, guidance jitter, temperature non-uniformity in the primary mirror, and scattering of light in the photographic film. These factors are likely to result in a transfer function which is reduced from the ideal by nearly a factor of two at one-half the limiting spatial frequency (see figure 1 (a)). This corresponds to an rms wavefront deviation of approximately $\lambda/10$. The resulting point spread profile is also shown in figure 1 (b). It is clear that the effect of the reduced transfer function is to decrease the fraction of energy in the central diffraction peak.

PROCESSING PROCEDURE

From Flight 1959-D, we chose four high quality photographs of a sunspot all taken within an interval of one minute. Since the characteristic time changes in the umbral dots require about one-half hour (1,2), these photographs should be identical. The photographs were digitized at 40 samples per mm. Neutral density filters, located in small strips at the outer edges of the focal plane, provided the intensity calibration.

Unfortunately for solar imagery, there is no simple way to obtain the instrumental transfer function; there is no point source that can be photographed to obtain the point spread profile. In order to process Stratoscope I pictures, we have rather arbitrarily taken the reduced transfer function shown in figure 1 as the instrumental transfer function. This

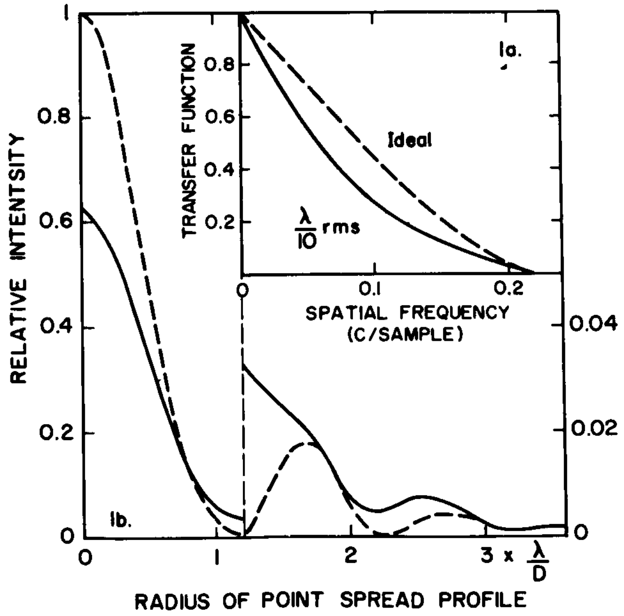

Figure 1.-Ideal transfer functions and point spread profiles. Note magnification change at 1.2 λ/D; λ, wavelength; D, telescope diameter. (a) Ideal transfer function of an unobscured aperature and transfer function corresponding to an rms wavefront deformation of 1/10th wave. (b) Corresponding point spread profiles.

transfer function implies larger image degradation than does the transfer function derived by Gaustad and Rogerson (3) from photographs of the sun's limb during the same flight. The Stratoscope I pictures covered a sufficiently small wavelength interval (the half intensity wavelengths of the film-filter combination were 5280Å and 5650Å) that a monochromatic transfer function is adequate for our purposes.

Figure 2 shows the four photographs reproduced from the digital intensity data stored on tape. The display equipment consists of a facsimile type scanner normally used to make color separation negatives (4). Basically, it consists of a film on a rotating drum illuminated by a small light source, the brightness of which is a power law function of the digitized intensities recorded on tape.

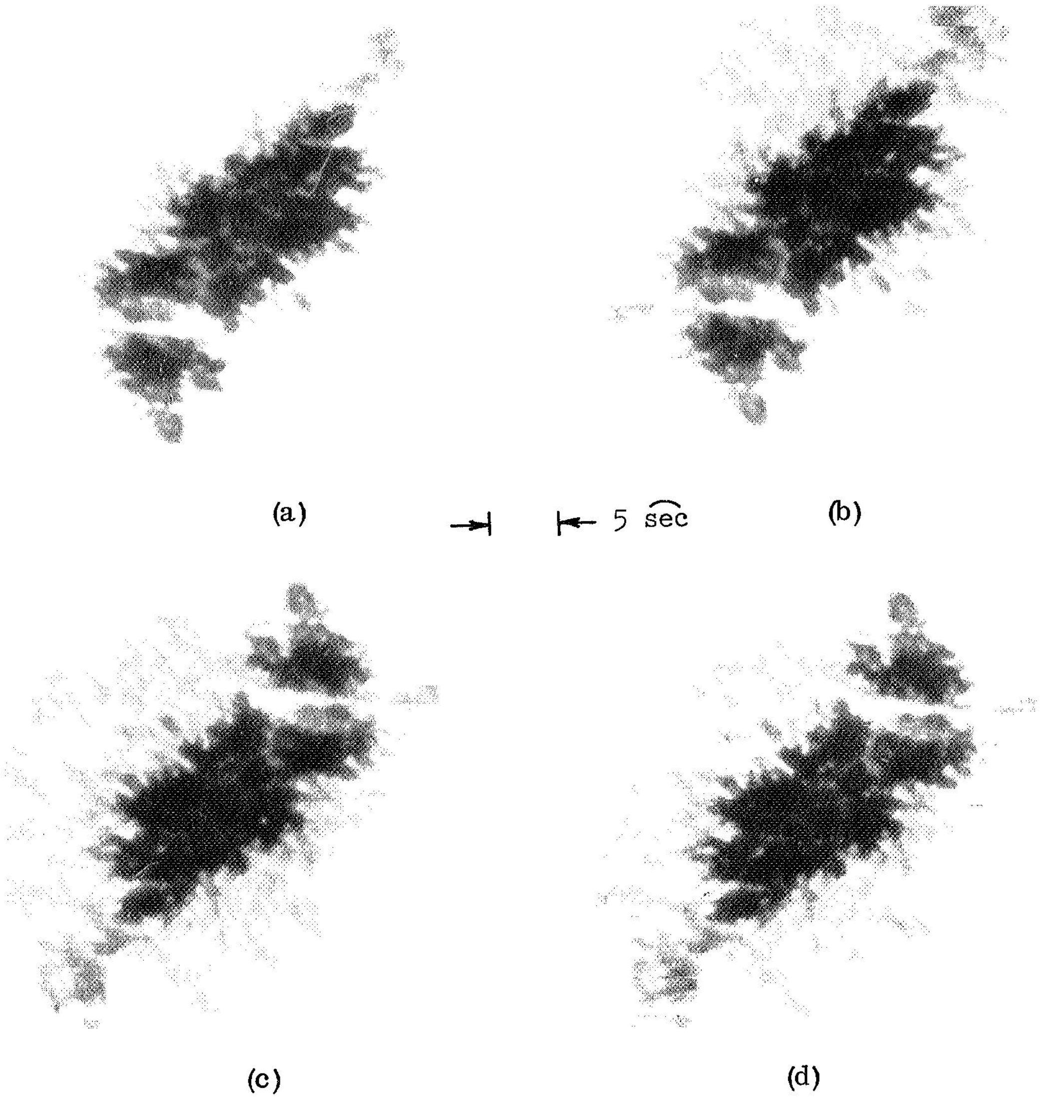

Figure 2. - The original stratoscope photographs displayed from the digitized intensities. (a) 5934 D. (b) 5941 D. (c) 5951 D. (d) 5957 D.

Next, the four pictures were registered by finding the amount of shift which produced the maximum correlation. To compensate for slight rotation misalignments occurring in the digitization procedure, the pictures were also rotated to produce maximum correlation. The average of the registered pictures is shown in figure 3(a). As expected, the noise is substantially reduced in the averaged picture (see figure 3).

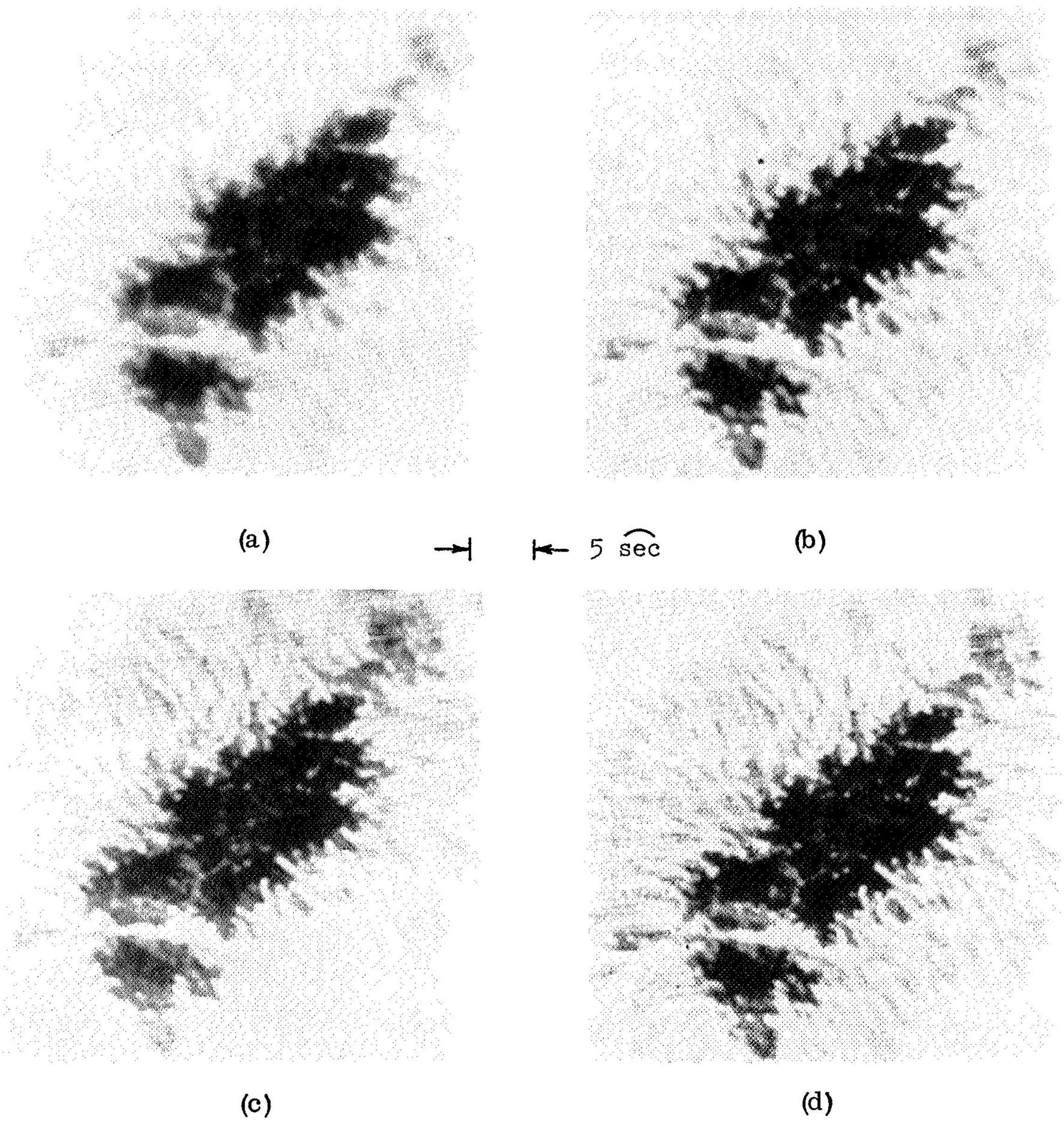

Figure 3. - Comparison of the average of the photographs shown in figure 2 with three enhanced photographs. (a) Average picture. (b) Enhanced with T_r2 . (c) Enhanced with T_r3. (d) Enhanced with T_r4.

The last step in the image processing procedure is to sharpen the picture by amplifying the larger spatial frequencies to compensate for the reduction in amplitude shown in figure 1. Since the inverse transfer function, T^{-1}, goes to infinity (see figure 4) at the limiting optical spatial frequency, T_r, the transfer function used to restore the averaged picture must be limited at the higher spatial frequencies in a way determined by the noise in the picture. Brault and White (5) have shown that an optimum correction function is given by

$$T_r = T^{-1}\Phi$$

where $\Phi = S/S+N$ and where S is the signal in the power spectrum and where N is the noise. The expression for Φ arises from the requirement that the restored picture present the best rms approximation to the true picture.

Figure 4 shows the value of Φ which was computed from the power spectrum. It is evident that S/N, the signal to noise ratio, becomes very low as the limiting spatial frequency is approached. Consequently, $T_{r2} = \Phi\ T^{-1}$, also shown in figure 4, reaches a maximum of two at 0.1 cycles/sample and approaches zero at 0.225 cycles/sample, the limiting optical frequency. Because the separation of the signal from the noise in the power spectrum computed from the averaged picture shown in figure

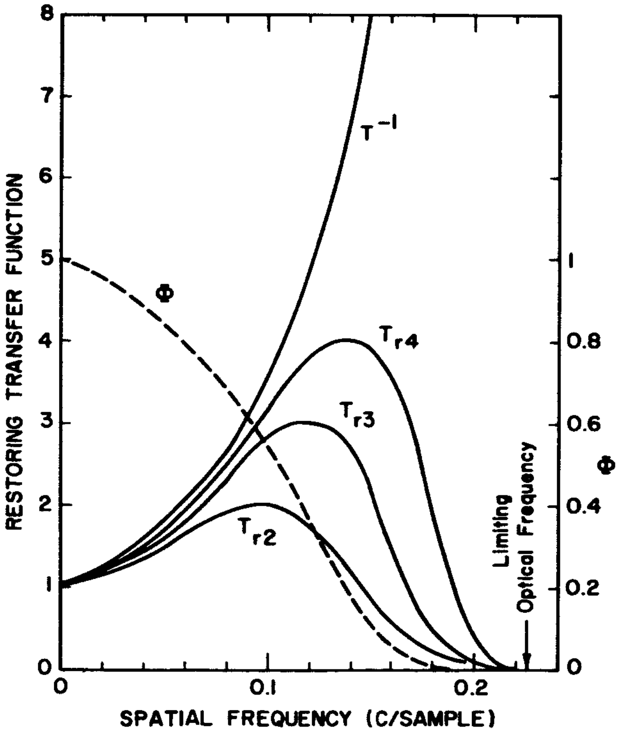

Figure 4.-In the absence of noise, T^{-1} would be the correct restoring transfer function. $T_{r2} = T^{-1}\Phi$ is the optimum transfer function derived from the signal to noise ratio in the averaged picture. T_{r3} and T_{r4} are similar restoring transfer functions.

3 (a) was rather uncertain, two similar restoring transfer functions which have maximum magnifications of three (T_{r3}) and four (T_{r4}) were also tried.

Figures 3(b)-3(d) display the enhanced pictures using T_{r2}, T_{r3}, and T_{r4}, respectively. The processing was accomplished by a convolution of the average picture with the Hankel transforms of T_{r2}, T_{r3}, and T_{r4}. To limit the computing time, the above filters were limited to 17 x 17 samples for the first two filters and 21 x 21 samples for the last. Since the limiting optical frequency was 0.225 cycles/sample, the size of the weighting functions is comparable with the second dark ring in the point spread profile which is 20 samples in diameter.

From inspection of these photographs, one can see the enhancement resulting from the amplification of the intermediate spatial frequencies. In particular, the small points of light in the dark umbra of the sunspot, called umbral dots (1), are much more visible in the enhanced pictures. The half intensity diameter of the umbral dots is about 6 samples, the expected half intensity diameter of the point spread profile in the restored pictures. Thus, the umbral dots are evidently unresolved by the 12-inch diameter Stratoscope I telescope.

DISCUSSION OF RESULTS

The main technical conclusion emerging from this work is that image enhancement of diffraction limited photographs will very often be accomplished by selectivity amplifying the intermediate spatial frequencies, i.e., those near one-half the limiting optical frequency. The reason the highest frequencies can not generally be amplified is that the grain noise is a few percent when sampled in accordance with the sampling theorem. This results in the signal to noise ratio rapidly dropping below unity (Φ dropping below 0.5) as the limiting frequency is approached, especially for a low contrast scene. Of course, the noise could be decreased by optically enlarging the image on the film; however, there are limits to this. Enlarging the image increases the required exposure time by the square of the picture size. In the case of Stratoscope I, which used Background X film at f/200, the exposure times could not be lengthened because of the limitations of the servo system. For diffraction limited stellar telescopes such as Stratoscope II, the exposure times for the great majority of astronomical objects is very long even at a focal ratio of f/50 which is 16 times faster than that used by Stratoscope I.

The visibility of the umbral dots increases from T_{r2} through T_{r4}, suggesting that none of the filters used are optimum for visual presentation. However, the best visual presentation may not be the best quantitative representation of a picture. It would be quite possible to improve the appearance of a picture by amplifying the intermediate spatial frequencies higher than in the original scene. This has probably not happened in our case, although the possibility exists since the amount of instrumental blurring may have been overestimated (3). In any case, to avoid misleading comparisons, an effort was made to insure that the average intensity of the umbra in each of the photographs in figures 2 and 3 remained approximately equal.

The main scientific result emerging from this work is that the sunspot umbra contains more detailed structure than was previously apparent (1). It appears that this structure consists mostly, if not entirely, of unresolved bright points (i.e. umbral dots). The photometric correction which converted densities to intensities was not carefully done. As a result, no safe quantitative results can be given without a careful re-examination of the photometric correction. Nevertheless, it is interesting that the peak intensity of the most prominent umbral dots is roughly 0.25 of the photospheric brightness. If, as suggested by the color measurements (2), the true brightness of the brightest umbral dots is equal to the photospheric brightness, then their true half intensity diameter can be estimated from their apparent half intensity diameters. The latter value is about 6 samples or about 0.50 arcsec, corresponding to an apparent distance of 360 km on the sun. The corresponding true half intensity diameter is roughly 180 km and is in general agreement with (2).

FUTURE PLANS

The successful flight of Stratoscope II on March 26-27, 1970 yielded many high definition photographs of Uranus, Jupiter, and Io. Images of comparison stars reveal point spread profiles which show diffraction rings characteristic of a 36-inch aperture. Although the rings are not of uniform brightness and the central peak is somewhat elongated, the instrumental profile appears to be quite stable with time.

The proper enhancement of these photographs will require the use of a non-symmetric weighting function in the restoring convolution. Preparations are now underway to compute the required two dimensional complex Fourier transforms.

ACKNOWLEDGEMENTS

Of the many individuals who contributed to the development of the image processing program at Princeton, special recognition is due to Arthur Miller, John Lowrance and Paul Zucchino of Princeton and Dave Lovell of IBM. Most of the computer processing utilized the JPL VICAR program, kindly supplied by Mr. Tom Rindfleisch of JPL. The program was supported by NASA Grant NGR-31-001-142.

REFERENCES

1. Danielson, R.E., The Structure of Sunspot Umbras. I. Observations, Astrophysical Journal, Vol. 139, 1964, pp. 45-47.

2. Beckers, J.M. and Schröter, E.H., The Intensity, Velocity and Magnetic Structure of a Sunspot Region. II. Some Properties of Umbral Dots, Solar Physics, Vol. 4, 1968, pp. 303-314.

3. Gaustad, J.E. and Rogerson, J.B., Jr., The Solar Limb Intensity Profile, Astrophysical Journal, Vol. 134, 1961, pp. 323-330.

4. Zucchino, P.M., Progress Report on the Development of the SEC Vidicon for Astronomy, Proceedings of Symposium on the Astronomical Use of Television Type Image Sensors, 1970, pp. 37-74

5. Brault, J.W. and White, O.R., The Analysis and Restoration of Astronomical Data via the Fast Fourier Transform, 1970, submitted to Astrophysical Journal.

THE PROCESSING OF ELECTRONIC CAMERA IMAGES

Gerald E. Kron
U. S. Naval Observatory
Flagstaff Station

The principle of the Electronic Camera was conceived by Prof. A. Lallemand of the Paris Observatory (1) in 1936. A functional model was constructed in his laboratory after the war. The electronic camera can produce, by direct electronic recording, a permanent picture on any kind of silver halide emulsion. By means of a study of pictures made with his camera, Lallemand and his co-workers reached the conclusion that the electronic camera method would be of exceptional value in recording astronomical data.

The results obtained by Lallemand stimulated a developmental project at the Lick Observatory in 1958 (2) to produce a Lallemand type of electronic camera that would be of increased practicability and simpler technology than the prototype. This project reached success at the Flagstaff Station of the U. S. Naval Observatory (3) in 1967 with the production of a low-background electronic camera (Figure 1) that could be used to take pictures indefinitely with one permanent photocathode. The relative simplicity of operation of this camera has made it possible for our group of investigators to make a thorough new study of its properties and to begin the process of developing practical methods of removing and processing the astronomical data recorded on the plates. Collaborators in this study are Drs. Harold Ables and Anthony Hewitt of the Flagstaff Station.

TECHNICAL DISCUSSION

Comparison With Photography – Though the photographic and electrographic processes both deliver pictures on silver halide emulsions – pictures that generally appear to the eye to be much alike – many differences do, in fact, exist. These differences are subtle, but important. Often quoted, and much emphasized, is the relatively large superiority of the electronic method in detective quantum efficiency (4) which results in a significant information gain over the best photographic emulsions (5). More important, however, are the practically linear relation between density and exposure of the electronic method and the range over which the operator can select emulsions with different data storage capacities. These storage capacities run from about equal to that of photographs up to more than 100 times the photographic capacity. Additional advantages of the electronic camera method over photography are lack of reciprocity failure, better uniformity

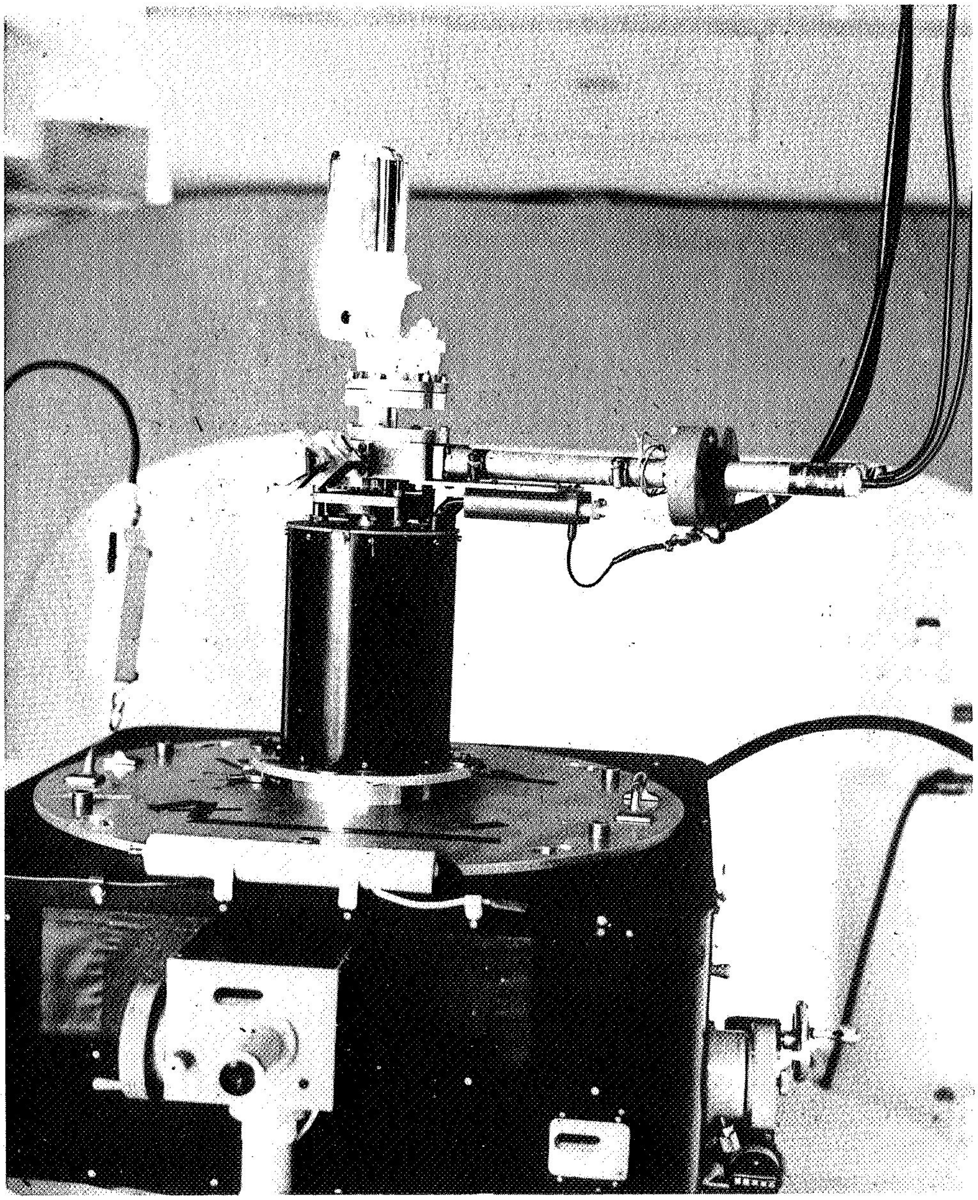

Figure 1.-The electronic camera mounted on the U.S. Navy 61-inch astrometric reflector.

of sensitivity over the plate, reduced proximity and diffusion effects, and total lack of halation. The electronic camera is thus an efficient, simple device for permanently storing photometric data in a form that is compact and readily available, especially for fast initial appraisal.

Data Removal – Complete removal of all data from an astronomical recording would permit a recovery of the recorded photometric and spatial data of the original scene. A linear relationship between exposure and some measurable property (usually density) of the picture simplifies data handling because point-by-point corrections from a characteristic curve are unnecessary. Incomplete simple photometric recovery is, however, often sufficient, as in stellar photometry, which requires only an appraisal of the integrated exposure. A linear characteristic curve makes feasible the removal of the photometric data by scanning the image and integrating each scan by means of a simple analogue integrating device; the sum of the integrals for all scans is then proportional to the brightness of the object. Photometry by this method is in principle the exact analogue of astronomical photoelectric photometry. Extrapolation beyond the range of the standards is possible, an attribute that can be appreciated by those astronomers who have done iris photometry from photographs.

The electronic camera has several advantages over the simple photoelectric approach. Background separation is optimum, and many objects can be recorded at once (as with photography) with the same exposure, thus saving telescope time needed for problems such as the photometry of stars in clusters.

The linearity of the relationship between density and exposure for electrographic recordings has been the subject of many investigations by electron microscopists and by astronomers. Results are still controversial (6). In our laboratory, Ables (5) has obtained results with Ilford nuclear track emulsions that appear to be more encouraging than those obtained elsewhere. A sample density vs exposure curve for Ilford L.4 emulsion ten microns thick on glass is shown in Figure 2. Development was for five minutes in fresh D-19 with agitation at 68°F, and the sample densities were measured with a Joyce-Loebl densitometer. Generally, we find linearity within the errors of measurement for Ilford G.5 and K.5 emulsions, but to lower densities than for L.4. We also find practical linearity to densities between two and three for Agfa-Gevaert holographic emulsions 8E56 and 10E56, which are very fine grained and consequently of high storage. An experimental electrographic emulsion of finer grain and higher storage than L.4, produced by Eastman Kodak and designated Q-166-10, has been found to be linear to density four.

Stellar Photometry – Stellar photometry has been accomplished with electrographic plates by Lallemand et al.(7), who measured the images with an iris photometer, by Walker and Kron (8), by Walker (9), and by Kron, Ables and Hewitt (3). Walker and Kron extracted data with single scans employing a slit-shaped scanning aperture, Walker used superimposed multiple scans across the image center employing a small, square scanning aperture, and Kron, Ables and Hewitt employed isophotic recordings made with a Joyce-Loebl-Tech-Ops Isodensitracer. In that case each isophote for each star was measured for area by means of a planimeter; with these data and the known density steps, the spatial-density solid representing all of the photometric information in each image could be reconstructed, but only with much labor. The scanning methods and the isophotic method all produced photometric output that agreed well with direct photoelectric photometry over ranges as great as five magnitudes for a single electronic exposure, and with experimental errors comparable with those of photoelectric photometry. The isophotic method we regard as the best because it gives a more complete sampling of the background, of importance in measuring faint stars, and

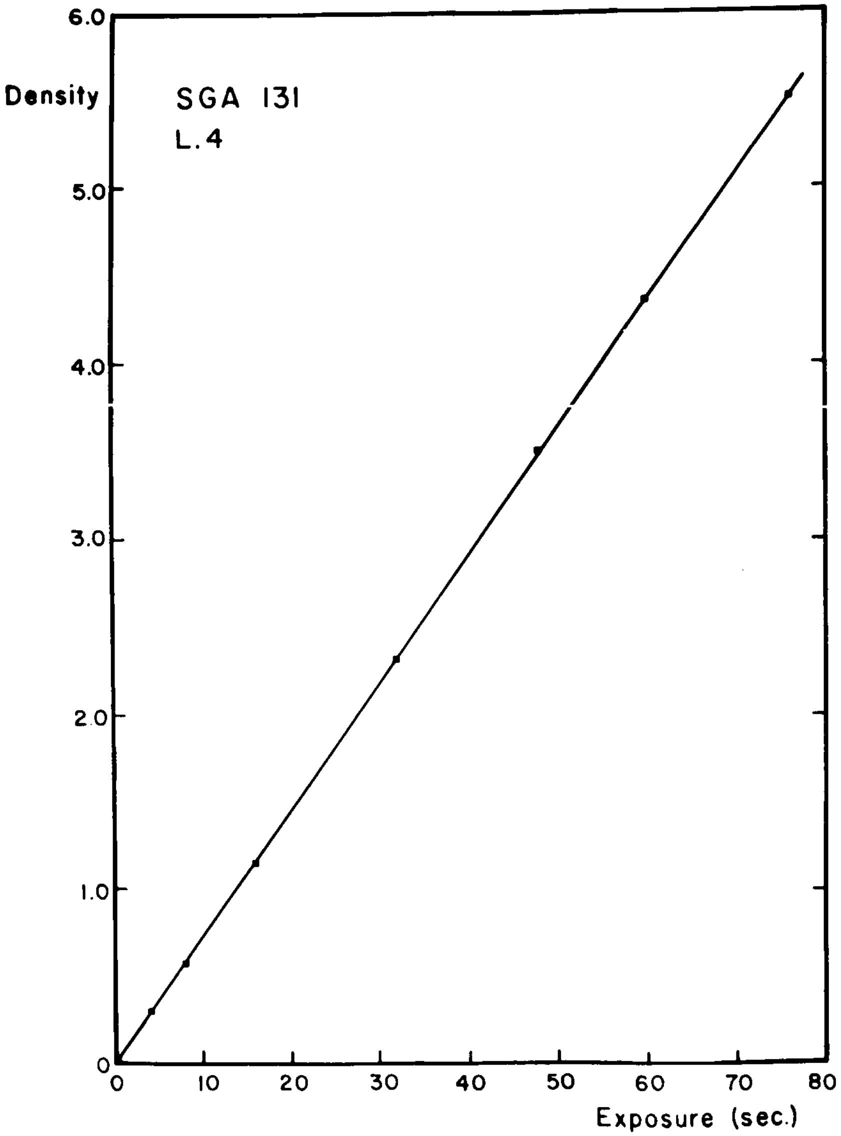

Figure 2.-Density vs exposure for Ilford L.4 nuclear track emulsion. The light is a straight line drawn through the origin.

because the output is insensitive to field distortions and aberrations. The large amount of labor required by the isophotic method makes it impracticable (one measurement of one star takes more than a man-hour of effort) but Hewitt has developed an integrating, scanning microphotometric method that accomplishes the same result with relatively little human effort.

Hewitt fitted the Isodensitracer with an analogue electrical output which is integrated by an electronic integration circuit and recorded as a line on a strip-chart recorder; simultaneously the data are punched on a card by an IBM punch. The strip-chart output and the monitor isodensity recording for a double star are shown in Figure 3. The strip-chart and isodensity outputs are examined for plate defects, but data from these examinations are not used in the computations. The punched cards containing the

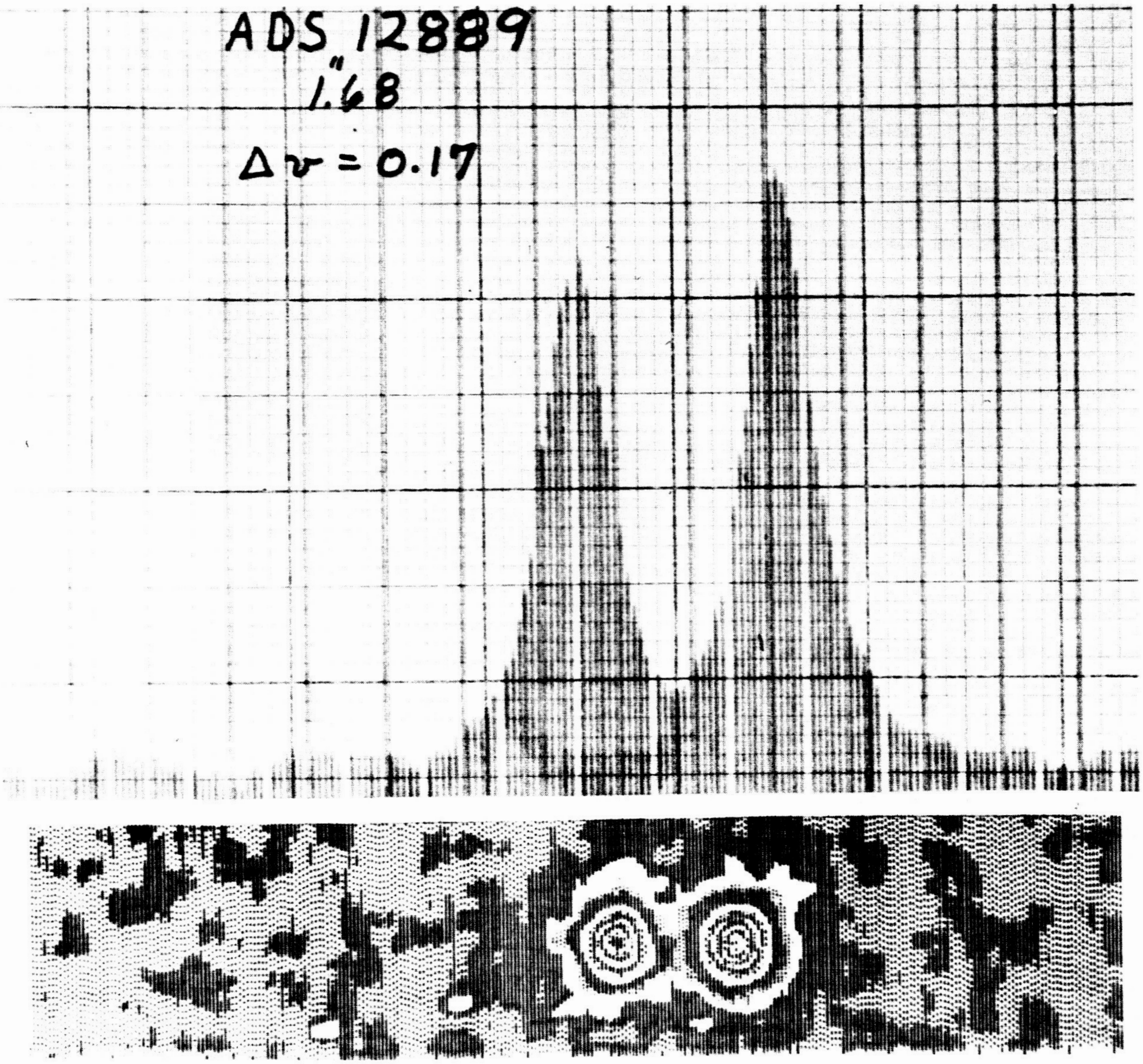

Figure 3.-Isophots and strip-chart recordings of scan integrals illustrating the output from the integrating isodensitometer employed at the Flagstaff Station for removing data from electronic camera plates.

observational data are fed into an IBM 1130 computer which evaluates the background level and subtracts it from the sum of the integrals to get the volume of the density solid. The measuring error was investigated by scanning a star image in different directions and was found to be less than one percent. With this equipment, Ables has obtained a magnitude sequence of stars in the cluster NGC 6791, which had been measured with high precision by Kinman (10). Kinman's photometry was done photoelectrically and photographically employing the 120-inch reflector of the Lick Observatory. Ables' photometry was based upon three exposures made on L.4 emulsion with our electronic camera, employing the Navy 61-inch astrometric reflector, and was measured and reduced as described above, with the assumption that the emulsion had a linear response. Kinman's and Ables' magnitudes are compared in Figure 4, where the solid line is at a slope of 1.00 and is drawn up to magnitude 21, where Kinman's data stop. Ables carried the sequence two magnitudes further; these data are symbolically entered as an extension beyond the solid line and are coded with solid squares and open circles. Ables' measurements covered a range of nine magnitudes, obtained from exposures of 30-minute and 0.5-minute duration, reduced to each other by the exposure ratio of 60/1; i.e., lack of reciprocity failure was assumed. Over the magnitude range of 18 to 21, Kinman estimated a mean experimental error in his measurements of about 0.05 magnitude per star, whereas Ables finds the same from an intercomparison of the measures from his two 30-minute exposures (11). It can be concluded that electronic camera plates, when measured with Hewitt's integrating densitometer, yield stellar magnitudes on the Pogson scale with the assumption of a linear response, and that the experimental errors are comparable to those that accompany presently accepted methods of photometry. In addition, it has been found easily possible to extend a magnitude sequence to a B magnitude of 23 on the basis of reasonable exposure times with the electronic camera and a 61-inch telescope.

We have also made a comparison of our capability with limiting photoelectric stellar photometry made by W.A. Baum (12) on stars in the globular star cluster M13. Baum carried photoelectric photometry to the faintest magnitudes that appeared to be at all practical with the 200-inch Hale Reflector. We obtained an electronic camera plate of one-hour exposure during good "seeing" with the Navy 61-inch astrometric reflector of Baum's star field and found that we could identify and measure all of the stars in Baum's sequence and that we could extend the sequence further by another half magnitude. We are convinced that we could extend a magnitude sequence to B = 24^m with the same operating conditions but with astronomical "seeing" conditions of the best that we ever enjoy at our Flagstaff observing site.

Storage Capacity and Deconvolution – Of all the interesting properties of the electronic camera, its ability to store large quantities of data is most remarkable and least developed. In the accompanying table are listed the number of grains available at unit density for a number of emulsions. The numbers for IIa-O, G.5 and L.4 emulsions are from actual counts (3), whereas the numbers for the finer grained emulsions have been inferred from density ratio data obtained recently at the Flagstaff Station. For all

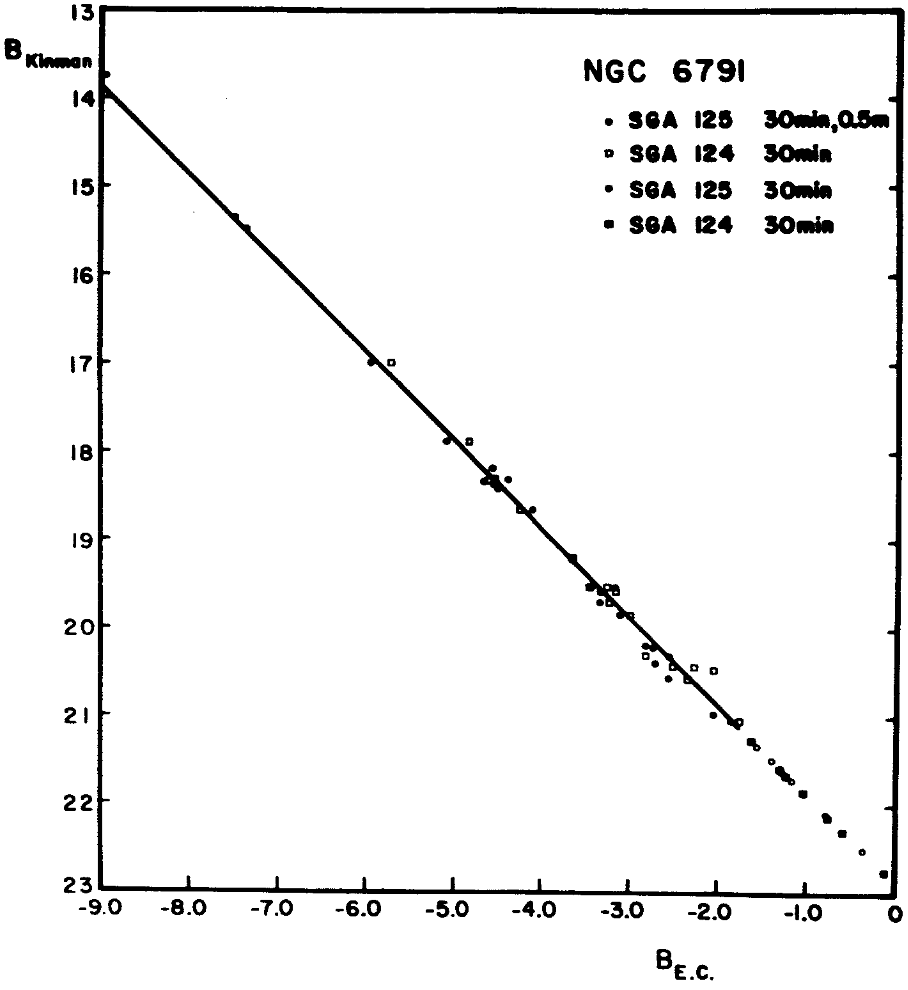

Figure 4. -Stellar magnitudes determined with the electronic camera and integrating isodensitometer compared with photoelectric magnitudes by Kinman. The line is a straight line drawn at a slope of unity.

emulsions except the IIa-O, which had been exposed to light, the "grains" counted were actually the electron tracks made by 30 kV electrons.

Emulsion	Grains/sq mm at unit density
IIa-O	0.6×10^6
G.5	1.3
L.4	5.4
10 E 56	50
Q-166-10	50
8E56	135
649-O	500 (non linear)

A qualitative illustration of a simple application of storage capacity can be seen in Figure 5, which shows recordings of three double stars on IIa-O, L.4, and 8E56 emulsions; the IIa-O recording is, of course, a photograph. Although the double star photographed on the IIa-O has the widest spacing in the sky, the recorded resolution is the poorest of the lot by far; of the remaining two, the separations in the sky are about equal, but the resolution is clearly better for the 8E56 emulsion. This is the result of collecting and storing more data, though the photograph may have suffered somewhat from diffusion and proximity effects. Figure 3 shows integrals and isophots for the double star recorded with the L.4 emulsion. Quantitative work done on a number of double stars with such integrals indicates that the best available way to measure the separations, position angles, and magnitude differences of double stars is by means of the electronic camera.

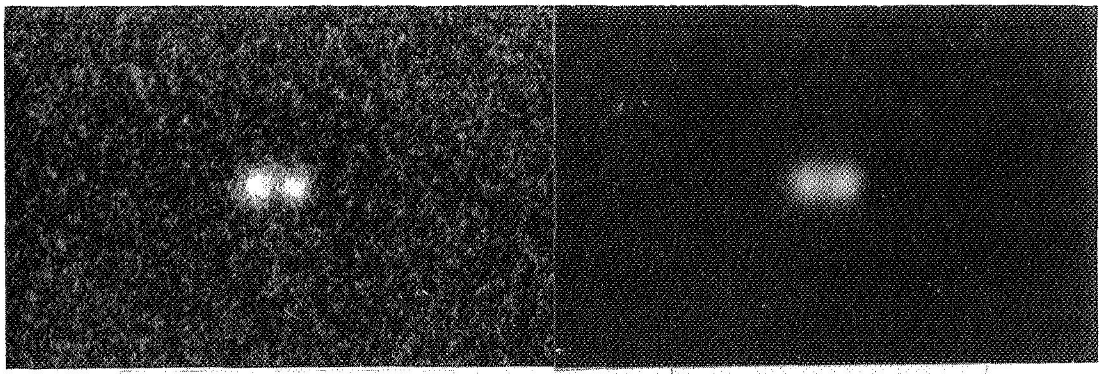

IIa-O Emulsion
2".7 Separation

L.4 Emulsion
1".7 Separation

8E56 Emulsion
2".0 Separation

Figure 5.-Recordings of double star images showing the effect of using larger and larger storage of information. The recording on IIa-O emulsion is a photograph; the others are electrographs. The separations quoted are the actual separations in the sky in seconds of arc. The apparent separations have been rendered equal by scaling with the enlarger.

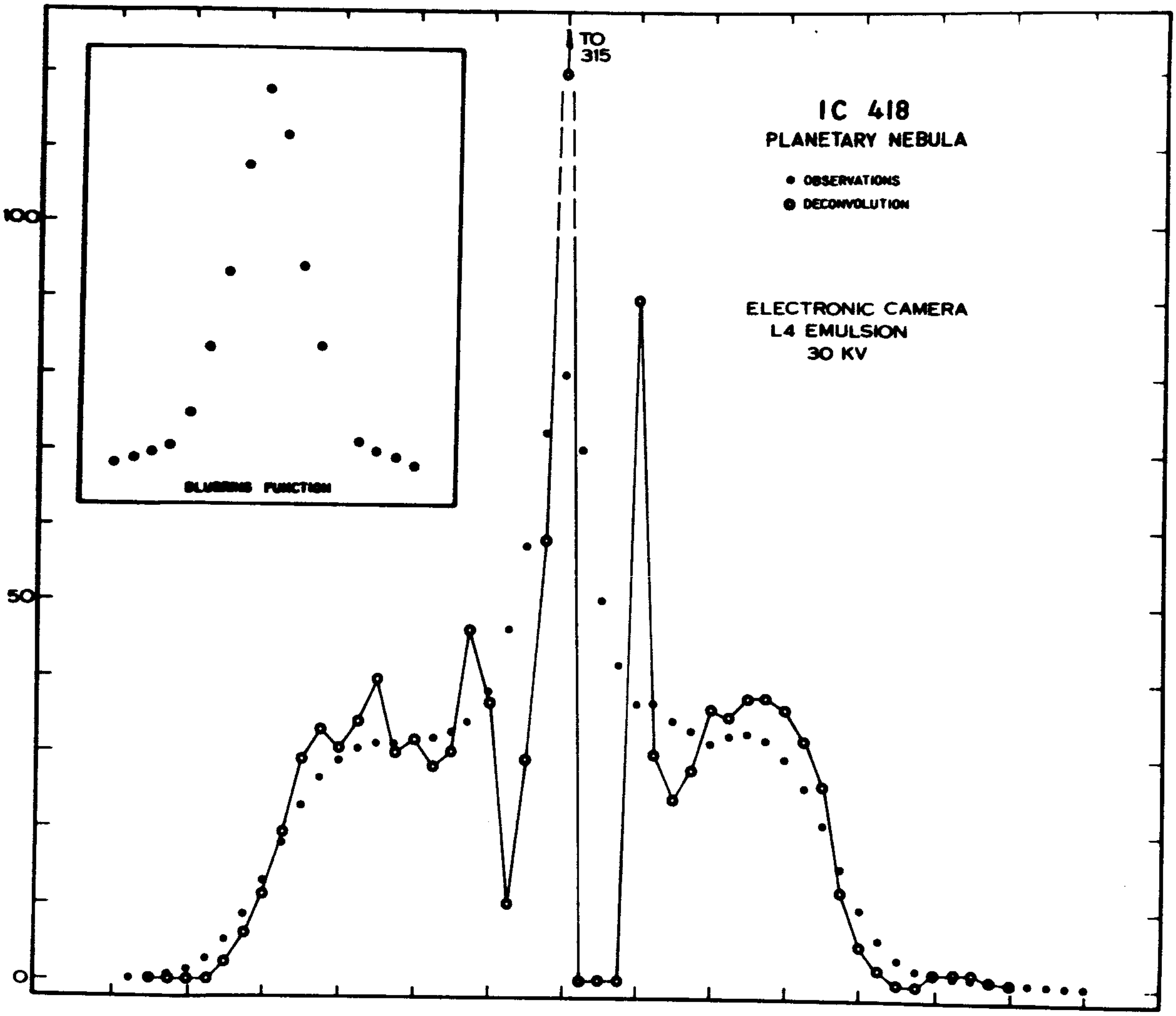

Figure 6.-A deconvolution of an electronic camera image of a planetary nebula. Note extreme central intensity of central star and relatively dark areas on each side of star.

One of the most fascinating future applications of electronic camera recordings will be for the recovery of spatial information by the deconvolution of the observed image with the instrumental profile function. This kind of recovery represents practically a trade-off of photometric information for spatial information. Photographic recordings can, of course, be used for this purpose, but little is to be gained unless one can store much more photometric information than astronomical photographic emulsions can hold within their limited linear ranges. A partial solution to the problem lies in taking many photographs and superimposing them, but the gain won by doing this is partly lost by the accumulated background and difficulties with the superposition process. The electronic camera employed with an emulsion like 8E56 can store about 200 times more information in one picture than one can store on a single exposure with a IIa-O photograph. A star image, recorded at the same time as the subject, gives the instrumental profile, or blurring function. It should be possible, by this method, to obtain superior recordings of planetary detail, galactic nuclei, planetary nebulae, distant star clusters, and other difficult astronomical objects. The deconvolution would have to be preceded by a complete removal of the photometric information followed by storage in a large computer, which would have to be programmed for a full-dress two dimensional deconvolution. We have been unable to undertake such a large problem, but we have accomplished the deconvolution of a single slice of the planetary nebula IC 418. The electrograph from which the data were taken by a scan with our Joyce-Loebl microdensitometer was obtained with a McGee Spectrocon by Dr. Merle F. Walker working with telescopic equipment at the Cerro Tololo International Observatory. The blurring function was obtained from the profile of a star image obtained with another exposure on the same night. The deconvolution was accomplished by means of a very crude process, using the assumption that both the subject and the blurring functions were plane sections instead of three dimensional solids. The calculation was aided by the use of a programmable desk calculator with a procedure set up by Mr. Richard Walker of the Flagstaff Station. The process consisted in guessing at a deconvolution and then convolving this with the blurring function by means of serial products, a common way of employing trial and error for this problem. After seven trials the observed curve was closely fitted. The **results** are shown in Figure 6. The deconvolved profile, shown by the open circles has, of course, steeper slopes than the observed one, shown by solid dots. The central star becomes, as expected, very sharp and of extremely high central amplitude and constitutes a rough test of the efficacy of the process. The surprise was the discovery of a dark region adjacent to each side of the central star, a property not even suspected from the appearance of the original recording.

CONCLUSIONS

The electronic camera is now a useful astronomical tool with a potential that is only beginning to be appreciated. Diligent application of the electronic camera will make it possible to employ all telescopes with much greater efficiency than when these same telescopes are used with photography. The electrograph is a compact, permanent storehouse of photometric information whose storage can be controlled over a large range by the operator. The electrograph can be analysed under laboratory conditions, though present methods are primitive and, for the higher storage emulsions, inadequate. Considerable further development is needed on both the camera itself and data handling methods.

REFERENCES

1. Lallemand, A., Application de l'Optique Electronique a la Photographie, Vol. 203, 1936, p. 243.

2. Kron, G.E., An Image Tube Experiment at the Lick Observatory, Pub. Astron. Soc. Pac., Vol. 71, 1959, pp. 386-387.

3. Kron, G.E., Ables, H.D. and Hewitt, A.V., A Technical Description of the Construction, Function, and Application of the U.S. Navy Electronic Camera, Advances in Electronics and Electron Physics, Vol. 28A, 1969, pp. 1-17.

4. Lallemand, A., Sur l'Application a la Photographie d'une Methode Permettant d'Amplifier l'Energie des Photons, C.R. Acad. Sci. (Paris) 203, 990, 1936.

5. Ables, H.D. and Kron, G.E., The Linearity and Information Gain of an Electronic Camera, Pub. Astron. Soc. Pac., Vol. 79, 1967, pp. 423-424.

6. Bied-Charreton, P., Bijaoui, A., Duchesne, M., and LeContel, J.M., Sur Quelques Progres Recents Apportes a la Camera Electronique a Focalisation Electrostatique et sur son Application en Physique et en Astronomie, Advances in Electronics and Electron Physics, Vol. 28A, 1969, pp. 27-37.

7. Lallemand, A., Canavaggia, R., and Amiot, F., Comptes Rendus, Vol. 262, 1966, p. 838.

8. Walker, M.F., and Kron, G.E., The Determination of Stellar Magnitudes by Electronography, Pub. Astron. Soc. Pac., Vol. 79, 1967, pp. 551-568.

9. Walker, M.F., in press.

10. Kinman, T.D., The Star Cluster NGC 6791, Astrophys. Jour., Vol. 142, 1965, pp. 655-680.

11. Ables, H.D., Kron, G.E., and Hewitt, A.V., Electrographic Stellar Photometry (abstract), Bulletin of the Amer. Astron. Soc., Vol. 1, 1969, p. 231.

12. Baum, W.A., The Tentative Identification of the Main Sequence of Population II from Photoelectric Observations in M13, Vol. 59, 1954, pp. 422-432.

NASA-Langley, 1971 —— 14

NATIONAL AERONAUTICS AND SPACE ADMINISTRATION
WASHINGTON, D.C. 20546

OFFICIAL BUSINESS
PENALTY FOR PRIVATE USE $300

FIRST CLASS MAIL

POSTAGE AND FEES PAID
NATIONAL AERONAUTICS AN
SPACE ADMINISTRATION

POSTMASTER: If Undeliverable (Section 158
Postal Manual) Do Not Retur

> *"The aeronautical and space activities of the United States shall be conducted so as to contribute . . . to the expansion of human knowledge of phenomena in the atmosphere and space. The Administration shall provide for the widest practicable and appropriate dissemination of information concerning its activities and the results thereof."*
>
> —NATIONAL AERONAUTICS AND SPACE ACT OF 1958

NASA SCIENTIFIC AND TECHNICAL PUBLICATIONS

TECHNICAL REPORTS: Scientific and technical information considered important, complete, and a lasting contribution to existing knowledge.

TECHNICAL NOTES: Information less broad in scope but nevertheless of importance as a contribution to existing knowledge.

TECHNICAL MEMORANDUMS: Information receiving limited distribution because of preliminary data, security classification, or other reasons.

CONTRACTOR REPORTS: Scientific and technical information generated under a NASA contract or grant and considered an important contribution to existing knowledge.

TECHNICAL TRANSLATIONS: Information published in a foreign language considered to merit NASA distribution in English.

SPECIAL PUBLICATIONS: Information derived from or of value to NASA activities. Publications include conference proceedings, monographs, data compilations, handbooks, sourcebooks, and special bibliographies.

TECHNOLOGY UTILIZATION PUBLICATIONS: Information on technology used by NASA that may be of particular interest in commercial and other non-aerospace applications. Publications include Tech Briefs, Technology Utilization Reports and Technology Surveys.

Details on the availability of these publications may be obtained from:

SCIENTIFIC AND TECHNICAL INFORMATION OFFICE
NATIONAL AERONAUTICS AND SPACE ADMINISTRATION
Washington, D.C. 20546